

ELECTICAL FACILITY EFFECTS ON HALL EFFECT THRUSTER OPERATION

A Dissertation
Presented to
The Academic Faculty

by

Jonathan A. Walker

In Partial Fulfillment
of the Requirements for the Degree
Doctor of Philosophy in the
Daniel Guggenheim School of Aerospace Engineering

Georgia Institute of Technology
December 2016

Copyright © 2016 by Jonathan A. Walker

ELECTICAL FACILITY EFFECTS ON HALL EFFECT THRUSTER OPERATION

Approved by:

Professor Mitchell L. R. Walker II,
Advisor
Daniel Guggenheim School of
Aerospace Engineering
Georgia Institute of Technology

Professor Jerry M. Seitzman
Daniel Guggenheim School of
Aerospace Engineering
Georgia Institute of Technology

Professor Wenting Sun
Daniel Guggenheim School of
Aerospace Engineering
Georgia Institute of Technology

Professor Carol S. Paty
School of Earth and Atmospheric
Sciences
Georgia Institute of Technology

Dr. Daniel Herman
Electric Propulsion Systems Branch
NASA Glenn Research Center

Date Approved: October 26, 2016

ACKNOWLEDGEMENTS

Let me first start by saying, “Thank you and good luck!” to all those who are attempting to read this document. I will apologize in advance for any confusion, frustration, and general hopelessness that you feel from reading this document. It has taken me 6 years to reach a point in my studies that I now feel comfortable enough to write this culminating manuscript. I will tell you that at the end of the Ph.D. road, there is a fair amount of scramble and craziness that goes along with it. So see if you can fair better! As you are reading this, it is my sincere hope that you find something useful in the following work. If you ever have questions about the work performed, please do not hesitate to contact me. I am very proud of my dissertation work, and I would be more than happy to talk about it with anyone.

I have been only able to complete this work due to the amazing amount of support my wonderful wife, Elizabeth, has given me. As experimental work goes, things almost never go right the first time or even the second time, and so there have been many long nights spent at the lab. Thank you so much for your support, love, and patience as you put up with what Natalie would describe as a manic experimentalist. If it weren't for you, I would have been a shriveled husk of a graduate student. To my children who might be reading this document for some crazy reason, I hope that you girls one-day find something that engages and challenges you as much as this dissertation work has done for me. There is nothing like working on something that requires 100% of your faculties. When I would run an experiment, I could not wait to get to the lab to start the experiment for the day. I hope that you girls find something like that one day.

Mom, Dad thank you so much for being there throughout my education and my life. I know that I have been a source of much worry and grief, and I appreciate everything that you have done me. Kathryn and Gene, I cannot thank you enough for all the support that you have given me and Lizzy. You guys have been an amazing support network to not

only me but also to my fledging family. I don't know what I would have done without your help. Thank you!

I owe a great deal of thanks and appreciation to my advisor Dr. Walker (no relation). Thank-you so much for mentoring and for supporting me all these years. At heart, I am dreamer and an optimist, so thank-you for keeping me from pursuing thesis ideas that would have had no end in sight for sure. I don't think my marriage could have withstood an indefinite tenure as a graduate student. I don't know how you do what you do, but I sincerely appreciate all your patience and guidance that you have given me.

I would like to thank all the members of the committee, Dr. Jerry Seitzman, Dr. Wenting Sun, Dr. Carol Paty, and Dr. Daniel Herman for taking time out of your busy schedules to listen to my presentation and read through this document. Thank you so much Dr. Sun for letting me borrow your nice oscilloscope as many times as I did. Without it, this thesis would have been dead in the water. Thank you Dr. Herman for all your mentorship while I was at NASA Glenn. I thoroughly enjoyed working out in the real world and was able to work on some pretty cool stuff because of you. I hope that I didn't cause too much of a headache for you. Thank you Dr. Seitzman for being a thoroughly challenging professor and educator. The way in which you teach your classes and your fundamental principles of learning are something that I one day will model in my own classroom. Thank you Dr. Paty for opening my eyes to wider world of space and interplanetary research. I was cloistered away in the aerospace department for so long; I was down in the weeds of research for so long that I almost forgot about why I wanted to do work in the space field. Every day in class was like, "Wow that's really cool! We should really send more instrumentation to [insert planet, moon, or region of space] to find out what is really going on." I thoroughly enjoyed being in your class and being able to get an idea of what the real end game is for all this research and development into space related technologies.

I owe a huge thank-you to all the members of the High Power Electric Propulsion Laboratory. Graduate school has been a tough and challenging road. I appreciate all the company and support that you have given me. Without you guys, I don't think finishing graduate school would have been possible. To the old hands of the lab, Gabe and Logan, you guys set the bar in the proficiency that a skilled researcher needs to have to be a successful experimentalist. Also, you guys did an amazing job building a community that we youngsters could thrive in. I appreciate all the help you guys gave me when I was frantically trying to get my experiments underway. Lake (like a body of water), from working in the lab to cooking food out in my backyard, I always enjoyed hanging out with you. You have a wit and intellect that always kept me on my toes, and I thoroughly enjoyed being in graduate school with you. Scott, you are one thorough researcher and engineer. The devil is in the details, and man you can hammer it out like no-one else. The COMET is one beautiful thruster. Sam, Brenna, Natalie, and Brent, I can't thank you guys enough for all the support and friendship that you gave me and my family throughout graduate school. Sam, you are one cool cucumber, and somehow you have this amazing ability to pinpoint the true heartache of a problem. Your level-headed, even keeled approach to problem solving and life is something that I strive to achieve. Natalie, you are the wisest graduate student that the lab will ever know. I don't know how you did it but somehow you were able to put up with all our craziness and still be the glue that held our lab community together. Aaron, you are definitely one of the smartest people that I have ever met. I thoroughly enjoyed our discussions about physics, plasmas, and general phenomenon in the world. You are never satisfied with one-line answers, and I am always amazed at how much deeper your understanding goes on any subject. Cheong, I don't know where I would be without all your help that you have given me on my thesis research. I can't thank you enough for spending all hours of the night helping me run my experiment and helping me analyze data. Nathan P., always "Be excellent to each other", and I will always remember

to “Party on!”. I am glad that I was able work alongside you and get to know you. Remember man, you’ve got this. Tom, you are one of the most patient people I have ever met. Thank you so much for all your help. The lab can be a crazy place, but it’s a much a better place because of all your efforts. Jason, you have a work ethic that is second to none. All the work that you have poured into VTF-2 has made it an amazing facility to test in. I know that the lab is in good hands. Connie, Nathan B., and David, you guys are the new blood that the lab needs, and I wish you guys the best of luck. Remember there is a light at the end of the tunnel.

TABLE OF CONTENTS

ACKNOWLEDGEMENTS	iv
LIST OF TABLES	xvi
LIST OF FIGURES	xvii
NOMENCLATURE.....	xxvi
SUMMARY	xxviii
Chapter I.....	1
1.1 A Brief Overview of Hall Effect Thrusters.....	1
1.1.1 Rocket Equation.....	2
1.1.2 Hall Effect Thrusters.....	3
1.1.3 Ground Testing of Hall Effect Thrusters	5
1.1.3.1 Neutral Pressure Effects on Performance	6
1.1.3.2 Neutral Pressure Effects on the HET Plume.....	8
1.2 Motivation.....	9
1.2.1 On-Orbit Behavior Not Explained through Neutral Pressure Considerations	9
1.2.1.1 Express-A Geostationary Telecommunication Satellites.....	10
1.2.1.2 SMART-1 European Space Agency Mission	12
1.2.1.3 Conclusions Drawn from Flight Experience.....	15
1.2.2 Motivations for Further Research into Electrical Facility Effects	15
1.3 Thesis Overview on Electrical Facility Effects	16
Chapter II	17
2.1 Basic Aspects of Hall Effect Thruster Operation	17
2.1.2 Accelerations of Ions in a Hall Effect Thruster	22

2.1.2.1 Acceleration Voltage	22
2.1.2.2 Beam Divergence.....	24
2.1.3 Hollow Cathode Coupling Efficiency.....	25
2.1.4 Plasma Oscillations in the Discharge.....	26
2.1.4.1 Predator Prey Model of the Discharge Current Oscillation: Breathing Mode	27
2.2 Preliminary Efforts in Electrical Facility Research	30
Chapter III.....	33
3.1 Research Goals.....	33
3.1.1 Chamber Wall Charge Recombination Pathways Effects on HET Operation.....	34
3.1.2 Thruster Body Charge Recombination Pathways Effects on HET Operation.....	34
3.2 Control Methods	34
3.2.1 Chamber Wall Charge Recombination Pathway Control Methodology..	35
3.2.1.1 Control via Cathode Position in the HET Magnetic Field.....	35
3.2.1.2 Bias of the downstream axial plate	36
3.2.2 Thruster Body Bias Voltage Control Methodology	37
3.3 Measurement Characteristics Key to the Research Goals	39
3.3.1 Measurements Regarding the Hall Effect Thruster.....	39
3.3.2 The Electrical Witness Plates and Conductive Surfaces	40
CHAPTER IV.....	41
4.1 Testing Facility	41
4.2 Plasma Source.....	42
4.2.1 T-140 HET	42
4.2.2 Cathode.....	43

4.2.3	Propellant System.....	44
4.2.4	Electrical Circuit	44
4.3	Chamber Plates	45
4.3.1	Locations of Plates	45
4.3.2	Design of Plates.....	47
4.4	Thruster Body Plates.....	49
4.4.1	Locations of Plates	49
4.4.2	Design of Thruster Body Plates	51
4.5	Diagnostics.....	52
4.5.1	Plume Diagnostics.....	53
4.5.1.1	Langmuir Probes.....	53
4.5.1.1.1	Plume	53
4.5.1.1.2	The Chamber Plates	53
4.5.1.1.3	Estimating the Plasma Potential with Langmuir Probes.....	56
4.5.1.2	Emissive Probes	57
4.5.1.3	Faraday Probes.....	58
4.5.1.4	Retarding Potential Analyzer	59
4.5.2	Thrust Stand	60
4.5.3	Electrical Circuit Diagnostics.....	61
4.5.3.1	Oscilloscope Configuration	61
4.5.3.2	Oscilloscope Probe Types.....	63
4.5.3.2.1	Voltage Probes	63
4.5.3.2.2	Current Probes	63
4.5.3.2.3	Time Delay Induced by the Wiring Length.....	65
4.5.3.3	Statistical and Fourier Techniques used for Analysis.....	65

4.5.3.3.1	Statistical Correlation.....	66
4.5.3.3.2	Fourier Transform and Frequency Domain Averaging	67
4.5.3.3.3	Time-Delay Analysis Using Statistical Correlation.....	69
CHAPTER V	74
5.1	Cathode Positioning Experimental Configuration	74
5.1.1	Experimental Layout.....	74
5.1.1.1	Cathode Translation	75
5.1.1.2	Regions of Cathode Position.....	76
5.1.1.3	T-140 HET Operating Conditions	78
5.1.1.4	Configuration of Plates	79
5.1.1.5	Thruster Body Electrical Configuration.....	81
5.1.1.6	Summary of Electrical Diagnostics Layout	82
5.1.1.6	Probe Diagnostics Configuration	82
5.1.2	Time Averaged Results.....	83
5.1.2.1	Time-Average Plate and Thruster Current and Voltages.....	83
5.1.2.2	Plume Diagnostics	85
5.1.2.2.1	Plasma Potential.....	85
5.1.2.2.2	Most Probable Ion Energy	86
5.1.2.2.3	Thrust Measurements.....	87
5.1.3	Time Resolved Results	89
5.1.3.1	Discharge Current	89
5.1.3.2	Radial and Axial Chamber Plate.....	94
5.1.3.3	Radial Chamber Plate and Axial Chamber Plate Time-Delay	98
5.1.3.4	HET Cathode-to-Ground Voltage and Cathode Keeper Time-Delay..	101
5.1.3.5	Thruster Body Time-delay and Correlation	103

5.2 Axial Plate Biasing Experimental Configuration	104
5.2.1 Experimental Layout.....	105
5.2.1.1 Configuration of the Chamber Plates.....	105
5.2.1.2 Thruster Body Witness Plates Electrical Configuration	106
5.2.1.3 Summary of Electrical Diagnostics Layout	107
5.2.1.4 T-140 HET Operating Conditions	108
5.2.1.5 Probe Diagnostics Configuration	109
5.2.2 Time-Averaged Results	111
5.2.2.1 Axial Chamber Plate Behavior	111
5.2.2.2 Radial Plate Facility Interaction.....	114
5.2.2.3 Influence of the Axial Chamber Plate Bias on the HET.....	116
5.2.2.4 Plume Plasma Properties.....	117
5.2.3 Time-Resolved Results	121
5.2.3.1 Variation of the Discharge Current.....	121
5.2.3.2 Oscillation Response of the HET.....	122
5.2.3.1.1 Discharge Current Oscillations	123
5.2.3.1.2 Axial Chamber Plate Oscillation Frequency Coupling.....	125
5.2.3.1.3 Radial Chamber Plate Oscillation Frequency Coupling	126
5.2.3.1.4 Thruster Body and Thruster Body Plate Oscillation Frequency Coupling 128	
5.2.3.3 Statistical Correlation and Time Delay Measurements	130
5.2.3.3.1 The Discharge Current Peak Event and Limits of Correlation	130
5.2.3.3.2 Radial and Axial Chamber Plate Measurements	132
5.2.3.3.3 Thruster Body Plates Measured Time Delay	134
5.3 Thruster Body Biased Experimental Configuration	136

5.3.1 Experimental Configuration.....	137
5.3.1.1 Thruster Body and Thruster Body Plate Electrical Configuration.....	137
5.3.1.2 Summary of Electrical Diagnostics Layout	139
5.3.1.3 T-140 HET Operating Conditions	140
5.3.1.4 Probe Diagnostic Configuration	141
5.3.2 Time Averaged Results.....	143
5.3.2.1 Effect of the Thruster Body Bias on HET Thrust and Plume	144
5.3.2.1 Electrical Characteristics of HET and Thruster Body Plates.....	145
5.3.2.2.1 T-140 Discharge Current	145
5.3.2.2.2 Thruster Body Plates and Total Thruster Body Current	145
5.3.3 Time-Resolved Results	149
5.3.3.1 Peaks of Power Spectra.....	150
5.3.3.1.1 Discharge Current Oscillations of the HET	150
5.3.3.1.2 Thruster Body and Thruster Body Plates.....	151
5.3.3.2 Peak to Peak and Standard Deviation of Signals	157
5.3.3.2.1 HET Discharge Current	157
5.3.3.2.2 Thruster Body Plates.....	158
5.3.3.3 Time Delay and Correlation of the Thruster Body Plates.....	162
5.3.3.3.1 Discharge Peak Event	162
5.3.3.3.2 The Thruster Body Plates.....	162
Chapter VI.....	166
6.1 Discussion of Findings from Cathode Positioning Experimental Configuration ..	166
6.1.1 Cathode Position: Regions of Correlation	166
6.1.2 Electrical Interaction between the Thruster and the Radial Chamber Plate	168

6.1.2.1 Evidence of Cathode Coupling to Radial Plate.....	168
6.1.2.2 Higher Frequency Spectral Peak of the Radial Plate Power Spectra...	172
6.1.3 HET Discharge Current Oscillation.....	173
6.1.4 The Impact of the Conductive Wall on HET Operation	174
6.1.5 Timescale of Physical Mechanisms in the Hall Current Thruster Plume ...	175
6.1.6 Summary of Findings from Cathode Positioning Experimental Configuration	179
6.2 Discussion of Results from Biasing of the Axial Chamber Plate	181
6.2.1 Plasma Potential and Plate Current.....	181
6.2.2 Interaction Between the HET and the Chamber Recombination Pathway .	186
6.2.3 Decoupling of the Radial Chamber Plate from the HET discharge.....	188
6.2.4 Impact of the Axial Chamber Plate Electrical Power	189
6.2.5 Enhanced Current Density in the Off-Axis Plume	190
6.2.6 Summary of Findings from Biasing the Axial Chamber Plate Experimental Configuration	193
6.3 Discussion of Results from Thruster Body Biasing Experimental Configuration.	194
6.3.1 Manipulation of Localized Recombination Currents on the Thruster Body	194
6.3.2 Influence of the Thruster Body Recombination Pathway on the HET Discharge	195
6.3.3 Thruster Body as an Electrical Load.....	198
6.3.4 Summary of Findings from Thruster Body Biasing Experimental Configuration	200
6.4 Implications for Ground Testing of Hall effect Thrusters	202
6.4.1 Cathode Coupling of the HET	202
6.4.2 Comparison Hall Effect Thruster Operation to The SMART-1 Mission ...	203
6.4.3 Electrical Configuration of the Thruster Body	205

6.4.4 The Configuration of Ground-Based Vacuum Facilities	206
Chapter VII	209
7.1 Electrical Facility Effects Contributions.....	209
7.1.1 Contributions to the Understanding of Chamber Wall-Hall Effect Thruster Interactions.....	209
7.1.2 Contributions to the Understanding of the Thruster Body-Hall effect Thruster Interaction.....	210
7.2 Future Work	211
REFERENCES.....	214
VITA	222

LIST OF TABLES

Table 1: Estimated cable induced signal delay. Path length uncertainty is ± 0.3 m	65
Table 2: Approximate magnetic field strength as a function of cathode orifice radial location away from thruster centerline.	76

LIST OF FIGURES

Figure 1: T-140 HET Operating in Vacuum Chamber. HET is operating with xenon propellant at a discharge voltage of 300 V and a discharge power of 3.1 kW. Ambient chamber pressure is 7.3×10^{-6} Torr corrected for Xenon.	4
Figure 2: Notional Diagram of HET Structure	5
Figure 3: Ion current density profile of a P5 HET. Data is taken at a discharge voltage of 300 V and discharge current of 4.3 A. The off-axis region of the profile is labeled as “Tail Regions” Figure is taken from Walker, et al. [14].....	9
Figure 4: Ion energy distribution from the Express satellite diagnostics in the “tail regions” of the HET plume. Circled in red is the high-energy ion population. Figure taken from Manzella, et al. [47]	11
Figure 5: Cathode-to-satellite ground voltage for the SMART-1 PPS-1350 HET. Taken from Koppel, et al. [51].....	14
Figure 6: Measurements of the Ion energy distribution from the SMART-1 Electric Propulsion Diagnostics Package (EPDP) Circled in red is secondary high-energy population of ions. Figure is taken from Passaro, et al. [55]	14
Figure 7: Functional diagram of a notional operating Hall effect thruster. Figure is used with permission from Scott King (Figure not scale).....	18
Figure 8: Potential diagram of a typical HET operating in a vacuum chamber.	19
Figure 9: Notional Electrical Circuit Diagram of HET	21
Figure 10: A single trace representative ion energy distribution function of a HET. The HET is operating at 300 V, 3.1 kW. The chamber pressure is 7.3×10^{-6} Torr Xe	23
Figure 11: Representative discharge current power spectra. The HET operation condition is at 300 V, 3.5 kW.	27
Figure 12: Percentage change in breathing mode frequency as a function of percentage change in ionization electron temperature. <i>Greyed regions denote non-physical solutions from the zeroth-order model.</i>	30
Figure 13: Axial and radial chamber plate sweeps taken while a T-140 HET was operating at a discharge voltage of 300 V and a discharge current of 5.16 A. Figure is taken from Frieman, et al. [72]	31

Figure 14: Relative potentials of key HET electrical references A) Typical ground testing environment B) Typical on-orbit environment C) Elevated cathode potentials taken from the SMART-1 mission.	38
Figure 15: Electrical diagram of current and voltage measurements of the HET discharge circuit	45
Figure 16: Left) Radial chamber plate. Right) Axial chamber plate	48
Figure 17: T-140 HET and installed witness plate locations. Witness plate encircled in red Left) Front view of thruster Right) Opposite side of the cathode view of the thruster	50
Figure 18: Diagram of the magnetic field topology labeled to show placement of witness plates Magnetic field magnitude (B_{mag}) is normalized by the maximum magnetic field strength along the thruster discharge channel centerline (B_{max}).	51
Figure 19: Axial Plate Langmuir Probe	55
Figure 20: Image of the Axial Chamber Plate as Installed	55
Figure 21: Front view of the RPA.....	60
Figure 22: Diagram of Oscilloscope Triggering and Clock Sync.....	63
Figure 23: Side by side comparison of FFT Scans Left: 1 scan Right: Average of 30 scans. The HET operating condition is 300 V, 3.1 kW	69
Figure 24: (Top) Discharge current peak event at cathode position of 18.1 cm (Bottom) Corresponding segment of radial chamber plate current-to-ground. The HET operating condition is 300V, 3.1 kW	73
Figure 25 Schematic of VTF-2 and the Layout of the Experimental Apparatus	75
Figure 26: HET Electrical Configuration	79
Figure 27: Plate circuit configurations: a) grounded, b) floating, and c) connected.	80
Figure 28: Electrical diagram of current and voltage time-resolved measurements of the HET discharge circuit.	82
Figure 29: Cathode-to-ground voltage of the HET taken at 300 V, 3.1 kW.....	84
Figure 30: The floating voltages for the radial plate, axial plate, and the thruster body floating voltage for the floating type configurations. The HET operating condition is 300 V, 3.1 kW.....	84

Figure 31: The radial plate, axial plate, and thruster body current-to-ground as a function of cathode position for connected and grounded configurations. The HET operating condition is 300 V, 3.1 kW.	85
Figure 32: Plasma potential measurements taken at thruster centerline at 1 m downstream. The HET operating condition is 300 V, 3.1 kW.	86
Figure 33: Most probable ion energy results taken at thruster centerline at 1 m downstream. RPA measurement variability is $\pm 10\%$. The HET operating condition is 300 V, 3.1 kW.	87
Figure 34: Grounded thruster body configuration. The absolute uncertainty $\pm 1.7\%$. The variability between cathode positions, (<i>i.e.</i> , relative uncertainty) for a given plate configuration is less than 1%. The HET operating condition is 300 V, 3.1 kW.	88
Figure 35: Floating thruster body configuration. The variability between plate configurations is $\pm 3\%$. The variability between cathode positions for a given plate configuration is less than 1%. The HET operating condition is 300 V, 3.1 kW.	88
Figure 36: Left: Peak-to-peak discharge current as a function of cathode radial distance. is Right: Standard deviation of the discharge current as a function of cathode radial distance Mean discharge current for each waveform measured is 10.2 A with a variability of ± 0.1 A between data points and testing configurations. The HET operating condition is 300 V, 3.1 kW.	90
Figure 37: Peak frequency of the discharge current power spectra as function of cathode position for the thruster body and plate electrical configurations. The HET operating condition is 300 V, 3.1 kW.	93
Figure 38: Left: Full-width-half-maximum of the peak frequency of the power spectrum as a function of cathode radial distance for the electrically grounded thruster body configuration. Right: Full-width-half-maximum of the peak frequency of the power spectrum as a function of cathode radial distance for the electrically floating thruster body configuration. The HET operating condition is 300 V, 3.1 kW.	94
Figure 39: Top: power spectra of the discharge current. Bottom: power spectra of the radial plate current. Waveforms measured for a floating thruster body and grounded radial plate configuration at a cathode position of 18.1 cm relative to thruster centerline. The HET operating condition is 300 V, 3.1 kW.	96
Figure 40: Peak frequency of the radial plate current and voltage power spectra as function of cathode position for the thruster body and plate electrical configurations. The HET operating condition is 300 V, 3.1 kW.	97
Figure 41: Peak frequency of the axial plate current and voltage power spectra as function of cathode position for the thruster body and plate electrical configurations. The HET operating condition is 300 V, 3.1 kW.	98

Figure 42: Radial chamber plate current time-delay and correlation coefficient as a function of cathode radial position away from thruster centerline. The HET operating condition is 300 V, 3.1 kW.	100
Figure 43: Axial chamber plate current time-delay and correlation coefficient as a function of cathode radial position away from thruster centerline. The HET operating condition is 300 V, 3.1 kW.	100
Figure 44: Cathode-to-ground voltage time-delay and correlation coefficient as a function of cathode radial position away from thruster centerline. The HET operating condition is 300 V, 3.1 kW.	102
Figure 45: Cathode keeper floating voltage time-delay and correlation coefficient as a function of cathode radial position away from thruster centerline. The HET operating condition is 300 V, 3.1 kW.	103
Figure 46: Thruster body current to ground time-delay and correlation coefficient as a function of cathode radial position away from thruster centerline. The HET operating condition is 300 V, 3.1 kW.	104
Figure 47: Overhead view of the vacuum chamber test facility, HET, chamber plates.	105
Figure 48: Electrical configuration of the thruster body plates for the axial plate bias experimental configuration.	107
Figure 49: Electrical diagram of current and voltage measurements of the HET discharge circuit.	108
Figure 50: Overhead view of the vacuum chamber test facility, HET, and plume diagnostics.	109
Figure 51: Probe arm with plume diagnostics attached A) Langmuir Probe B) Faraday Probe C) Emissive Probe	110
Figure 52: Overhead view of notional layout of the radial diagnostics probe arm.	111
Figure 53: Axial chamber plate current collected as a function of axial plate bias voltage. The HET operation condition is at 300 V, 3.16 kW. <i>Error bars are encompassed by plot markers.</i>	113
Figure 54: Radial chamber plate current collection as a function of axial chamber plate bias voltage relative to ground. HET nominal condition is at 300 V, 3.16 kW. <i>Error bars are encompassed by plot markers.</i>	115
Figure 55: Plasma potential measured at 25.4 cm radial distance away from the radial plate. HET nominal condition is at 300 V, 3.16 kW. Measurement is centered on radial plate centerline.	116

Figure 56: Cathode-to-ground voltage and centerline plasma potential as a function of axial plate bias. The HET operating condition is 300 V, 3.16 kW. *Error bars for Cathode-to-Ground Voltage are encompassed by plot markers*.....117

Figure 57: Ion current density profile as a function of increasing axial plate bias voltage for the grounded thruster body configuration. The HET operating condition is 300 V, 3.16 kW. Left) Full Plume Profile Right) One side of the HET Plume in the “charge-exchange ion” region.118

Figure 58: Plasma potential profile as a function of axial plate bias voltage for the grounded thruster body. The HET operating condition is 300 V, 3.16 kW.....119

Figure 59: Ion number density profile as a function of axial plate bias voltage. The HET operating condition is 300 V, 3.16 kW.....120

Figure 60: The discharge current peak to peak and standard deviation. The HET operating condition is 300 V, 3.4 kW.....122

Figure 61: Side by Side Comparison of the Cathode Positioning Power Spectra and Axial Plate Power Spectra. Left) Power spectra of the discharge current using a single scan. The HET operating condition is 300 V, 3.1 kW. Right) Power spectra of the discharge current using a 30 scan average. The HET operating condition is 300 V, 3.4 kW.....123

Figure 62: Discharge Current Power Spectra for the 300 V, 3.4 kW HET operating condition.124

Figure 63: Discharge oscillation peak frequency as a function of axial plate bias voltage. The HET operating condition is 300 V, 3.4 kW.....125

Figure 64: Discharge oscillation secondary peak frequency as a function of axial plate bias voltage. The HET operating condition is 300 V, 3.4 kW.....125

Figure 65: Axial plate current-to-ground power spectra peaks Left: Primary peak. Right: Secondary Peak. The HET operating condition is 300 V, 3.4 kW.126

Figure 66: Radial plate current-to-ground power spectra peaks. The HET operating condition is 300 V, 3.4 kW. Left: Primary peaks. Right: Secondary peaks128

Figure 67: TP2, TP3, and thruster body current-to-ground power spectra peaks. The HET operating condition is 300 V, 3.4 kW. Left: Primary peaks. Right: Secondary peaks. It is important to note that the “Body2GND” data points are just the current collected on the thruster body surfaces that are not TP1, TP2, or TP3.....129

Figure 68: TP1 current-to-ground power spectra peaks. The HET operating condition is 300 V, 3.4 kW. Left: Primary Peak. Right: Secondary peaks.130

Figure 69: Representative discharge current peak event for the axial chamber plate bias configuration at an axial chamber plate bias voltage relative to ground of 0 V. The HET operating condition is 300 V, 3.4 kW.	131
Figure 70: Axial chamber plate time delay and correlation coefficient. The HET operating condition is 300 V, 3.4 kW.	132
Figure 71: Radial Chamber plate time delay and statistical correlation. The HET operating condition is 300 V, 3.4 kW.	133
Figure 72: TP1 thruster body plate time delay and correlation coefficient. The HET operating condition is 300 V, 3.4 kW.	134
Figure 73: TP2 thruster body plate time delay and correlation coefficient. The HET operating condition is 300 V, 3.4 kW.	135
Figure 74: TP3 thruster body plate time delay and correlation coefficient. The HET operating condition is 300 V, 3.4 kW.	136
Figure 75: Overhead view of the vacuum chamber test facility, HET and probe diagnostics.	137
Figure 76: Thruster body and thruster body plate electrical configuration	139
Figure 77: Electrical Diagnostics Diagram for Thruster Body Bias Experimental Configuration	140
Figure 78: Probe arm with plume diagnostics attached A) Langmuir Probe B) Faraday Probe C) Emissive Probe.	142
Figure 79: Overhead view of notional layout of the radial diagnostics probe arm.	143
Figure 80: Cathode-to-ground voltage as a function of thruster body to ground voltage for the thruster body bias experimental configuration. The HET operating condition is 300 V, 3.5 kW.	144
Figure 81: Discharge current average as a function of thruster body-to-cathode voltage. The HET operating condition is 300 V, 3.5 kW.	145
Figure 82: Total thruster body current-to-ground as a function of thruster body-to-cathode voltage. The HET operating condition is 300 V, 3.5 kW.	147
Figure 83: Average TP1 current-to-ground as a function of thruster body-to-cathode voltage. The HET operating condition is 300 V, 3.5 kW.	147
Figure 84: Average TP2 current-to-ground as a function of thruster body-to-cathode voltage. The HET operating condition is 300 V, 3.5 kW.	148

Figure 85: Average TP3 current-to-ground as a function of thruster body-to-cathode voltage. The HET operating condition is 300 V, 3.5 kW.148

Figure 86: The cathode-to-ground voltage of the HET electrical circuit as a function of the Thruster body to ground voltage. The HET operating condition is 300 V, 3.5 kW. .149

Figure 87: Peak of the discharge current power spectra for the thruster body bias experimental configuration. The HET operating condition is 300 V, 3.5 kW.....151

Figure 88: Secondary Peak of the discharge current power spectra for the thruster body bias experimental configuration. The HET operating condition is 300 V, 3.5 kW.151

Figure 89: Primary Peak of the TP1 Current-to-ground power spectra. The HET operating condition is 300 V, 3.5 kW.153

Figure 90: Secondary Peak of the TP1 current-to-ground power spectra. The HET operating condition is 300 V, 3.5 kW.153

Figure 91: Primary Peak of the TP2 Current-to-ground power spectra. The HET operating condition is 300 V, 3.5 kW.154

Figure 92: Secondary Peak of the TP2 current-to-ground power spectra. The HET operating condition is 300 V, 3.5 kW.154

Figure 93: Primary Peak of the TP3 Current-to-ground power spectra. The HET operating condition is 300 V, 3.5 kW.155

Figure 94: Secondary Peak of the TP3 current-to-ground power spectra. The HET operating condition is 300 V, 3.5 kW.156

Figure 95: Primary Peak of the total thruster body current-to-ground power spectra. The HET operating condition is 300 V, 3.5 kW.156

Figure 96: Secondary Peak of the total thruster body current-to-ground power spectra. The HET operating condition is 300 V, 3.5 kW.157

Figure 97: Discharge current fluctuations as a function of thruster body-to-cathode voltage. The HET operating condition is 300 V, 3.5 kW. Left: Discharge current peak to peak. Right: Discharge current standard deviation.158

Figure 98: Left) Total thruster body current-to-ground peak to peak. Right) Total Thruster body current-to-ground standard deviation. The HET operating condition is 300 V, 3.5 kW.160

Figure 99: TP1 current-to-ground peak to peak (left) and standard deviation (right). The HET operating condition is 300 V, 3.5 kW.160

Figure 100: TP2 current-to-ground peak to peak (left) and standard deviation (right). The HET operating condition is 300 V, 3.5 kW.	161
Figure 101: TP3 current-to-ground peak to peak (left) and standard deviation (right). The HET operating condition is 300 V, 3.5 kW.	161
Figure 102: Representative discharge current peak event occurring at thruster body-to-cathode voltage of 11.12 V. The HET operating condition is 300 V, 3.5 kW.....	162
Figure 103: TP1 time delay and correlation coefficient. The HET operating condition is 300 V, 3.5 kW.....	164
Figure 104: TP2 time delay and correlation coefficient. The HET operating condition is 300 V, 3.5 kW.....	164
Figure 105: TP3 time delay and correlation coefficient. The HET operating condition is 300 V, 3.5 kW.....	165
Figure 106: Representative cathode-to-ground voltage power spectra. The HET operating condition is at 300 V, 3.1 kW.	170
Figure 107: Radial plate current-to-ground power spectra for the floating thruster body electrical configuration. Top: Cathode position is at 32.1 cm from thruster centerline (Region 2). Bottom: Cathode position is at 77.8 cm from thruster centerline (Region 3). The HET operating condition is at 300 V, 3.1 kW	172
Figure 108: Plasma potential as a function of axial plate bias voltage, model versus experiment. The HET operating condition is at 300 V, 3.1 kW.	184
Figure 109: Axial plate current collected as a function of applied bias voltage, model versus experiment. The HET operating condition is at 300 V, 3.1 kW	184
Figure 110: Thruster body current-to-ground and Thruster body floating voltage as a function of axial plate bias voltage. The HET operating condition is 300 V, 3.1 kW. <i>Error bars are encompassed by plot markers.</i>	187
Figure 111: Notional Diagram of Electron Pathways. A) No axial plate bias voltage or nominal condition B) Low axial plate bias voltage C) High axial plate bias voltage.	188
Figure 112: Power sourced by the axial chamber plate for both thruster electrical configurations. The HET operating condition is at 300 V, 3.1 kW. <i>Error bars are encompassed by plot markers.</i>	190
Figure 113: Current density profiles in the off-axis region of the HET plume for varying cathode positions relative to thruster centerline. The HET operating condition is at 300 V, 3.1 kW. A) 18.1 cm B) 21.9 cm C) 27.0 cm D) 43.4 cm.	192

Figure 114: Discharge current peak event. Left) grounded thruster body. HET operating condition is 300 V, 3.5 kW. Right: electrically floating thruster body, HET operating condition is 300 V, 3.6 kW.	197
Figure 115: Power dissipation through the thruster body. The HET operating condition is at 300 V, 3.5 kW	199
Figure 116: Thruster body power dissipation at a thruster body-to-cathode voltage of 2.8 V. The HET operating condition is at 300 V, 3.5 kW.	200
Figure 117: Potential difference between Plasma Potential and Cathode-to-Ground Potential as a function of axial plate bias voltage. (<i>Plasma potential is taken at an angular position of -45°</i>). The HET operating condition is 300 V, 3.1 kW	204

NOMENCLATURE

Symbol	Description	Dimensions	Units
ΔV	Change in velocity	$L T^{-1}$	$km s^{-1}$
V_e	Exit velocity of reaction mass	$L T^{-1}$	$km s^{-1}$
m_o	mass of vehicle with propellant	M	kg
m_f	mass of vehicle without propellant	M	kg
V_d	Discharge voltage	$M L^2 I^{-1} T^{-3}$	V
V_{accel}	Acceleration voltage	$M L^2 I^{-1} T^{-3}$	V
V_p	Plasma potential	$M L^2 I^{-1} T^{-3}$	V
V_{cg}	Cathode-to-ground Voltage	$M L^2 I^{-1} T^{-3}$	V
T_{HET}	Thrust produced by HET	$M L T^{-2}$	N
X_i	Charge state fraction	-	-
I_b	Ion beam current	$Q T^{-1}$	A
m_i	Ion mass	M	kg
m_e	Electron mass	M	kg
e	Elementary charge	Q	C
Q_i	Charge state	-	-
η_{cg}	Cathode coupling efficiency	-	-
ω	Breathing mode frequency	T^{-1}	s^{-1}
\dot{n}_i	Ion production rate	T^{-1}	s^{-1}
n_i	Ion density	L^{-3}	cm^{-3}
n_n	Neutral density	L^{-3}	cm^{-3}
$\langle \sigma_i v_e \rangle$	Ionization rate coefficient	LT^{-1}	$cm s^{-1}$
T_e	Electron temperature	$M L^2 T^{-2}$	eV
β	Hall parameter	-	-
Ω_e	Electron gyro-frequency	T^{-1}	s^{-1}
ν_e	Electron-neutral collision rate	T^{-1}	s^{-1}

Symbol	Description	Dimensions	Units
B	Magnetic field strength	$M T Q^{-1} T^{-2}$	T
P_c	Corrected pressure	$M L^{-1} T^{-2}$	Torr
P_i	Indicated pressure	$M L^{-1} T^{-2}$	Torr
P_b	Base pressure	$M L^{-1} T^{-2}$	Torr
V_f	Floating potential	$M L^2 I^{-1} T^{-3}$	V
k	Boltzmann constant	$M L^2 T^{-2} \Theta$	$J K^{-1}$
r_p	Probe radius	L	mm
δ_l	Debye length	L	mm
η_f	Geometric correction factor	$I^{-1} T^{-1}$	$V eV^{-1}$
P_{db}	Spectral power in decibels	-	dB
P_{calc}	Spectral power in arb units	-	arb
P_{min}	Minimum spectral power in arb units	-	arb
γ_i	Ion ratio of specific heats	-	-
T_i	Ion temperature	$M L^2 T^{-2}$	eV
v_a	Ion acoustic velocity	$L T^{-1}$	$m s^{-1}$
v_e	Electron thermal speed	$L T^{-1}$	$m s^{-1}$
j_i	Ion current density	$I L^{-2}$	$A m^{-2}$
θ	Beam divergence	-	deg
n_e	Electron number density	L^{-3}	cm^{-3}

SUMMARY

The Hall effect thruster (HET) is a type of spacecraft propulsion that is used for satellite orbit raising and station keeping. HET development and lifetime qualification tests are performed in ground-based vacuum facilities. To ensure predictable flight operation of HETs, the ground-based testing environment must be representative of the on-orbit environment, or there must be a clear path to correlate the ground test results to expected on-orbit HET behavior. Much of the previous work related to understanding how to correlate HET ground-testing behavior and HET on-orbit behavior is focused on understanding the impact on HET operation of the elevated neutral gas pressures that HETs experience in ground-based test facilities. Flight data, from satellite missions using HETs, shows that HETs have variations in behavior that cannot be explained through neutral pressure considerations. As experienced during the SMART-1 mission, certain characteristics of the on-orbit HET electrical circuit can be influenced by external electrical factors. For ground-based testing, the vacuum facility walls represent an artificial electrical boundary that is not present during in-flight operation. The electrical impact that the walls and other conductive surfaces in the vacuum chamber have on the behavior of HETs is unknown. The results of the SMART-1 mission demonstrate that there is a gap in the knowledge of HET-vacuum facility interactions. The goal of this work is to better understand how HET thruster operation is influenced by electrical interactions with the conductive walls of the vacuum chamber and other conductive surfaces that are only present within the ground-based testing environment.

To examine these electrical interactions, this work varies the electrical boundary conditions of key electrical surfaces in the vacuum facility environment and measures how those electrical boundary conditions influence a testbed 3 kW HET. This work identifies two key conductive surface systems in the vacuum testing facility that influence the

operation of HETs: the walls of the vacuum facility and the HET body. The walls of vacuum facility influence the plume of the HET by mediating the charge-loss rate to the walls of the vacuum facility. The results of this work suggest that the walls of the vacuum facility artificially bound the plasma properties of the HET plume. This augmentation of the plasma plume indicates that there can be variations in the on-orbit plume characteristics that are not measured during ground testing. For the HET body, the conductive metal structure of the thruster is found to be an active component of the HET electrical circuit. While on-orbit, the HET body is directly connected to the satellite electrical common, and the HET electrical circuit voltage relative to the HET body has been measured to change significantly on-orbit. The results of this work indicate that the thruster body of the HET can play a critical role in the oscillations of the discharge current. Due to the complex plasma conditions present in the near-field of the thruster body, it is difficult to pinpoint the exact physical mechanisms governing the electrical interaction between the thruster body and the HET. The results of this work strongly indicate that the electrical boundary condition of the thruster body is an important consideration for the ground testing of HETs.

Collectively, this work provides valuable insight into the field of HET ground testing. Understanding HET-facility interactions are integral to both HET development and HET-satellite integration.

Chapter I

INTRODUCTION

The goal of Chapter 1 is to better acquaint the reader with the subject matters important to understanding the content of this thesis. The subject matter covered in the following chapter is a brief overview of the basic motivations of the this dissertation work. The following chapter goes over the rocket equation, the basic characteristics of Hall effect thrusters (HET), major issues that have been considered when testing HETs in ground-based vacuum facilities, and concludes by identifying a key gap in the knowledge about ground testing of HETs.

1.1 A Brief Overview of Hall Effect Thrusters

Electric rocket propulsions systems can be divided into three broad categories based on their primary acceleration mechanisms: electrothermal, electrostatic, and electromagnetic systems [1]. In electrothermal electric propulsion, the working gas is heated and then expanded to generate thrust. In electrostatic electric propulsion, the working gas is ionized and a standing electric field accelerates the working gas to generate thrust. In electromagnetic propulsion, the working gas is ionized and accelerated through the Lorentz force interaction between the working gas and the thruster. The work in this thesis focuses on electrostatic type thrusters, specifically HETs. In order to better understand HETs, the following sections explain the basic operational characteristics of HETs.

1.1.1 Rocket Equation

Before delving into HETs, a brief description of the basics of spacecraft propulsion systems is necessary. The goal of any propulsion system is to provide a change in momentum to the vehicle. For in-space propulsion systems, the lack of ambient mass surrounding the vehicle means that most in-space propulsion systems eject a reaction mass from the spacecraft to generate thrust. In general, the first-order analysis of this situation is captured in the famous *Tsiolkovsky Rocket Equation* [2], as shown in Equation (1)

$$\Delta V = V_e \ln \left(\frac{m_o}{m_f} \right) \quad (1)$$

where ΔV is the change in spacecraft velocity, V_e is the exhaust velocity, m_o is the initial mass, and m_f is the mass without propellant. The propulsive requirements for orbital maneuvers and transfer orbits to various destinations in the solar system can be conveniently reduced down to a ΔV requirement. The ability of a spacecraft propulsion system to meet that ΔV requirement, as demonstrated by the rocket equation, is determined to first order by the exit velocity of the reaction mass from the propulsion system and the amount of available propellant. For a given ΔV requirement, a spacecraft propulsion system can either carry more fuel or increase the exit velocity of the reaction mass to meet that requirement. This dichotomy of choices forms the basis of the two broad categories of in-space propulsion systems: chemical propulsion and electric propulsion. Chemical rocket engines use chemically-energetic propellants to heat the reaction mass, that is the by-product of the chemically-energetic propellant. Chemical rockets have an exit velocity that is chemistry limited to ~ 4 km/s, but they are able to produce thrust levels on the order of kN's to MN's. Electric rocket engines or electric propulsion devices, separate the energy source from the reaction mass. This separate energy source is typically electrical power

generated from satellite solar panels. Electric propulsion devices infuse kinetic energy into the reaction mass through various means to generate thrust. Electric propulsion devices are classified by their acceleration mechanism. In practice, electrostatic accelerator can have exit velocities in the 10 km/s range but only produce thrust on the order mN to N due to electrical power limitations. Because of the large improvement in the exhaust velocity of electric propulsion devices as compared to chemical rocket engines, spacecraft that use electric propulsion systems can carry much less fuel than their chemical counterparts for a given mission. The reduction in fuel allows for spacecraft to carry more payload or meet more demanding ΔV missions. This makes electric rockets engines for in-space propulsion a very attractive option for satellite builders and forms the basic motivations for all electric propulsion research and development.

1.1.2 Hall Effect Thrusters

HETs are concentric, grid-less, electrostatic ion accelerators and are a subset of electric propulsion devices [3-5]. Figure 1 shows an image of an operating HET. Current state-of-the-art flight qualified HET have power processing capabilities in the 5-kW range. This power regime fits well within current satellite electrical power envelopes [6]. HETs capable of processing more power are currently being developed [7]. HET have a wide throttling capability and are used for both orbit raising and satellite station keeping applications [3, 6, 8].

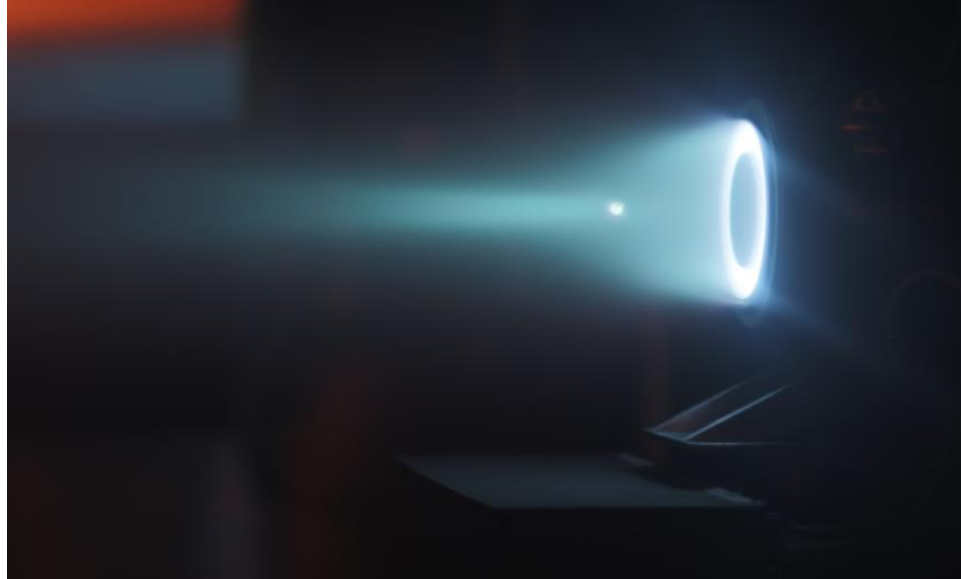


Figure 1: T-140 HET Operating in Vacuum Chamber. HET is operating with xenon propellant at a discharge voltage of 300 V and a discharge power of 3.1 kW. Ambient chamber pressure is 7.3×10^{-6} Torr corrected for xenon.

The major sections of the HET plasma environment can be divided into the discharge and the plume as shown in Figure 2. The plasma discharge of the HET is contained within the thruster channel. The discharge is responsible for ionizing neutral propellant and accelerating the ions to generate thrust. Within the discharge channel of the thruster, a stationary radial magnetic field maintains a Hall current. This Hall current is responsible for both ionizing neutral propellant and forming the electrostatic gradient to accelerate ions. The plume of the HET is composed of ions accelerated by the thruster, charge exchange ions created through ion-neutral collisions, and electrons supplied by the cathode. The plasma in the plume is quasi-neutral (*i.e.*, the local electron number density is approximately equal to the local ion number density), and the cathode of the thruster supplies electrons to both the HET discharge and the ion beam. The electrons sourced to the ion beam maintain the electrostatic potential gradient between the HET discharge plasma and the plume plasma. Understanding both sections of the plasma environment of

the HET is an active area of research and characterizing them is critical for actual satellite integration issues and in-flight operations issues.

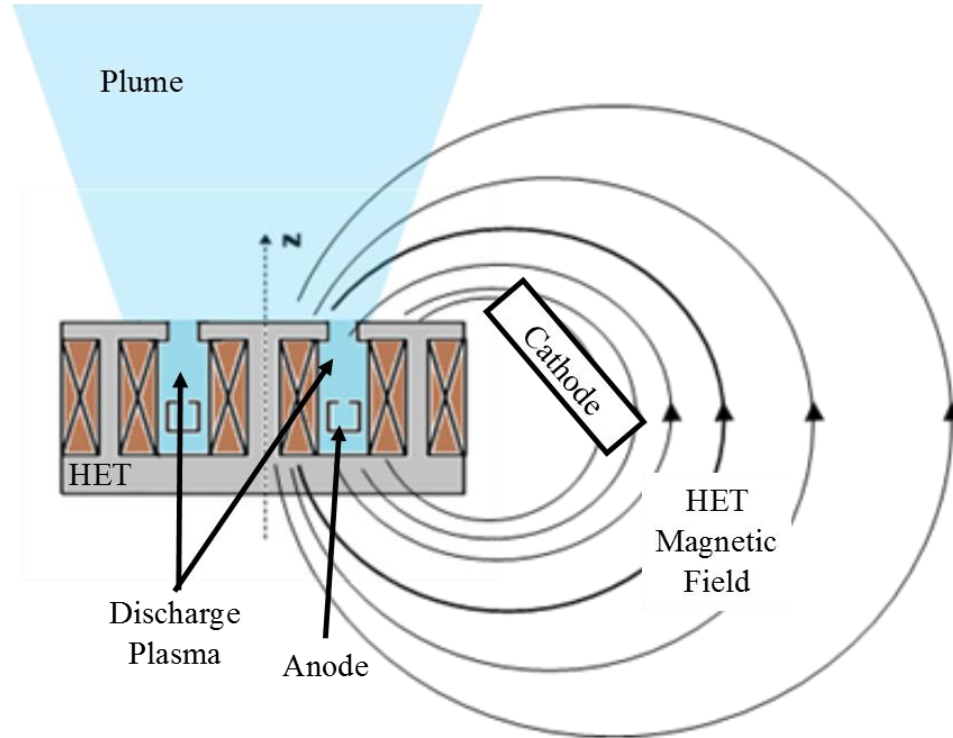


Figure 2: Notional Diagram of HET Structure.

1.1.3 Ground Testing of Hall Effect Thrusters

Due to the complexity of the physical processes present in the HET, the present predictive capability of HET performance and plasma characteristics through modeling is limited [3, 5, 9-11]. The lack of predictive capability necessitates extensive experimental testing of each new HET design to characterize its performance and operating characteristics. A HET is a steady-state plasma device, and so the operation of a HET requires a mean free path that is several times larger than the geometric size of the HET thruster. The testing of HETs must occur in a vacuum-like, low-pressure (less than $\sim 10^{-5}$ Torr) environments. A consequence of the physical pumping limitations of the ground-

based vacuum testing facility is that background neutral pressure during testing is much higher than the flight environment [3, 12-39]. The presence of additional neutral atoms in the testing environment can produce a myriad of undesirable effects in electric propulsion testing [12-39]. Tracing heritage back to gridded ion engines, pressure standards have been established empirically for HET testing and have been used for lifetime qualification testing of many HET designs [7, 12, 40, 41]. However, recent work demonstrates that the presence of background neutrals in the vacuum chamber environment heavily influences HET behavior in a ground based vacuum chamber environment at these recommended pressures [17, 32, 41, 42]. As a result, multiple research efforts have been aimed to understand the impact of neutrals on HET operation at lower pressures than were previously accepted [17].

1.1.3.1 Neutral Pressure Effects on Performance

Since a HET discharge channel is physically open to the downstream environment and the neutral density is low enough that there is free molecular flow within the discharge channel, there is no physical mechanism that prevents ambient neutral propellant atoms from propagating back into the discharge channel. Any neutrals that do reenter the discharge channel have a high probability of being ionized and accelerated out of the thruster. This effect is known as “neutral ingestion” and has widely documented effects on the HET thrust and discharge characteristics [12, 17]. The overall trend among thrusters is that elevated background pressure relative to the on-orbit conditions increases thrust by augmenting the mass flow rate into the thruster from the propellant feed system. Early testing of the SPT-100 shows that performance increases with elevated background

pressures and that vacuum facility pressures below 5×10^{-5} Torr-Xe¹ are desirable to maintain neutral ingestion to below 3% of the anode flow rate [12]. However, much work since then indicates that HETs exhibit pressure dependent performance behavior below the aforementioned pressure limit. Furthermore, simple coefficient correction factors that assume free molecular flow factors have not been able to account for pressure dependent

¹ Torr-Xe is unit of pressure measurement and stands for "Torr corrected for xenon". For measurements of pressure below 1×10^{-4} Torr, direct measurement of the ambient pressure is difficult. For these pressure ranges, it is much easier to measure the pressure indirectly. Because indirect pressure measurements are gas composition sensitive, the devices that are used to make this measurement are calibrated against a known gas composition. This is mostly commonly done with nitrogen. Based on what type of pressure measurement device that is used and the composition of gas being measured, it is possible to correct the readout of a gauge calibrated for a specific gas to the kind of gas that is actively being measured. As a way to ensure good bookkeeping, the pressure measurement from an indirect pressure gauge must also contain information about the gas composition from that measurement.

43. "571 Ionization Gauge Tube Instruction Manual." Vol. Manual No. 6999905571 Revision C, 2002.
44. Tilford, C. R. "Sensitivity of hot cathode ionization gages," *Journal of Vacuum Science & Technology A* Vol. 3, No. 3, 1985, pp. 546-550.
doi: <http://dx.doi.org/10.1116/1.572991>
45. Tilford, C. R., McCulloh, K. E., and Woong, H. S. "Performance characteristics of a broad range ionization gage tube," *Journal of Vacuum Science & Technology* Vol. 20, No. 4, 1982, pp. 1140-1143.
doi: <http://dx.doi.org/10.1116/1.571590>

performance behavior. Measurements confirm that thrust, anode efficiency,² specific impulse, and discharge current vary from pressures ranging from 5×10^{-5} Torr-Xe to below 1×10^{-6} Torr-Xe [41, 42]. In the 1×10^{-6} Torr-Xe pressure regime, it is thought that acceleration of charge exchange ions via potential gradients that exist near the thrust exit plane can affect the overall net thrust [26]. Cathode coupling efficiencies may also be affected through elevated neutral background pressures [46]. Currently facility effect correction techniques involve measuring HET performance (thrust, anode efficiency, specific impulse) at multiple neutral background pressures and extrapolating that behavior to space comparable neutral background pressures [17]. This methodology is empirical, and the extrapolation technique is not a robust method for predicting on-orbit performance. Understanding the impact of neutral background pressure on HET performance remains an active area of research [17].

1.1.3.2 Neutral Pressure Effects on the HET Plume

Accounting for differences between the HET plume in a ground testing facility and the actual flight environment is important when considering spacecraft system integration issues. Plume impingement can lead to generation of disturbance torques on the spacecraft and enhance degradation rates of solar panels. Elevated background neutral pressure has demonstrated effects on the HET plume. Particularly, plume charge-exchange ion

² Anode efficiency is calculated simply as the ratio of the beam (jet) power of the HET to the discharge power of the HET. The anode efficiency is just one measure of efficiency that is used to characterize the overall HET efficiency.

3. Goebel, D. M., and Katz, I. *Fundamentals of Electric Propulsion: Ion and Hall Thrusters*. Hoboken, New Jersey: John Wiley & Sons, 2008..

production is enhanced by the presence of thermalized neutral propellants present in the vacuum facility [26]. Increases in plume divergence angle have been reported with elevated background pressure [14, 15]. In Figure 3, the “tails” of the HET plume show an increase in the ion-current density. Walker [15] measured changes in the electron temperature, plasma potential, and ion current density with increasing background neutral pressure. Continuing to understand the impact of neutral pressure on the HET plume remains an active area of research.

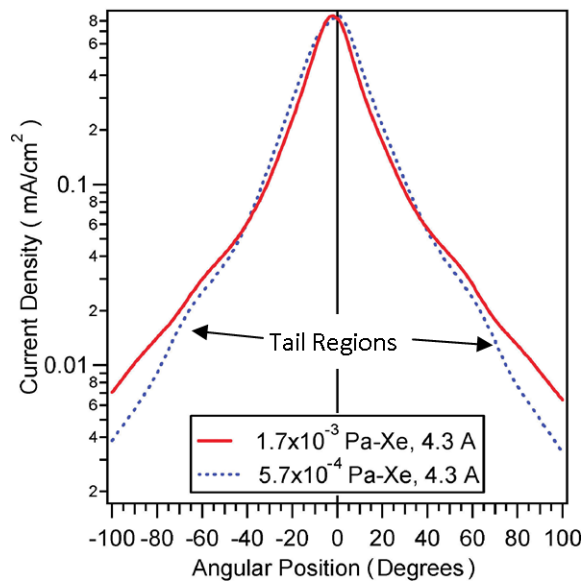


Figure 3: Ion current density profile of a P5 HET. Data is taken at a discharge voltage of 300 V and discharge current of 4.3 A. The off-axis region of the profile is labeled as “Tail Regions” Figure is taken from Walker, et al. [14].

1.2 Motivation

1.2.1 On-Orbit Behavior Not Explained through Neutral Pressure Considerations

While HETs have been in use since the 1970s, many of the data collected for HET in-flight operation remain either proprietary or controlled information. Much of the public facility effects research effort has stemmed from two satellite missions using HETs, the

Russian Express-A geosynchronous satellites and European Space Agency's SMART-1 lunar mission [47-53]. Below is brief description of publicly available information regarding discrepancies between in-flight and ground-tested HET performance and plume characteristics.

1.2.1.1 Express-A Geostationary Telecommunication Satellites

The Express-A geostationary telecommunication satellites use a total of four Fakel SPT-100 HET thrusters for North-South and East-West station-keeping [47]. The Fakel SPT-100 is a mature, well-tested HET design and has been used for many in-flight applications [47, 54]. In order to better understand the impact of the HET on Ku and C band communications and general satellite operation, ion current densities, ion energy, electric field strength, disturbance torques, and solar panel power degradation were measured in-situ on two of the eight geostationary telecommunication satellites.

With respect to the thruster, the in-flight measurements revealed discrepancies between ground-tested behavior and on-orbit behavior in discharge current, thrust, ion-density distribution, and ion-energy distribution [47]. It was found that the average discharge current and discharge voltage measured in-flight differed by 2% and 3%, respectively as compared to ground-based acceptance testing. The impact of this discrepancy is not yet known and the source of the discrepancy is attributed to issues in power processing unit compatibility with the SPT-100 and satellite bus voltage limits [47]. On-orbit thrust measurements were measured based on satellite range data. The measurements show that initial thruster firing produced 8% less thrust than what was demonstrated on the ground. It is reported that the on-orbit thrust increased after a 24-hour burn-in time, but overall in-flight thrust production was less than what was demonstrated in a ground based facility. Some of this deficit was attributed to direct plume impingement on satellite surfaces, but this does not fully account for deficits in thrust production [47, 48]. The impingement of the HET beam on satellite would result in the generation of

disturbance torques. Analysis of the attitude control system response revealed the presence of additional disturbance torques only present during HET operation [47]. The source of ion-impingement was attributed to changes in the HET plume in the space environment.

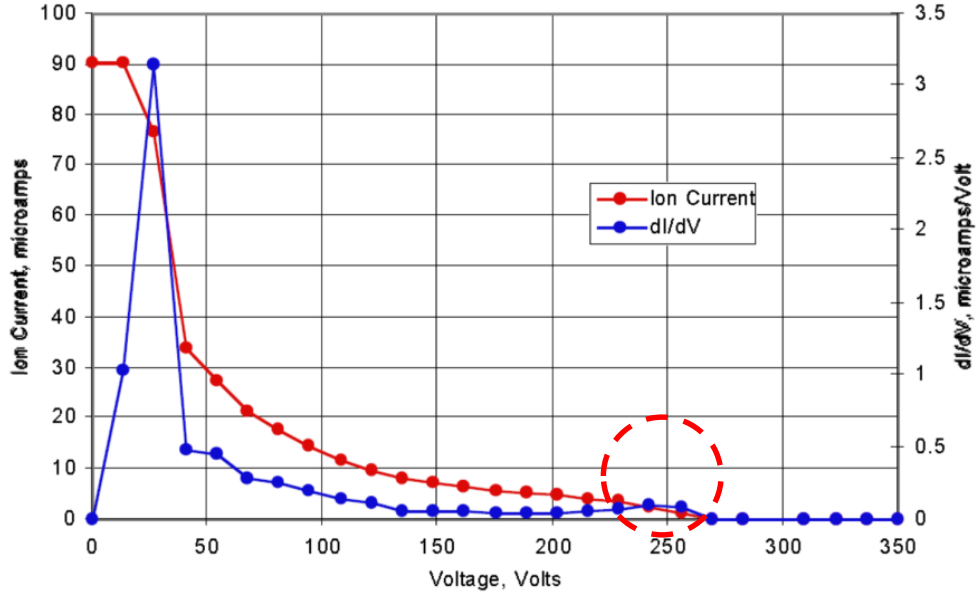


Figure 4: Ion energy distribution from the Express satellite diagnostics in the “tail regions” of the HET plume. Circled in red is the high-energy ion population. Figure taken from Manzella, et al. [47].

The plume of the SPT-100 HET onboard the Russian Express satellite exhibited marked difference between ground-based and in-flight HET operation. As shown in Figure 4, analysis of the ion energy distribution reveals the presence of high-energy ions at large angles relative to the thruster centerline. These energetic ions are present at angles outside the ground-measured ion beam divergence angle [47, 48]. From analysis of the data collected from the Express satellites and modeling by Manzella, et al. [47], Boyd and Dressler [48], the following conclusions were made about the source of the anomalous plume ion-energy profile: In the ground-testing environment, the elevated neutral propellant density near the discharge channel exit creates region of increased charge-exchange collisions not present in the space environment. As mentioned above, the HET magnetic field topology is designed such that the primary acceleration of the ionized

propellant is aimed downstream. Due to the nature of the shape of the electrostatic potential gradient, there are accelerated ions with high tangential-to-the thrust axis velocity components. This acceleration of ions in a direction misaligned with the thruster centerline is approximately axisymmetric. The net result is a reduction in total HET thrust and efforts are made in the design of a particular HET to minimize the production of these ions. Therefore, the majority of the ions accelerated downstream have small off-axis velocities. Boyd and Dressler [48] argue that because of the presence of additional neutral propellant atoms in the ground testing environment, accelerated ions near the discharge channel exit can collide with those neutrals and produce “low” energy charge-exchange ions. Because of the relatively small population of ions with large tangential velocities, the charge-exchange ion plasma produced during collisions dominates the composition of plasma in the off-axis regions of the beam. In the space environment, only the neutral propellant atoms present in the near-discharge channel exit plane and the plume are from un-ionized propellant from the cathode or HET discharge. Therefore, the production of charge exchange atoms is significantly reduced and ions with large off-axis velocities can propagate outward; thus increasing the effective divergence of the thruster plume in space. Replication of this behavior has not yet been documented in ground-based test facilities.

1.2.1.2 SMART-1 European Space Agency Mission

The SMART-1 satellite used a Snecma PPS-1350G HET for its primary propulsion system. Thruster diagnostics of this mission were much more limited as compared to the Express satellites [47, 49]. The most interesting result of the analysis of the flight data was the influence of the solar panels on the HET. Based on disturbance torque analysis, the HET plume did not impinge on the solar panels [50]. However, during certain solar panel orientations, the HET floating voltage drifted above the satellite bus common [49, 55]. Figure 5 shows the cathode-to-satellite ground voltage as a function of time. There are periods of time that display positive cathode-to-satellite ground voltage during periods of

elevated plasma potential. The cathode-to-satellite ground voltage rose to levels that were outside of the measurement capability of the diagnostics system. In a ground-testing environment, earth-ground is used as a reference voltage; however, during on-orbit operation, the satellite bus electrical common is used as an electrical reference. The HET floating circuit voltage is normally negative relative to earth ground and so a positive HET floating voltage had not yet been demonstrated in a ground testing facility. This deviation from expected behavior merited further investigation to determine if this change in relative potentials impacted the performance of the PPS-1350G HET. As reported, this anomalous cathode-to-satellite ground voltage did not influence thruster performance or operational stability. Plume modeling determined that the positive cathode-to-satellite ground voltage configuration was due to exposed low-voltage interconnects on the rear of the solar array exposed to the off-axis HET plume [55]. The overall magnitude of predicted cathode-to-satellite common voltage could not be reproduced with plume model. The difference between the magnitudes in cathode-to-satellite common voltages is attributed to the interaction between the HET and the vacuum chamber walls, but the actual mechanisms governing that interaction have not yet been explored in detail [55]. The model, however, accurately predicted changes in the cathode-to-satellite common voltage with respect to solar panel angle that were similar to those changes shown in the in-flight data. Ion energy analysis of the PPS-1350G HET plume revealed high-energy ions in the off-axis plume as illustrated in Figure 6. The presence of high-energy ions seen in SMART-1 is similar to what was observed with the Express satellites. The design between the PPS-1350G and the SPT-100 is different and the SMART-1 satellite missions utilized only one HET. This allowed the HET on SMART-1 to be placed differently on the satellite bus than the Express satellite HETs. These contributing factors meant that high energy beam ions did not impinge directly on SMART-1 satellite surfaces [50].

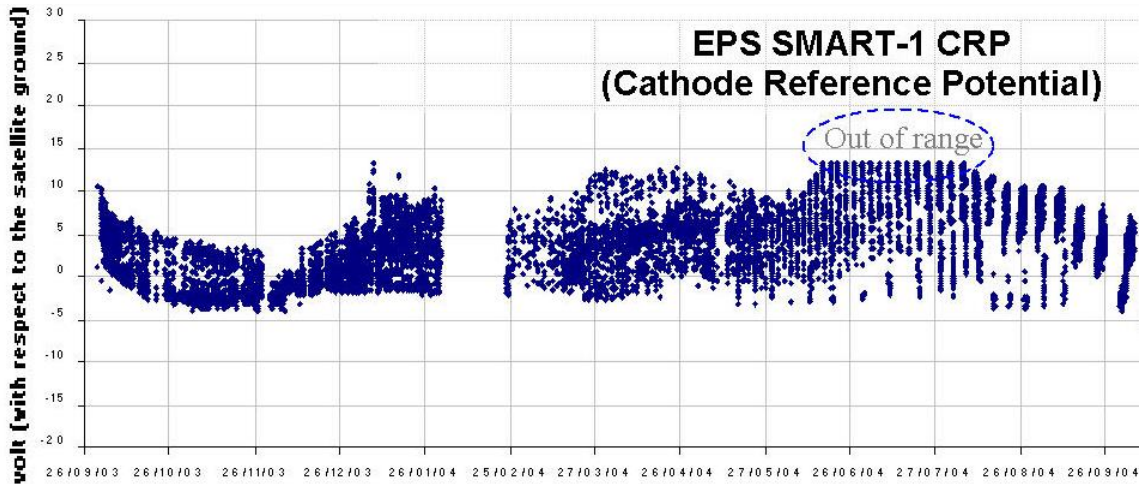


Figure 5: Cathode-to-satellite ground voltage for the SMART-1 PPS-1350 HET. Taken from Koppel, et al. [51].

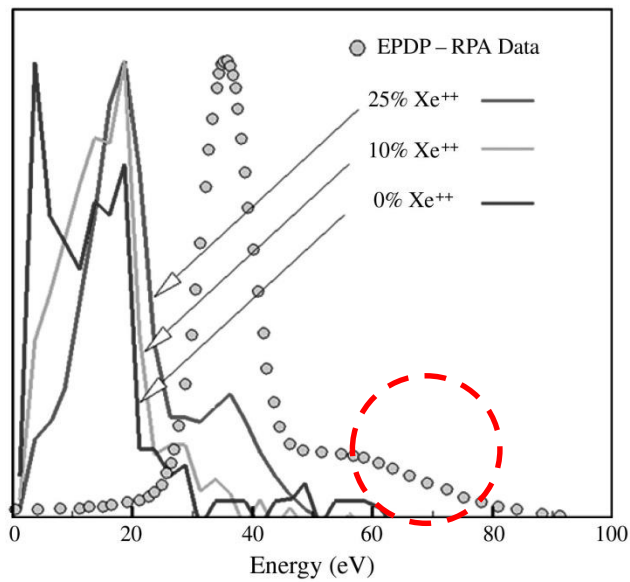


Figure 6: Measurements of the Ion energy distribution from the SMART-1 Electric Propulsion Diagnostics Package (EPDP) Circled in red is secondary high-energy population of ions. Figure is taken from Passaro, et al. [55].

1.2.1.3 Conclusions Drawn from Flight Experience

As illustrated by the in-flight performance of the SPT-100 and the PPS-1350 HETs, the physical mechanisms that govern the interaction between the vacuum chamber and the HET are still not fully understood. Simple correction coefficients to account for the differences in HET operation at various operating pressures have been found to be inadequate. For a given thruster, it is possible to establish empirical trends to correlate vacuum facility back pressures to in-flight neutral pressures, but such characterization is not extensible to another thruster without testing. As demonstrated by the literature, creation of HET testing standards has been difficult as each thruster exhibits different pressure dependent performance behavior. With the presently limited understanding of facility effects, characterization of a specific HET background neutral pressure dependent behavior is necessary. This presents a technical challenge to ground-based HET lifetime testing as it is unclear as to how background neutral pressure effects evolves over the lifetime of the thruster. From past flight experience and past research efforts in HET testing, it is evident that further investigation into facility effects on HET is warranted.

1.2.2 Motivations for Further Research into Electrical Facility Effects

A major difference between the in-flight and ground-testing environment, overlooked in the research of facility effects, is the effect of the electrically conductive vacuum facility walls and other conductive surfaces in the vacuum chamber. In the on-orbit HET plume, ions and electrons produced by the HET are free to propagate outward from the spacecraft until they recombine. In contrast, in the ground-testing environment, the conducting vacuum facility walls create an artificial recombination site that does not require ions and electrons to be in the same physical location. It has been mentioned in the literature that the presence of the conductive vacuum facility removes energy from the plume [56, 57]. However, research into the impact of the conductive walls of the vacuum chamber has not been thoroughly pursued. In the past, it was commonly assumed that the

HET cathode will compensate for the presence of the artificial conductive boundary condition through changes in the floating potential of the HET plume; however, this line of inquiry has not been pursued further and evidence from the SMART-1 on-orbit data indicates that the cathode may not compensate for the artificial electrically conductive boundary.

1.3 Thesis Overview on Electrical Facility Effects

Based on the electrical measurements from SMART-1, there are aspects of the HET electrical circuit that can be influenced by external electrical factors. Specifically, the voltage of the HET circuit relative to a reference can vary greatly between ground-testing and on-orbit operation. Since it is unclear, yet, as to how the walls of the vacuum chamber interact with the HET plume, this work will attempt to improve the understanding of how the vacuum testing facility electrically interacts with the HET. Chapter II provides background information on the key characteristics of HETs that may be influenced by electrical interactions with the vacuum facility and covers some of the exploratory work done in electrical facility effects. Chapter III describes the research goals, experimental approach, and the control methods. Chapter IV details the experimental apparatus and diagnostic techniques used. Chapter V goes over the results of each of the experimental trials. Chapter VI is the discussion of the impact of those results on the operation of HETs. Chapter VII provides a summary of the major contributions and conclusions of this work. It also provides recommendations for future work in electrical facility effects.

Chapter II

Background

The following chapter provides a background for the key components of the HET and its operation. The chapter includes a brief overview of the major components in a HET, relevant behaviors exhibited by HETs, electrical configuration of HETs, and concludes with an overview of some of the exploratory work done in electrical facility effects.

2.1 Basic Aspects of Hall Effect Thruster Operation

Figure 7 shows a notional cross-section diagram of a HET. Neutral gas propellant is injected via a propellant distribution system near the rear of the discharge channel [5, 58]. It is common for the neutral propellant gas distribution system, and the positive electrode of the HET discharge circuit to be the same physical component and is referred to as the “anode” [5]. The neutral gas continues to move axially downstream to the exit plane of the discharge, where it encounters high-energy electrons. The neutral propellant atoms collide with electrons and are ionized. The electrostatic potential setup by the anode and the electrons undergoing azimuthal drift accelerates the newly generated ions out of the discharge channel [5, 58]. It is this ion acceleration through the electrostatic potential gradient that enables the HET to produce thrust. To ensure that the thruster plume maintains a neutral balance of positive and negative charge, an external electron source emits an electron for every positive charge accelerated out of the discharge channel [5, 58].

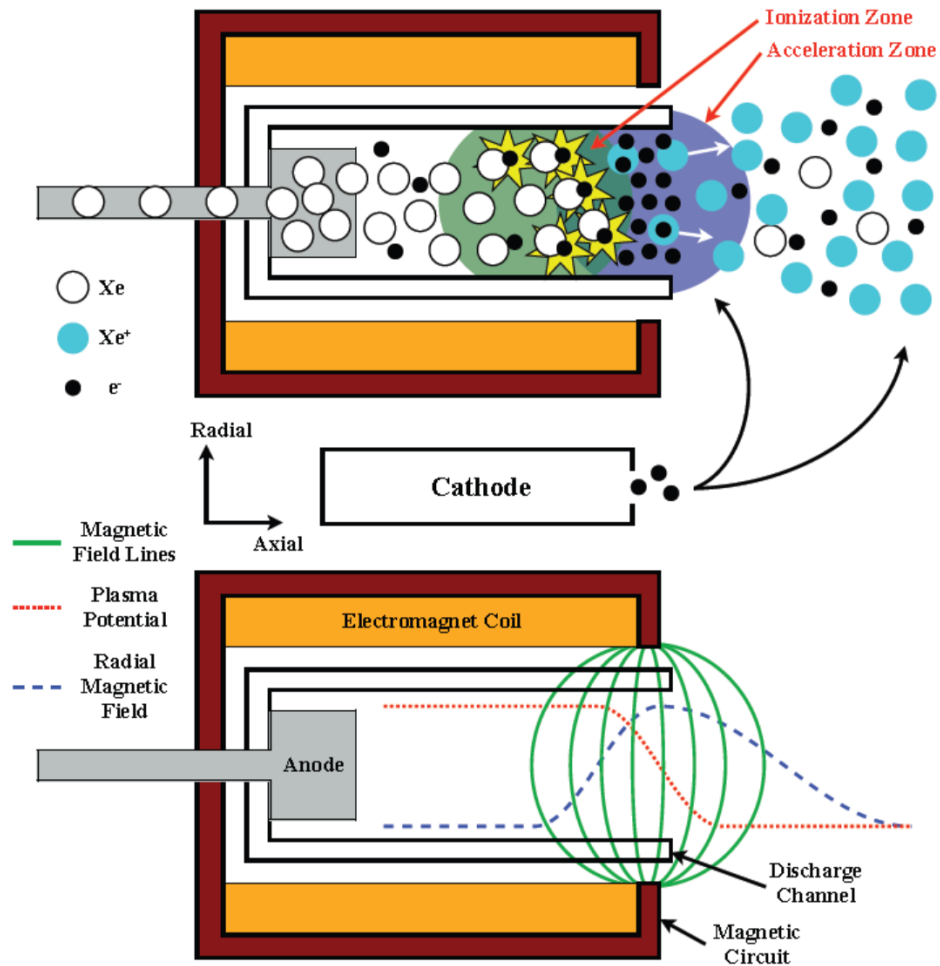


Figure 7: Functional diagram of a notional operating Hall effect thruster. Figure is used with permission from Scott King (Figure not scale).

The azimuthal drift of the electrons within the discharge channel is setup by the static magnetic field. Electrons sourced from the cathode and electrons created from ionization collisions are magnetized by the HET magnetic field. The magnetic field retards their progress towards the anode. The electrons undergo “ $E \times B$ ” azimuthal drift and a Hall current is established inside the thruster discharge. The Hall current serves two purposes: it ionizes neutral propellant and creates the electrostatic ion acceleration potential gradient. On a fundamental level, the strength of the magnetic field must be high enough to magnetize electrons but not strong enough to magnetize propellant ions. This constraint is

met because the mass of electrons is four to five orders of magnitude smaller than the ion mass and allows for a specific HET to have a wide range of operating conditions [3, 5, 59]. The specific topology of the magnetic field in the discharge channel varies significantly between HETs. The magnetic field shape controls almost all factors that govern thruster operation including but not limited to: thrust, power efficiency, beam divergence, erosion rate, and location of the ionization and acceleration region. The most basic electrical circuits of the HET are the discharge circuit and the neutralization circuit. The discharge circuit ionizes propellant via ion-electron collisions and accelerates ions out of the discharge channel of the HET. The neutralization circuit emits negative charges via thermionic electron emission as required by the acceleration of positive charges via ions out of the thruster. Both of these circuits are primarily driven by a single electrical discharge supply. The electrons necessary for both circuits are supplied by a single electron source, the cathode.

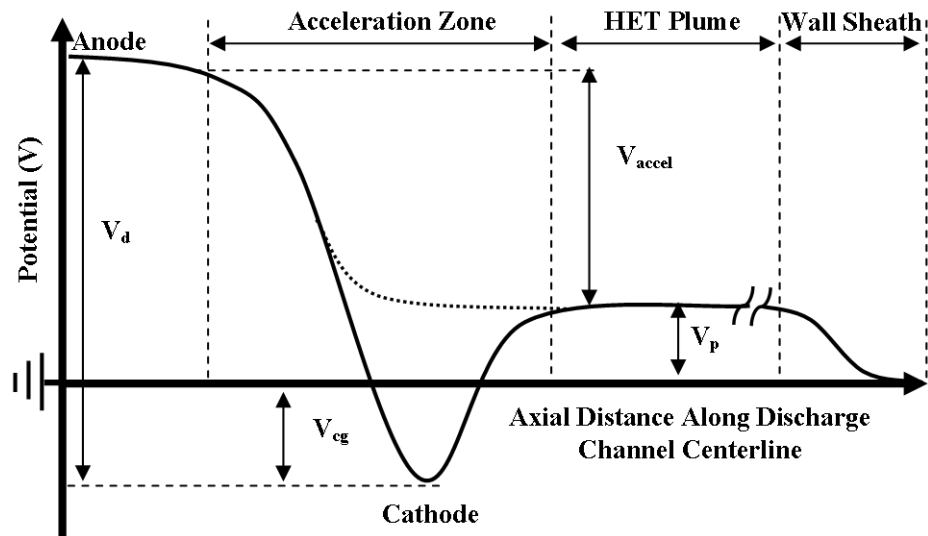


Figure 8: Potential diagram of a typical HET operating in a vacuum chamber.

Figure 8 shows a potential diagram that succinctly describes the operational potential for a HET. The floating potential of the HET circuit is established by the cathode

potential relative to ground (V_{cg}). The bias voltage of the anode (V_d) is established relative to the cathode. The azimuthal drift of the electrons (*i.e.*, Hall current) creates a steep potential gradient (V_{accel}) between the interior discharge channel plasma and the ambient plasma. Ions are accelerated along this potential gradient. The acceleration provided by this gradient is limited by the plume plasma potential (V_p). A secondary potential drop occurs between the thruster plume and vacuum chamber grounded surfaces or the space potential at infinity. This secondary potential drop occurs several collision length scales downstream of the HET exit plane through a pseudo-boundary layer, called a plasma sheath. The plasma sheath forms whenever charge quasi-neutrality in plasma cannot be maintained at a characteristic length-scale, for example the Debye length-scale [3, 60]. It is a physical structure that accommodates transitions between the plasma and a differing medium, including but not limited to: a conductive surface, an insulating surface, a charged surface, or plasma with differing characteristics. Overall, the various voltages in the HET electrical are governed by the discharge supply voltage, and their relationship to the discharge voltage is described by Equation (2):

$$V_d = V_{accel} + V_p + |V_{cg}|. \quad (2)$$

2.1.1 The Electrical Circuit of HET

The flow of positive charges (ions) and negative charges (electrons) created by the HET and the many conductive electrical surfaces in a vacuum chamber facility mean that there are several electrical pathways or circuits in a HET testing environment. The broadest categories of these circuits are the discharge circuit and the neutralization circuit. Within discharge circuit, there are two main circuits: the electron current that flows from the cathode to the anode necessary to maintain the plasma in the thruster and the second circuit is the ion current leaving the thruster discharge channel and the corresponding electron

current leaving the cathode to neutralize the ion beam. How these ion and electron currents complete a circuit forms the various parts of the neutralization circuit. These are the main pathways or circuits in which these circuits can close: Charges can terminate on facility walls, charges can terminate within the plume, and charges can terminate on conductive surfaces inside the testing volume. Figure 9 shows a notional diagram of these various circuits. It should be noted that the inclusion of the simple resistive element in each circuit shown Figure 9 is used for illustrative purposes only, and the actual specified circuit can have resistances, inductances, and capacitances that are governed by complex physical phenomena occurring throughout the plasma and test facility.

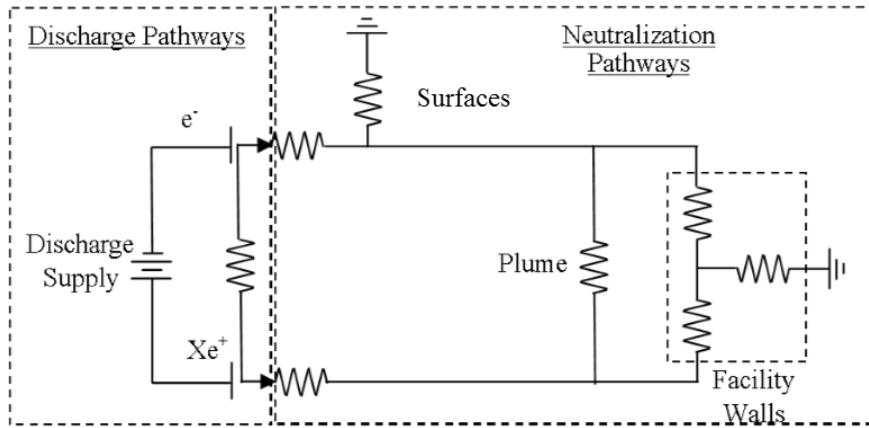


Figure 9: Notional Electrical Circuit Diagram of HET

A HET electrical circuit differs greatly on-orbit compared to a vacuum testing facility. In the on-orbit environment, the lack of an electrically-conductive wall surrounding the HET does not enforce charge recombination of ions and electrons. The lack of physical walls means that the local neutral pressure near the thruster can be of magnitude lower than what is achievable in a vacuum chamber facility. This lowers the overall population of charge-exchange ions present in the HET plume, and it has been shown that the elevated neutral pressure affects HET operation [16, 20, 25, 26, 61]. Since there is no electrical ground in space, the satellite bus common is used as the electrical

common [49, 51-53, 62]. This means that the HET electrical circuit reference is essentially a floating reference. As evidenced by the SMART-1 mission, this makes the HET electrical circuit susceptible to exposed electrical surfaces, spacecraft charging or other electrical influences. This floating reference has the potential to influence other aspects of the HET operation.

2.1.2 Accelerations of Ions in a Hall Effect Thruster

Because a HET relies on the formation of a Hall current to both ionize propellant and accelerate ions, the ionization region and the acceleration of a HET plasma discharge overlaps greatly and its position is not well defined [3]. This has the effect of making the ion energy distribution of the HET beam non-monoenergetic, *i.e.*, there is a distribution of ion energies. Additionally, the ions accelerated have an velocity vector that has non-negligible off-centerline velocity. This results in the beam of the HET to diverge. The following sections cover these two aspects of the HET in more detail.

2.1.2.1 Acceleration Voltage

Critical to understanding or calculating the thrust produced by a HET is the acceleration voltage, V_{accel} , of the ions created from the HET discharge. The thrust produced by a HET can be calculated via Equation (3) [3].

$$T_{HET} = \sum_{i=1}^{\infty} \left(X_i I_b Q_i \sqrt{\frac{2m_i V_{accel}}{e}} \right) \quad (3)$$

where X_i is the fraction of the ion beam in that charge state, I_b is the ion beam current, m_i is the mass of the ion, V_{accel} is the acceleration voltage, Q_i is the charge state (*e.g.*, 1, 2, or 3), and e is the fundamental charge. This equation assumes a mono-energetic acceleration

voltage and no beam divergence. Unlike ion-gridded engines, the acceleration voltage of the HET is not precisely controlled by a separate supply. As shown in Figure 7 and Figure 8, the discharge supply sets up the overall discharge potential difference between the anode and the cathode, V_d . The acceleration voltage is bounded by discharge voltage and the plume plasma potential V_p . In the HET discharge, the acceleration voltage varies spatially, and the resulting in a distribution of ion energies. Figure 10 below shows a sample ion energy distribution function for a HET with a discharge voltage of 300 V taken on thruster centerline. It is common for the ion energy distribution to be measured in units of Volts with an energy analyzer [3]. This data has been already corrected for the local plasma potential.

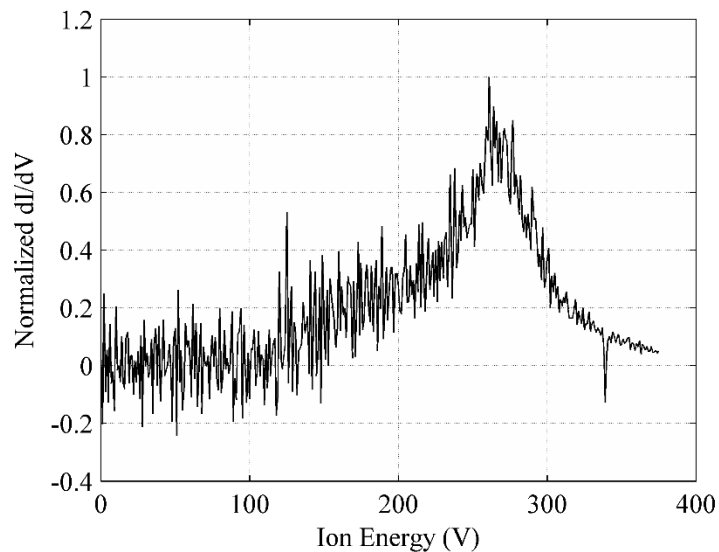


Figure 10: A single trace representative ion energy distribution function of a HET. The HET is operating at 300 V, 3.1 kW. The chamber pressure is 7.3×10^{-6} Torr Xe.

For this thruster (Figure 10), the most probable ion voltage is between 250 V and 270 V. The remaining potential difference generated by the discharge voltage can be thought as a loss in terms of thrust production. Since the discharge supply provides power

to maintain the HET discharge and to accelerate ions, it is difficult to measure the beam current precisely. Overall, total ion current and the electron current supplied by the discharge supply is balanced. For each positive charge accelerated by the thruster and electron must also be emitted by the cathode. Therefore, the discharge current is composed of a current related to the acceleration of ions and a current related to maintaining the discharge of the HET. Additionally, for an accurate prediction of thrust, the charge state of the ion population must be known. The number of multiply-charged ions depends on the many factors and normally represents a non-negligible fraction of the total ion population (>10%) [3]. In general, production of multiply-charged ions is not desirable as each additional ionization state requires more energy than the last ionization therefore production of multiply-charged ions results in an overall loss in thruster efficiency. In practice it is difficult to attain all the necessary information to accurately calculate thrust, and so the thrust is directly measured. For the purposes of this thesis, it is important to highlight the acceleration voltage of the HET beam. Since the acceleration voltage is determined by factors outside the thruster discharge channel, such as plume plasma potential or cathode-to-ground potential, the thrust of the HET may be influenced by the electrical facility effects that this work aims to understand.

2.1.2.2 Beam Divergence

Because the HET is a grid-less plasma accelerator, the electrostatic potential gradient is not directed uniformly downstream across the entire discharge channel [3, 26, 63]. The formation of ions throughout the ionization and acceleration regions in a HET means that a large portion of ions accelerated has a velocity vector that is not completely aligned with the thruster centerline axis. This leads the HET plume or ion beam to have a divergent plume. This off-centerline acceleration does not result in a net thrust, as HET are axis-symmetric devices. This off-centerline acceleration is also important to satellite integration. Since each individual accelerated ion carries with it a relatively large kinetic

energy, any surface that is impacted by these ions is eroded. For satellite integration issues, it is extremely important to avoid having satellite surfaces being impinged by the HET beam. In the case of the Russian Express Satellites, HET ion beam impingement lead to additional disturbance torques placed on the satellite [47]. Measuring the actual beam divergence in testing vacuum facilities is difficult because of the elevated neutral pressures [14]. The elevated pressures in the vacuum facilities allow for the production of charge-exchange ion production. The increased neutrals present in the vacuum chamber facility artificially inflate the measured plasma plume due to an increase in the production of charge-exchange ions. Additional work by Crofton and Pollard [26] demonstrated that charge-exchange ions formed in the near field of the HET, can be accelerated by local plasma potential gradients. Since the thruster body is a large conductive surface, it is possible that the beam divergence of the HET may be influenced by electrical facility effects.

2.1.3 Hollow Cathode Coupling Efficiency

Cathode coupling efficiency is a measurement of the power required to extract electrons from the cathode in a HET relative to the power necessary to sustain the in the discharge, as shown in Figure 8 [3]. The power needed to extract electrons is supplied by the discharge supply, and so power used to extract electrons from the cathode comes at the expense of acceleration voltage. The cathode coupling efficiency is defined as shown in equation (4), where η_{cg} is the cathode coupling efficiency and V_{cg} is the cathode-to-ground voltage and V_d is the discharge voltage [46]. It should be noted that cathode-to-voltages are typically negative.

$$\eta_{cg} \equiv 1 + \frac{V_{cg}}{V_d} \quad (4)$$

Outside of the physical design of the hollow cathode, many factors play into the cathode coupling efficiency. Cathode placement with respect to the magnetic field

topology is an active field of research and much work has done to study the impact of cathode placement on HET operation [3, 19, 38, 39, 46, 64-67]. Additionally, the dynamic processes that govern cathode operation and electron transport in the near field region of the cathode is an active field of research [10, 65, 68, 69]. These factors most pertinent to this work are the local plasma conditions at the cathode exit and the placement of the cathode relative to the HET.

2.1.4 Plasma Oscillations in the Discharge

Although the HET is a steady-state plasma device, the plasma environment inside the HET is dynamic [59] and operates on many different time-scales. It is a multi-species plasma with magnetic and electric fields. This gives rise to several plasma instability modes within the thruster discharge. Figure 11 shows a representative power spectra of a HET discharge current of a HET operating at 300 V. The breathing mode of the HET discharge is the fundamental plasma instability operating inside a discharge channel. The breathing mode of the discharge plasma can be identified in the power spectra of the discharge current. The breathing mode discharge oscillation is clearly identifiable as a peak in the power spectra at 32.5 kHz. For satellite integration issues, the discharge current oscillation breathing mode is one of the most important. This discharge current oscillation affects the global power requirements to maintain the plasma discharge and occurs at frequencies in the low kHz range [3, 59]. The breathing mode of the discharge oscillation causes the load on the discharge supply to fluctuate in the low kHz range. In terms of powering the HET, this load fluctuation is undesirable. In order to efficiently power the HET, the discharge supply or the power processing unit must be decoupled from the breathing mode oscillations and this oscillation is typically attenuated using a low-pass filter [3, 70, 71]. The discharge current breathing mode can be influenced by numerous factors such as but not limited to: propellant temperature, propellant type, anode mass flow rate, applied discharge voltage, thruster channel wall geometry, magnetic field topology, cathode

placement, cathode mass flow rate, and facility contamination [59]. Since the breathing mode has a direct influence on the HET electrical circuit and can be influenced by a large number of factors that are external to the HET circuit, the measurement of this dynamic mode of the HET discharge is of key importance to this dissertation work.

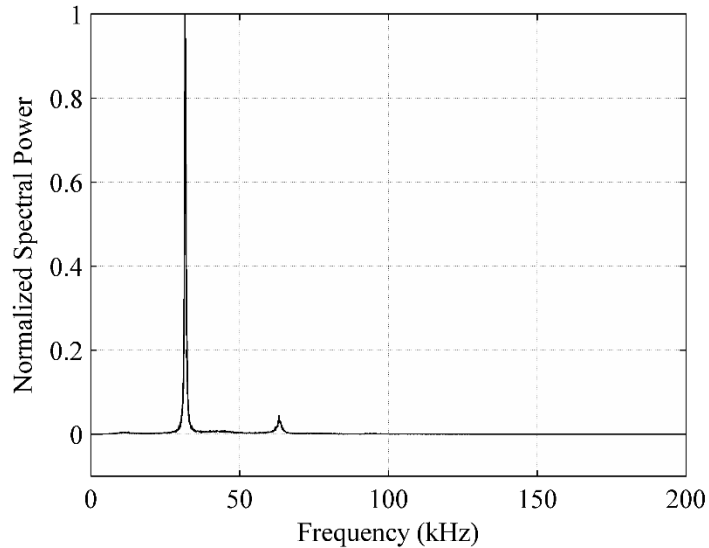


Figure 11: Representative discharge current power spectra. The HET operation condition is at 300 V, 3.5 kW.

2.1.4.1 Predator Prey Model of the Discharge Current Oscillation: Breathing Mode

To give the reader a better understanding of the breathing mode discharge oscillation and factors that can impact it, a brief overview of the predator-prey model of the breathing mode is described. The classical predator-prey description of the breathing mode plasma instability comes from the imbalance of the neutral propellant supply rate and the ionization and acceleration rates [3, 32, 59]. The neutral particle supply rate to the ionization/acceleration region is thermally limited, while the ionization rate is controlled by many factors, such as ionization cross-section, collision frequency, and electron temperature. Ionization and acceleration rates of propellant exceeds the neutral supply rate of propellant. This creates a cyclic behavior of increased ionization rate and acceleration,

decreased ionization and acceleration due to neutral propellant depletion. The end result of this oscillation is that the discharge current will concurrently fluctuate with the discharge; these fluctuations are classified as the breathing mode. A more complete description of this mechanism can be found in [3, 35, 59]. From this model, the breathing mode frequency is described by the relation shown in the following equation [59]:

$$\omega^2 \sim \frac{\dot{n}_i}{n_i n_n}. \quad (5)$$

Since the discharge oscillation mode frequency depends heavily on the ionization rate, any variations in the collision cross-section, ion density, neutral density, and electron temperature will change the frequency of oscillation. One of the fundamental operating principles of the HET is the retardation of electrons towards the anode via a radial magnetic field. On their way to the anode, the electrons experience azimuthal drift and they gain energy from the potential gradient set up by the positive bias of the anode. It is this azimuthal drift that enables the electrons to ionize and accelerate ions. From this perspective, the thermal energy of arriving cathode electrons plays a critical role in determining the electron temperature of the ionization region of the HET. The exact energy of these electrons in the ionization and acceleration zone is difficult to precisely predict, but an order of magnitude estimate is illustrated in Eq. (6), Eq. (7), and Eq. (8) using a zeroth-order formulation of the predator prey model [3, 59]:

$$\dot{n}_i = -n_n n_i \langle \sigma_i v_e \rangle \quad (6)$$

$$\langle \sigma_i v_e \rangle = 10^{-20} \left(-1.031 \times 10^{-4} T_e^2 + 6.386 e^{-\frac{12.177}{T_e}} \right) \quad (7)$$

$$\left(\frac{\omega^*}{\omega^o} \right)^2 = \left(-1.031 \times 10^{-4} T_e^{*2} + 6.386 e^{-\frac{12.177}{T_e^*}} \right) \left(-1.031 \times 10^{-4} T_e^{o2} + 6.386 e^{-\frac{12.177}{T_e^o}} \right) \quad (8)$$

where ω , \dot{n}_i , n_i , n_n , $\langle \sigma_i v_e \rangle$, T_e , and m_e are the breathing mode frequency, ion production rate, ion density, neutral density, ionization rate coefficient, electron temperature in eV, and electron mass, respectively. Assuming ion and neutral density remain constant, the discharge oscillation frequency is dependent solely on the ionization rate. Assuming a Maxwellian energy distribution of the electron population and neutral propellant population, it is possible to model the ionization rate as listed in Eq. (6) [3]. In reality, the ionization electron population is likely to not have equal Maxwellian energy distributions in both the azimuthal and axial direction. The isotropic Maxwellian energy distribution assumption made in this zeroth-order model will lead to an artificially higher ionization rate. Here the ionization rate is dependent on neutral and ion density as well as the reaction rate coefficient. This reaction rate coefficient takes into account xenon ionization cross section dependence on electron temperature and relative speed for a bimolecular ionization collision process. By combining Eq. (5), Eq. (6), and Eq. (7) and normalizing the discharge oscillation frequency by a nominal breathing mode frequency, the changes in discharge oscillation becomes solely dependent on changes in electron temperature as shown in Eq. (8). Since the collision cross-section for ionization is highly dependent on the electron temperature, an estimate for the electron temperature is needed. A reasonable estimate for the electron temperature of the discharge can be taken as 10% of the beam voltage [3]. From the retarding potential analyzer data presented in Frieman *et al.*, the beam voltage is measured to be approximately 250 V, and so to make an assessment of the ionization rate impact on the discharge oscillation frequency, it is assumed that the nominal electron temperature is 25 eV inside the discharge [3]. Figure 12 shows the results of the calculations. From this model, it is evident that even small changes in the electron temperature of the plasma in the ionization and acceleration region can cause changes in the breathing mode frequency. Outside of this zeroth order model, the discharge current breathing can be influenced by numerous factors such as but not limited to: propellant

temperature, propellant type, anode mass flow rate, applied discharge voltage, thruster channel wall geometry, magnetic field topology, cathode placement, cathode mass flow rate, and facility contamination [59].

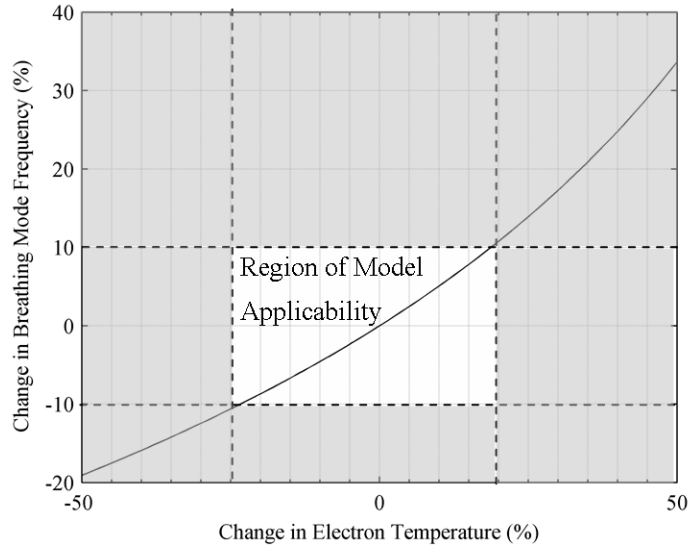


Figure 12: Percentage change in breathing mode frequency as a function of percentage change in ionization electron temperature. Greyed regions denote non-physical solutions from the zeroth-order model.

2.2 Preliminary Efforts in Electrical Facility Research

Initial exploratory work, done by Frieman, et al. [72], sought to establish whether or not the conductive walls played a significant role in the HET electrical circuit. Their experimental setup had a HET operating in a vacuum chamber and was surrounded by two distinct plasma environments. In the downstream of the HET exit plane, the charged-particle components of the plasma environment consist mainly of ions that are accelerated by the HET discharge and electrons. These ions have a large downstream component of their velocity and therefore lead to a non-isotropic plasma environment. In regions where the HET beam is not present, commonly referred to as “the off-axis” plasma environment,

the ions present are primarily created through a charge-exchange process. The ions have much lower energy than comparable beam ions and to zeroth-order have no preferential direction of travel. This leads to a more uniform, isotropic plasma environment. To investigate these environments, Frieman, et al. [72] placed two electrical witness chamber plates, one in the direct downstream plasma environment and one in the “off-axis” plasma environment. The T-140 HET served as a representative test bed [72].

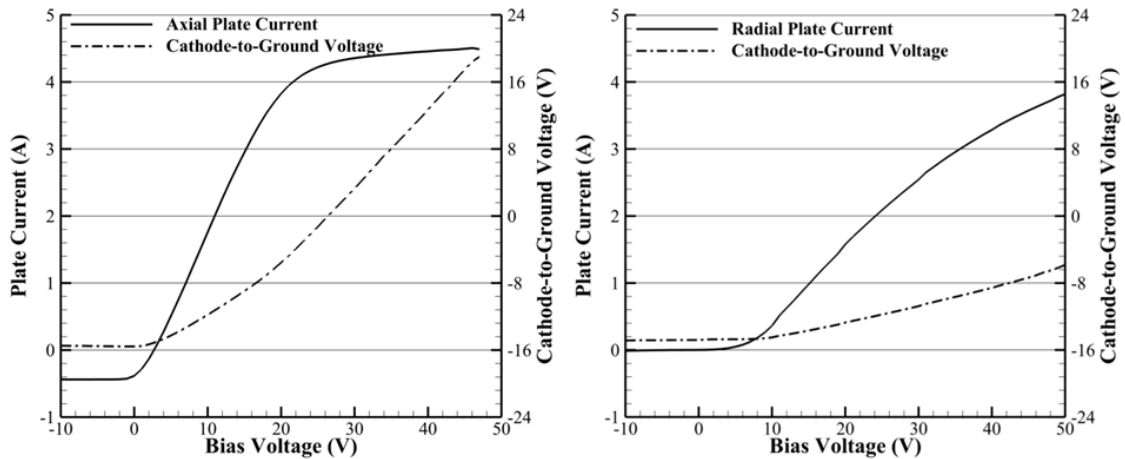


Figure 13: Axial and radial chamber plate sweeps taken while a T-140 HET was operating at a discharge voltage of 300 V and a discharge current of 5.16 A. Figure is taken from Frieman, et al. [72]

Figure 13 shows both the collected current and cathode-to-ground voltage as a function of plate bias voltage. Time-averaged measurements of the cathode-to-ground potential and current drawn were taken at each bias potential [40, 72]. As the plate bias voltage was increased the cathode-to-ground potential moved synchronously. The conductive wall of the vacuum chamber serves as a recombination site for positive and negative charges of the plasma plume. The floating potential, cathode-to-ground voltage, is set by the local plasma conditions and magnetic field conditions. Since the HET discharge circuit is floating, changes in the local plasma potential near the cathode will cause the whole HET thruster electrical circuit floating potential to change relative to

ground. Because of this, it is expected that the plasma potential of the HET plume is impacted by the changes in the plate voltage relative to ground. Frieman, et al. [72] conclude that the vacuum chamber facility is part of the HET discharge circuit.

The work by Frieman, et al. [72], demonstrated many possible promising avenues for further research. The overall conclusion of the work is that the vacuum chamber is a part of the electrical circuit. The movement of the HET floating voltage (cathode-to-ground voltage) with respect to plate bias voltage suggests that a mechanism similar to the one observed during the SMART-1 mission maybe at play in the interaction between the vacuum facility and the HET. It is unclear from the work as to whether the thrust of the HET is significantly impacted by add the chamber to the HET electrical circuit.

Chapter III

Experimental Approach

In the previous chapters, we discussed the fundamentals of HET operation, the state of research in facility effects, and documented in-space behavior of HET that deviates from our current understanding of facility effects. In this chapter, we discuss the selection of scope for this research effort.

3.1 Research Goals

While there are many questions and unknowns related to the influence of the ground testing facility of HETs, it is necessary to selectively narrow the scope of this study. This work seeks to investigate the basic physical aspects of the electrical HET-vacuum interaction that directly influence measurable characteristics of the HET. To better understand how this work narrows the scope of this investigation, it is important consider the entire HET electrical circuit. The total circuit includes both the HET discharge and cathode neutralizing circuits and the electrical circuit created when positive (ions) and negative (electrons) charges produced by the HET recombine in the ground testing environment. As demonstrated by the Frieman, et al. [72], the vacuum facility walls are just one possible pathway that this recombination circuit can form. Plasma interactions with any conductive surface can setup the possibility of a recombination pathway or circuit forming. The main requirement for this recombination pathway to form is that there is net differential flux of charges collected on these conductive surfaces. This flux of charge is dictated by the electrical potential of the conductive surface and the local floating potential of the plasma [73]. Since the HET testing environment is not a uniform plasma environment, these recombination currents can form in many places within the test facility. Based on previous research efforts, these recombination currents and the availability of these recombination currents have not been considered and are critical to the formation of

the understanding of how the vacuum testing facility electrically interacts with the HET. This dissertation work is subdivided into the following research goals:

3.1.1 Chamber Wall Charge Recombination Pathways Effects on HET Operation

- The walls of the vacuum test facility have been mentioned numerous times in the literature as a factor to influences the HET, but the physical mechanisms that govern that interaction has not yet been explored. Since HETs are ubiquitously tested in ground-based vacuum facilities this dissertation work seeks to answer the following question: How does the chamber wall charge recombination pathway interact with the Hall effect thruster?

3.1.2 Thruster Body Charge Recombination Pathways Effects on HET Operation

- The thruster body is commonly electrically connected to an electrical common, and the electrical common between the ground-testing environment and the on-orbit environment is fundamentally different. It has been demonstrated the HET floating circuit voltage relative to that common does not necessarily remained fixed. The physically closet conductive surface to the HET discharge is the thruster body. Since it is unknown whether the HET thruster body plays an important role in HET operation, this dissertation work seeks to answer the following question: How does the electrical boundary condition of the thruster body itself affect the operation of Hall effect thruster?

3.2 Control Methods

In order to examine each of the research goals, a control method has to be established. For each research goal a separate control methodology is established and the expected ranges for variation of these control methodologies is discussed in detailed below. In each of these methods detailed below, the goal is control or influence the availability of

charge recombination pathways. Since the electrons are the most mobile of the charge carriers, these discussed control methods seek to influence the pathways available for electrons to terminate and exit the HET electrical circuit.

3.2.1 Chamber Wall Charge Recombination Pathway Control Methodology

Based on the prior work performed by Sommerville and King [19, 64] and Frieman, et al. [72], there are two promising methods for controlling the availability of the chamber wall charge recombination pathways: (1) cathode position within the HET magnetic field and (2) the voltage bias relative to ground of a large electrode in the HET plume.

3.2.1.1 Control via Cathode Position in the HET Magnetic Field

The cathode positioning work by Sommerville and King illustrated that the position of the cathode relative magnetic field can influence the operational characteristics of the HET. Since the cathode of a HET is responsible for supplying electrons for both ionization and neutralization, the position of the cathode within HET magnetic might be able to influence how electrons propagate into the chamber for neutralization. The strength of this magnetization can be characterized by the electron Hall parameter. The electron Hall parameter is defined as the ratio of the electron cyclotron frequency to the electron-neutral collision frequency. In general, the Hall parameter is a way to quantify the magnetization of charged particles by comparing the tendency of the motion of the particle to be dominated by the magnetic field or through collisions with other particles. The Hall parameter can be calculated as shown in the following equation:

$$\beta = \frac{\Omega_e}{\nu_e} = \frac{eB}{m_e \nu_e} \quad (9)$$

where β is the electron hall parameter, Ω_e is the electron gyro-frequency, ν_e is the electron-neutral collision frequency, e is the elementary charge, B is the magnetic field strength, and m_e is the mass of the electron. An electron Hall parameter of much greater than unity

implies that the electrons are magnetized, *i.e.*, the electrons are able to complete many orbits around their guiding center before colliding with a neutral particle. In such a condition, the electron motion is confined by the magnetic field lines and they traverse along these magnetic field lines. An electron Hall parameter much less than unity implies that the electrons are no longer magnetized, *i.e.* the electrons can experience neutral collisions, ion collisions, or surface collisions before being able to complete one orbit around their guiding center. In such a condition, the electron motion is no longer confined by magnetic field lines.

By radially moving the position of the cathode relative to the HET (a notional diagram of this is shown in Figure 2), we can control the electron Hall parameter at the cathode orifice and move the cathode between spatial regions of strong electron magnetization and weak/no electron magnetizations. In doing so, we can control the available pathways that electrons sourced from the cathode can terminate and electrically exit the HET discharge circuit.

3.2.1.2 Bias of the downstream axial plate

The bias electrode work of Frieman, et al. [72] demonstrated that the voltage of witness plates placed inside the vacuum chamber can affect the cathode-to-ground potential of the HET circuit. This change was driven by electron current collection on the witness plates. Since the primary plasma source in the vacuum chamber environment is the HET, collection of electrons on these witness plates demonstrate a way to influence the electron termination pathways. In pursuit of overall goals of this work, this research effort uses the witness plate scheme to control the electron termination pathways and measure the impact of this change on HET operation.

3.2.2 Thruster Body Bias Voltage Control Methodology

The HET thruster body and magnetic circuit elements are made of electrically conductive materials and may be another important charge recombination pathway present in both the on-orbit and ground testing environment. As with the chamber walls, a spatial variation on charge flux incident on these conductive surfaces means that the thruster body thruster body can become a viable surface for charge recombination to occur. From a time-averaged/steady-state perspective, the magnetic field of the HET serves to already create spatial variations in the charge flux on incident surfaces. Electrons sourced from the cathode are guided towards specific spatial locations and the acceleration of ions near the discharge channel exit plane and the locally high neutral number density spatially concentrates charge-exchange ion production [25, 26, 74] to the near exit plane of the HET. Time-resolved electric field measurements near the HET discharge channel exit plane also demonstrate time-varying spatial distributions of plasma properties due to the oscillatory nature of the HET plasma discharge [63, 75]. As long as the spatial distribution of charge flux does not change from ground testing to on-orbit, then there should be no appreciable effect in HET operation. In the flight environment, the HET thruster body is typically electrically connected to the satellite system common [49, 51]. This configuration is to prevent charge accumulation between satellite bus and the HET chassis. In the ground testing environment, the thruster body is typically electrically grounded. In both the on-orbit and the ground-testing cases, the floating potential of the HET circuit is set via the cathode [3, 37, 65, 69]. In the ground-testing environment, the cathode floating voltage is below earth ground while the thruster body can be electrically floating or grounded. The flight data gathered about the SMART-1 PPS-1350G HET demonstrates that different voltages of the thruster body relative to the HET electrical circuit are possible. Figure 14 shows a diagram that illustrates the key HET voltage references in the typical ground test and from the SMART-1 flight data and how those voltage differences can influence the

possible pathways electrons can follow. As the thruster body was electrically connected to the satellite bus common [51, 53], a change in sign of the cathode-to-satellite bus common results a change in sign of the thruster body-to-HET floating circuit voltage. A change in sign of the thruster body-to-HET floating voltage means electrons generated by the cathode that were accelerated towards the thruster body would be repelled by the thruster body. Because this behavior has been observed on spacecraft, it sets up the possibility that the spatial charge flux distribution could change between ground testing and in-flight operation. These factors indicate that the thruster body voltage relative to the HET floating circuit voltage (*i.e.* cathode-to-ground voltage) is an important variable to control. By controlling the voltage of the thruster body relative to ground (via voltage biasing or by controlling the resistance to ground of the thruster body), this work is able to vary the thruster body-to-cathode voltage.

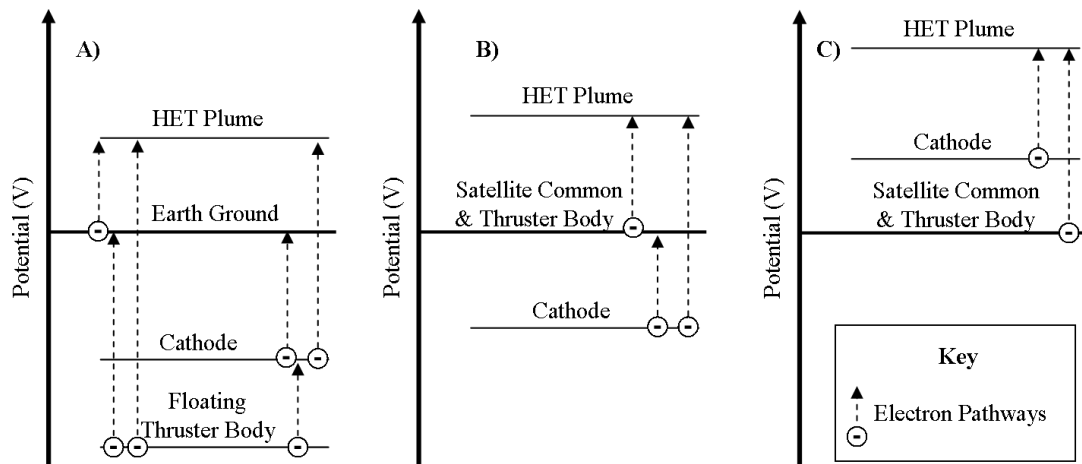


Figure 14: Relative potentials of key HET electrical references A) Typical ground testing environment B) Typical on-orbit environment C) Elevated cathode potentials taken from the SMART-1 mission.

3.3 Measurement Characteristics Key to the Research Goals

For each of the experimental configurations it is important to identify the key measurements to be able to address the aforementioned research goals. The following section details those measurements.

3.3.1 Measurements Regarding the Hall Effect Thruster

In order to address the outlined research goals, it is necessary to characterize the HET while it is operating. Based on the literature and the physics governing HET operation, the characteristics of interest are subdivided into three separate categories: the plume of the HET, the electrical circuit of the HET, and the thrust generated by the HET. As discussed in Chapter I and Chapter II, the thrust of the HET is affected by many different factors and is a key operational characteristic that is used to derive other operational characteristics of the HET such as but not limited to: the specific impulse and the anode efficiency. Therefore, it is important to directly measure the HET thrust response to any changes in the charge recombination currents. The plume of the HET has already been shown to be affected by external electrical factors [72]. These changes are expected to occur to the plume plasma potential. If the plume plasma potential has regional variations, then the structure of the near field plume may also change. This would in-turn affect the ion beam divergence or the ion energy distribution function. Therefore, it is important to characterize the HET plume's response to changes in the charge recombination currents by measuring changes in the plume's plasma potential, the beam divergence, and the ion energy distribution function. The components of the electrical circuit of the HET of interest are the discharge current and the cathode-to-ground voltage. The cathode-to-ground voltage is a measurement of the HET circuit floating voltage and has been demonstrated to depend on external electrical factors[51, 55]. The discharge current of the HET is directly impacted by the physical mechanisms that govern the HET discharge. Therefore, it is

important to characterize the HET electrical circuit response to changes in the charge recombination currents by measuring changes in the cathode-to-ground voltage and the HET discharge current. By characterizing the HET's thrust, plume, and electrical response to changes in the recombination currents this work is able to address the overall research goals.

3.3.2 The Electrical Witness Plates and Conductive Surfaces

Since the chamber and thruster body recombination currents are inherently electrical, it is necessary to gain an understanding of the electrical properties of these recombination currents. As described in the control methodologies section, the use of electrical witness plates is used as an indicator of changes occurring in the overall chamber and thruster body recombination currents. For electrical configurations where the witness plates are electrically grounded, it is only important to measure the collected current, as the voltage of the plate is held at earth-ground. For electrical configurations where the witness plates' voltage is controlled, it is important to measure both the current and the voltage of the witness plates. Spatial variations in the current collected on the electrical witness plates indicate the potential for a recombination current to form and changes in those spatial variations are indicative of changes to the recombination currents. Since the HET is the primary plasma source in the testing environment, changes in the current or voltage of the witness plate are also indicative of changes to the HET behavior. By measuring the current and voltage of the electrical witness plates and characterizing the chamber wall and thruster body recombination current, this work is able address the overall research goals.

CHAPTER IV

EXPERIMENTAL APPARATUS

In the previous chapters, we discussed the fundamentals of HET operation, the state of research in facility effects, documented in-space behavior of HETs that deviates from our current understanding of facility effects, the research goals of this work, and the control methodologies used to investigate those research goals. In this chapter, we discuss the experimental equipment and the experimental techniques used in the analysis of the data gathered in this thesis. For each control methodology, there is a specific experimental configuration. Those specific experimental configurations are described in Chapter V before the results of each experimental configuration is presented.

4.1 Testing Facility

All experiments were performed in the Vacuum Test Facility 2 (VTF-2) at the Georgia Institute of Technology High-Power Electric Propulsion Laboratory (HPEPL). The VTF-2 is a stainless-steel chamber measuring 9.2 m in length and 4.9 m in diameter. It is evacuated to rough vacuum using one 495 CFM rotary-vane pump and one 3800 CFM blower. High-vacuum is achieved using 10 CVI TM-1200i re-entrant cryopumps that have a liquid nitrogen cooled shroud and a helium cold-gas cycle cooled pumping surface. The cryopump shrouds are fed using the Stirling Cryogenics SPC-8 RL special closed-loop nitrogen liquefaction system detailed by Kieckhafer and Walker [76]. The vacuum facility can be configured to operate on any number of cryogenic pumps available. With all 10 cryopumps operating, the facility has a combined nominal pumping speed of 350,000 l/s on xenon and can achieve a base pressure of 1.9×10^{-9} Torr-N₂. Pressure in the VTF-2 was monitored using two Agilent BA 571 hot filament ionization gauges controlled by an Agilent XGS-600 Gauge Controller. Pressure measurement uncertainty of the Agilent BA 571 is expected to be +20%,-10% of indicated pressure [44]. One gauge was mounted to a

flange on the exterior of the chamber while the other was mounted 0.6 m radially outward from the thruster centered on the exit plane. In order to prevent plume ions from having a direct line of sight to the ionization gauge filament of the interior ion gauge and potentially affecting the pressure measurement, a neutralizer identical to the one used by Walker and Gallimore [16] was attached to the gauge orifice. Because the ion gauge is an indirect method of pressure measurement, the pressure read from the device is highly dependent on the present gases. In general, these ion gauges are calibrated against pure nitrogen gas and have to be corrected for a differing ambient neutral gas [44]. As specified by the manufacturer, the corrected pressure (P_c) is found by relating the indicated pressure (P_i) and the vacuum chamber base pressure (P_b) to a gas-specific constant using the following equation [43]:

$$P_c = \frac{P_i - P_b}{2.87} + P_b \quad (10)$$

4.2 Plasma Source

A key component of this investigation is the plasma source. Due to the observed in-flight abnormalities being specifically related to HETs, it is only natural that a HET serve as a representative HET testbed. The following section detail the testbed HET, cathode selection, propellant systems, and HET electrical circuit.

4.2.1 T-140 HET

Because of the variety of differing HET designs employed and the strict control of information related to flight proven HET technologies selection of the representative test bed HET is difficult. To be able to reproduce the key physical phenomenon investigated, the HET selected needed to have similar power levels and discharge voltages to what has

been used and is being used in orbit. Based on thruster specifications of the Snecma PPS-1350 (used on SMART-1), Fakel SPT-100 (used on Russian Express satellites), and the BPT-4000 (used on domestic satellites), a HET designed to operate in the kW power level range and the ~300 V discharge voltage is desirable [7, 41, 47, 51, 53]. These requirements are met by the Aerojet Rocketdyne T-140 HET originally developed by Space Power, Inc. in collaboration with the Keldysh Research Center and Matra Marconi Space [40]. The T-140 HET is a laboratory-model HET that has a discharge channel made of M26 grade boron nitride with an outer diameter of 143 mm and a nominal discharge power of 3 kW and a maximum discharge voltage of 400 V. The 140 HET thruster was designed as a domestic alternative to the Russian made Fakel SPT HETs, but was never developed into flight maturity. In pursuit of the T-140 HET development goals, the performance of the T-140 has been extensively mapped by prior investigations [40]. These aforementioned factors make the T-140 HET a good test-bed for examining the interactions between with facility chamber while being able to freely access and discuss pertinent information.

4.2.2 Cathode

Another important factor in the HET discharge circuit is the cathode (*i.e.*, electron source). The tested cathode with the T-140 in prior performance mapping, performed by W. Hargus, et al. [77] is unavailable and so other cathodes are considered. The main driving factor for selection of the cathode is the discharge current (electron current) that can be supplied by the cathode. The T-140 HET operates at a nominal 10 A of discharge current and so a cathode with at least 10 A current capacity is desirable. The Electric Propulsion Laboratory Hollow Cathode Plasma Electron Emitter (HCPEE) 500 series cathode is selected as the cathode because of its ability to supply up to 50 A of discharge and low self-heating current of the cathode. Using magnetic field simulations of the T-140 HET and optimizing the location of the cathode, the nominal location of the cathode orifice is located approximately 2.5 cm downstream of the thruster exit plane at a fixed declination

of 55 degrees with respect to the thruster centerline. The nominal radial position of the cathode was 18.1 cm outwards from thruster centerline. The cathode was located at the 9 o'clock position of the thruster. Typical cathode mass flow rates are 10% of the anode mass flow rate.

4.2.3 Propellant System

High-purity (99.9995%) xenon propellant is supplied to the thruster and cathode using seamless 316 stainless-steel lines metered with MKS 1179A mass flow controllers. The mass flow controller for the anode propellant line has a range of 200 SCCM, and the mass flow controller for the cathode has a range of 20 SCCM. The controllers are calibrated before each test by measuring gas pressure and temperature as a function of time in a known control volume. After calibration, the mass flow controllers have an uncertainty of ± 0.03 mg/s (5.1%) for the cathode flow and ± 0.12 mg/s (2%) for the anode flow [78].

4.2.4 Electrical Circuit

The T-140 HET discharge is controlled using a Magna-Power TSA800-54 power supply. The thruster inner and outer magnet coils are powered with TDK-Lambda GEN60-25 power supplies. A TDK-Lambda Genesys 150 V-10 A and a TDK-Lambda Genesys 40 V- 38 A power supply is used to power the cathode keeper and heater, respectively. The thruster discharge supply is connected to a discharge filter consisting of a $95\text{-}\mu\text{F}$ capacitor and $1.3\text{-}\Omega$ resistor in order to attenuate oscillations over 1.4 kHz in the discharge current from reaching the discharge supply. Diagnostic and power connections enter the VTF-2 through separate feedthroughs on separate flanges to eliminate potential cross-talk between the thruster discharge power lines and diagnostic lines. Figure 15 shows the circuit used to operate the T-140 HET in this work.

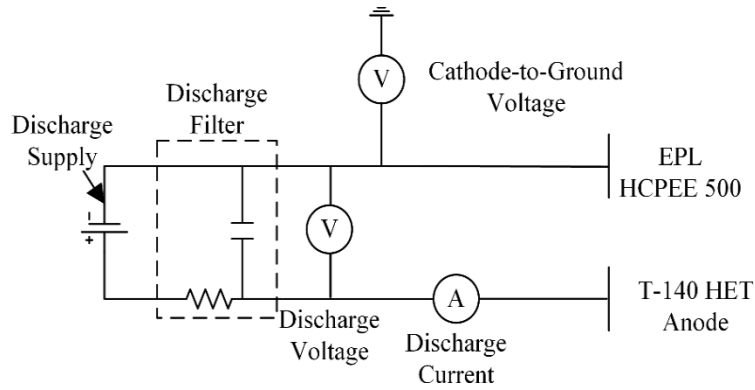


Figure 15: Electrical diagram of current and voltage measurements of the HET discharge circuit

4.3 Chamber Plates

Since it is logistically impractical and potentially dangerous to float the entire vacuum facility wall, a more localized approach is taken to assess the impact of the conductive walls of the vacuum chamber facility on HET operation. As Frieman, et al. [72] demonstrated, the use of large electrodes in the HET plume have the ability to influence the HET electrical circuit. This thesis effort uses electrically conductive plates as representative chamber surfaces. By controlling the electrical boundary condition of these witness plates and measuring the corresponding voltage of or current collected from the plates, this research effort is able to examine the connection between the HET electrical circuit and the walls of the vacuum facility.

4.3.1 Locations of Plates

Since the chamber witness plates are a localized electrical measurement, it is imperative to place them in plasma locations that are characteristic of key regions of the HET plasma environment. In a HET vacuum facility environment there is plasma throughout the testing volume. The plasma environment of the HET has two distinct regions in the vacuum test facility: the plume and the off-axis region [3]. The plume of the

HET contains large population of the ions that are accelerated by the HET discharge. These ions are uniquely different from the charge-exchange ions that are produced through ion-neutral collisions. The ions accelerated by the HET discharge have a much larger kinetic energy than charge exchange ions and a bulk velocity that is directed downstream. In general, the plasma within the plume of the HET has a higher plasma density, electron temperature, and plasma potential than compared to the plasma located in the off-axis region. The plasma in the off-axis region of the HET is primarily composed of ions that generated through charge exchange. The vacuum facility is filled with ambient neutral propellant atoms and those neutrals are thermalized through collisions with chamber surfaces. These ambient neutrals can collide with ions generated by the HET discharge and exchange charge. This results in a highly energetic neutral and a thermalized, low-energy ion. The low-energy, thermalized ions drift outwards from the HET plume and fill the test facility volume.

For the HET plume plasma environment, placement of the chamber witness plate is straightforward. The chamber witness plate needs to be inside the plume of the HET. To ensure that axial chamber plate is unobtrusive as possible, the chamber witness plate needs to be placed as close to the walls of the facility as possible. Based on those two aforementioned constraints, the chamber plate is placed 4.3 m downstream from the exit plane of the thruster, centered along the thruster centerline. This distance is the closest to the rear wall of the vacuum chamber without contacting any of the facility surfaces. This chamber plate referred to as the “axial chamber plate” or the “axial plate” throughout the rest of this work.

Because the off-axis plasma environment encompasses all testing volume outside of the HET plume, placement of the chamber witness plate is not as straightforward as the axial chamber plate. The chamber witness plate in the off-axis plasma must be placed in a region where the local plasma ions are primarily composed of charge exchange ions, and

the chamber plate should be placed as unobtrusively as possible. Additional guidance can be drawn from the results of the SMART-1 mission. During the SMART-1 mission, the electrical circuit of the HET was significantly altered when exposed low-voltage contacts had direct line of sight with HET plume [55]. These solar panel contacts were not in the direct ion beam of the HET but were in the ambient plasma. Drawing from those results, the chamber witness plates should also be placed in an area that has direct line-of-sight with the HET plume. This immediately removes regions of wall space behind the HET and regions below the support structures attached to the bottom of the vacuum chamber from consideration. This leaves the regions along the sidewalls of the vacuum chamber that are above the floor support structures. A natural consequence of the beam divergence of the HET is that as the distance away from the HET exit plane increases there is an expected increase in HET accelerated ions impacting the sidewalls of the chamber. Since the goal of the second chamber plate is to be in a region of plasma that is dominated by charge-exchange ions, the sidewalls of the chamber closest to the exit plane of the thruster is preferable. In terms of clocking of the chamber plate, Xu and Walker [21] demonstrated that the azimuthal placement of the cathode can influence the HET plume structure. Since one method of controlling the influence of the vacuum chamber on the HET electrical circuit is change the position of the cathode, placement of the chamber plate on the side that the cathode is mounted is preferential. The chamber plate in the charge-exchange environment is placed 2.3 m radially outward from the thruster centerline and centered on the exit plane of the T-140 HET and is referred to as the “radial chamber plate” or “radial plate” throughout the rest of this work.

4.3.2 Design of Plates

The chamber witness plates consist of two 0.91 m x 0.91 m x 0.16 cm thick square aluminum plates. The witness plates were isolated from electrical ground using G-10 fiberglass bolts and washers. The resulting electrical resistance of these to ground was

greater than $1.5 \text{ G}\Omega$ measured at 250 V. The radial plate was mounted adjacent to, but electrically isolated from, the walls of the vacuum test facility. RG-58 cabling is electrically connected to the radial chamber plate. This cabling is routed to one of the BNC vacuum feedthroughs and the electrical connection terminates inside the control room. Figure 16 shows an image of the radial chamber plate installed in the vacuum chamber. The axial plate is mounted as far down downstream as possible. The axial chamber plate is mounted such that the center of the plate is aligned with the HET centerline. Depending on the testing configuration, either RG-58 or 6-AWG wire is electrically connected to the axial plate. Like the radial plate electrical connection, the axial plate cabling is connected one of the vacuum chamber feedthroughs and is terminated inside the control room. Figure 16 shows an image of the axial chamber plate installed in the vacuum chamber.

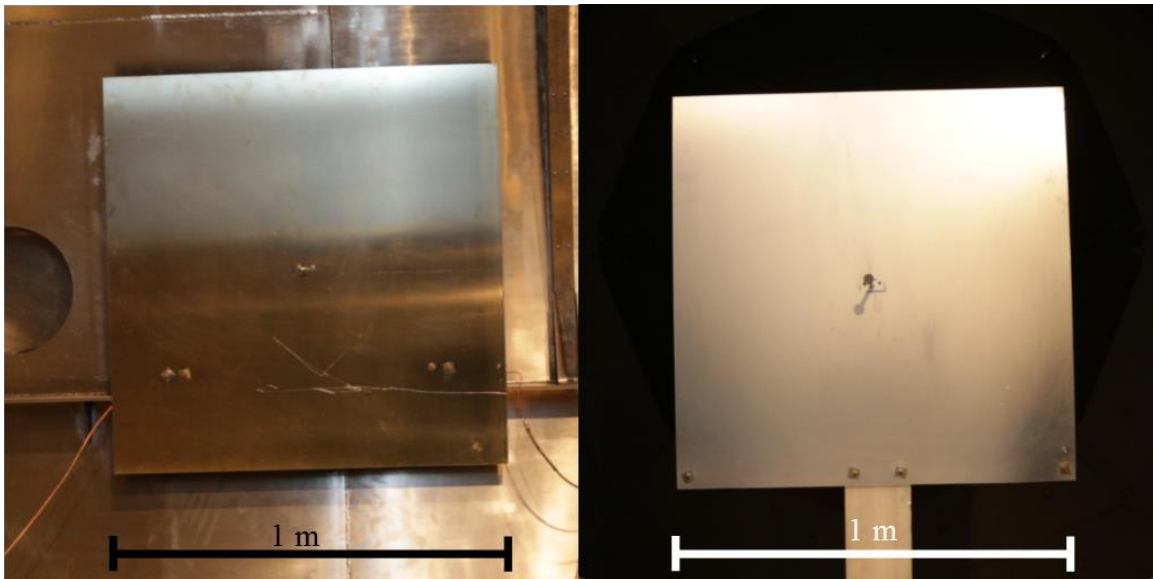


Figure 16: Left) Radial chamber plate. Right) Axial chamber plate

4.4 Thruster Body Plates

To further understand how the thruster body interacts with the HET electrical circuit, electrical witness plates are used. Like the chamber witness plates, the thruster body current or voltage is measured to examine the electrical interaction with the HET electrical circuit. In general, the locations of the thruster body witness plates already have electrical continuity to the thruster body and have electrically conductive surfaces exposed to the plasma, it is not expected that placing small, witness plates in this area will disturb the surrounding plasma environment.

4.4.1 Locations of Plates

Like the chamber witness plates, the thruster body witness plates are placed in regions that have distinct plasma environments. Like the chamber witness plates, there are regions of the thruster body that are directly exposed to the HET discharge plasma and other regions that are primarily exposed to charge-exchange plasma. Based on the time-resolved results from Lobbia [75] and Vaudolon, et al. [63], the electrical witness plates are placed in locations as shown in Figure 17 and Figure 18. For electrical chamber plates labeled “TP2” and “TP3”, the thruster body witness plates are placed in regions where there are magnetic field lines that intersect the thruster body surface, as shown in Figure 18. These magnetic field lines in these locations are strong enough to magnetize local electrons and can guide those electrons onto those surfaces. Because of these magnetic field lines, it is expected that these electrical witness plates will collect a net electron flux. Due to the external mounting of the cathode, it is important to place electrical witness plates on the cathode facing side of the HET body and the opposite side of the HET body, as shown in Figure 17.

However, not all components attached to the thruster body are electrically conductive to the plasma. Due to the proximity of magnetic circuit pole pieces to the HET

discharge plasma, exposed surfaces of the magnetic circuit elements of HET are coated with electrically non-conductive material. The mounting screws for these magnetic pole pieces do not necessarily have these electrically insulating coatings and are exposed to the ambient plasma. The inner magnetic pole piece for the T-140 HET, has mounting screws that are electrically exposed to the HET plasma environment, and so a thruster body chamber plate, labeled “TP1” is placed in that area, as shown in Figure 17. In the spatial location of TP1, the plasma environment consists of the bulk ion production and acceleration. With the presence of the high-energy ions, there is an expected flux of ions to impinging on the magnetic pole elements due to electrostatic potential gradients and charge-exchange ion production [25, 26, 74].

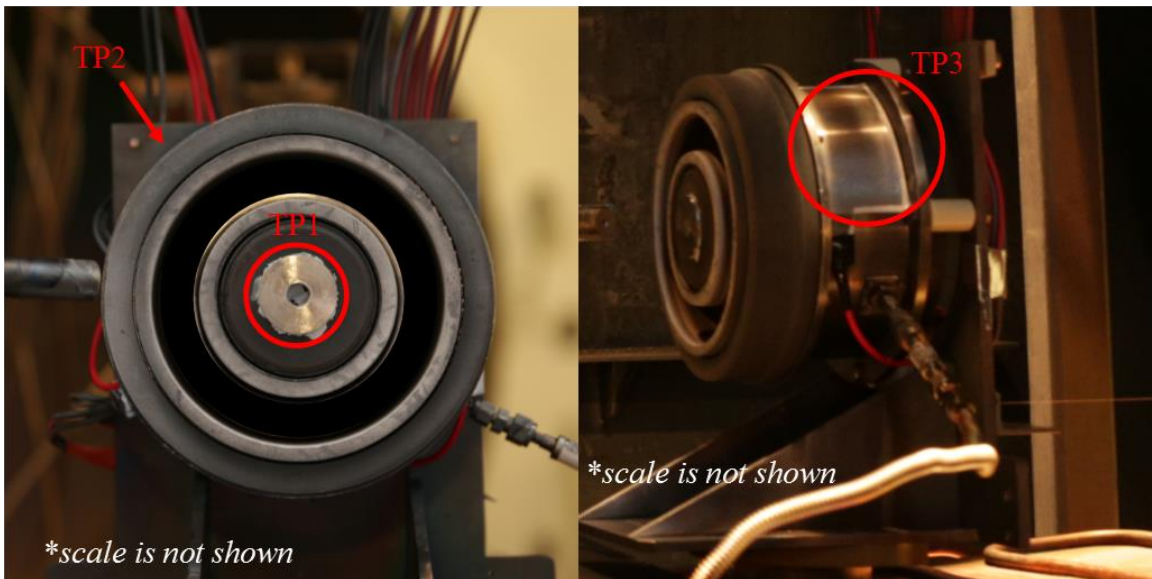


Figure 17: T-140 HET and installed witness plate locations. Witness plate encircled in red Left) Front view of thruster Right) Opposite side of the cathode view of the thruster

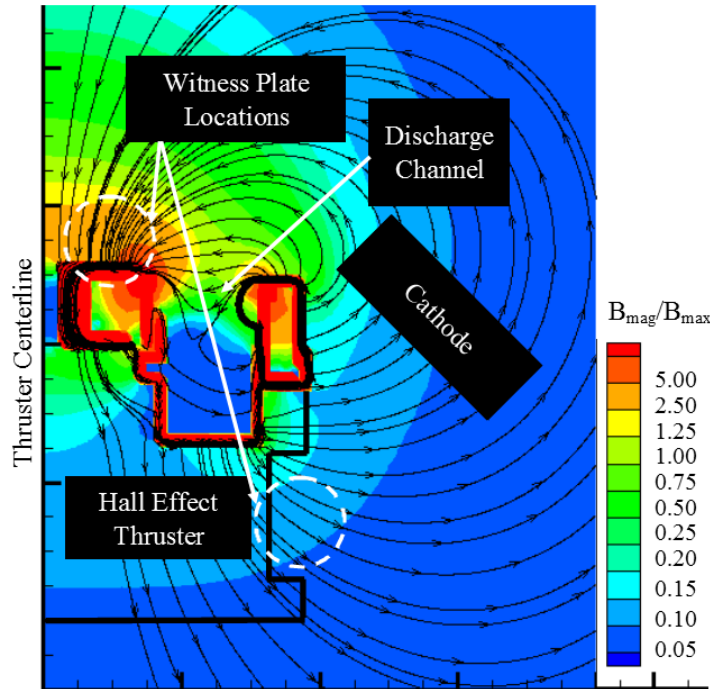


Figure 18: Diagram of the magnetic field topology labeled to show placement of witness plates Magnetic field magnitude (B_{mag}) is normalized by the maximum magnetic field strength along the thruster discharge channel centerline (B_{max})

4.4.2 Design of Thruster Body Plates

The design of the thruster body witness plates follows similar design principles as the chamber: electrical isolation and non-invasive placement. Since there are two distinct plasma environments and geometric constraints of the thruster body plates, there are two different designs for the thruster body plates. For TP2 and TP3, the thruster body plates are placed on the HET support chassis. These plates consist of 0.159 cm thick, 5.08 cm x 10.16 cm aluminum that is bent to match the curvature of the HET support chassis. The size of the plates is the largest that would physically fit into the two selected areas while still being able to be electrically isolated from the thruster body chassis. To maintain electrical isolation from the thruster body plates, the thruster body facing sides of the plates are coated with Aremco Ceramadip ceramic coating. Attachment of TP2 and TP3 to the thruster body chassis is accomplished using Permatex High Temperature Red RTV, acid-

cure silicone. Because these areas do not have direct line-of-sight to the HET discharge plasma, the temperature of the TP2 and TP3 is within functional temperature limits of the Permatex High Temperature Red RTV, acid-cure silicone. The electrical resistance between TP2, TP3 and the thruster body chassis is measured to be greater than 20 M Ω using a Fluke 87V model digital multi-meter. Figure 17 shows TP2 and TP3 as installed on the T-140 HET. An aluminum electrical contact comes off the plate surface, to which 14 AWG silicone jacket wire is attached. On the aluminum electrical contact, exposed metal area is covered in self-vulcanizing silicone tape.

For TP1, this thruster body witness plate is directly exposed to the HET thruster plume and discharge plasma. Because of the significant temperature load expected on thruster body plate TP1, the plate is made out of 316 stainless steel. The plate is 0.159-cm thick and has an outer diameter of 3.81 in. and an inner hole diameter of 1.02 inches. A steel electrical contact tab is spot welded to the rear of the plate. The rear side of the thruster body plate is coated with Aremco Ceramadip and the plate is bonded to the HET inner magnetic pole piece using Aremco Ceramabond ceramic adhesive. Attached to the steel electrical contact is 14-AWG silicone jacketed wire. The wire is run through the pre-existing hole in the inner magnetic bobbin of the HET and runs through the inside of the thruster body chassis volume. Electrical isolation between the thruster body witness plate and the thruster body chassis is measured to be greater than 20 M Ω using a Fluke 87V model digital multi-meter. Figure 17 shows TP1 mounted on the HET.

4.5 Diagnostics

In the following, a description of the diagnostics and the methodologies used with those diagnostics are discussed. The main goal of this discussion is to detail the thought process used in selection of the probes, the properties each diagnostic was used to measure,

and the uncertainty of each of the measurements. The actual experimental configuration of these diagnostics are discussed prior to each section of the results section.

4.5.1 Plume Diagnostics

4.5.1.1 Langmuir Probes

4.5.1.1.1 Plume

The ion and electron number densities are measured using a cylindrical Langmuir probe. Langmuir probe sweeps are performed at select thruster-to-centerline angles at a radius of 1 m from thruster centerline and discharge exit plane. The probe used for plume measurements is constructed using a 0.13 mm diameter, 22.6 mm long tungsten tip housed inside an alumina tube. The probe is bent at a right angle such the probe tip was not pointed at the HET and is pointed 90° out of the plane of the probe arm sweep. The bend in the probe was done to minimize the effect of the probe tip on the I-V trace of the Langmuir probe [79-81]. A Keithley 2410 1100 V Sourcemeter is used to control the probe tip bias and measure the collected current. During each current-voltage sweep, the tip voltage is varied over a range of -50 V to 100 V in 0.2 V increments with a 300-ms dwell time. Two sweeps are taken per measurement and are averaged together before processing. The results are interpreted using orbital-motion-limited (OML) theory with an expected uncertainty in ion and electron density measurements to be $\pm 40\%$ and an electron temperature uncertainty of ± 0.2 eV [79, 82].

4.5.1.1.2 The Chamber Plates

In front of the radial chamber, a cylindrical Langmuir probe of made of 0.13 mm diameter, 48.8-mm long, tungsten filament is placed housed in an alumina tube. The probe is mounted in the center of the radial plate and the plate to cylindrical distance is 177.8 mm. A Keithley 2410 1100 V Sourcemeter is used to control the probe tip bias and measure

the collected current. During each current-voltage sweep, the tip voltage is varied over a range of -50 V to 100 V in 0.2 V increments with a 300-ms dwell time. The results are interpreted using orbital-motion-limited (OML) theory with an expected uncertainty in ion and electron density measurements to be $\pm 40\%$ and an electron temperature uncertainty of ± 0.2 eV [79, 82]

Because of the differing plasma conditions near the axial chamber plate, measurement of the plasma properties was performed differently than at the radial chamber plate or on for the plume Langmuir probe measurements. Near the axial chamber plate, a significant population of ions consist of ions accelerated by the HET. These accelerated ions have energies on the order of the discharge voltage and a bulk velocity that is directed downstream [3]. This makes it difficult to interpret data collected using classical cylindrical or spherical Langmuir probes. The traditional sheath models used to calculate the local plasma properties assume the plasma properties are direction invariant [79, 83, 84]. The HET accelerated ions have bulk directionality and break this assumption. In such a situation, the probe itself creates a shadow effect and results in two very different plasma conditions around the probe. The region of plasma in-front of the probe has an ion population that contains a significant number of the HET accelerated ions, and the region of plasma behind the probe has an ion population that is primarily composed of charge exchange ions. In order to properly characterize the plasma environment in front of the axial chamber plate, it is then desirable to use a Langmuir probe that only measures the plasma properties in front of the probe. As discussed by Oksuz and Hershkowitz [85], “half-plate” Langmuir probes are typically undesirable because they only measure the plasma environment in front of the probe. In this case, however, this one-sided nature is desirable.



Figure 19: Axial Plate Langmuir Probe

Figure 19 shows the axial plate Langmuir probe. The collector disc of the probe is a 21.6-mm diameter stainless steel disc. To help reduce the amount of secondary electron emission through ion collisions with the metallic surface, the disc is coated in plasma-sprayed tungsten. The probe is attached to a stainless steel #8 threaded rod and housed in an alumina housing. The rear and side surfaces of the probe are insulated from plasma using Aremco Cermadip coating. The probe is mounted in the center axial plate, the distance between the axial plate surface and the probe surface is 178 mm, as shown in Figure 20.

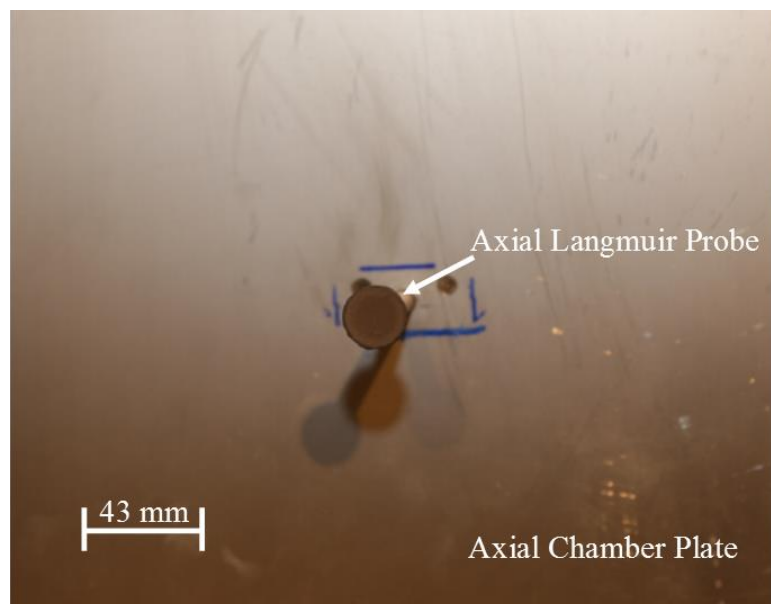


Figure 20: Image of the Axial Chamber Plate as Installed

A Keithley 2410-1100 V Sourcemeter is used to control the probe voltage bias and measure the collected current. During each current-voltage sweep, the tip voltage is varied over a range of -20 V to 20 V in 0.2 V increments with a 300-ms dwell time. Due to the current limitations in the Keithley Sourcemeter and size of the planar Langmuir probe, the voltage sweep range is limited to the aforementioned -20 V to 20 V range. To ensure that the axial plate I-V sweep covered the necessary voltages, a Xantrax 60V-9A power supply biases the reference side of the Sourcemeter. The probe data is interpreted using standard planar probe theory [85, 86]. Based on the theory, it is expected that the electron temperature can be measured to ± 0.2 eV and the plasma density can be measured to within $\pm 40\%$ [79].

4.5.1.1.3 Estimating the Plasma Potential with Langmuir Probes

In general, it is possible to measure the plasma potential with a Langmuir probe. The plasma potential is traditionally determined by the voltage at which the collection current “knees” over [79]. This occurs between the exponential growth region and the electron saturation region of the I-V sweep. There are many factors, however, that cause this knee to broaden making it difficult to measure out the exact voltage, so it is common to extrapolate the curve fits between the exponential growth and electron saturation region and the intersection of these two functions occurs at the plasma potential [79]. Taking voltage sweeps into the electron saturation region can create its own problems. The resulting electron current onto the probe at high current can heat up the probe tip significantly. If the heating is high enough that the probe starts to thermionically emit, the I-V trace can be distorted. Chen, et al. [87] proposes another way to estimate the plasma potential from the floating potential. By measuring the electron temperature, the ion number density, and the floating potential of the plasma, one can calculate the plasma

potential as measured by a planar probe via Equation (11) [87]. For cylindrical probes and spherical probes, it is necessary to correct for geometric differences, and the correction function is shown in Equation (12) and Equation (13) [87]. This method can estimate the plasma potential with as much uncertainty as the knee method and has a plasma potential measurement uncertainty $\pm 20\%$.

$$V_f = V_p - \frac{kT_e}{2e} \ln\left(\frac{2m_i}{\pi m_e}\right) \quad (11)$$

$$\frac{1}{\eta_f^6} = \frac{1}{\left(0.583 \ln\left(\frac{r_p}{\delta_l}\right) + 3.732\right)^6} + \frac{1}{-0.027 \ln\left(\frac{r_p}{\delta_l}\right) + 5.431} \quad (12)$$

$$V_f - V_p = \eta_f T_e \quad (13)$$

Where V_f is the floating voltage, V_p is the plasma potential, T_e is the electron temperature, e is the fundamental charge, m_i is the mass of the ion, and m_e is the mass of the electron, r_p is the radius of the probe, δ_l is the Debye length, and η_f is the geometric correction factor.

4.5.1.2 Emissive Probes

The emissive probe is used to measure plasma potential. The probe tip used for this work is constructed from a loop of 0.13 mm-diameter, thoriated-tungsten wire housed in a 4.8-mm double-bore alumina tube. Emissive probe sweeps were performed at select thruster-to-centerline angles at a radius of 1 m from thruster centerline and discharge exit plane. The inflection point method was used for data collection. In this method, the probe is heated and then the emission current is monitored as the probe bias voltage is swept in a manner similar to that used with Langmuir probes. The changing characteristic of the emission current trace as a function of applied bias voltage is then used to determine the plasma potential [88]. During each measurement, the heating current to the emissive probe

filament is held at five different heating current values to change the electron emission of the probes. These heating current values varied throughout the probe lifetime, but are within a range between 1.2 A to 2.2 A. One bias voltage sweep was taken per emissive probe filament heating current. During each bias voltage sweep, the probe voltage is varied over a range of 0 to 100 V in 1-V increments with a 300-ms dwell time. The inflection point is then found in each of the I-V traces for each of the different heating current levels, and the plasma potential was found by linearly extrapolating these values to zero emission [88]. The uncertainty associated with this method is approximately ± 0.5 V [88]. The heating current was controlled using a Xantrex XPD 60-9 power supply. The probe bias is controlled by a Keithley 2410 1100 V Sourcemeter and the current is measured using the same Keithley 2410 Sourcemeter. The sourcemeter is controlled using a LabView Virtual Instrument to ensure synchronous recording of the probe bias voltage and emitted current.

4.5.1.3 Faraday Probes

The ion current density was measured using a nude-type JPL Faraday probe [89]. Faraday probe measurements occurred continuously along a 180° $1\text{ m} \pm 0.01\text{ m}$ arc that is centered along the HET centerline and exit-plane. Angular resolution during the sweep was limited by the multiplexor hardware required settling time given a measurement voltage range. Angular resolution ranges from 0.34° in the “wings” of the plume to 0.2° in the center of the HET plume. The diameter of the collector is 2.31 cm. The probe has guard-ring diameter of 2.54 cm with a 0.036-cm gap between the collector and guard ring. The guard-ring and collector is biased to -30 V below ground for all axial plate bias voltages. To measure the current flowing to the collector, the voltage drop across a $100\ \Omega \pm 1\%$ precision resistor was measured using an Agilent 34980A Mainframe with an Agilent 34922A armature multiplexor. Rotary table encoder information and voltage drop measurements were taken using a LabView Virtual Instrument to ensure synchronous recording of angular position and voltage drop across the shunt resistor. Data reduction and

correction factors used to calculate the ion current density from the Faraday probe data was performed according to Brown [90] and Brown and Gallimore [18].

4.5.1.4 Retarding Potential Analyzer

The ion energy distribution in the thruster plume was measured using a retarding potential analyzer (RPA). An image of the RPA used in this experiment is shown in Figure 21. The RPA is a well-known diagnostic that uses a set of electrostatically biased grids to act as a high-pass energy filter and selectively filter ions based on the ion energy [91]. The resulting measured current collection is the cumulative density function of the ions within the plasma. To obtain the ion energy distribution function, the numerical derivative is applied to the voltage and current sweep obtained. The grids are (in order from the plasma from the collector): the floating grid, the electron repulsion grid, the ion repulsion grid, and the electron suppression grid. The floating grid is allowed to electrically float in order to shield the plasma from perturbations caused by the presence of the probe. The electron repulsion grid is biased negative relative to ground in order to prevent plasma electrons from reaching the collector. The electron suppression grid is similarly biased in order to repel any secondary electrons created within the probe. The ion repulsion grid is biased positive relative to ground in order to impede the motion of the incident ions, and thus filter the ion population based upon directed kinetic energy.

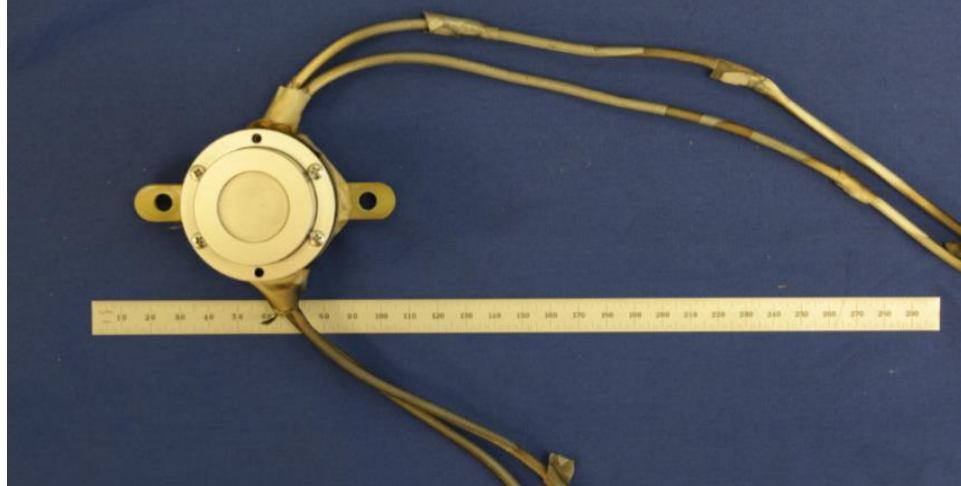


Figure 21: Front view of the RPA

The electron suppression and repulsion grids were both biased to -30 V using two TDK-Lambda GENH 60-12.5 power supplies. The ion repulsion grid bias, swept from 0 V to 450 V , was controlled by a Keithley 2410 Sourcemeter and the collector current was measured using a Keithley 6487 Picoammeter. The grids have a 2.286 cm collection diameter and 31% open area. To prevent the RPA from overheating, the RPA is attached to a motion table system and is able to move to the same position as emissive probe measurements. RPA data were collected along a 1 m arc downstream from the exit plane of the T-140 HET. The RPA data is then corrected to account for the plasma potential measured in the same location. The variability in the RPA measurement of the ion energy distribution peak between sweeps of the same condition were $\pm 10\%$.

4.5.2 Thrust Stand

Thrust is measured using the null-type, water-cooled, inverted pendulum thrust stand of NASA Glenn Research Center design detailed in the work of Xu and Walker [92]. The thrust stand consists of a pair of parallel plates connected by a series of four flexures that support the top plate and permit it to deflect in response to an applied force. The position of the upper plate is measured using a linear voltage differential transformer

(LVDT) and is controlled using two electromagnetic actuators. During operation, the current through each actuator is controlled using a pair proportional-integral-derivative (PID) control loops that use the LVDT signal as input and then modulate the current through the actuators in order to remove any vibrational noise (damper coil) and hold the upper plate stationary (null coil). The thrust is correlated to the resulting current through the null coil required to keep the upper plate stationary. The null coil current is recorded using a Cole-Parmer 200-mm flatbed recorder. The thrust stand is constructed primarily of aluminum and is surrounded by a water-cooled copper shroud in order to maintain thermal equilibrium.

The thrust stand is calibrated by loading and off-loading a set of known weights that span the full range of expected thrust values. A linear fit is then created in order to correlate null coil current to force applied to the thrust stand. The thruster is shut down and a recalibration is performed every 40-60 minutes in order to minimize thermal drift of the zero position. In order to ensure the thruster is at thermal equilibrium, a warm-up period of 3 hours is taken before thrust measurements begin. During this warm-up period, the thruster is run at the nominal condition of 3.1 kW. The thrust stand uncertainty for the data presented in this thesis is ± 3 mN ($\pm 1.7\%$ full scale).

4.5.3 Electrical Circuit Diagnostics

4.5.3.1 Oscilloscope Configuration

In Chapter II, we discussed that the HET is a dynamic plasma device with many time-varying plasma modes. Since the HET is the dominate plasma source in the chamber, it is expected that the electrical interaction between the HET and the conductive walls have electrical characteristics in the frequency range similar to the fundamental plasma modes of the HET. With respect to the discharge of the HET, the fundamental plasma mode operates on the order of kHz [3, 31, 59]. Fortunately, common oscilloscopes available have

high enough sampling rates and memory depths to adequately capture electrical features on the kHz timescale, and the oscilloscope current and voltage probes have sufficient bandwidth to resolve the time-varying modes of the HET. For this work, two Teledyne Lecroy HDO6104 12-bit 2.5 GHz oscilloscope are used. This allows for the synchronous measurement of signals of up to eight different sources. The internal 10 MHz timing clock output of one oscilloscope was used as a clock reference to sync the second oscilloscope. Time delay between synchronous data capture of the two oscilloscopes is measured to be less than 26 ns. Depending on the experimental configuration, the scopes are either triggered via a current threshold of the discharge current or an external 5 V square wave trigger source. The configuration of the oscilloscopes is shown in Figure 22. For time-delay measurements, the oscilloscopes are configured for 2.5 GB/s sampling rate and a sample length of 12.5 MS. The triggering for data capture is set to be a current threshold. For power spectra measurements, the oscilloscopes are configured for a sampling rate of 125 MS/s and a sample length of 2 MS. The triggering for the data capture is handled by an Agilent 33250A Function / Arbitrary Waveform Generator. The triggering waveform is a 5-V amplitude square wave with a 0.5-s period.

For both types of oscilloscope configurations, pre-buffering of the waveform capture is employed. This is to ensure that all characteristics of the triggering event in the waveforms are captured. For oscilloscope configurations of 125 MS/s sampling rate, 2 MS waveform length, the pre-buffering is set to 50% of the entire waveform capture period. For oscilloscope configurations of 2.5 GB/s sampling rate, 12.5 MS waveform length, the pre-buffering is set to 25% of the entire waveform capture period.

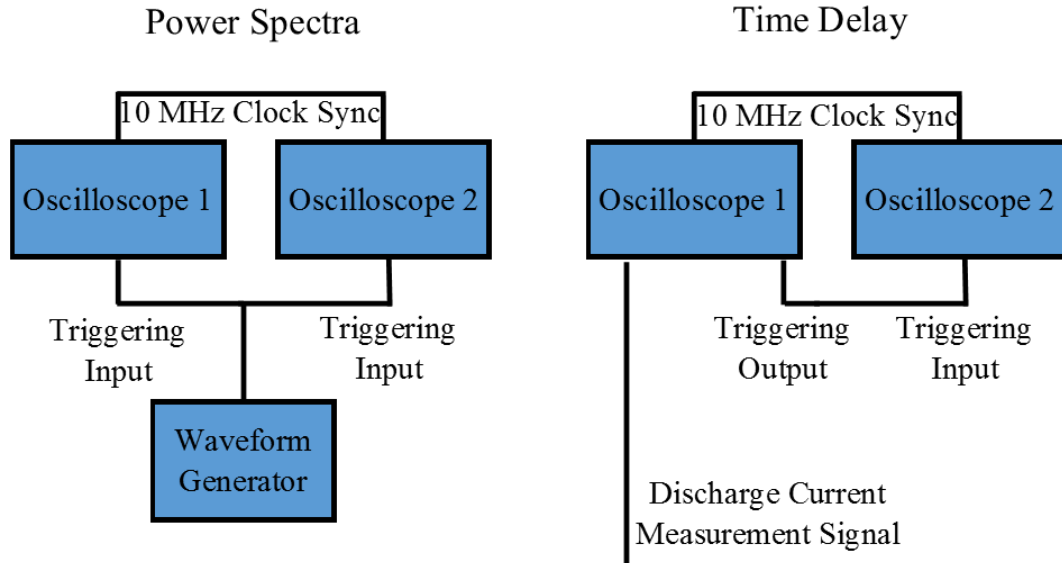


Figure 22: Diagram of Oscilloscope Triggering and Clock Sync

4.5.3.2 Oscilloscope Probe Types

4.5.3.2.1 *Voltage Probes*

For all voltage measurements, passive voltage dividers are used. The voltage probes fall into two categories of voltage dividers: 10:1 and 100:1. Teledyne LeCroy PP018 10:1 passive probes measure voltages of circuits that are not wired directly into the HET discharge supply. The PP018 passive probes have a frequency bandwidth of 500 MHz, a measurement accuracy of $\pm 1\%$ of measured signal, and voltage limit of 600 V. Teledyne LeCroy PPE2KV 100:1 passive probes measured voltages of circuits that are directly connected to the HET discharge circuit. The PPE2KV passive probes have a bandwidth of 400 MHz, a measurement accuracy of $\pm 1\%$, and a voltage limit of 2000 V.

4.5.3.2.2 *Current Probes*

Traditional resistive current shunt measurements could not be used to measure the time-varying characteristics of HET and facility surface circuits. This is due to the resistance of the shunt having a frequency dependent resistance, which would artificially

influence the measured time-varying current. Fortunately, non-invasive active, high bandwidth DC current monitors are available for the Teledyne-Lecroy line of oscilloscopes. These active current monitors are similar to passive current monitors in that they can non-invasively measure the current and have wide frequency bandwidths. Due to magnetization of the components of the active current monitor and resistive heating of ferrous elements in the clamp, the maximum current measurable for a given active current monitor is frequency dependent. HET oscillations occur in the 10s of kHz. So when sizing these probes for HET circuit measurement, this derating must be taken into account. For example, a Teledyne Lecroy CP-030 has a nominal 30 A rating, but when measuring currents that oscillate in the 10s of kHz, the current monitor will only be able to measure up to 9 A accurately. Since Teledyne Lecroy oscilloscopes are used in this work and these active current monitors require manufacture specific interfaces, Teledyne Lecroy active current monitors were used to measure the time varying current of the various circuits investigated. The discharge current of the HET was measured using a Teledyne Lecroy CP-150 current monitor, which has a nominal current rating of 150 A and a derated (based on the HET being used) current rating of 60 A. Since the discharge current of the HET being used is expected to be in the 10 A range, this probe has sufficient capacity to measure the discharge current. The CP-150 has an accuracy of greater than 1% of the measured value, a noise floor of ± 6 mA, and a sensitivity of 100 mA/div. For the chamber plates current collection, Teledyne Lecroy CP-30 current monitors were used. The CP-30 current monitor has an accuracy of greater than 1% of the measured value, a noise floor of ± 2.5 mA, and a sensitivity of 10 mA/div. For the thruster body plates, the expected current collection is expected to be in the mA to 100 mA range, so the Teledyne CP-30A current monitors are used. The CP-30A current monitor has an accuracy of greater than 1% of the measured value, a noise floor of ± 150 μ A, and a sensitivity of 1 mA/div.

4.5.4.2.3 Time Delay Induced by the Wiring Length

Due to the distance from the control room and the vacuum facility, it is important to estimate the amount of signal induced delay for certain measurements. Based on Johnson and Graham [93], the expected signal delay induced by line length is expected to be 4.9 ns/m on RG-58 cable and 3.9 ns/m on 6-AWG THHN wire and RG-142 cable. Table 2 shows the estimated time-delay induced by line length for the diagnostic wire lengths and the discharge current line length. All time-delay results presented have been corrected for the estimated cable induced time-delay.

Table 1: Estimated cable induced signal delay. Path length uncertainty is ± 0.3 m

Signal Source	Wire Type		Path Length (m)		Estimated Cable Induced Time-Delay (ns)
	External	Internal	External	Internal	
Discharge Current Radial	6 AWG	6 AWG	16.7	8.5	98
	THHN	M16878/5BPL			
Chamber Plate Axial	RG-58U	RG-142	16.7	0.6	84
Chamber Plate	6 AWG	6 AWG	11.2	9.6	81
	THHN	M16878/5BPL			
Thruster Body	6 AWG	6 AWG	16.7	8.5	98
	THHN	M16878/5BPL			
Cathode-to-Ground	6 AWG	6 AWG	16.7	8.5	98
	THHN	M16878/5BPL			
Thruster Body	6 AWG	6 AWG	16.7	8.5	98
	THHN	M16878/5BPL			

4.5.3.3 Statistical and Fourier Techniques used for Analysis

Due to the immense size of the captured waveform files from the oscilloscopes, it is necessary to use statistical and Fourier methods to reduce the data. In the following

sections, a summary of these techniques are discussed with respect to the electrical diagnostics data.

4.5.3.3.1 Statistical Correlation

Classical statistical correlation is used to assess whether or not the voltage or current waveforms measured from the chamber plates are coupled to the discharge plasma. The correlation coefficient between chamber plate electrical waveforms and the discharge current waveform is calculated via MATLAB. The coefficient is calculated via the following equations:

$$cov(X, Y) = \sum_{i=1}^N \frac{(x_i - \bar{x})(y_i - \bar{y})}{N} \quad (14)$$

$$R(X, Y) = \frac{cov(X, Y)}{\sqrt{cov(X, X)cov(Y, Y)}} \quad (15)$$

where X , Y , N , cov , and R are the set of numbers representing one waveform, the set of numbers representing the other waveform, the sampling size of the waveform, the covariance between the two waveforms, and the correlation coefficient between waveforms, respectively. The correlation coefficient is a measure of how likely a change in one waveform corresponds to a change in another waveform. For the purposes of this investigation, the distinction between waveforms that are strongly correlated versus waveforms that are weakly correlated is deemed important. A correlation coefficient near unity between two waveforms is classified as strongly correlated and a correlation coefficient near zero is classified as weakly or not correlated. When analyzing the results of the correlation analysis, changes from strongly correlated to weakly correlated or vice-versa correspond to wholesale changes in the nature of the two waveforms being compared. From this perspective, for the purposes of this investigation, small changes, for example correlation coefficient changes from 0.95 to 0.91, are not deemed physically significant.

To evaluate whether this correlation is attributed to random happenstance and therefore trivial, the P-value is also calculated using a standard null hypothesis test. The P-value is a calculation of the percent probability of correlation calculated to be the result of a random sampling of two normal distributions or random processes. Classically, P-values below 0.05 are indicative of the correlation between two waveforms due to non-random processes and therefore statistically significant. For the work in this thesis, the P-value is less than 0.001 for all oscilloscope waveform captures.

4.5.3.3.2 *Fourier Transform and Frequency Domain Averaging*

Application of a Fast Fourier Transform (FFT) to a waveform taken in the time-domain results in the waveform being resolved in the frequency domain; the square of each amplitude term in the series is known as the power spectrum. The power spectrum shows the distribution of power amongst the various fundamental frequency modes of a given signal. To obtain only the alternating current (AC) portion of the signal, the time-averaged mean from each waveform was subtracted from the raw waveform. An FFT was applied to that subtracted signal post thruster testing using MATLAB. In measuring the time-resolved current and voltage of the various circuits, peaks in the power spectrum can be then correlated to fundamental frequencies associated with different dynamic plasma mechanisms. One advantage of using high-speed oscilloscope diagnostics and high bandwidth probes is that they afford high frequency-space resolution. A consequence of application of the Fourier transform to real measured waveform is that the noise floor is amplified in the Fourier space. While the noise floor may be inherently small in the time domain, random fluctuations are amplified in the frequency domain and can either mask or artificially broaden peaks in the power spectrum. One way to combat this noise amplification is to average together multiple time-domain captured waveforms. Since the HET is an inherently unsteady, non-periodic plasma device, time-domain averaging becomes ineffective because the phases of the waveforms cannot be aligned with any

certainty. Work done in the field of laser diagnostics on HET have come up various methods for enforcing a periodicity to the HET discharge have been devised, but ultimately, such frequency locking techniques are invasive and not desirable [63].

Fortunately, a fundamental property of the Fourier transform is that the frequency information and phase information of a signal is separated into real and imaginary components. If the frequency information (real) is kept and the phase information (imaginary) is discarded, then the resulting transform signal becomes decoupled from time. Because the Fourier signal is no longer coupled in time, it is then possible to average together multiple Fourier transformed different signals without having to worry about aligning the signal phase. By averaging together, the real parts of a Fourier transformed signal, the true peaks are amplified and the peaks associated with random noise is attenuated. For this work, it was found that averaging 30 power spectra together resolved the power spectrum enough that fundamental modes could be identified. A progression of this averaging process is illustrated in Figure 23. It is important to note that the power spectra data presented for the cathode positioning experimental configuration is based only on a single waveform capture. The other experimental configurations, axial chamber plate bias and thruster body bias, have power spectra data based on the average of 30 waveforms.

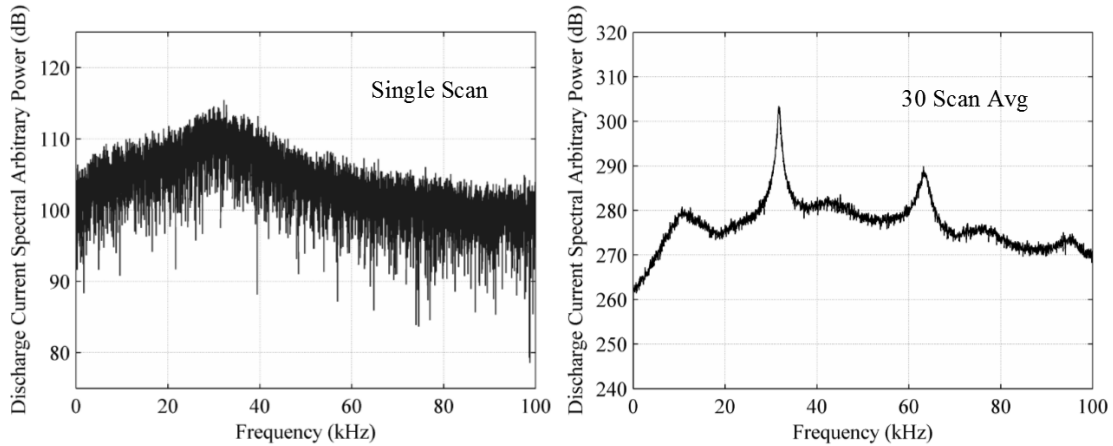


Figure 23: Side by side comparison of FFT Scans Left: 1 scan Right: Average of 30 scans. The HET operating condition is 300 V, 3.1 kW

4.5.3.3.3 Time-Delay Analysis Using Statistical Correlation

In general, the measurement of the time-delay between two signals can be done via computation of the cross-correlation. The cross correlation is calculated by computing the convolution integral between two entire signals for varying offsets as shown in Equation 2. The time-offset that corresponds to the largest absolute value of the cross-correlation function can be interpreted as the time-delay between the two signals if only if the two signals are strongly correlated given the time-offset. Because of the unsteady nature of the HET discharge current, a more localized approach of the cross-correlation technique is used. In this localized approach, the cross-correlation between a subset of the discharge current, the reference waveform, and an equally sized subset of a secondary waveform is calculated. By varying the time at which the second subset starts, the convolution integral between the reference waveform subset and the secondary waveform is calculated as a function of time. The peak value as a function of time is the time delay between the reference waveform and the secondary waveform. For each of the waveform sets captured

at each cathode position location, the triggering threshold was set such that only the HET steady-state maximum peak of the discharge current triggered waveform capture. For each cathode position, the current threshold for that maximum peak had to be adjusted. For the T-140 HET, it was observed that such a maximum peak of the discharge current occurred only once per waveform capture period, thus making it a unique event in the waveform capture period. A representative sample of the discharge current peak trigger event is shown in Figure 24. In this work, a ± 0.1 ms length of time around the maximum peak of the discharge current peak that triggers data capture is referred to as the “discharge current peak event” and that a ± 0.1 ms length of time around the maximum peak of the discharge current peak The 2-ms length of time of this discharge current peak event remained fixed for all cathode positions. To help aid in the sensitivity of this analysis, the global mean of each respective signal is subtracted from each of the subsets before the convolution integral is computed as shown in Equation 2 and Equation 3:

$$(\mathbf{f} \star \mathbf{g})(\tau) \equiv \int_{-\infty}^{\infty} \mathbf{f}^*(t) \mathbf{g}(t + \tau) dt \quad (16)$$

$$(\mathbf{f} \star \mathbf{g})(\tau) = \int_{-\infty}^{\infty} (\mathbf{f}(t) - \bar{\mathbf{f}})(\mathbf{g}(t + \tau) - \bar{\mathbf{g}}) dt \quad (17)$$

where f is the reference waveform, g is the compared waveform, τ is the time-offset, and t is time. Since previous measurements of the discharge current power spectra [35, 94] show that the primary power containing frequencies are in the sub-100 kHz spectra range. Electrical waveforms (current and voltage) are post-process filtered through a 2nd-order Butterworth low-pass filter with a cut-off frequency of 100 kHz. This process removes frequency components in the compared waveform that were not directly sourced from the HET discharge. The entire time-delay measurement process was performed via MATLAB.

Figure 24 shows an individual case of the results of this calculation. The data shown are truncated to only show the calculated subsets of data that maximized the cross-correlation function.

To determine if this calculated time-offset corresponds to a statistically significant predicted time-delay, the correlation coefficient is calculated between the discharge current peak event and the subset of the waveform voltage or current data that maximizes the cross-correlation function. The correlation coefficient can be used as indicator of statistically connected data. The threshold of the correlation coefficient that results in strong statistical significance is not well-defined and can be arbitrarily chosen. For this investigation, correlation coefficient values greater than ± 0.7 are deemed strongly statistically correlated and correlation coefficients below ± 0.3 are deemed weakly statistically correlated. It was found that from analysis of data that correlation coefficients below 0.6 resulted in zero-time-delay or negative measured time-delay between the discharge current peak event and the other electrical waveform. In this work, signals with a correlation coefficient above 0.6 but below 0.7 are designated as correlated and the measured time delay is statistically significant. A zero or negative time-delay was deemed to be non-physical because the cable path induced delay is on the order of 100 ns and the oscilloscope sample rate yields a temporal resolution of 0.4 ns. For the purposes of this investigation, small changes in the correlation coefficient are deemed unimportant. Large changes in correlation coefficient that change correlation between strongly correlated to weakly correlated are deemed important. When calculating the correlation coefficients, it is important to capture the likelihood of random happenstance impacting the calculated correlation coefficient. The calculation of the P-value is a way to quantify this effect of random happenstance and is

commonly used to determine the statistical significance of the correlation coefficient. Due to the large number of data-points (5.0×10^5 data points) measured during the 0.2-ms long discharge current peak event, the P-value calculated for the correlation coefficient values for all cathode position is of the order 10^{-3} and is an order of magnitude lower than the traditionally accepted 0.05 value. This indicates that the correlation coefficient calculated for all time-delays is statistically significant. This does not mean that all time-delays calculated for all cathode positions result in a statically significant correlation, but it means that the correlation coefficient values computed are unlikely a result of random happenstance.

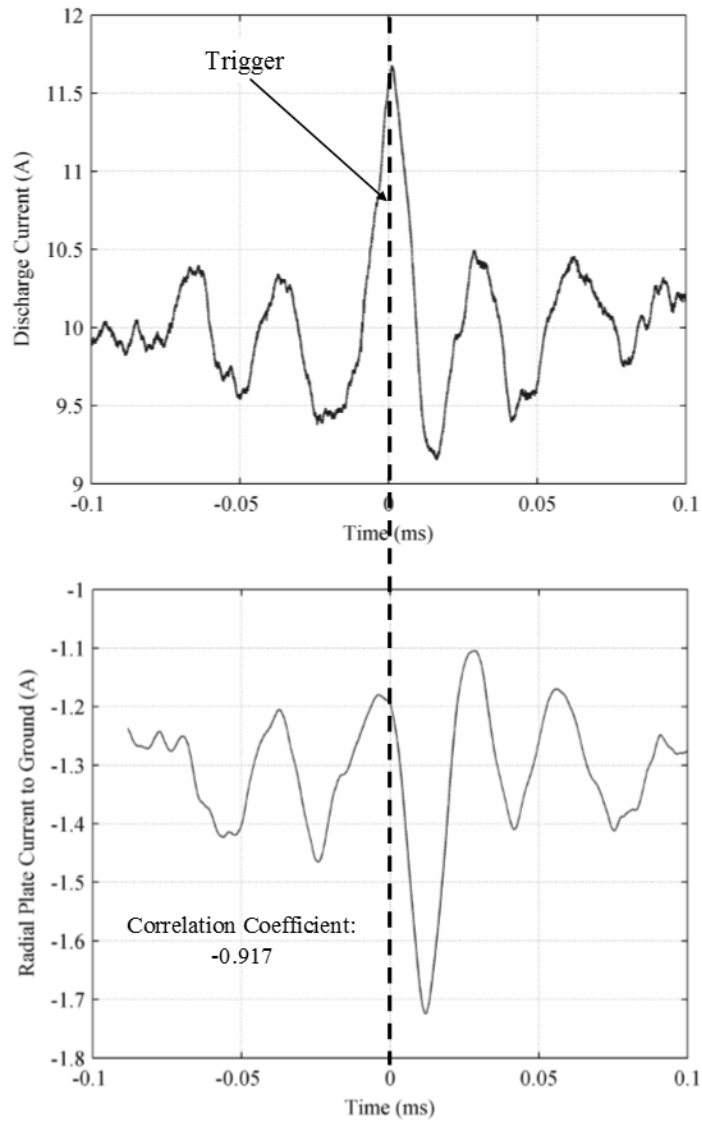


Figure 24: (Top) Discharge current peak event at cathode position of 18.1 cm (Bottom) Corresponding segment of radial chamber plate current-to-ground. The HET operating condition is 300V, 3.1 kW

CHAPTER V

Results of Experimental Investigation

5.1 Cathode Positioning Experimental Configuration

For this experimental configuration, the main goal is to examine how the vacuum facility interacts with the HET electrical circuit by manipulating the chamber recombination current pathway. To manipulate the chamber recombination current pathway, the HET thruster is operated at a fixed operating condition and the cathode position is translated outward radially from thruster centerline. At each radial cathode position, the thrust of the HET, the plume of the HET, the electrical characteristics of the HET electrical circuit, and the electrical characteristics of the chamber witness plates are measured and presented below. The section begins with an overview of the experimental layout of the configuration and then follows with the results of the cathode positioning experimental configuration.

5.1.1 Experimental Layout

The goal of this experimental configuration was to determine if moving the cathode position was able to impact the interaction between the HET electrical circuit and the vacuum facility. The overall experimental configuration for the cathode positioning work is shown Figure 25. The T-140 HET, the chamber witness plates, and the position of plume diagnostics are shown. It is important to note that for the cathode positioning work, the thruster body plates were not implemented and the overall current-to-ground or voltage relative ground of the thruster body was measured.

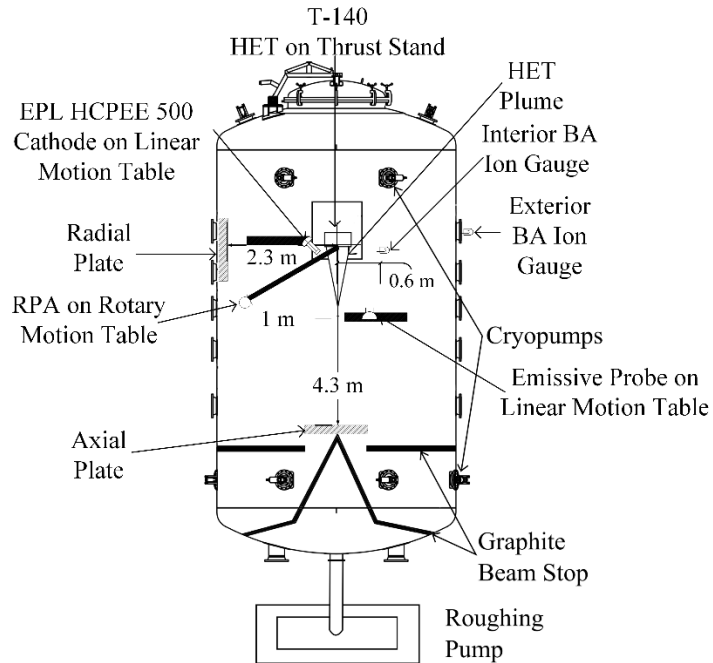


Figure 25 Schematic of VTF-2 and the Layout of the Experimental Apparatus

5.1.1.1 Cathode Translation

The nominal radial position of the cathode was 18.1 cm outwards from thruster centerline. Time-resolved measurements of the discharge current, radial chamber plate current and voltage, and axial chamber plate current and voltage were taken for the radial positions of the cathode orifice from 18.1 to 77.8 cm outward from the thruster centerline using a Parker Daedal 406XR precision linear motion stage with a 2000 mm travel. The positional uncertainty of the motion stage is $\pm 159 \mu\text{m}$. Table 2 shows the computed strength of the magnetic field at the cathode orifice as a function of radial location away from the thruster centerline. The magnetic field topology listed in Table 2 is calculated using a 2-dimensional Infolytica MagNet model of the T-140 HET magnetic circuit.

Table 2: Approximate magnetic field strength as a function of cathode orifice radial location away from thruster centerline.

Radial Location (cm)	Magnetic Field Strength (G)
18.1	30
19.4	20
39.0	10
47.5	0

The magnetic circuit configuration of the T-140 HET (two concentric coils centered on the thruster centerline) restricts the position of the magnetic field separatrix to the thruster centerline and precludes the T-140 HET from exhibiting the off-centerline separatrix surfaces shown in HETs with magnetic coils placed off thruster centerline [19, 46, 64]. This magnetic field topology eliminates any concerns about the changing nature of the near-field plume properties and cathode coupling as a function of cathode position relative to the absent off-centerline separatrix surface [19, 46, 64].

5.1.1.2 Regions of Cathode Position

In order to more clearly discuss the HET and chamber plate behavior observed at various cathode locations, the discussion of the data presented in the following is divided into regions based on the electron Hall parameter. The electron Hall parameter is defined as the ratio of the electron cyclotron frequency to the electron-neutral collision frequency. In general, the Hall parameter is a way to quantify the magnetization of charged particles by comparing the tendency of the motion of the particle to be dominated by the magnetic field or through collisions with other particles. For clarity, a method to calculate the electron Hall parameter is shown again in the following equation:

$$\beta = \frac{\Omega_e}{\nu} = \frac{eB}{m_e \nu} \quad (18)$$

where β is the electron Hall parameter, Ω_e is the electron gyro-frequency, ν is the electron-neutral collision frequency, e is the elementary charge, B is the magnetic field strength, and m_e is the mass of the electron. An electron Hall parameter of much greater than unity implies that the electrons are magnetized, *i.e.* the electrons are able to complete many orbits around their guiding center before colliding with a neutral particle. In such a condition, the electron motion is confined by the magnetic field lines and they traverse along these magnetic field lines. An electron Hall parameter much less than unity implies that the electrons are no longer magnetized, *i.e.* the electrons encounter neutral and/or ion collisions before being able to complete one orbit around their guiding center. In such a condition, the electron motion is no longer confined by magnetic field lines. This approach was used by Frieman, et al. [22] and was able to segment the time-averaged data into regions of distinct behavior. The estimation of the electron Hall parameter at the cathode orifice as a function of cathode position is more thoroughly covered in Frieman, et al. [22]. The results of those regional demarcations based on electron Hall parameter are summarized here. It is important to note that the exact regional delineation based on electron Hall parameter is approximate, and there are transitional Hall parameters between electrons being magnetized and not magnetized. To help with the discussion, these regional positions listed in this work are demarcated by known positions of the cathode at which data was taken. Cathode positions from 18 cm to 22 cm from thruster centerline correspond to a region where the electron Hall parameter is much greater than unity. Electrons sourced from the cathode within this spatial region are confined to the magnetic field lines generated by the

HET magnetic coils. These cathode locations are referred to as “Region 1.” From cathode positions from 24 cm to 44 cm from thruster centerline correspond to a region where the electron Hall parameter is of order unity. Electrons sourced from the cathode are only weakly magnetized, electron Hall parameter of order unity, by the HET magnetic circuit. These cathode locations are referred to as “Region 2.” Cathode positions from 47 cm to 78 cm from centerline correspond to a region where the electron Hall parameter is much less than unity. The thermal energy of the electrons sourced from the cathode allows them to propagate outward. These cathode locations are referred to as “Region 3.” In the following data figures shown, these regions are demarcated by a dashed line overlay. Because of the approximate nature of the regional divisions, there are cathode positions between labeled regions.

5.1.1.3 T-140 HET Operating Conditions

All data was collected with the T-140 HET operating at a discharge voltage of 300 V, discharge power of 3.16 kW, an anode xenon flow rate of $11.6 \text{ mg/s} \pm 0.03 \text{ mg/s}$, and a cathode xenon flow rate of $1.61 \text{ mg/s} \pm 0.12 \text{ mg/s}$. The operating chamber pressure as measured by the external ion gauge is 7.3×10^{-6} Torr-Xe, the operating chamber pressure as measured by the internal ion gauge is 1.3×10^{-5} Torr-Xe. The thruster discharge voltage, inner and outer magnet currents, anode mass flow rate, and cathode mass flow rate were held constant for all cathode positions and plate configurations. The thruster was run through a 3-hour conditioning cycle prior to data collection in order to allow the thruster to approach thermal equilibrium [40]. The discharge current of the T-140 HET is measured using a Teledyne Lecroy CP150 10 MHz current clamp (see Chapter 3 for technical specs). To be able to clearly measure the discharge oscillations, the discharge current is measured

on the thruster side of the discharge filter. The discharge voltage relative to ground is measured using a Teledyne Lecroy PPE2KV 100:1 voltage divider and the cathode-to-ground voltage is measured using a Teledyne Lecroy PPE2KV 100:1 voltage divider (see Chapter 3 for technical specs). These probes are placed at measurement points downstream of the discharge filter. Since the HET discharge circuit is a floating circuit, the discharge voltage of the HET is measured differentially as the difference between the discharge voltage relative to ground minus the cathode-to-ground voltage. For this experimental configuration, the HET discharge voltage is measured differentially using a Tektronix 3034B, and the time-average of the differential waveform is used to verify that the HET is operating at the desired operating condition.

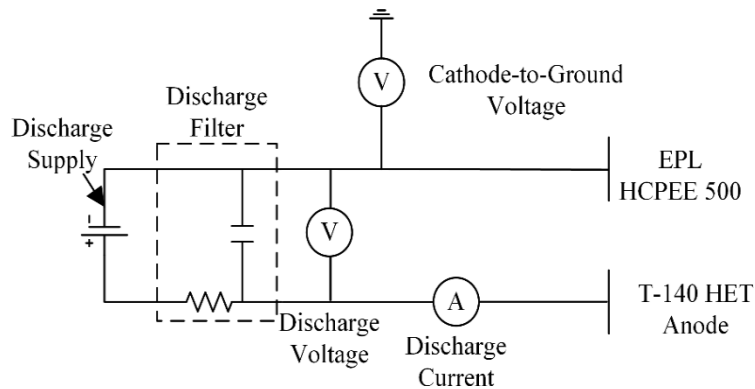


Figure 26: HET Electrical Configuration

5.1.1.4 Configuration of Plates

Figure 27 shows each of the three plate electrical configurations used in this experiment. In all three cases, the electrical connection to the plates was made using a RG-58 coaxial cable with a grounded shield that passed through a BNC feedthrough into the chamber. Based on current measurements made by Frieman *et al.* [22, 72], the current

capacity of the inner conductor is sufficient and would not pose any thermal issues during thruster testing. For grounded chamber plate configurations, grounding occurred in a star type distribution, as shown in Figure 27, to the walls of the VTF-2. To prevent ground loops in the measurements in voltage measurements, the oscilloscope was also grounded to the walls of the VTF-2. For current measurements, ground loops were not a concern as the current probes are active clamp current monitors.

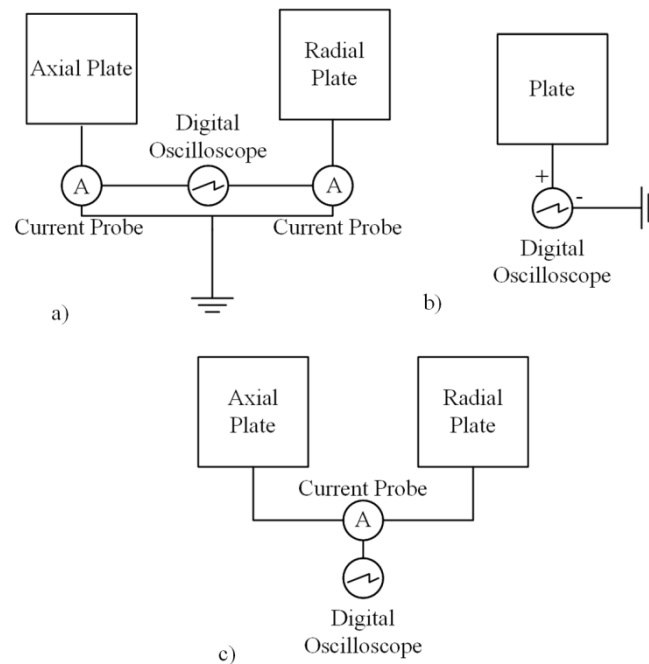


Figure 27: Plate circuit configurations: a) grounded, b) floating, and c) connected.

In configuration A (grounded), each plate was directly connected to chamber ground with the current conducted between each plate and ground measured with a Teledyne LeCroy CP030 current sensor connected to a Teledyne LeCroy HDO6104 oscilloscope; the plate currents and thruster telemetry waveforms were measured simultaneously at a sampling frequency of 125 MS/s for a 20 ms window to ensure that multiple fundamental discharge current mode periods were captured. In configuration B

(floating), the plates were electrically isolated, and the floating voltage was measured directly using a Teledyne LeCroy PP018 passive probe connected to the Teledyne LeCroy oscilloscope; these voltage measurements were also taken simultaneously with measurements of the T-140 HET discharge current oscillations at a sampling frequency of 125 MS/s. In configurations A and B both plates were simultaneous grounded or floated, respectively. In configuration C (connected), the plates were connected to each other instead of to ground, and the current conducted between the two plates was measured with a Teledyne LeCroy CP030 current probe connected to the Teledyne LeCroy oscilloscope; the current conducted between the two plates and the discharge current were measured simultaneously at a sampling frequency of 125 MS/s.

5.1.1.5 Thruster Body Electrical Configuration

In this work, time-resolved waveform measurements were taken when the thruster body of the HET was electrically grounded and when the HET was electrically floating. Since it is typically common for the HET to be tested with the thruster body electrically grounded, as demonstrated by Hofer and Anderson [27] and prior time-averaged measurements of Frieman, et al. [22] demonstrated the HET body collects a significant electron current during operation, this investigation data collection focused on measuring time-resolved electrical changes for the thruster body floating configuration. As a result, data collection occurred at more cathode locations with the thruster body electrically floating than the thruster body electrically grounded. To serve as a baseline of comparison, data collection for the thruster body electrical grounded occurred at fewer cathode positions, but with at least one data point in each of the aforementioned regions. By having at least one data point in each cathode position region, trends drawn from analysis of the

floating thruster electrical configuration can be compared against the data points taken for the grounded thruster body electrical configuration.

5.1.1.6 Summary of Electrical Diagnostics Layout

For the sake of clarity, the overall electrical diagnostics layout is shown in Figure 28. Each current or voltage measurement shown is a measurement that is time-resolved. Since the HET discharge circuit is floating, the cathode-to-ground voltage is a measurement of the floating voltage of the HET electrical circuit. A diagram showing the different voltages important to a HET can be seen in Figure 8 and Figure 14.

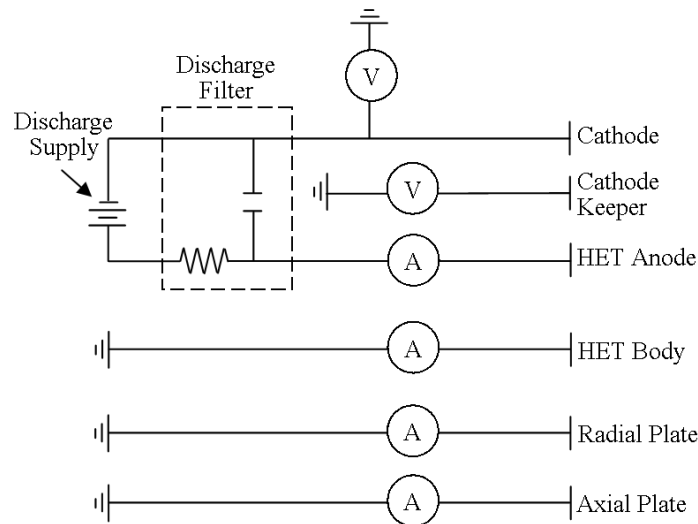


Figure 28: Electrical diagram of current and voltage time-resolved measurements of the HET discharge circuit.

5.1.1.6 Probe Diagnostics Configuration

Because of the large number of individual testing conditions, each of the following plume diagnostic measurements were taken only once at 1 m downstream of the exit plane and at the thruster centerline. In this way, the general trends of the beam plasma can be measured. The emissive probes are mounted on a linear stage located 1 m downstream from the thruster as shown in Figure 25. The spacing between the probes is kept at 16.51

cm to mitigate the sheath interaction between the probes. To reduce beam exposure time on the retarding potential analyzer (RPA), the diagnostic is mounted to a 1-m long boom capable of sweeping a 180° arc around the thruster.

5.1.2 Time Averaged Results

5.1.2.1 Time-Average Plate and Thruster Current and Voltages

For the time averaged voltage and current measurements, the oscilloscopes are configured for a sampling rate of 125 MS/s and a sample length of 2 MS. The average voltages and currents presented below are the arithmetic average value over the 2 MS waveform length. The cathode-to-ground voltage shown in Figure 29 shows three distinct regions of behavior: Region 1, the cathode-to-ground voltage remains constant, Region 2, the cathode-to-ground voltage decreases in magnitude, and Region 3, the cathode-to-ground voltage begins to increase in magnitude. As the cathode moves outwards from the nominal position, the time-averaged values of the radial and axial plate electrical and thruster body-to-ground currents reveal three distinct regions of behavior. The clearest indicator of these regions, the thruster body floating voltage, is shown in Figure 30. Figure 31 shows the time average currents for the plate and thruster diagnostics. The trends in this figure also correlate with behavior shown in the floating voltages.

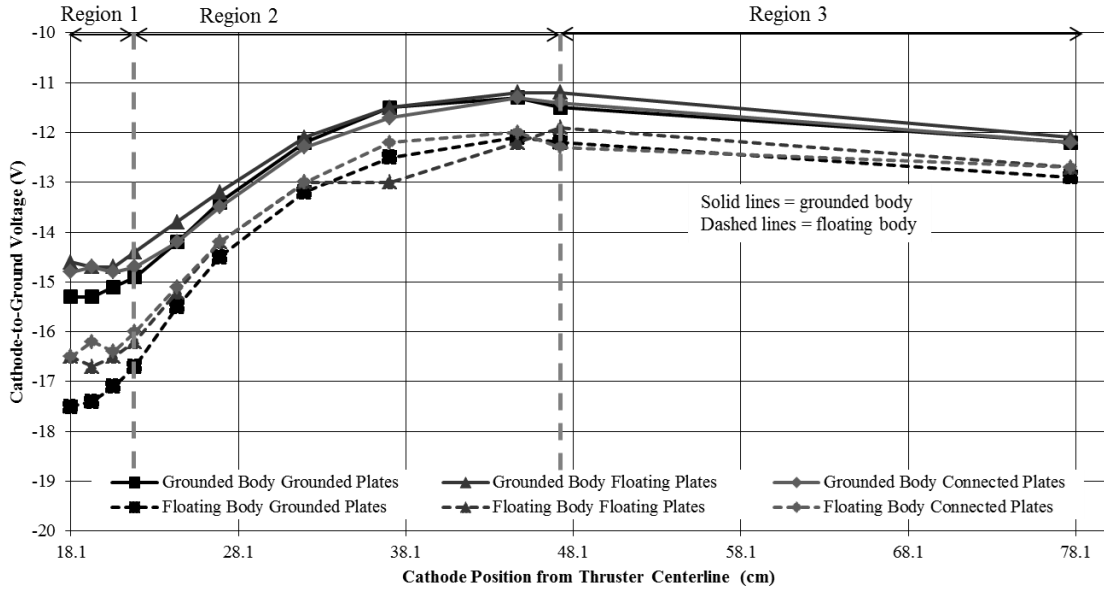


Figure 29: Cathode-to-ground voltage of the HET taken at 300 V, 3.1 kW. Error bars are encompassed by plot markers.

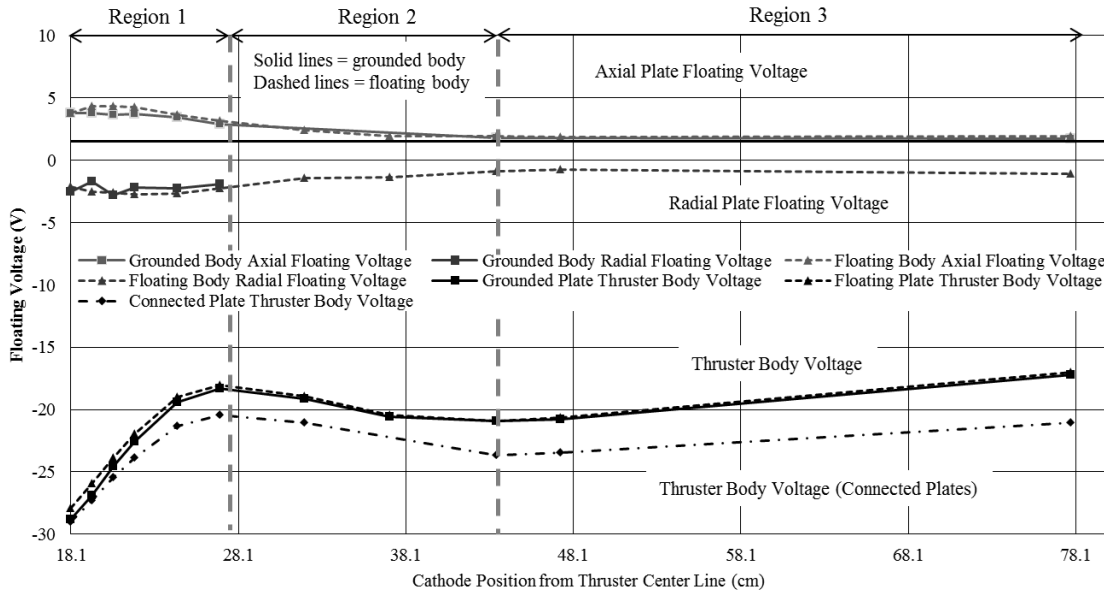


Figure 30: The floating voltages for the radial plate, axial plate, and the thruster body floating voltage for the floating type configurations. The HET operating condition is 300 V, 3.1 kW. Error bars are encompassed by plot markers.

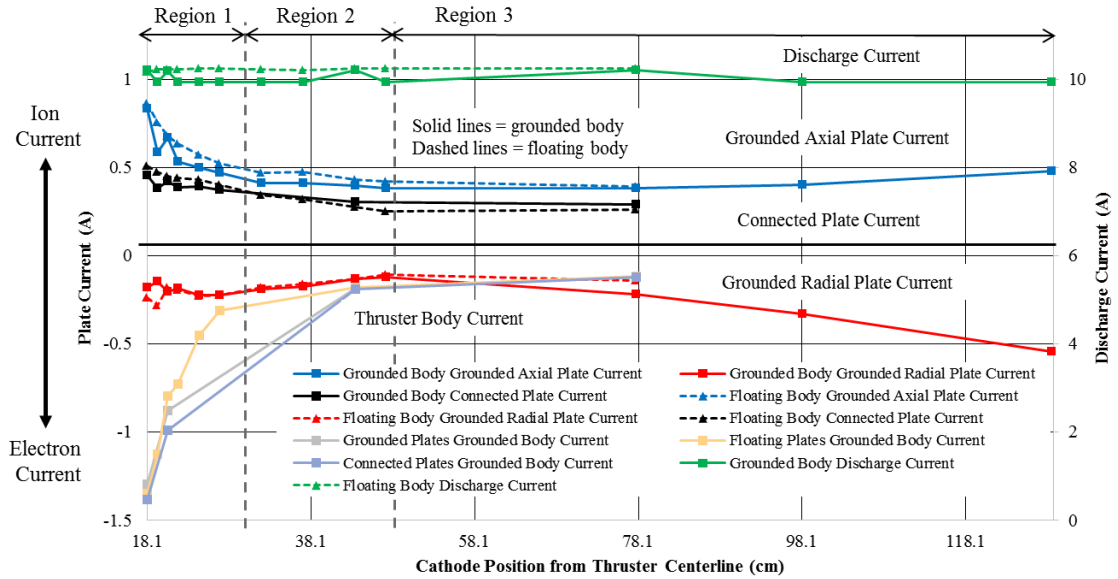


Figure 31: The radial plate, axial plate, and thruster body current-to-ground as a function of cathode position for connected and grounded configurations. The HET operating condition is 300 V, 3.1 kW. Error bars are encompassed by plot markers.

As shown in Figure 31, the sign of the current-to-ground reveals the nature of the kind of current collected. As a matter of convention, positive current is in the direction of positive charge movement. Negative current indicates the net collection of electrons and a positive current indicates the net collection of ions. The radial plate and the thruster body current and voltage trends indicate an electron dominated plasma environment, whereas the axial plate indicates an ion dominated plasma environment. This observation agrees with the fact that the radial and thruster body region are dominated by energetic cathode electrons and low-energy charge-exchange ions and that the axial plate region is located at the center of the beam and thus dominated by highly-energetic beam ions.

5.1.2.2 Plume Diagnostics

5.1.2.2.1 Plasma Potential

The plasma potential measured along thruster centerline at 1 m downstream as a function of cathode position is shown in Figure 32. The plasma potential behavior for both the grounded and floating plates exhibit three different regions of behavior. In Region 1, the grounded thruster body configuration plasma potential measured monotonically increases by 1 V to 2 V. In Region 1, the floating thruster body configuration downstream plasma potential changes non-monotonically. From Region 2 to Region 3, the downstream plasma potential decreases by 1 V to 2 V. Overall, there are small variations in the downstream plasma potential and those variations can be roughly segmented by the magnetization of electrons near the cathode orifice.

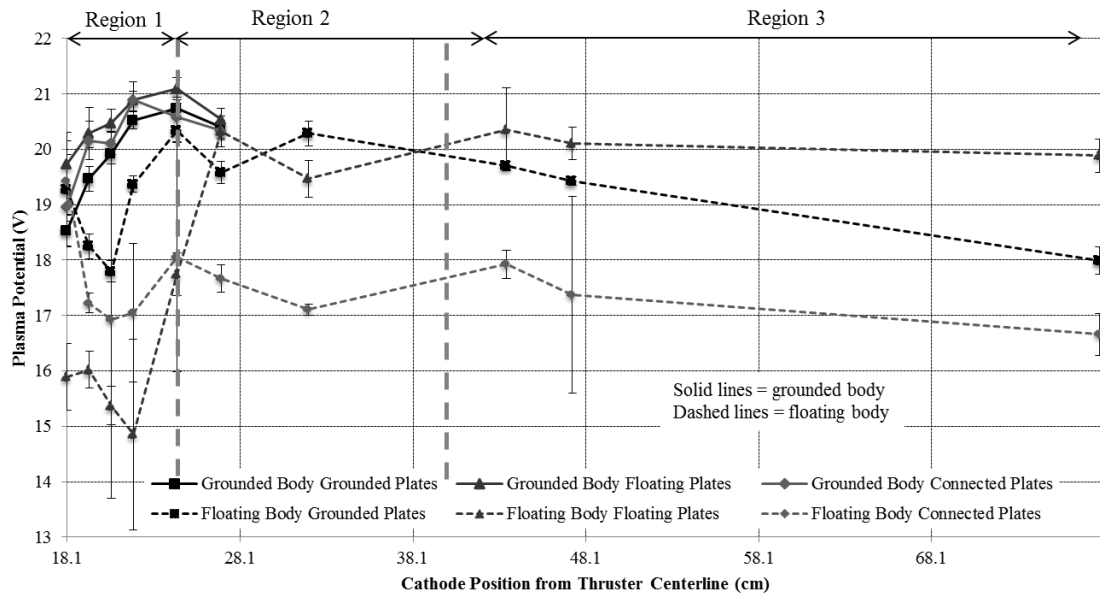


Figure 32: Plasma potential measurements taken at thruster centerline at 1 m downstream. The HET operating condition is 300 V, 3.1 kW

5.1.2.2.2 Most Probable Ion Energy

The most probable ion energy from the ion energy distribution function is shown in Figure 33. Because of the variability in the most probably ion energy is $\pm 10\%$ of indicated value, the most probable ion energy does not show any cathode position based

variation outside the measurement's uncertainty. The data presented has already been corrected for the local plasma potential.

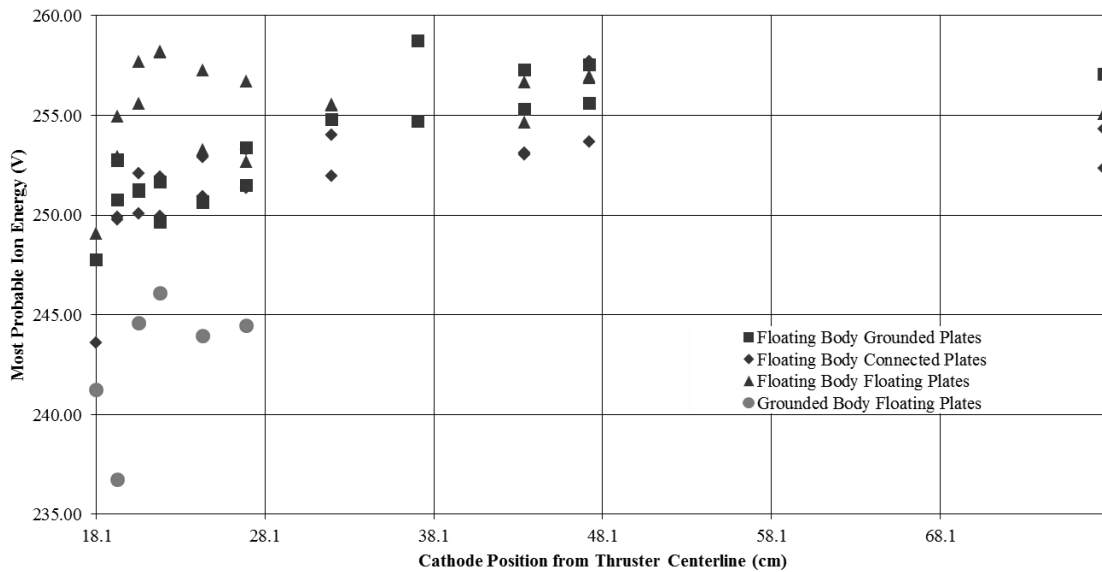


Figure 33: Most probable ion energy results taken at thruster centerline at 1 m downstream. RPA measurement variability in the most probable ion energy is $\pm 10\%$. The HET operating condition is 300 V, 3.1 kW.

5.1.2.2.3 Thrust Measurements

Figure 34 and Figure 35 show the thrust measurements for the various experimental configurations. The changes expected in thrust due to cathode radial position are expected to be less than the overall uncertainty of the thrust measurements. To overcome this limitation, thrust measurements are taken consecutively with a spacing of two minutes between cathode radial positions. This means that between plate and thruster body configurations, the variability is still 3.4%, but at least the changes for a given plate configuration can be observed with less than 1% uncertainty.

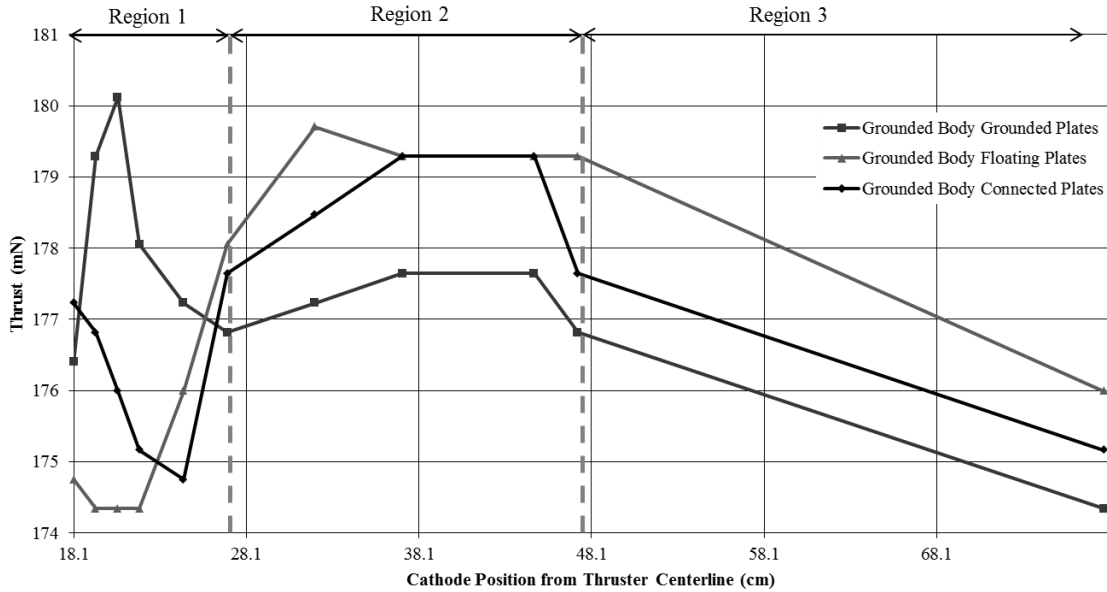


Figure 34: Grounded thruster body configuration. The absolute uncertainty $\pm 1.7\%$. The variability between cathode positions, (*i.e.*, relative uncertainty) for a given plate configuration is less than 1%. The HET operating condition is 300 V, 3.1 kW.

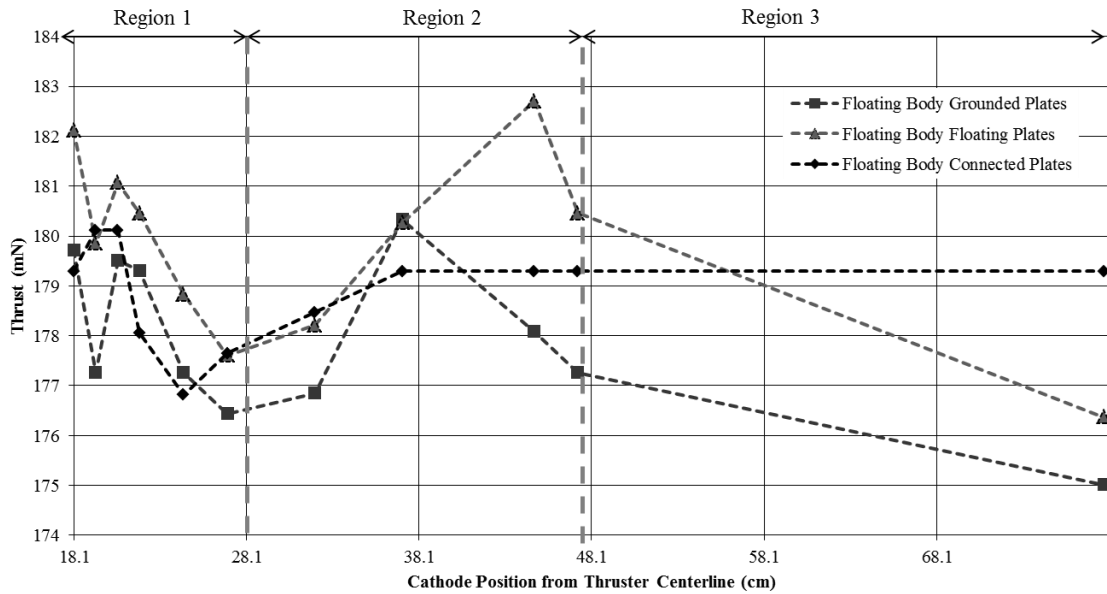


Figure 35: Floating thruster body configuration. The variability between plate configurations is $\pm 3\%$. The variability between cathode positions for a given plate configuration is less than 1%. The HET operating condition is 300 V, 3.1 kW.

5.1.3 Time Resolved Results

5.1.3.1 Discharge Current

To reduce the discharge current oscillation variability, the discharge current waveform data presented for all cases were collected within a 4-hour period, without turning off the thruster. In Frieman *et. al.*, the mean value of the discharge current did not vary significantly with changes in cathode radial position [22]. However, a time-resolved analysis of the discharge current indicates that other waveform properties do show a dependence on cathode position. As displayed in Figure 36, the peak-to-peak of the discharge current, measured as the difference between the maximum current measured and the minimum raw (without filtering) current data measured during an oscilloscope waveform capture period, has a non-monotonic dependence on cathode radial position. The legend labels in Figure 36 and all subsequent figures, abbreviated the plate and thruster body electrical configurations as the following: “GND” represents a grounded electrical configuration, “FLT” represents a floating electrical configuration, and “CON” represents a connected electrical configuration. As the cathode moves from Region 1 to Region 3, the peak-to-peak discharge current drops to approximately 55% of its maximum value for the floating thruster body configurations and to 65% of its maximum value for the grounded thruster body configuration. The peak-to-peak discharge current for the floating thruster body configuration is 13% - 18% larger than comparable grounded thruster body conditions throughout all cathode positions. From Region 1 to Region 2 cathode positions, the floating thruster body configuration peak-to-peak of the discharge current is 60% greater than the grounded thruster body configuration. From Region 2 to Region 3 cathode positions, the difference between floating and grounded thruster body configuration drops

to less than 30%. Because the sampling time of the waveforms is 20 ms, which is hundreds of fundamental breathing mode cycles, it is possible that the peak-to-peak discharge current is not representative of the actual large-scale changes in discharge current variability. To verify that the peak-to-peak discharge current behavior is showing behavior that is representative of aggregate changes in the discharge current variability, the standard deviation of the discharge current as a function of cathode position is shown in Figure 36. Because the standard deviation is a statistical quantity that takes into account the variability of the current over the entire sampling window, it is expected that the standard deviation of the discharge current would show smaller overall magnitudes of changes in the discharge current. However, the relative changes in discharge current standard deviation show similar cathode position dependent behavior as the peak-to-peak discharge current.

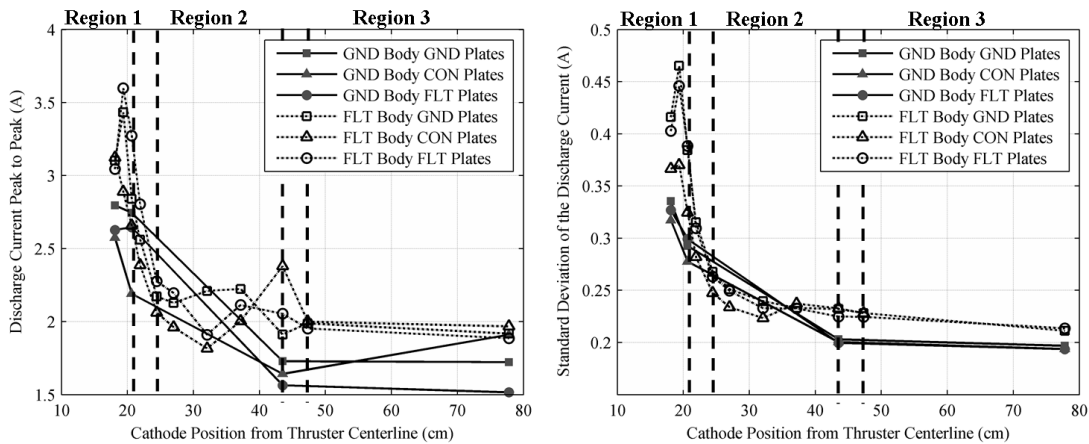


Figure 36: Left: Peak-to-peak discharge current as a function of cathode radial distance. Right: Standard deviation of the discharge current as a function of cathode radial distance. Mean discharge current for each waveform measured is 10.2 A with a variability of ± 0.1 A between data points and testing configurations. The HET operating condition is 300 V, 3.1 kW.

For all plate and thruster configurations, the peak-to-peak discharge current magnitude is dependent on cathode radial position. Since the peak-to-peak discharge current behavior is indicative of time-dependent processes, it is expected that there is a frequency domain dependent behavior as well. Application of a Fast Fourier Transform (FFT) to a waveform taken in the time-domain results in the waveform being resolved in the frequency domain; the square of each amplitude term in the series is known as the power spectrum. The power spectrum shows the distribution of power amongst the various fundamental frequency modes of a given signal. To obtain only the alternating current (AC) portion of the signal, the time-averaged mean from each waveform was subtracted from the raw waveform. An FFT was applied to that subtracted signal post thruster testing using MATLAB. To aid in the presentation of the power spectrum data, the calculated spectral power is converted to units of decibels as described by Equation 3.

$$P_{dB} = 10 \log_{10} \frac{P_{calc}}{P_{min}} \quad (19)$$

P_{dB} is the spectral power in units of decibels, P_{calc} is the spectral power in arbitrary units as calculated via the application of the FFT, and P_{min} is the minimum spectral power of the waveform in arbitrary units as calculated via the application of the FFT. The Nyquist-Shannon frequency for current measurements is hardware limited with discharge current power spectra being able to resolve frequencies up to 10 MHz and the chamber plate current power spectra being able to resolve frequencies up to 30 MHz. The Nyquist-Shannon frequency for floating voltage measurements is sample rate limited at 62.5 MHz. Based on the sampling size of each waveform, the spectral resolution is 12 Hz. Based on

the sampling time length, the Rayleigh frequency or minimum frequency resolvable is 50 Hz for each power spectra.

Application of a FFT to the taken discharge current waveform reveal that the fundamental mode of the discharge current waveform has a non-monotonic dependence on cathode position as is shown Figure 37. A representative power spectra of the discharge current is shown in Figure 39. The peak discharge current oscillation corresponds to the HET discharge current breathing mode [3, 32, 59]. While there are other fundamental plasma instabilities that occur in the discharge, these modes are not readily identifiable in the measured discharge current power spectrum decomposition [59]. The discharge current peak frequency has an overall inverse proportional dependence on cathode position. From Region 1 to Region 3, the discharge current peak frequency drops by 15%-23% (depending on the plate configuration) for the floating thruster body configuration and by 17%-35% for the grounded thruster body configuration. In Region 1, both the grounded thruster body and the floating thruster body discharge current frequency peak shows a decrease of approximately 13% and 11%, respectively. In Region 2, the grounded thruster body discharge current frequency continues to drop to 45% of its 18.1 cm cathode position value. As compared to the grounded thruster body, the floating thruster body configuration exhibits a different behavior: in Region 2, specifically 30 cm to 42 cm, the peak discharge current oscillation increases to approximately 92% of its Region 1 value of 32 kHz.

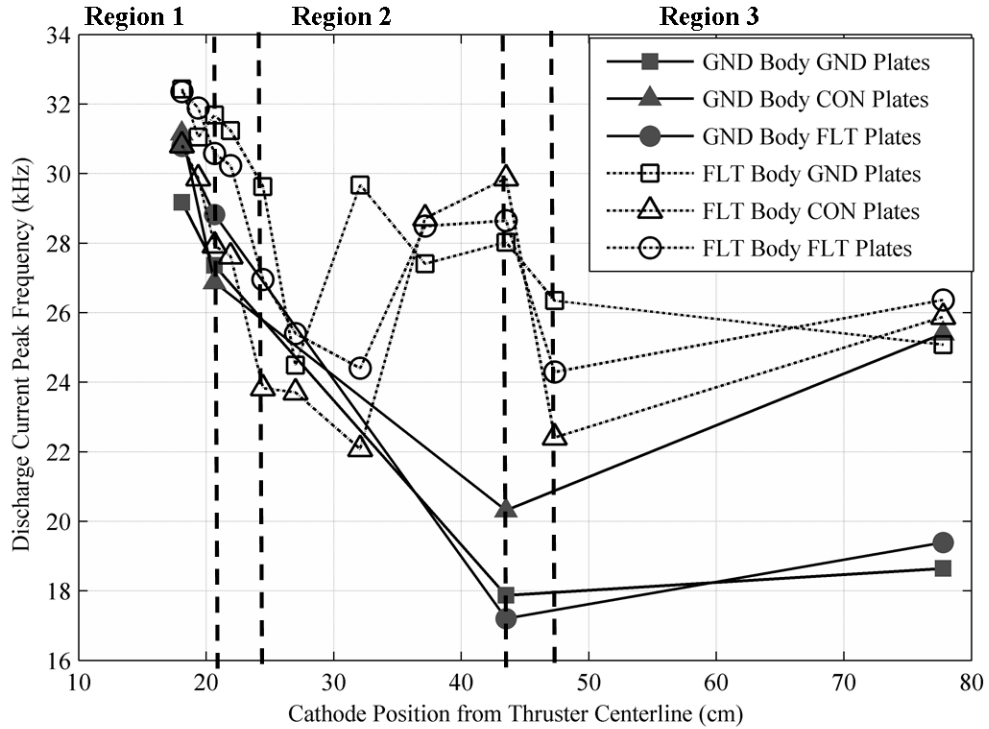


Figure 37: Peak frequency of the discharge current power spectra as function of cathode position for the thruster body and plate electrical configurations. The HET operating condition is 300 V, 3.1 kW.

The discharge current peak frequency is only indicative of the dominant mode of the HET discharge and does not capture the unsteadiness of the physical plasma process occurring in the HET discharge. The full-width-half-maximum (FWHM) is a way to measure such unsteadiness in a time-resolved signal. If the FWHM grows in size, then the thruster begins operating over a larger range of frequencies, thus meaning the HET discharge is operating over a larger range of frequencies. The FWHM is determined by measuring the bandwidth between a 3 dB drop or 50% decrease in power from the peak associated with discharge current oscillation. Figure 38 shows the full-width-half-maximum (FWHM) of the discharge current oscillation peak. At cathode positions greater than 30 cm, the FWHM becomes difficult to measure as the discharge current oscillation

peak broadens to a point where the FWHM is on the order of the peak frequency. Even so, the Region 1 FWHM is approximately 10 kHz smaller than in Region 2 and Region 3. Overall, the trend shown in Figure 38 is that the FWHM increases with cathode radial distance.

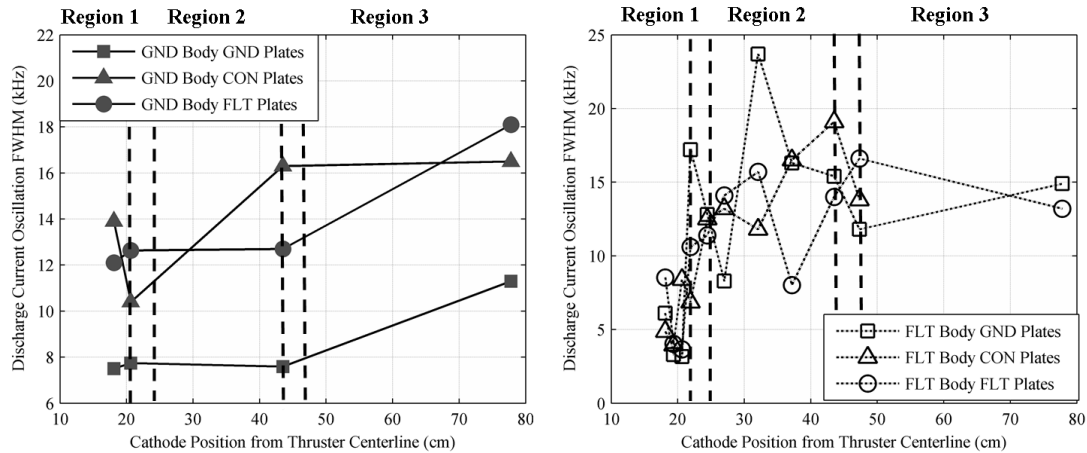


Figure 38: Left: Full-width-half-maximum of the peak frequency of the power spectrum as a function of cathode radial distance for the electrically grounded thruster body configuration. Right: Full-width-half-maximum of the peak frequency of the power spectrum as a function of cathode radial distance for the electrically floating thruster body configuration. The HET operating condition is 300 V, 3.1 kW.

5.1.3.2 Radial and Axial Chamber Plate

Similar to the power spectra of the discharge current, an FFT is applied to both the radial plate's collected current and floating voltage waveforms. Figure 39 shows one representative example of the radial plate current power spectra and the corresponding discharge current power spectra. The floating voltage power spectrum shows similar peak structure of the current power spectrum and is not shown. The most notable feature of the radial plate power spectrum waveform is the double peak occurring near the discharge

oscillation peak frequency. The discharge oscillation frequency is 32.2 kHz. In the radial plate power spectra, there is a spectral peak near the discharge frequency oscillation frequency at 34.2 kHz and another one at 45 kHz. There is also significant power relative to the noise floor of the power spectra in the sub-10 kHz range. Figure 39 only shows the spectra up to 100 kHz; however, the power spectra is computed up to the sample rate limited Shannon-Nyquist frequency of 62.5 MHz. Due to limitations in the 3 dB falloff of the electrical probes, peaks in the radial power spectra above 30 MHz are artifacts. This does not pose an issue for the analysis, as this investigation is primary concerned with plasma phenomenon occurring in the kHz range. At frequencies higher than 100 kHz, the power spectra falls-off precipitously and indicates the primary energy containing frequencies are in the sub-100 kHz range. Although Figure 39 corresponds to one configuration, the multiple peak nature, the double peak near the discharge current oscillation is especially prevalent across all thruster configurations where the discharge current oscillation FWHM is below 10 kHz.

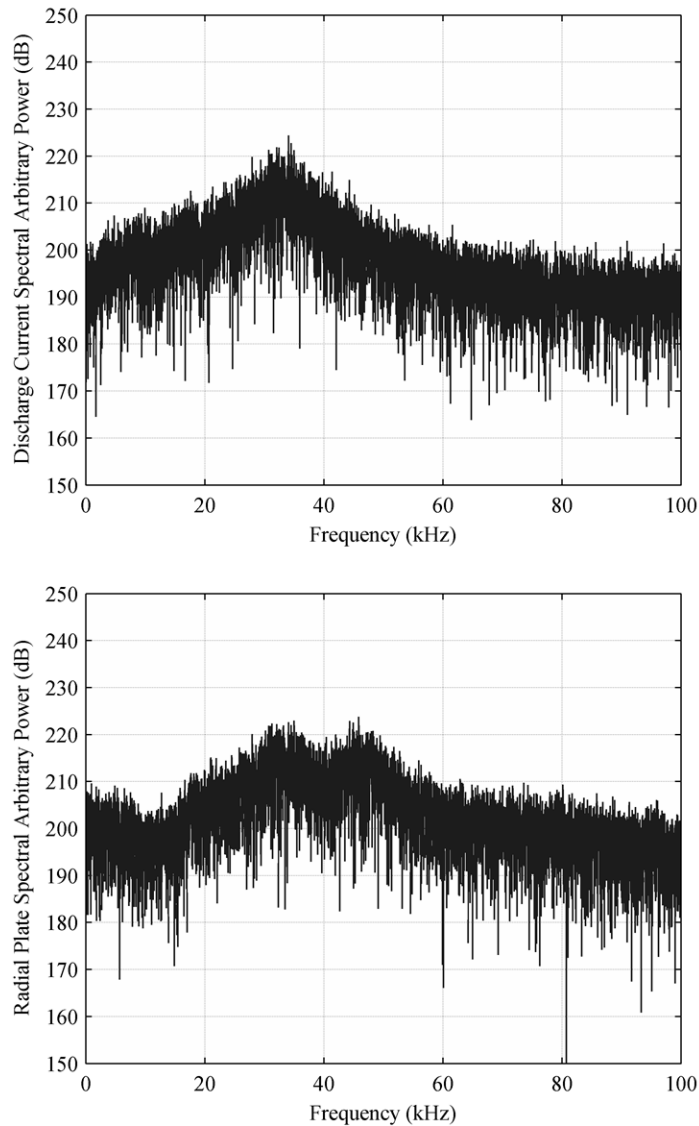


Figure 39: Top: power spectra of the discharge current. Bottom: power spectra of the radial plate current. Waveforms measured for a floating thruster body and grounded radial plate configuration at a cathode position of 18.1 cm relative to thruster centerline. The HET operating condition is 300 V, 3.1 kW.

The radial plate peak frequency has a proportional inverse dependence on cathode position. Figure 40 shows the radial plate spectral peak frequency drop from the 50 kHz range in Region 1 to the 5 kHz range in Region 3. It is important to note that the Region 1 spectral peak frequency is on the order of 50 kHz, but as demonstrated in Figure 39, current and voltage radial plate power spectra have a double peak structure that includes a lower

frequency spectral peak. The frequency of this secondary peak is on the order of the discharge current oscillation frequency. In Region 2, radial plate peak frequencies are of the same order of the discharge current oscillations. For the floating body configurations, the Region 2 peak frequency is in the 30 kHz range, and for the grounded thruster body configuration, the Region 2 peak frequency is in the 20 kHz range. In Region 3, both thruster body electrical configurations have peak frequencies in the sub 5 kHz range. Figure 41 shows that the axial plate peak frequency cathode position dependent behavior exhibits similar peak frequency characteristics as the discharge current and confirm previous conclusions drawn by Frieman, et al. [72] on the direct coupling of the axial plate to the thruster discharge.

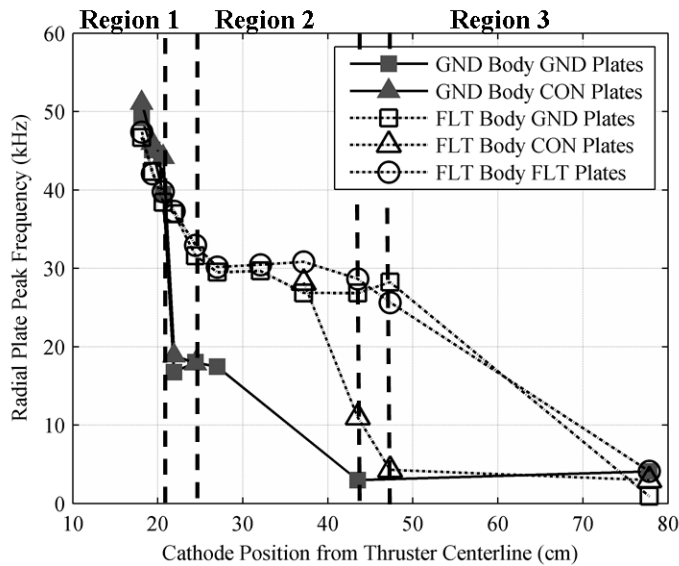


Figure 40: Peak frequency of the radial plate current and voltage power spectra as function of cathode position for the thruster body and plate electrical configurations. The HET operating condition is 300 V, 3.1 kW.

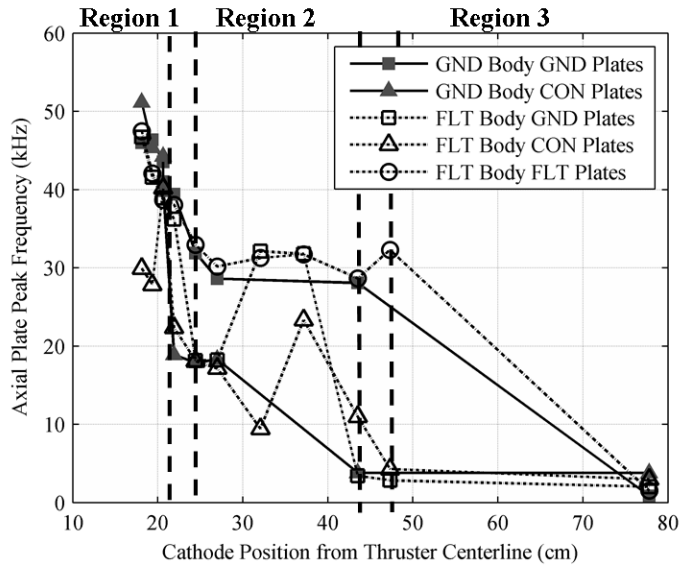


Figure 41: Peak frequency of the axial plate current and voltage power spectra as function of cathode position for the thruster body and plate electrical configurations. The HET operating condition is 300 V, 3.1 kW.

5.1.3.3 Radial Chamber Plate and Axial Chamber Plate Time-Delay

The time-delay between the discharge current and the radial chamber plate current and correlation coefficient as a function of cathode radial position is shown in Figure 42. At a cathode position of 15.6 cm radially away from thruster centerline (Figure 42), the radial chamber plate current waveform is weakly correlated to the discharge current peak event. Because of this weak correlation, the negative time-delay of any of the measured waveform is interpreted as non-physical and for clarity is omitted from Figure 42 through Figure 46. At cathode positions greater than 15.6 cm radially away from thruster centerline (Figure 42), the correlation coefficient increases to the strongly correlated regime. At cathode radial positions greater than 94.3 cm (Figure 42), the correlation coefficient decreases, but the signals have a correlation coefficient value that remains within the correlated to strongly correlated regime. This strong correlation agrees with previous

results that were obtained via global correlation calculations between the radial plate current-to-ground and discharge current (this is discussed in greater detail in section 6.1.1). The time-delay between the discharge current and radial plate across all cathode positions varies from $9.5 \mu\text{s}$ to $11.8 \mu\text{s}$.

When compared to the radial chamber plate time-delay data, the axial chamber plate time-delay shows a much different cathode position dependent behavior. Strong statistical correlation between the discharge current peak event and the axial chamber plate current-to-ground only occurs for cathode radial positions between 32.1 cm to 94.3 cm away from thruster centerline. For cathode radial positions less than 32.1 cm and greater than 107 cm away from thruster centerline, the axial plate waveform is weakly correlated to the discharge current peak event. At cathode radial positions between 32.1 cm to 107 cm away from thruster centerline, the axial chamber plate current waveform is strongly correlated to the discharge current event. Within this region, the time-delay between the discharge current peak event and the axial chamber plate current-to-ground varies between $8.1 \mu\text{s}$ to $9.3 \mu\text{s}$.

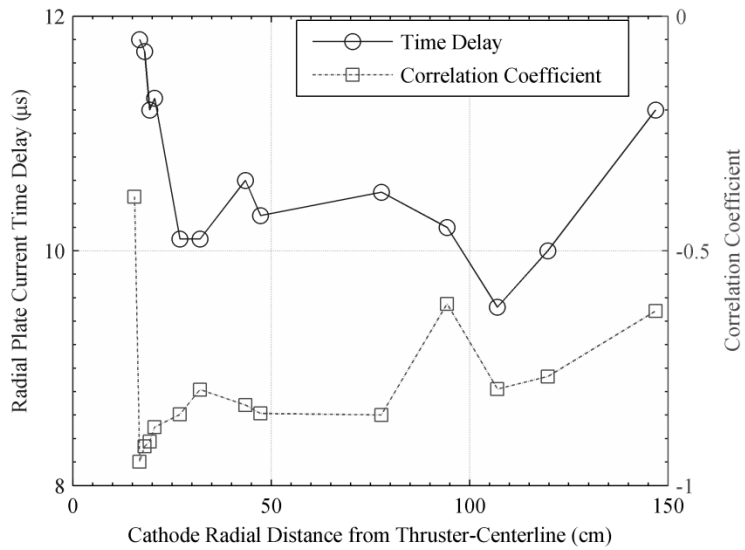


Figure 42: Radial chamber plate current time-delay and correlation coefficient as a function of cathode radial position away from thruster centerline. The HET operating condition is 300 V, 3.1 kW.

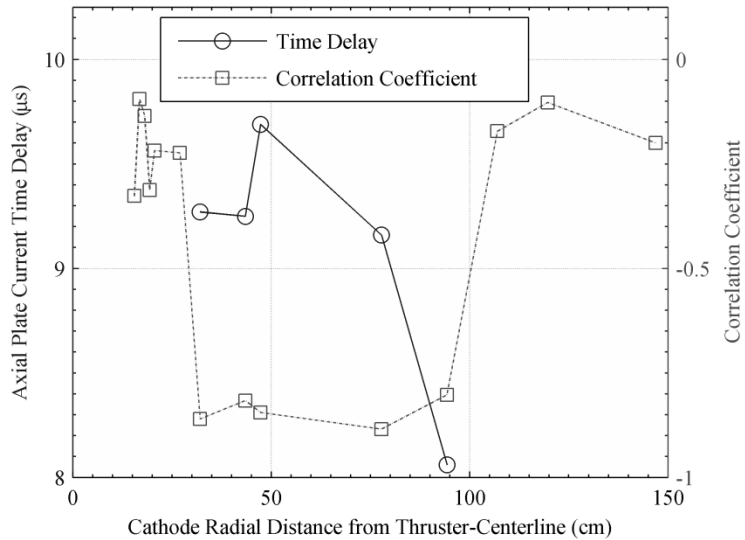


Figure 43: Axial chamber plate current time-delay and correlation coefficient as a function of cathode radial position away from thruster centerline. The HET operating condition is 300 V, 3.1 kW.

5.1.3.4 HET Cathode-to-Ground Voltage and Cathode Keeper Time-Delay

Figure 44 shows the results of the time-delay analysis between discharge current peak event and the HET cathode-to-ground voltage. The time-delay between the discharge current peak event and the corresponding signature in the cathode-to-ground voltage waveform is referred to as the “cathode-to-ground voltage time delay.” At a cathode radial position of 15.6 cm from thruster centerline, the HET cathode-to-ground voltage is weakly correlated to the discharge current peak event. At all other cathode radial positions, the HET cathode-to-ground voltage is strongly correlated to the discharge current peak event. At cathode radial positions of 18.1 cm, 19.4 cm, and 27.0 cm relative to thruster centerline, the correlation is positive. Physically, this means that as the discharge current increases, the cathode-to-ground voltage decreases in magnitude. A smaller magnitude of the cathode-to-ground voltage results in a higher cathode coupling efficiency [19, 46]. At the aforementioned cathode positions (18.1 cm, 19.4 cm, and 27.0 cm), the cathode experiences a marked change in its time-resolved behavior as an increase in discharge current results in increases in cathode coupling efficiency. This may be in part to favorable magnetic field topologies near the cathode orifice at those positions, but with the current data collected, it is unclear as to the exact causes behind this behavior. The cathode-to-ground voltage time delay for the aforementioned specific cathode positions is between 20 μ s and 26 μ s. For all other cathode positions, the cathode-to-ground voltage time-delay is between 2 μ s and 5 μ s.

The time-delay between the discharge current peak event and the corresponding signature in the cathode keeper floating voltage waveform is referred to as the “cathode keeper floating voltage time delay”. As shown in Figure 45, the cathode keeper floating

voltage time-delay varies bi-modally. For a majority of cathode positions, the time-delay of the cathode keeper floating voltage is the same order of magnitude of the time-delay of the cathode-to-ground voltage. However for cathode positions at 94.3 cm and 107 cm, the time-delay of the cathode keeper floating voltage is $29 \mu\text{s}$ and $28 \mu\text{s}$, respectively, while the cathode-to-ground voltage time-delay is $3.7 \mu\text{s}$ and $2.8 \mu\text{s}$. The change in the cathode keeper floating voltage time delay coincides with a sign change in the correlation coefficient and is indicative of a change in the fundamental process governing the floating voltage [94]. At cathode radial positions of 15.6 cm, 18.1 cm, and 20.6 cm relative to thruster centerline, the cathode keeper floating voltage is weakly correlated to the discharge current peak event. At all other cathode positions, the cathode keeper floating voltage is strongly correlated to the discharge current peak event.

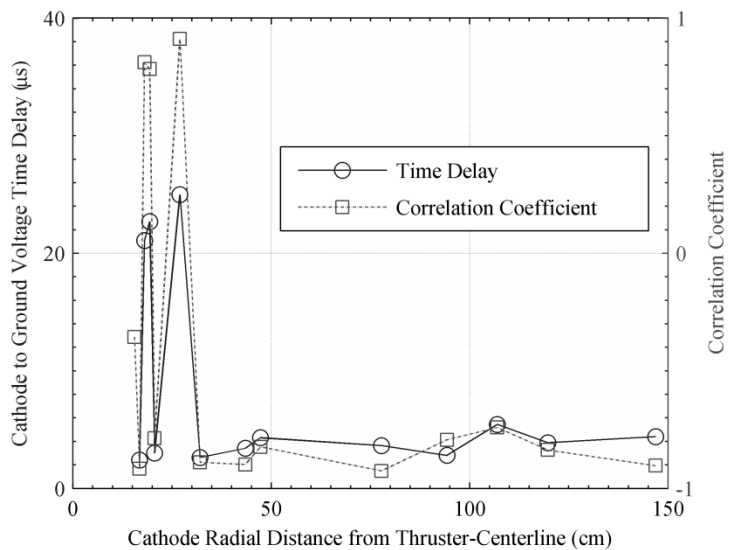


Figure 44: Cathode-to-ground voltage time-delay and correlation coefficient as a function of cathode radial position away from thruster centerline. The HET operating condition is 300 V, 3.1 kW.

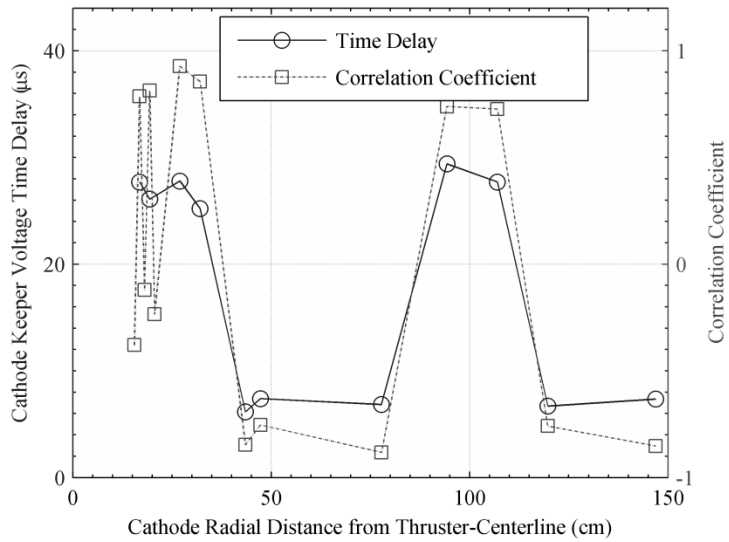


Figure 45: Cathode keeper floating voltage time-delay and correlation coefficient as a function of cathode radial position away from thruster centerline. The HET operating condition is 300 V, 3.1 kW.

5.1.3.5 Thruster Body Time-delay and Correlation

The time-delay between the discharge current peak event and the corresponding signature in the thruster body current-to-ground is referred to as the “thruster body time delay”. Figure 46 shows the thruster body time-delay and correlation. The thruster body current-to-ground becomes uncorrelated or weakly correlated to the discharge current peak event at cathode positions 16.8 cm to 20.6 cm and cathode positions that are greater than 107.1 cm. The cathode positions that have strongly correlated thruster body current-to-ground waveforms and discharge current waveforms roughly overlap with axial chamber plate cathode positions as shown in Figure 43. With the exception of the smallest cathode radial position (15.6 cm), the time-delay between the thruster body and discharge current peak event is on average $12 \mu\text{s}$.

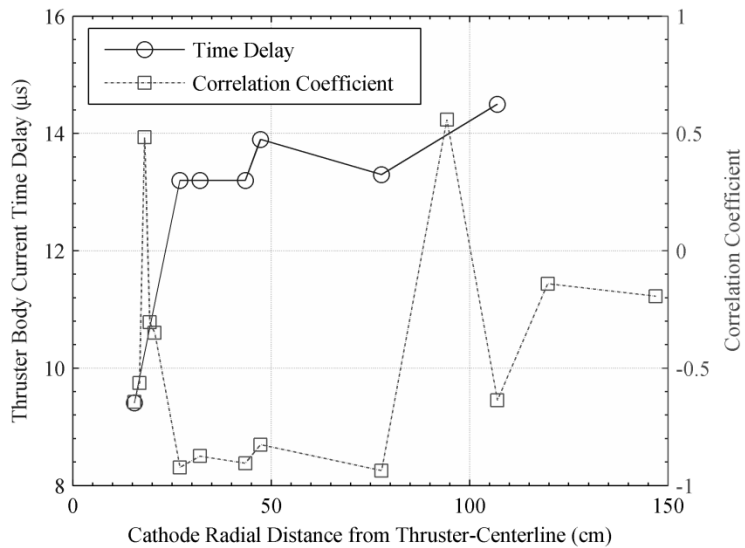


Figure 46: Thruster body current to ground time-delay and correlation coefficient as a function of cathode radial position away from thruster centerline. The HET operating condition is 300 V, 3.1 kW.

5.2 Axial Plate Biasing Experimental Configuration

For this experimental configuration, the main goal is to examine how the vacuum facility interacts with the HET electrical circuit by manipulating the chamber recombination current pathway. In this experimental configuration, the HET thruster is operated at a fixed operating condition and the voltage bias relative to ground of the axial chamber plate is altered. As the axial chamber plate voltage bias relative to ground is changed, different aspects of the HET are measured and presented below. The section begins with an overview of the experimental layout of the configuration and then follows with the results of this experimental configuration.

5.2.1 Experimental Layout

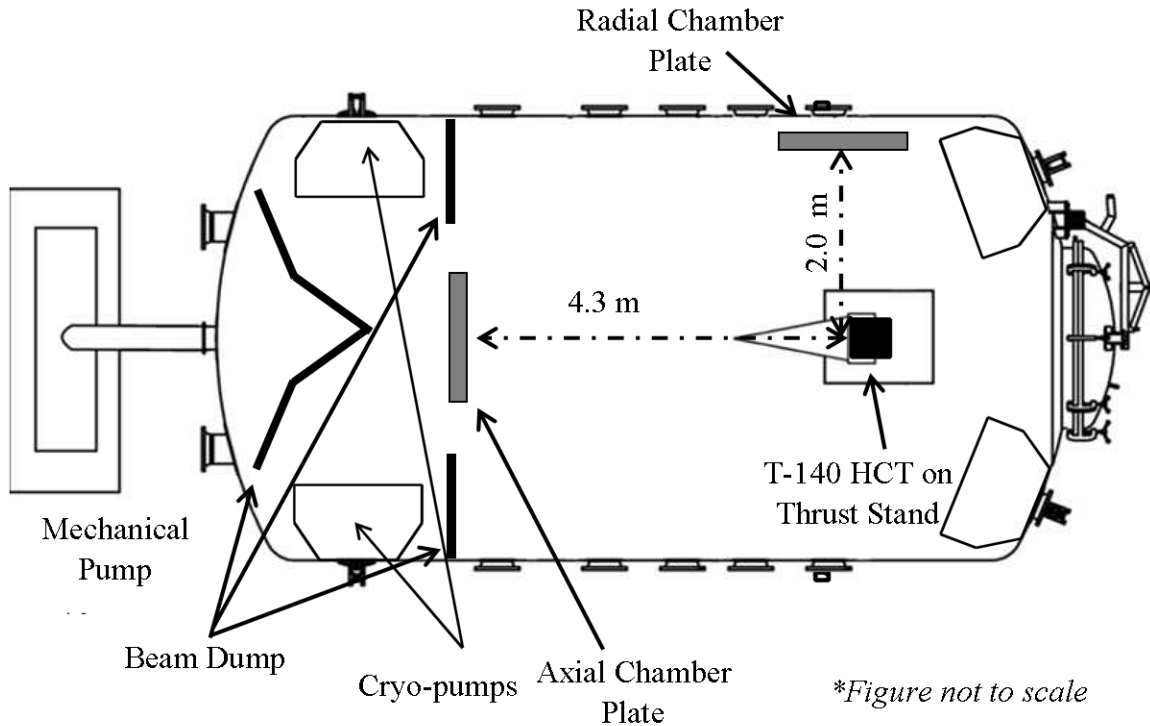


Figure 47: Overhead view of the vacuum chamber test facility, HET, chamber plates.

5.2.1.1 Configuration of the Chamber Plates

For clarity of the experimental configuration, Figure 47 shows the physical location of the plates with respect to the T-140 HET. Identical plates have been used in previous studies of electrical facility effects [22, 24, 72]. The radial chamber plate was electrically grounded using RG-58 coaxial cable with a grounded shield that passed through a BNC feedthrough into the chamber. The resistance between the radial chamber plate and the chamber walls is measured to be 1.1Ω . Based on current measurements made by Frieman *et al.* [22, 72], the current capacity of the inner conductor of the RG-58 is sufficient for radial plate current collection and would not pose any thermal issues during thruster testing.

For radial plate current measurements, ground loops were not a concern as the current probes are active clamp current monitors. The axial chamber plate was biased relative to ground using a TDK Gen 60 V, 12.5 A power supply. To avoid thermal issues with maintaining the axial plate bias voltage, the axial chamber plate was connected to the power supply via 6-AWG copper wire that connected to a 150-A power vacuum feed-through. During this investigation, the axial plate current did not exceed 10 A for testing conditions. The resistance between the axial chamber plate and the chamber walls is measured to be less than 0.2 Ω .

The current and voltage waveforms of the axial chamber plate were measured using a LeCroy CP030 current clamp and a PP005A 10:1 voltage divider connected to a Teledyne LeCroy HDO6104 oscilloscope. The radial chamber plate was connected to chamber ground with the current conducted to ground measured with a Teledyne LeCroy CP030 current sensor connected to a Teledyne LeCroy HDO6104 oscilloscope; the plate currents and thruster telemetry waveforms were measured simultaneously at a sampling frequency of 125 MS/s for a 20-ms window to ensure that multiple fundamental discharge current mode periods were captured.

5.2.1.2 Thruster Body Witness Plates Electrical Configuration

Figure 48 shows the electrical configuration of the thruster body plates. To prevent ground loop issues, the thruster body plates are electrically grounded using a star ground configuration. The electrical ground used is a common reference ground for all diagnostics and is electrically tied to the walls of the vacuum facility. Since the voltage of the thruster body plates are held constant via the electrical ground, it is only necessary to measure the current flowing through each of the thruster body plates and thruster body to ground. Using Kirchhoff's law of currents, the total current flowing to ground through the thruster body can be calculated as the summation of all the measured currents. For the thruster body plates, Teledyne Lecroy CP030A (see Chapter II for technical specs), high sensitivity

current clamps are used to measure the current flowing through each plate. For the remaining thruster body surfaces connection, a Teledyne Lecroy CP030, current clamp is used to measure the current flowing to ground.

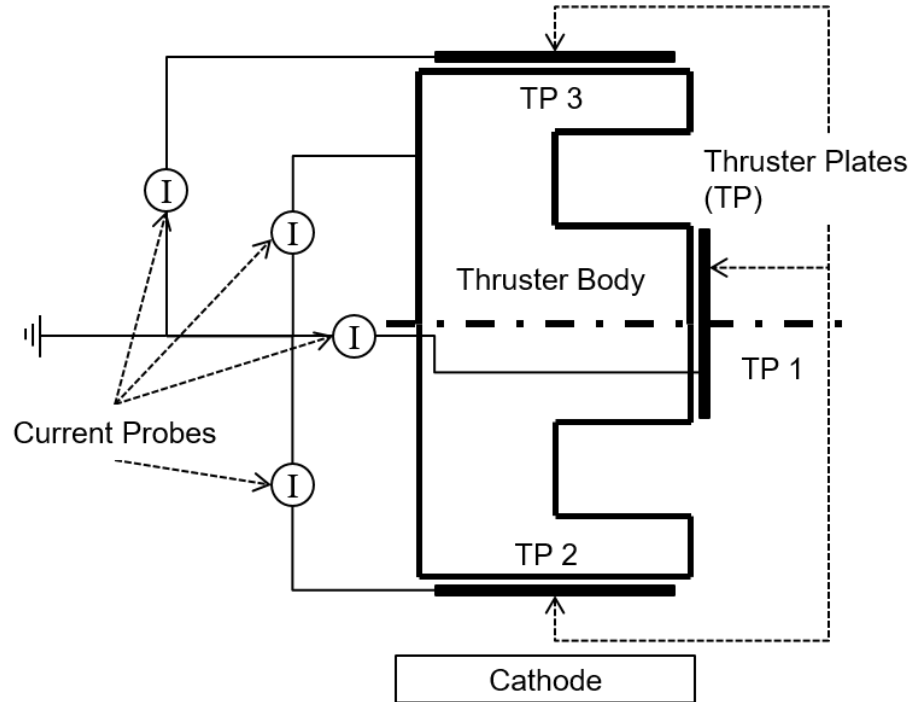


Figure 48: Electrical configuration of the thruster body plates for the axial plate bias experimental configuration.

5.2.1.3 Summary of Electrical Diagnostics Layout

A summary of all electrical diagnostics connection are shown notionally in Figure 49. The measurement located are all electrical signals that are time-resolved. The discharge voltage of the HET was measured separately and was used to verify that the HET was operating at the desired operating condition. Since the HET discharge circuit is floating, the cathode-to-ground voltage is a measurement of the floating voltage of the HET electrical circuit. A diagram showing the different voltages important to a HET can be seen in Figure 8 and Figure 14.

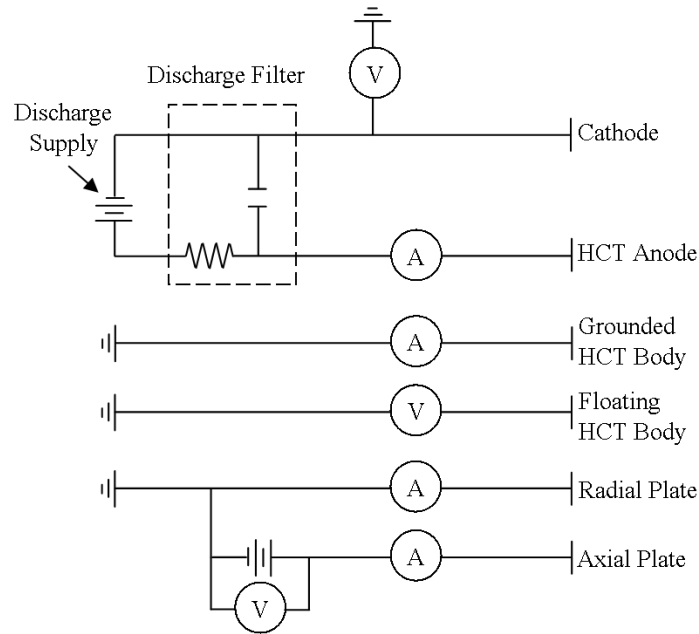


Figure 49: Electrical diagram of current and voltage measurements of the HET discharge circuit.

5.2.1.4 T-140 HET Operating Conditions

All data was collected with the T-140 HET operating at a discharge voltage of 300 V, discharge power of 3.16 kW, an anode xenon flow rate of $11.6 \text{ mg/s} \pm 0.03 \text{ mg/s}$, and a cathode xenon flow rate of $1.61 \text{ mg/s} \pm 0.12 \text{ mg/s}$. The operating chamber pressure as measured by the external ion gauge is $7.3 \times 10^{-6} \text{ Torr-Xe}$, the operating chamber pressure as measured by the internal ion gauge is $1.3 \times 10^{-5} \text{ Torr-Xe}$. The thruster discharge voltage, inner and outer magnet currents, anode mass flow rate, and cathode mass flow rate were held constant for all cathode positions and plate configurations. The thruster was run through a 3-hour conditioning cycle prior to data collection in order to allow the thruster to approach thermal equilibrium [40]. The discharge current of the T-140 HET is measured using a Teledyne Lecroy CP150 10 MHz current clamp (see Chapter III for technical specs). To be able to clearly measure the discharge oscillations, the discharge current is measured on the thruster side of the discharge filter, as shown in Figure 49. The discharge

voltage relative to ground is measured using a Teledyne Lecroy PPE2KV 100:1 voltage divider and the cathode-to-ground voltage is measured using a Teledyne Lecroy PPE2KV 100:1 voltage divider (see Chapter III for technical specs). These probes are placed at measurement points downstream of the discharge filter. Since the HET discharge circuit is a floating circuit, the discharge voltage of the HET is measured differentially as the difference between the discharge voltage relative to ground minus the cathode-to-ground voltage. For this experimental configuration, the HET discharge voltage measurement was not time-resolved and was used to verify that the HET was operating at the desired operating condition.

5.2.1.5 Probe Diagnostics Configuration

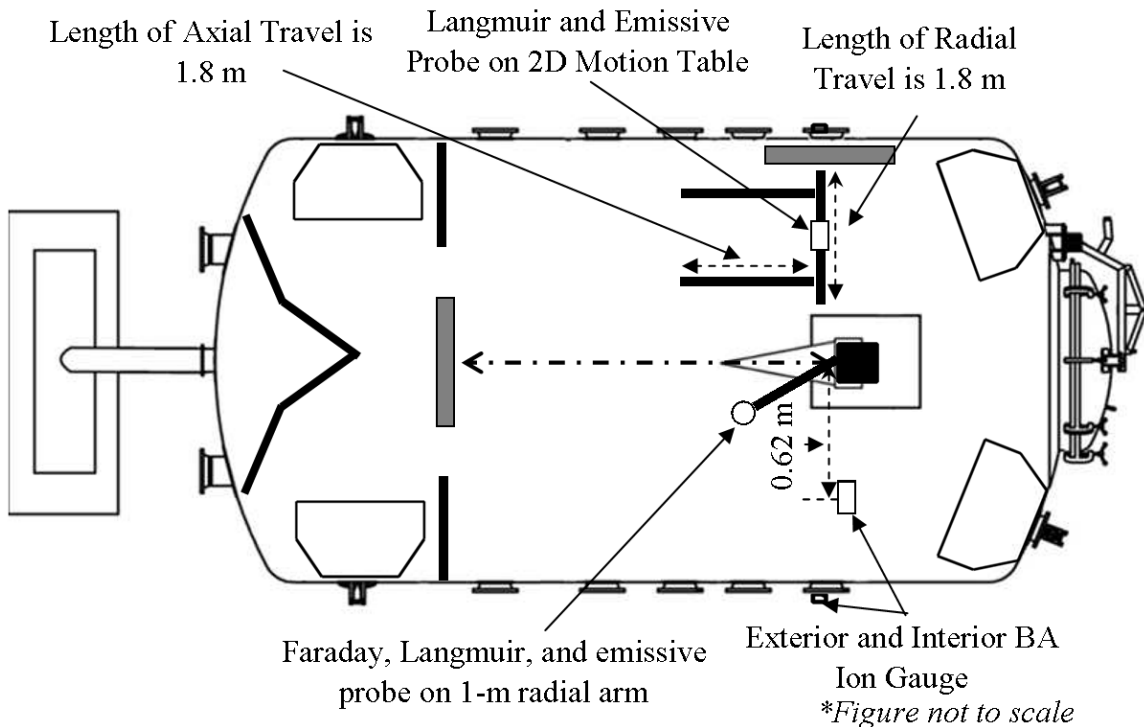


Figure 50: Overhead view of the vacuum chamber test facility, HET, and plume diagnostics.

Plume diagnostics were taken along a $1 \text{ m} \pm 0.01 \text{ m}$ radius centered at the thruster centerline and discharge plane. Ion current density measurements occurred throughout a full range of 180° while emissive probes and Langmuir probes sweeps were taken at select angular positions based on the ion current density profile of the HET plume. An schematic overview of the plume diagnostics relative to the HET are shown in Figure 50. The probe diagnostics were mounted to a Parker Daedal RT series 8-in rotary motion table. All three of the plume diagnostics: a Langmuir probe, JPL nude style Faraday probe, and an emissive probe were attached in an array on radial probe arm. The arms of the array were angled such that probe-to-probe centerline linear distance was at $0.17 \pm 0.01 \text{ m}$ apart and remained at a 1 m radial distance throughout the probe arm sweep. Figure 50 shows the relative position of the diagnostics arm and Figure 51 and Figure 52 show an image and notional diagram of the probe arrangement on the diagnostics arm.

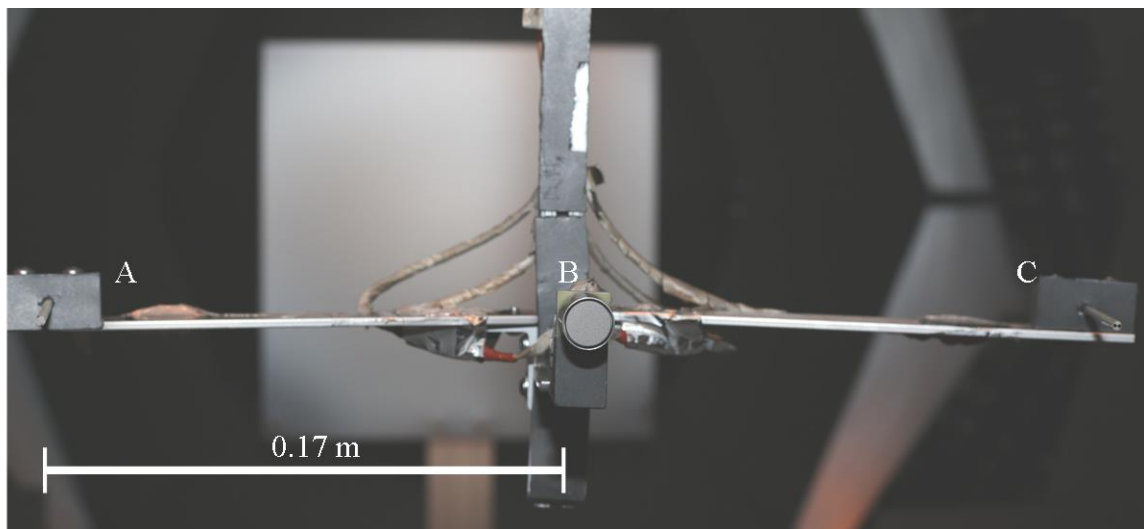


Figure 51: Probe arm with plume diagnostics attached A) Langmuir Probe B) Faraday Probe C) Emissive Probe

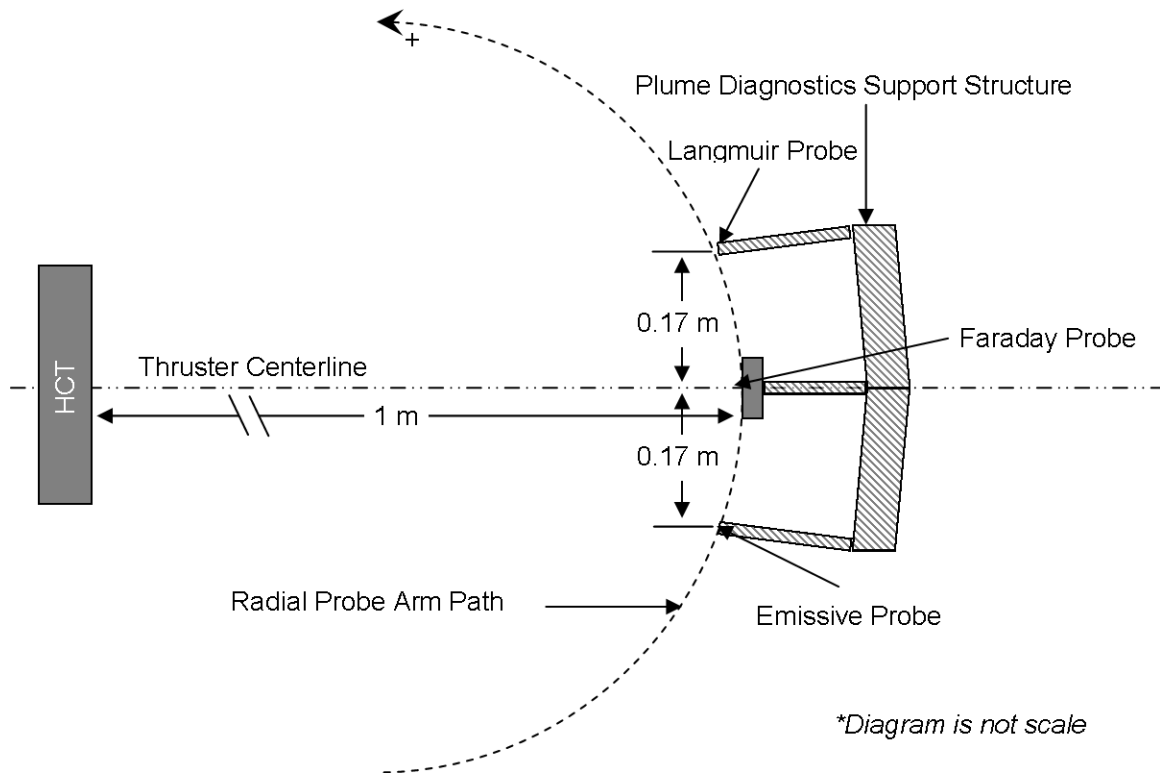


Figure 52: Overhead view of notional layout of the radial diagnostics probe arm

5.2.2 Time-Averaged Results

For the time-averaged voltage and current measurements presented below, the oscilloscopes are configured for a sampling rate of 125 MS/s and a sample length of 2 MS. The average voltages and currents presented below are the arithmetic average value over the entire 2 MS waveform length.

5.2.2.1 Axial Chamber Plate Behavior

As shown in Figure 53, the axial chamber plate current collection behavior exhibited three distinct regions. Because the plate was biased with a positive voltage relative to ground, the current collected on bias plate transitions from a net flux of ions to a net flux of electrons. With the axial chamber plate bias at 0 V, the beam ions generated by the HET compose the majority of the net charge flux to the plate. As the bias voltage

increases, more electrons are gathered to the axial chamber plate. Between 0 V and 5 V, sufficient electrons are collected by the plate such that there is no net charge flux to the plate. This voltage is also known as the floating voltage of the axial plate and is not precisely measured during this study. Based on measurements of Frieman *et al.* [22], the floating voltage of the axial plate is expected to be approximately 4 V. At axial chamber plate bias beyond the floating voltage, there is net electron current collection reaching the axial chamber plate. This increase in electron current continues monotonically until the net electron current collection approaches the beam current of the HET. Based on the acceleration voltage and thrust measured by Frieman *et al.* [3, 22], the beam current of the HET can be estimated as follows:

$$I_b = \frac{T_{HET}}{\sqrt{2m_i V_{accel}}} \quad (20)$$

where I_b is the beam current, T_{HET} is the thrust produced by the HET, m_i is the mass of a xenon atom, and V_{accel} is the acceleration potential. Using this model, the beam current is estimated to be near 7 A. This relationship neglects the presence of multiply-charged ions, does not take into account the beam divergence, and neglects the ion energy distribution of the beam ions. Based on E x B measurements by Ekholm and Hargus [95] running a BHT-200 HET at 250 V, a lower range to the beam current estimate can be made, and it is expected that for the T-140 HET operated at 300 V will have a doubly charged xenon population that is approximately 12% of the total ion population. This reduces the estimated beam current to be on the order of 6 A. A better estimate of the beam current is not possible using the Faraday probe because testing occurred at one operating background pressure. Without current density profile measurements at multiple background pressures,

it was not possible to extrapolate the vacuum current density profile, thus making the beam current measurement via an integrated current profile artificially inflated.

For an axial plate bias greater than 20 V, the slope of the electron current collection vs axial plate bias voltage decreases by approximately 85%. Data collection above axial chamber plate bias of 50 V above ground was not possible due to arcing events on grounded surfaces within the vacuum chamber. After raising the potential of the axial chamber plate past the floating voltage of the chamber plate, the axial chamber plate begins collecting a net flux of beam electrons from the surrounding plasma. As the plasma sheath begins to expand to collect more electrons, the plasma potential begins to increase. Once the axial chamber plate begins to collect a net electron current equal to the expected beam current, the electron current collection as a function axial bias plate voltage above ground begins to level off, forming a knee in the curve.

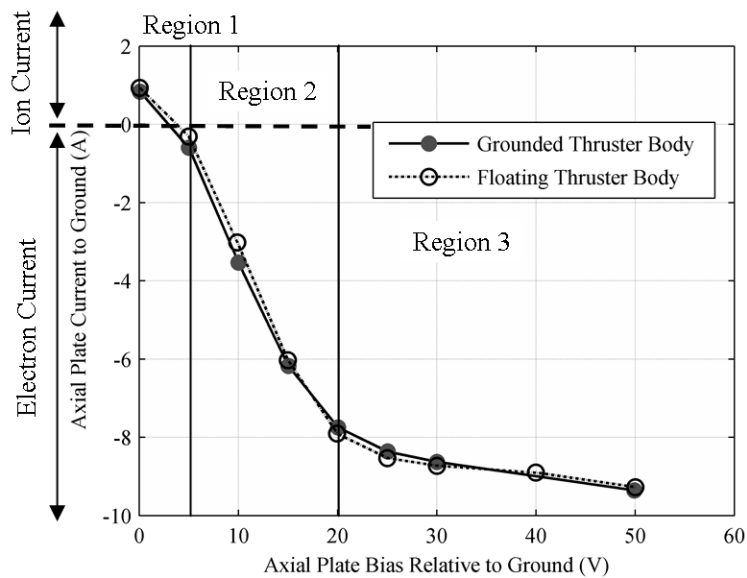


Figure 53: Axial chamber plate current collected as a function of axial plate bias voltage. The HET operation condition is at 300 V, 3.16 kW. Error bars are encompassed by plot markers.

The floating thruster body and the grounded thruster body configurations have similar overall current collection behavior, but at biases larger than 0 V but smaller than 15 V, the floating thruster body configuration has an axial chamber plate current collection between 49% and 15% less current than comparable grounded thruster body configurations. At greater than 15 V of axial plate bias voltage above ground, the floating thruster body configuration has axial chamber plate current collection 1%-2% greater than comparable grounded thruster body configurations. The reason for the discrepancy between the thruster body configurations is not yet clear.

5.2.2.2 Radial Plate Facility Interaction

As seen in prior work, the grounded radial chamber plate collects a net-flux of electron current [22]. As the bias voltage of the downstream axial chamber plate increases, the electron current collected on the radial plate decreases. Figure 54 shows the radial chamber plate current collection as a function of axial chamber plate bias voltage. Negative current collected corresponds to net electron current and positive current collected indicates net ion current.

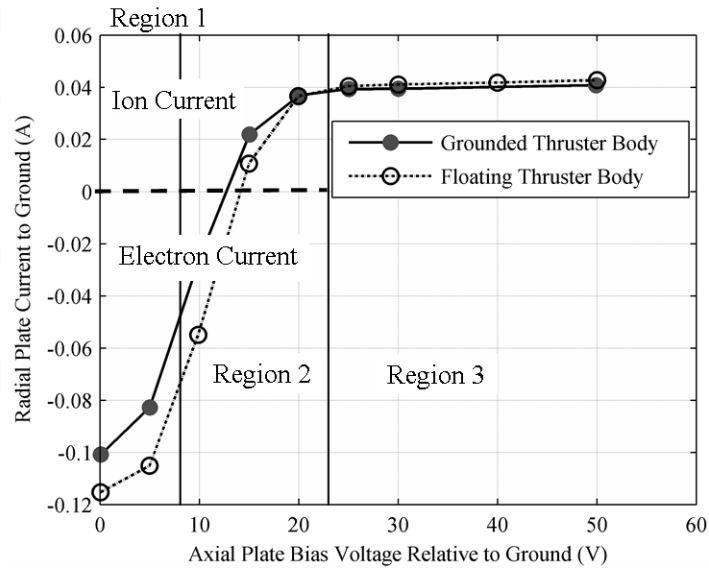


Figure 54: Radial chamber plate current collection as a function of axial chamber plate bias voltage relative to ground. HET nominal condition is at 300 V, 3.16 kW. Error bars are encompassed by plot markers.

Between 10 V to 15 V of axial chamber plate bias potential, the current collection on the radial chamber plate transitions from a net flux of electron current to a net flux of ion current. At axial bias chamber plate biases greater than 15 V, the plasma potential near the radial chamber plate rises sufficiently relative to the chamber walls that the potential difference between the plasma and the grounded radial chamber plate repels electrons. The current collection behavior of the radial chamber plate as shown in Figure 55 indicates that for axial bias plate voltages greater than 25 V, electrons are driven away from the radial chamber plate, and the radial chamber only collects a net ion-current.

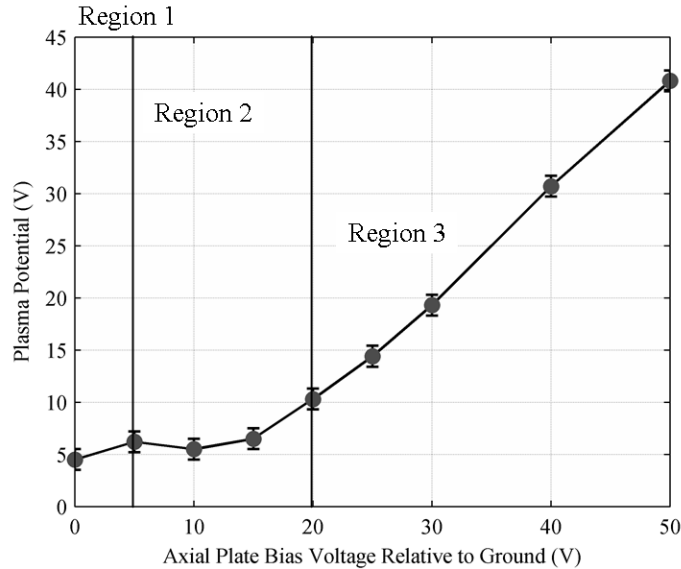


Figure 55: Plasma potential measured at 25.4 cm radial distance away from the radial plate. HET nominal condition is at 300 V, 3.16 kW. Measurement is centered on radial plate centerline.

5.2.2.3 Influence of the Axial Chamber Plate Bias on the HET

The effect of the downstream bias voltage of the axial chamber plate on the HET was measured in two ways: thrust and characteristics of the HET electrical circuit. Measurements of thrust showed no statistically significant change in thrust production of HET circuit. Based on the conclusions drawn by Frieman *et al.* [72], this is expected. In Figure 56, the cathode-to-ground voltage and centerline plasma potential measurements as a function of axial plate bias voltage above ground are shown. As the axial plate bias voltage increased, the cathode-to-ground voltage began to move synchronously with the plasma potential. The cathode-to-ground voltage relative to ground changes sign between 20 V and 25 V of axial chamber plate bias. This axial plate bias voltage range corresponds to collected electron current on the axial chamber plate above the HET estimated beam current. From axial chamber plate bias of 5 V to 50 V, the difference between the centerline plasma potential and the cathode-to-ground voltage remains a constant $32 \text{ V} \pm 2 \text{ V}$. Because the difference between the cathode-to-ground voltage and the plasma potential remains

nearly constant, there is no expected measurable change in thrust of the HET with axial chamber plate bias voltage. This was confirmed with direct thrust measurements. Thrust stand measurements show that the time-averaged thrust of the HET remained $177 \text{ mN} \pm 3 \text{ mN}$ for all axial bias plate conditions.

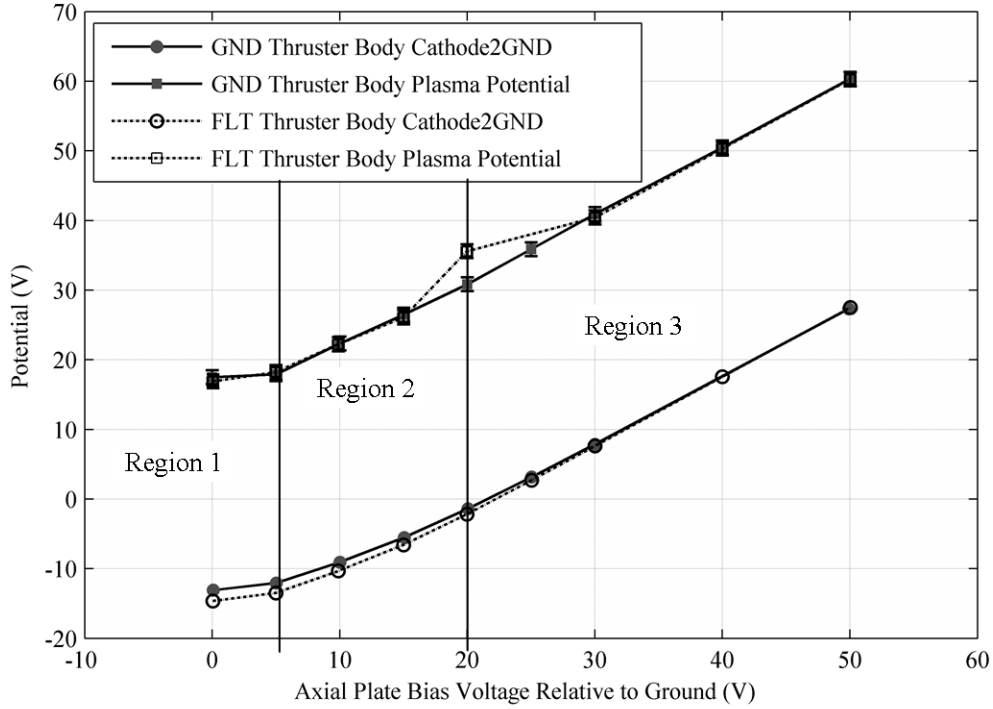


Figure 56: Cathode-to-ground voltage and centerline plasma potential as a function of axial plate bias. The HET operating condition is 300 V, 3.16 kW. Error bars for Cathode-to-Ground Voltage are encompassed by plot markers.

5.2.2.4 Plume Plasma Properties

Figure 57 shows the HET plume profile. The HET beam and exponential decline region of the current density profile show little to no dependence on axial chamber bias plate bias. At angular positions greater than 50° off thruster centerline, elevated current densities at high ($>20 \text{ V}$) axial plate bias relative to ground are measured. In this region, colloquially referred to as the “wings”, the ions present are primarily composed of charge-

exchange ions [3, 90]. This region is highlighted in Figure 57. It is important to note that the Agilent 34980A data acquisition unit used to measure the voltage across the precision resistor of the Faraday probe electrical circuit has an uncertainty of $\pm 0.004\%$ of the measured voltage. This low level of uncertainty leads to a current density profile measurement uncertainty between different axial plate bias voltages that is encompassed by the plot line width; therefore, the uncertainty of the current density profile is not visible in Figure 57. The current density profiles of the grounded thruster body and floating thruster body show no significant differences and so Faraday probe sweeps for the floating thruster body is not shown.

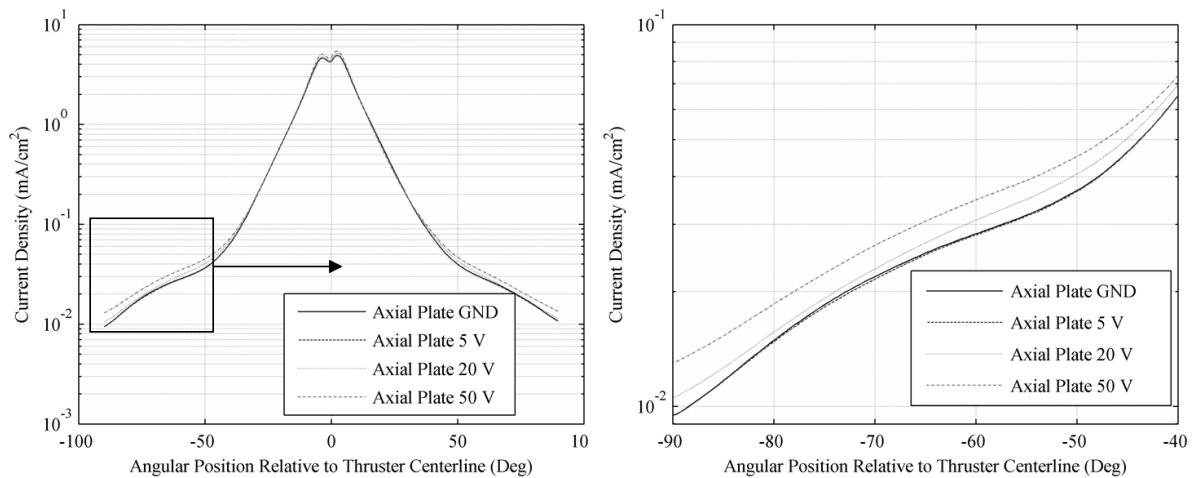


Figure 57: Ion current density profile as a function of increasing axial plate bias voltage for the grounded thruster body configuration. The HET operating condition is 300 V, 3.16 kW. Left) Full Plume Profile Right) One side of the HET Plume in the “charge-exchange ion” region.

At least two Langmuir probe and emissive probe measurements were sweeps taken in each ion current density profile region: thruster centerline, exponential decline, and the “wings”. Assuming the plasma properties to be axisymmetric, Langmuir and emissive probe measurements were taken throughout an arc of 90° relative to thruster centerline. As shown in Figure 58, the plasma potential measurements show a global increase in potential

with respect to axial plate bias voltage. The plasma density profile shows no change outside the uncertainty of the measurement with respect to axial plate bias voltage as shown in Figure 59. For both plasma potential and ion number density, the floating thruster body configuration HET plume profile did not show a measurable difference as compared to the grounded thruster body and is not presented.

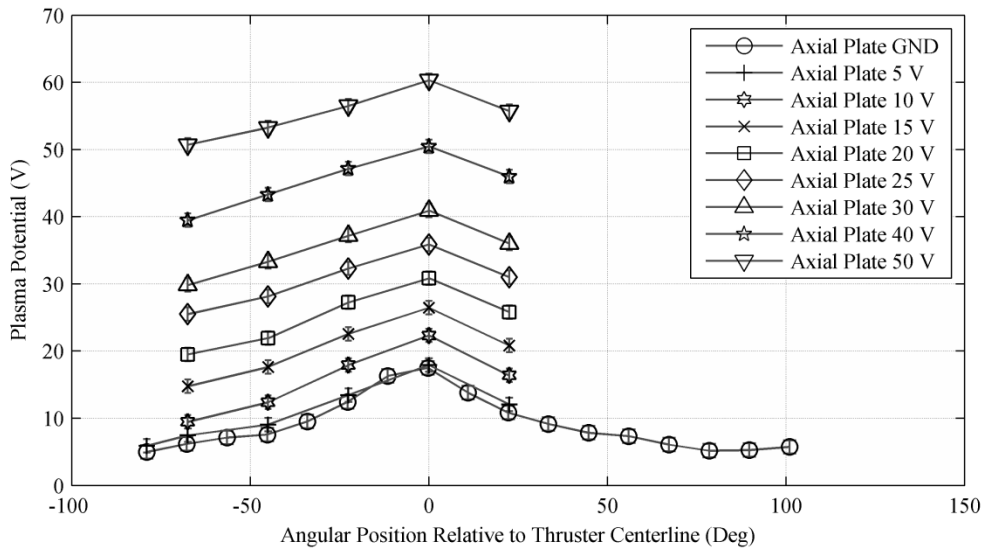


Figure 58: Plasma potential profile as a function of axial plate bias voltage for the grounded thruster body. The HET operating condition is 300 V, 3.16 kW.

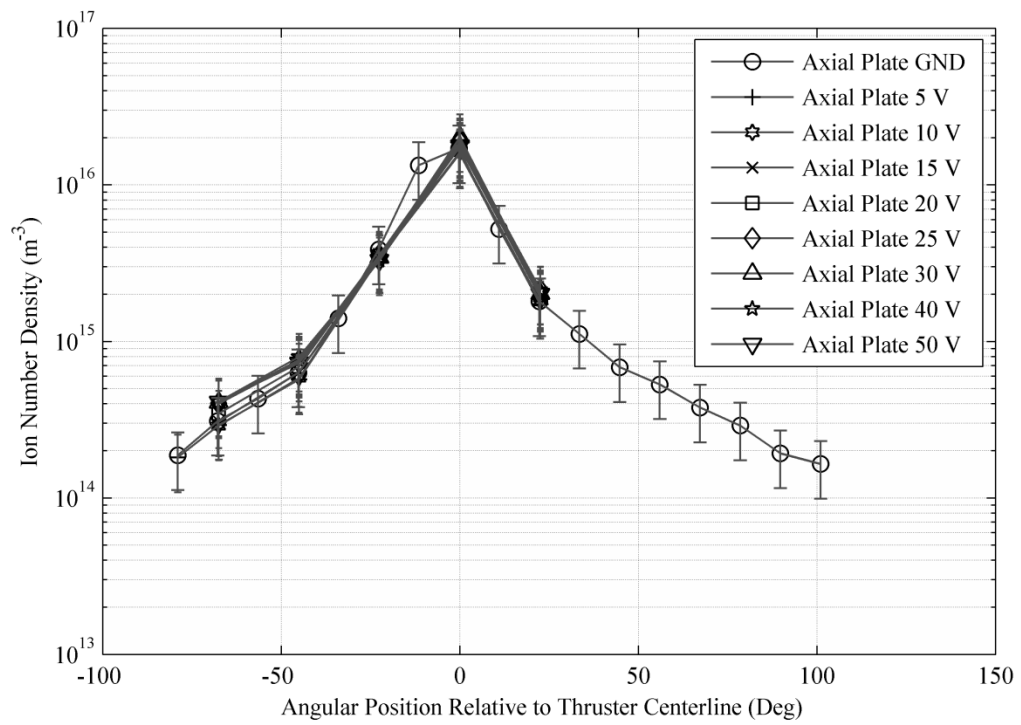


Figure 59: Ion number density profile as a function of axial plate bias voltage. The HET operating condition is 300 V, 3.16 kW.

5.2.3 Time-Resolved Results

5.2.3.1 Variation of the Discharge Current

The HET discharge is an inherently unsteady process with many plasma instability modes operating on many timescales. As such the discharge current varies rapidly as function of time. The peak to peak and standard deviation is one way to characterize these fluctuations. The results of the peak to peak and standard deviation of the discharge current as function of axial chamber plate voltage is shown in Figure 60. The overall trend for both the peak-to-peak and the standard deviation of the discharge current decreases as a function of increased axial bias plate bias. Both of these measurements decrease by approximately 30% from an axial chamber plate bias voltage of 0 V to 45 V. The largest decrease in the peak-to-peak and the standard deviation of the discharge current occurs after the axial chamber plate bias voltage is such that it is able to collect an electron current that is equal to the HET beam current. Based on beam current estimates, this occurs near an axial chamber plate bias voltage relative to ground of 20 V.

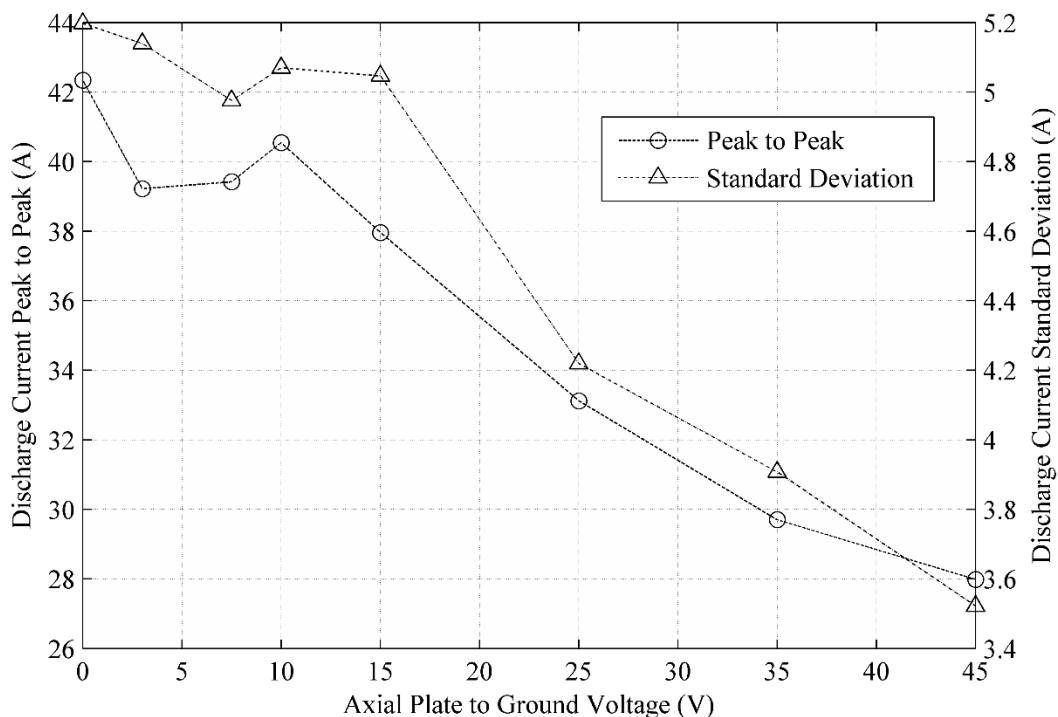


Figure 60: The discharge current peak to peak and standard deviation. The HET operating condition is 300 V, 3.4 kW.

5.2.3.2 Oscillation Response of the HET

In the following results that show the peaks of the power spectra of each of the oscilloscope waveforms, the uncertainty of the frequency at a spectral peak is Nyquist limited to 47.7 Hz. This is a much smaller uncertainty than what was obtainable during the cathode positioning experimental configuration. In Figure 61, a comparison is made between a discharge current power spectra taken in the cathode positioning and a discharge current power spectra taken during the axial plate biasing. For the axial plate bias and thruster body bias experimental configuration, the power spectra of each signal is averaged over 30 waveform captures. The averaging process has greatly reduced the noise floor and narrowed the full-width-half-maximum of the peaks in the power spectra as illustrated in Figure 61.

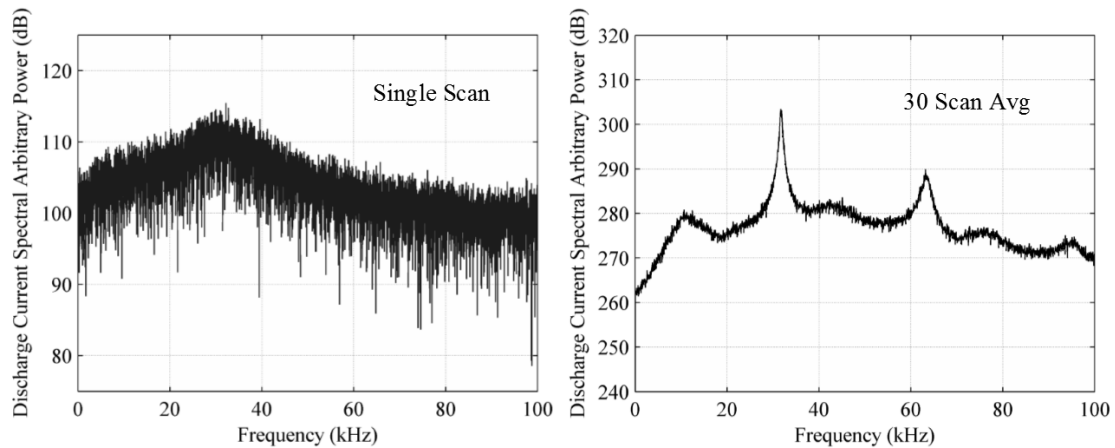


Figure 61: Side by Side Comparison of the Cathode Positioning Power Spectra and Axial Plate Power Spectra. Left) Power spectra of the discharge current using a single scan. The HET operating condition is 300 V, 3.1 kW. Right) Power spectra of the discharge current using a 30 scan average. The HET operating condition is 300 V, 3.4 kW.

5.2.3.1.1 Discharge Current Oscillations

The T-140 HET discharge current peak oscillation as a function of axial plate bias is shown in Figure 63. The secondary peak of the discharge current oscillation behavior is shown in Figure 64. The strongest frequency peak at 32.5 kHz (as shown in Figure 62) corresponds with the fundamental HET discharge breathing mode instability [59]. For all axial bias plate voltages, the total variation in discharge current primary peak oscillation frequency is less than 3% of the discharge current oscillation frequency at a grounded axial chamber plate voltage. There is a secondary primary peak in the discharge current power spectra at a frequency of 64.8 kHz. For all axial bias plate voltages, the total variation in discharge current secondary peak oscillation frequency is less than 4% of the discharge current oscillation secondary peak frequency at a grounded axial chamber plate voltage. Due to the various plasma modes operating in the discharge, determining which fundamental plasma instability mode the secondary power spectra peak frequency of the

discharge current corresponds to is difficult. When compared to the primary discharge current oscillation peak, the secondary discharge current oscillation peak has a spectral power that is an order of magnitude smaller. Both of these peaks are important to track as corresponding spectral peaks appear on the measured currents from the axial, radial, and thruster chamber plates.

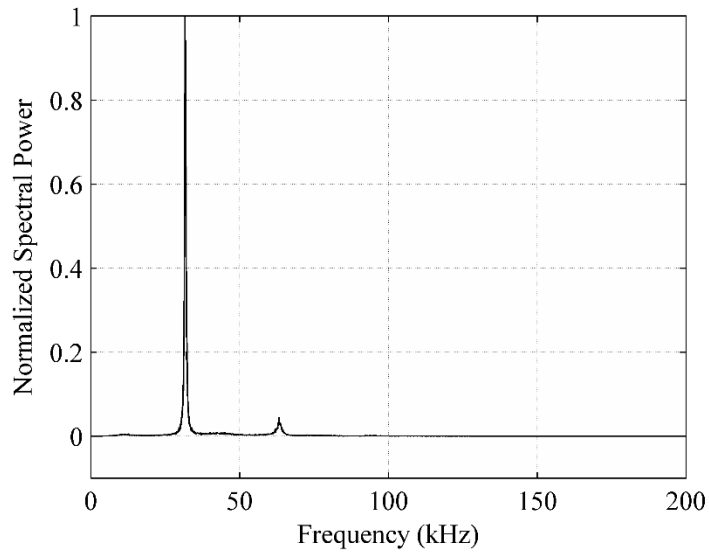


Figure 62: Discharge Current Power Spectra for the 300 V, 3.4 kW HET operating condition.

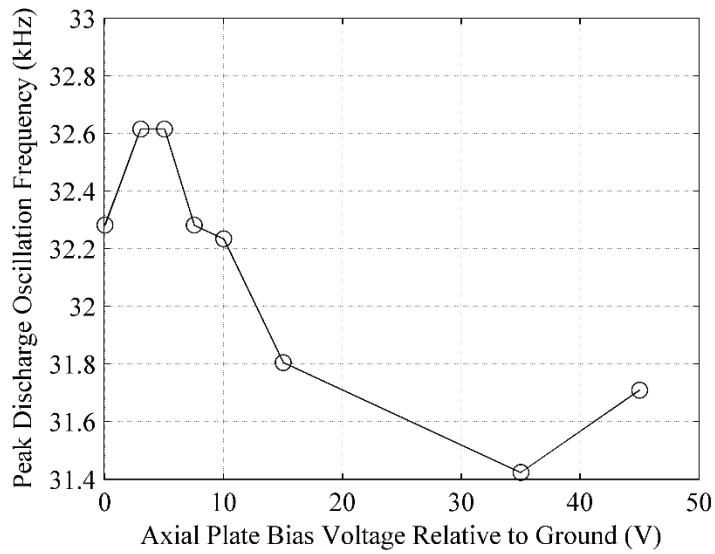


Figure 63: Discharge oscillation peak frequency as a function of axial plate bias voltage. The HET operating condition is 300 V, 3.4 kW.

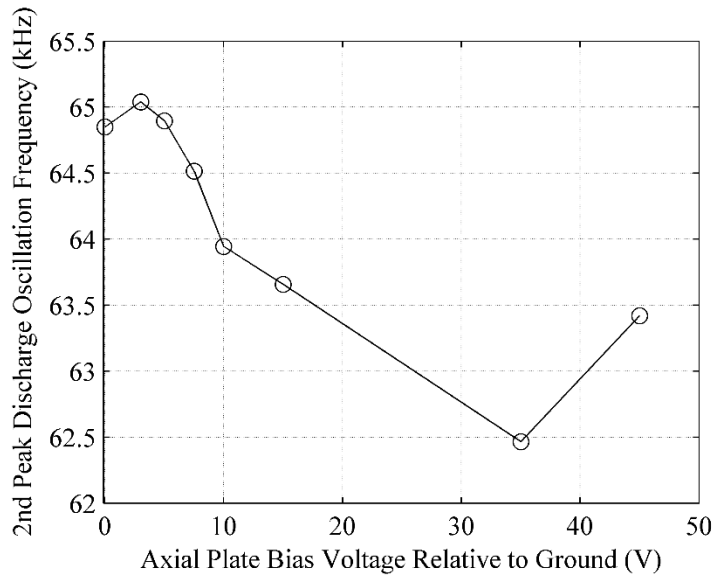


Figure 64: Discharge oscillation secondary peak frequency as a function of axial plate bias voltage. The HET operating condition is 300 V, 3.4 kW.

5.2.3.1.2 Axial Chamber Plate Oscillation Frequency Coupling

Figure 65 shows the axial plate power spectra primary and secondary peak as a function of axial plate bias voltage. Both the primary and second power spectra peak

frequency measured from the axial chamber plate have frequency shifts that are in lock-step with changes in the discharge current oscillation peak at each axial chamber plate bias tested. When compared to the primary power spectra peak, the secondary power spectra peak of the axial chamber plate current has a spectral power that is an order of magnitude smaller. The axial chamber plate power spectra peak behavior, in both frequency and spectral power, has the same characteristics as the discharge current oscillation behavior as a function of axial chamber plate bias voltage. This similarity in behavior suggests that the axial chamber plate time-resolved current is firmly coupled to the discharge current of the HET.

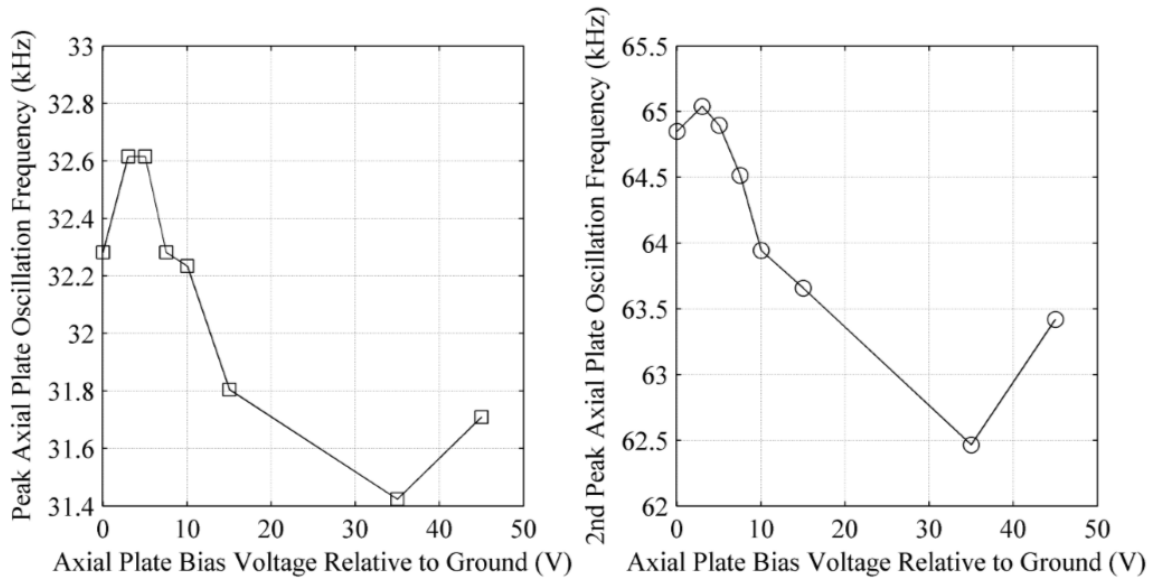


Figure 65: Axial plate current-to-ground power spectra peaks Left: Primary peak. Right: Secondary Peak. The HET operating condition is 300 V, 3.4 kW.

5.2.3.1.3 Radial Chamber Plate Oscillation Frequency Coupling

Figure 66 shows the primary and secondary power spectra peak of the radial chamber plate current-to-ground. The frequency behavior of the secondary power spectra peak is commensurate with the secondary power spectra peak frequency of both the axial

chamber plate and the HET discharge current. The primary peak frequency behavior of the radial chamber plate shows a distinctly different behavior than the HET discharge current oscillation current peak frequency behavior. At axial plate bias voltages above 15 V, the radial plate current-to-ground power spectra peak frequency shifts from being approximately 32 kHz to 142 kHz. As evidenced by the data presented for the discharge current primary peak frequency behavior (Figure 63), the 32 kHz peak closely corresponds to the HET discharge current oscillation. It is unclear from the data gathered as to what the 142 kHz peak corresponds to as none of the waveforms measured showed spectral power in this frequency range. As described in the time-averaged results section, at axial chamber plate bias voltages above 20 V relative to ground, the entire electron beam current of HET is collected by the axial chamber plate. At axial chamber plate bias voltages above 15 V relative to ground, it should be noted that there is still a power spectra peak of the radial chamber plate to ground at a frequency near 32 kHz, but its spectral power is an order of magnitude smaller than the spectral peak at 142 kHz. This change in dominant peak frequency at higher axial chamber plate bias voltages suggests that the radial chamber plate current-to-ground time-resolved behavior begins to decouple from the discharge current oscillations.

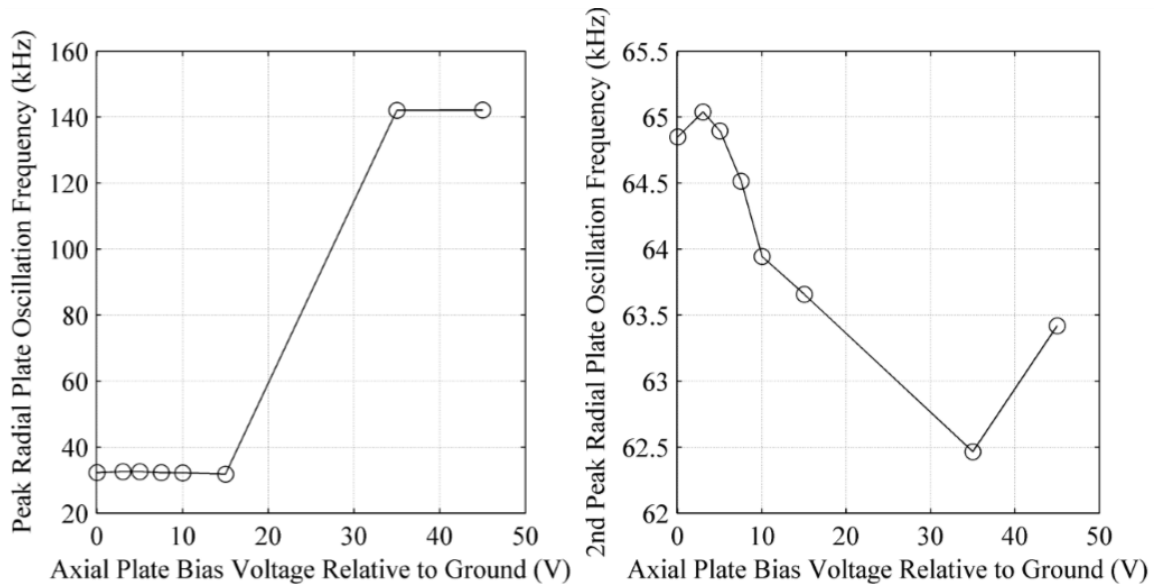


Figure 66: Radial plate current-to-ground power spectra peaks. The HET operating condition is 300 V, 3.4 kW. Left: Primary peaks. Right: Secondary peaks

5.2.3.1.4 Thruster Body and Thruster Body Plate Oscillation Frequency Coupling

Figure 67 shows the thruster body plates, TP2 and TP3 current collected power spectra peak frequency behavior, and the body to ground current collected power spectra peak frequency behavior. It is important to note that the “Body2GND” data set is from the current collected on the thruster body surfaces that are not TP1, TP2, or TP3. The total thruster body current to ground is not directly measured and so the power spectra analysis is not done for the total thruster body current to ground. The frequency of both the primary and secondary peaks as measured from the power spectra of TP2, TP3 and the Body2GND track the HET discharge current oscillation behavior shown in Figure 63 and Figure 64. At axial plate bias voltages above 40 V relative to ground, the TP2, TP3, and Body2GND primary and secondary peak frequency do not match the HET primary and secondary peak frequency behavior. Instead of the frequency rising 1-2% from axial bias plate voltages 35 V to 45 V relative to ground (see Figure 62 and Figure 63), the primary and secondary power spectra peak frequency remains constant. In general, however, the overall frequency

behavior of the primary and secondary power spectra peaks of the TP2, TP3, and Body2GND is similar to the discharge current oscillation behavior.

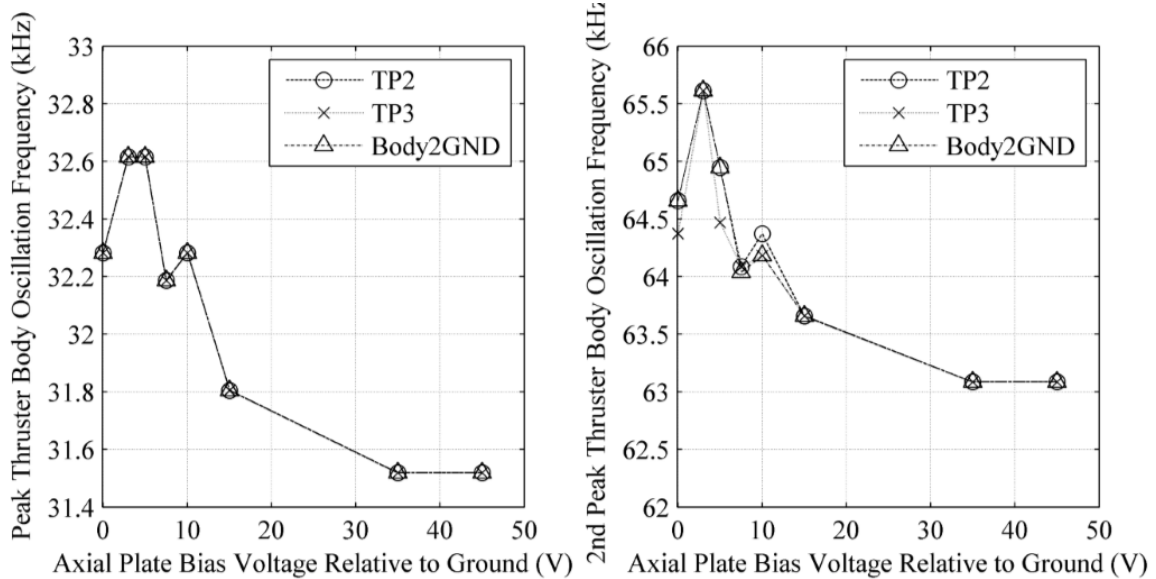


Figure 67: TP2, TP3, and thruster body current-to-ground power spectra peaks. The HET operating condition is 300 V, 3.4 kW. Left: Primary peaks. Right: Secondary peaks. It is important to note that the “Body2GND” data points are just the current collected on the thruster body surfaces that are not TP1, TP2, or TP3.

Figure 68 shows the primary and secondary power spectra peak frequency behavior of the thruster body plate TP1. The spectral peak frequency behavior of TP1 is very different than the behavior measured from TP2, TP3, and Bod2GND. Like the radial chamber plate, the primary spectral peak from TP1 shifts from the 32 kHz range to the 62 kHz range above axial chamber plate bias voltages of 15 V relative to ground. At an axial chamber plate bias voltage of 5 V relative to ground, there is a singular frequency shift. The primary spectral peak frequency changes from 32.7 kHz to 66.2 kHz and the secondary spectral peak frequency changes from 65.6 kHz to 44.1 kHz. It is unclear from the data collected as to why this singular change occurs. Overall, the TP1 primary and secondary

spectral peak frequency indicates that the TP1 decouples from the primary discharge oscillation frequency at axial chamber plate bias voltages above 15 V relative to ground.

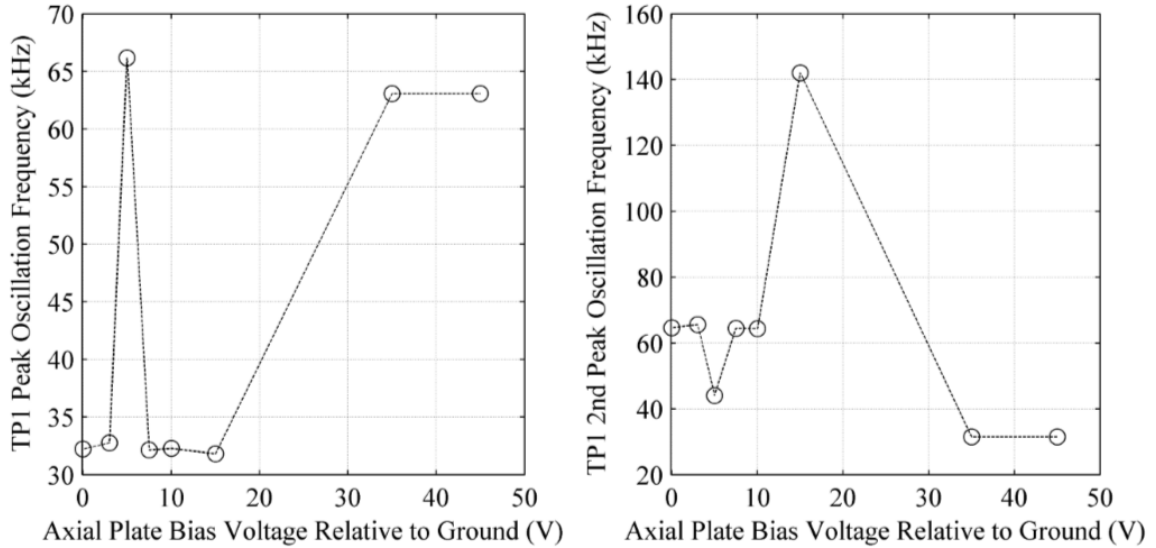


Figure 68: TP1 current-to-ground power spectra peaks. The HET operating condition is 300 V, 3.4 kW. Left: Primary Peak. Right: Secondary peaks.

5.2.3.3 Statistical Correlation and Time Delay Measurements

5.2.3.3.1 The Discharge Current Peak Event and Limits of Correlation

Entire waveform correlation coefficient calculations calculated between the discharge current and the other waveforms measured during the axial chamber biased plate experimental configuration revealed strong statistical correlation for all axial chamber plate biases. As experienced in the cathode positioning experimental configuration, time delays calculated based on the entire waveform lead to non-physical time delays. In order to compute an effective time delay, a more localized approach is taken. The waveform capture from the oscilloscopes are initiated by the largest discharge current peaks observed. This discharge current peaks occurred in temporally close groups and occurred once per waveform capture period. These peaks in the discharge current are referred to as the

“discharge current peak event” and a representative discharge current event is shown in Figure 69.

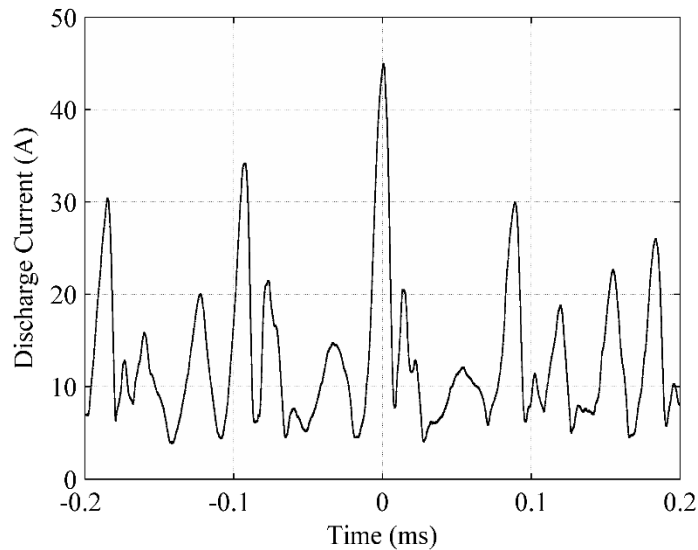


Figure 69: Representative discharge current peak event for the axial chamber plate bias configuration at an axial chamber plate bias voltage relative to ground of 0 V. The HET operating condition is 300 V, 3.4 kW.

Because of the extended length of the discharge current peak event as compared to the cathode positioning experimental configuration, the correlation coefficient calculations yield a lower computed value for all waveforms captured. By manually comparing the discharge current peak event and the computed segment of a measured waveform that yielded the time-delay measurement, it is revealed that statistical correlation coefficients with a magnitude greater than 0.4 yielded physically realistic time-delays.

5.2.3.3.2 Radial and Axial Chamber Plate Measurements

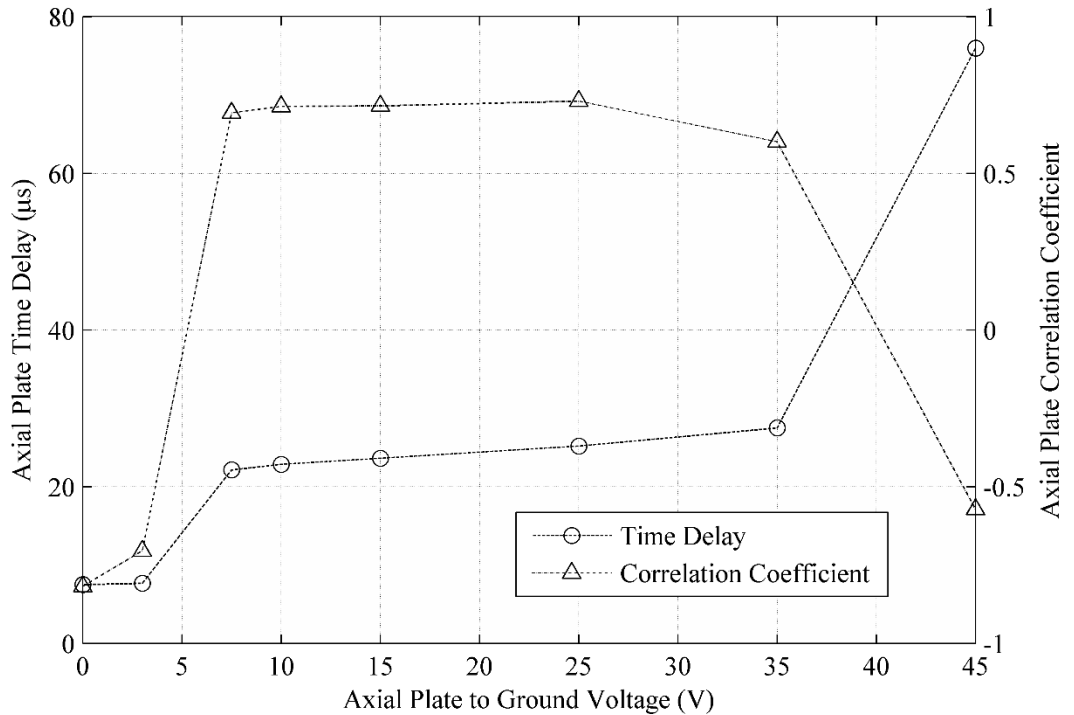


Figure 70: Axial chamber plate time delay and correlation coefficient. The HET operating condition is 300 V, 3.4 kW.

Figure 70 shows the time delay between the discharge current peak event and response measured in the axial chamber plate current. There are three distinct regions of time delay. When the axial chamber plate bias voltage relative to ground is below the floating voltage of the plasma, the measured time-delay is on the order of $5 \mu\text{s}$. When the axial chamber plate bias voltage relative to ground is between 7.5 V to 35 V, the measured time delay increases to be on the order of $25 \mu\text{s}$. At an axial chamber plate bias voltage relative to ground is at 45 V, the time delay measured increases to $76 \mu\text{s}$.

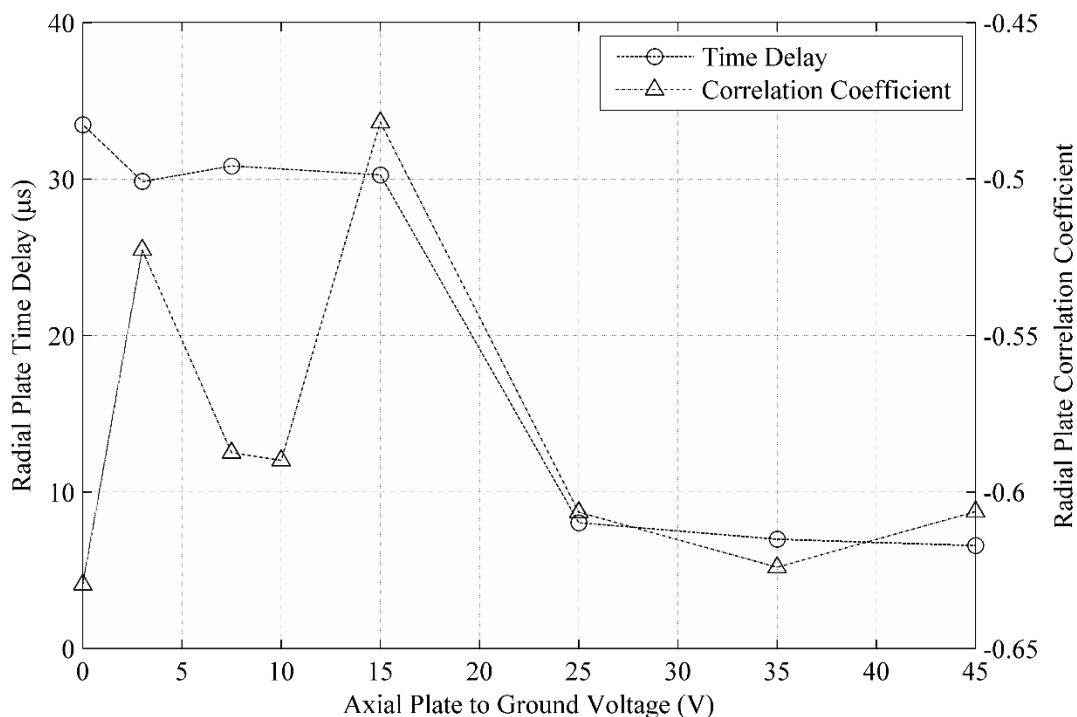


Figure 71: Radial Chamber plate time delay and statistical correlation. The HET operating condition is 300 V, 3.4 kW.

Figure 71 shows the time delay measured between the discharge current peak event and the response measured from the radial chamber plate current to ground and statistical correlation. The radial chamber plate time delay as a function of axial chamber plate bias has two distinct regions of behavior. While the axial chamber plate electron current collection is lower than the HET beam current, which occurs at an axial chamber plate bias voltage near 20 V, the measured time delay between the radial chamber plate current response and the discharge current event is on the order of 30 μs . Above an axial chamber plate bias of 20 V, the measured time delay between the radial chamber plate current response and the discharge current event decreases to be on the order of 7 μs .

5.2.3.3.3 Thruster Body Plates Measured Time Delay

Figure 72, Figure 73, and Figure 74 show the time delay measured between the discharge current peak event and the response measured from each of the thruster plates to ground and statistical correlation. The TP1 thruster body witness plate time delay shows the most sensitivity to changes in the axial chamber plate bias voltage. Barring the spike in time delay measured at an axial chamber plate bias voltage relative to ground of 7.5 V, the time delay between the discharge current peak event and the response measured on the TP1 thruster body plate decreases from the 6 μs range to the 0.4 μs range. The sign of the correlation coefficient shifts from being negative at low axial chamber plate bias voltages and positive at high axial chamber plate bias voltages. This transition occurs at an axial chamber plate bias voltage relative to ground between 15 V and 25 V. This is the same voltage range where the axial chamber plate is able to collect an electron current equal to the beam current of the HET.

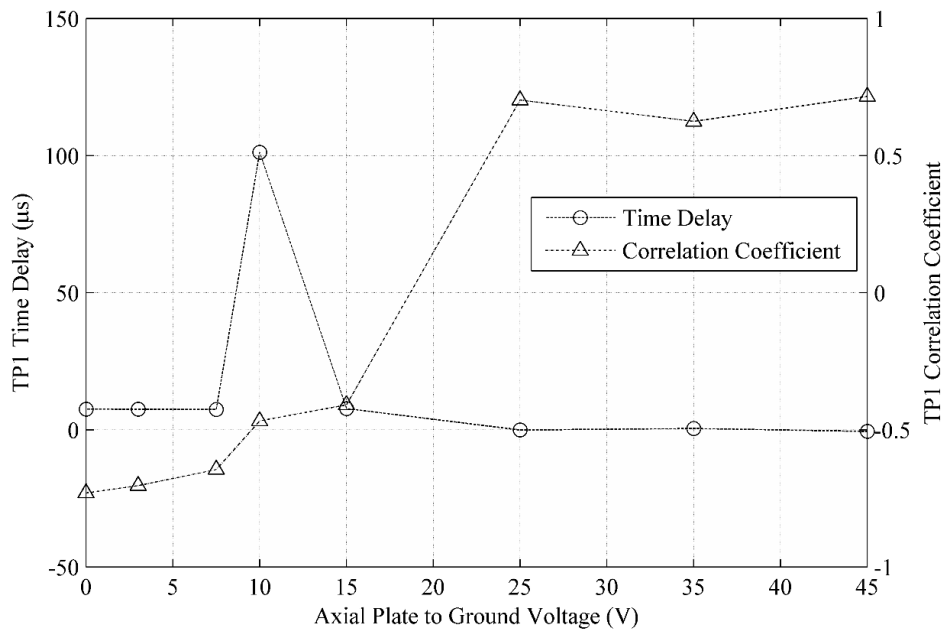


Figure 72: TP1 thruster body plate time delay and correlation coefficient. The HET operating condition is 300 V, 3.4 kW.

The TP2 and TP3 thruster body plates time delay has a much smaller sensitivity to the axial chamber plate than the TP1 thruster body plate. Throughout the entire axial chamber plate bias voltage range, the TP2 and TP3 have a 12% and 1% change between 0 V axial chamber plate bias relative to ground and an axial chamber plate bias relative to ground of 45 V. The time delays of the current response from TP2 and TP2 remain on the order of 8 μ s throughout the axial chamber plate bias voltage range.

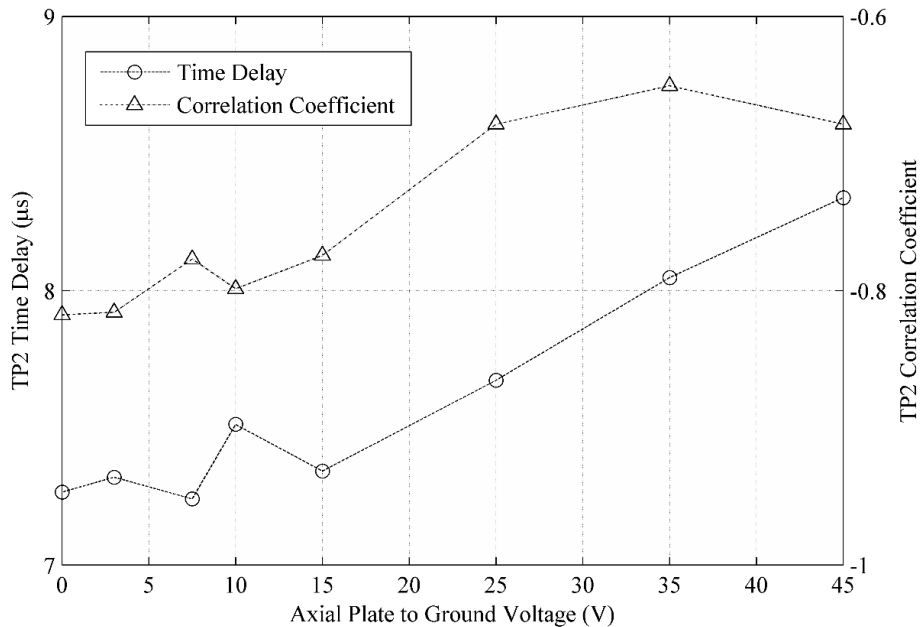


Figure 73: TP2 thruster body plate time delay and correlation coefficient. The HET operating condition is 300 V, 3.4 kW.

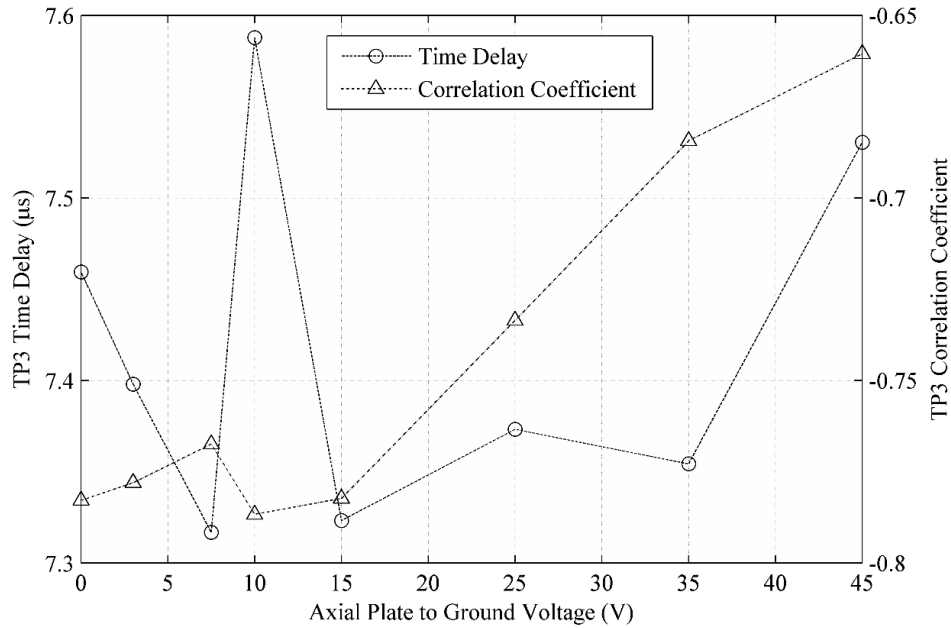


Figure 74: TP3 thruster body plate time delay and correlation coefficient. The HET operating condition is 300 V, 3.4 kW.

5.3 Thruster Body Biased Experimental Configuration

For this experimental configuration, the main goal is to examine how the thruster body recombination current pathway interacts with the HET electrical circuit. To manipulate the thruster body recombination current pathway, the HET thruster is operated at a fixed operating condition and the thruster body voltage relative to ground is altered. At each thruster body electrical resistance to ground, different aspects of the HET are measured and presented below. The section begins with an overview of the experimental layout of the configuration and then follows with the results of the cathode positioning experimental configuration.

5.3.1 Experimental Configuration

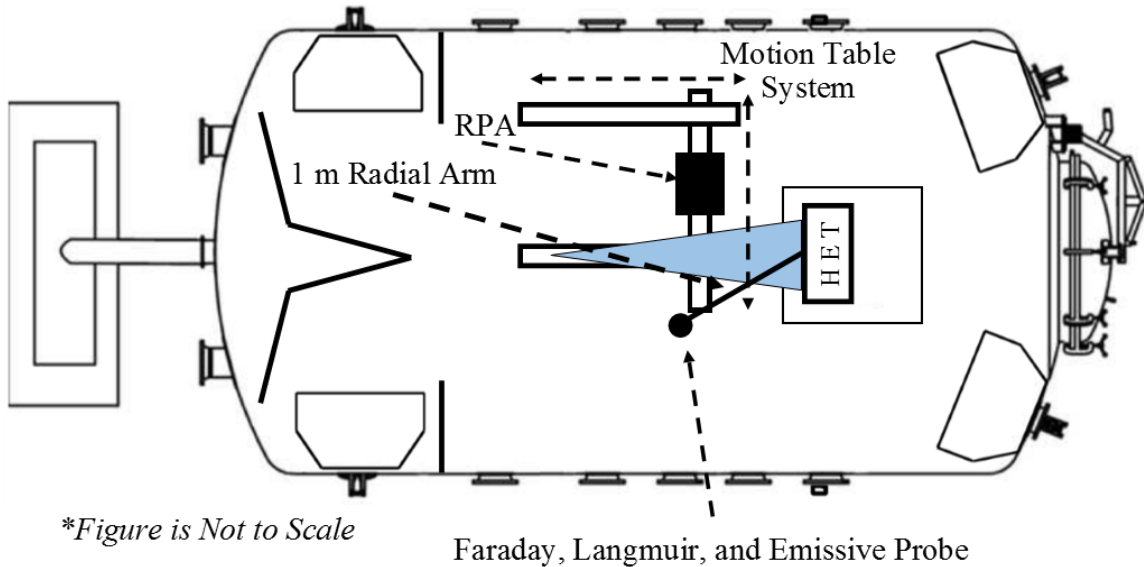


Figure 75: Overhead view of the vacuum chamber test facility, HET and probe diagnostics.

5.3.1.1 Thruster Body and Thruster Body Plate Electrical Configuration

Following a similar methodology as the axial chamber plate biasing, the voltage of the thruster body and the thruster body plates relative to ground are manipulated. In order to influence the thruster body recombination pathway, the voltage of the thruster body relative to the cathode-to-ground voltage is controlled. Since for normal HET operation in a vacuum facility, the cathode-to-ground voltage is negative, the thruster body must be biased negatively. Unlike the axial chamber plate bias experimental configuration, the thruster body and the thruster body plates could not be controlled to a negative voltage relative to ground with a power supply. Instead, the thruster body and thruster body plate voltage relative to ground is controlled in a much simpler manner. The work done in the cathode positioning experimental configuration (Figure 34) demonstrated that the thruster body, when electrically isolated from ground, floats to a negative potential of approximately -30 V. Between electrically grounded (0 V) and electrically floating (~30

V), the thruster body voltage goes from being positive relative to the cathode voltage to negative relative to the cathode voltage. When the thruster body is electrically grounded, the resistance to ground is essentially zero, and when the thruster body is electrically floating, the resistance to ground is essentially infinite. Therefore, for this experimental configuration, the thruster body and the thruster body plates voltage relative-to-ground is controlled by using two 50-W, 25- Ω ceramic variable resistors. To minimize any ground loop issues, the thruster body and thruster body plates are connected to the resistor and ground connection in a star configuration. The voltage of the thruster body is measured using a Teledyne Lecroy PP18 10:1 voltage divider. The current flow to ground for each of the thruster body plates is measured using Teledyne Lecroy CP30A High Sensitivity Active Current Monitors. The total thruster body current and thruster body plate current-to-ground is measured using a Teledyne Lecroy CP30 Active Current Monitor. It is important to note that the thruster body bias experimental configuration for the thruster body plates has a different electrical measurement configuration. Figure 76 shows the thruster body and thruster body plate electrical configuration. The main difference between this experimental configuration and the axial plate bias experimental configuration is that the total thruster body current-to-ground is measured. For the thruster body bias experimental configuration, the thruster body witness plates are examined in detail, and so the radial and axial chamber plates are not examined.

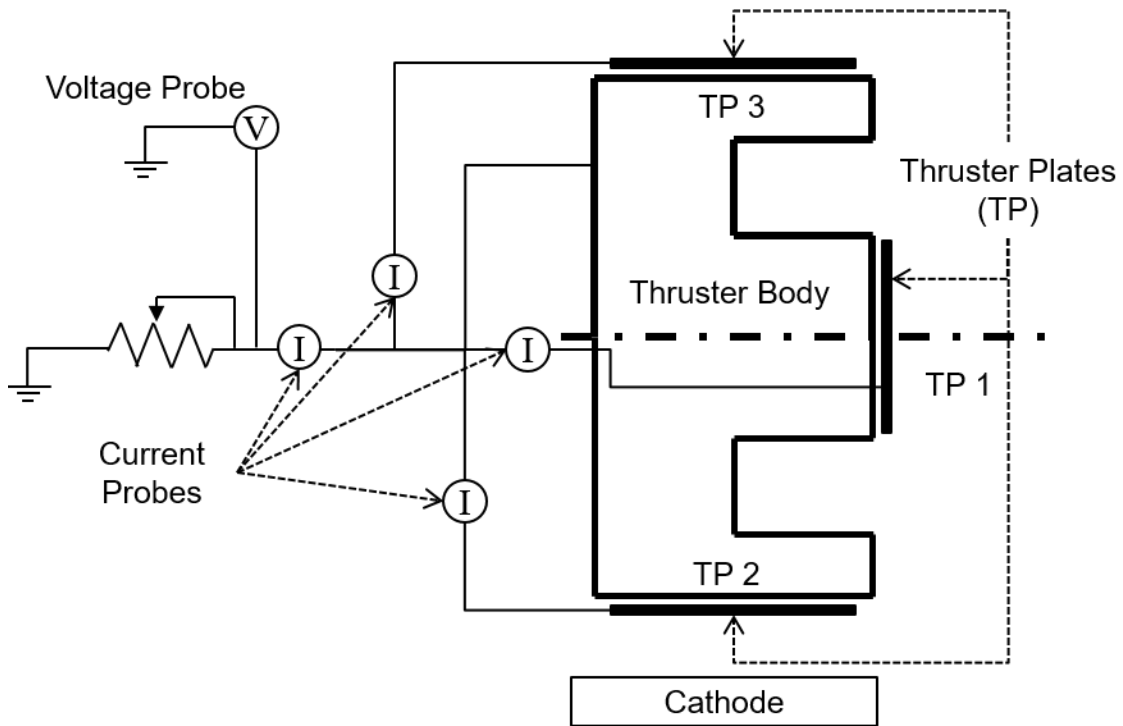


Figure 76: Thruster body and thruster body plate electrical configuration

5.3.1.2 Summary of Electrical Diagnostics Layout

Figure 77 shows a summary of the electrical diagnostic configuration collected for the biased thruster body configuration. Each indicated voltage or current measurement location is temporally resolved. To prevent ground loops, the thruster body and thruster body plates are connected to a single point ground in a star configuration.

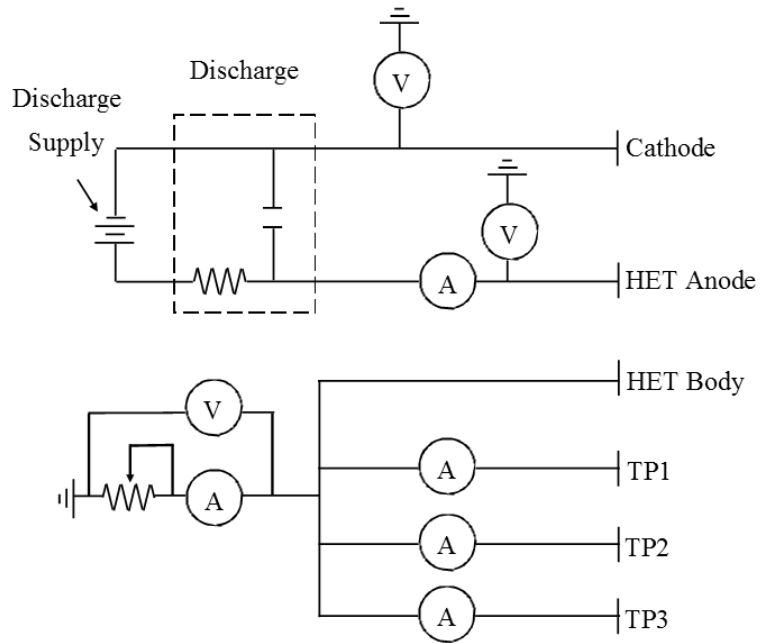


Figure 77: Electrical Diagnostics Diagram for Thruster Body Bias Experimental Configuration

5.3.1.3 T-140 HET Operating Conditions

All data was collected with the T-140 HET operating at a discharge voltage of 300 V, discharge power of 3.5 kW, an anode xenon flow rate of $11.6 \text{ mg/s} \pm 0.03 \text{ mg/s}$, and a cathode xenon flow rate of $1.61 \text{ mg/s} \pm 0.12 \text{ mg/s}$. The operating chamber pressure as measured by the external ion gauge is $8.7 \times 10^{-6} \text{ Torr-Xe}$, the operating chamber pressure as measured by the internal ion gauge is $1.3 \times 10^{-5} \text{ Torr-Xe}$. The thruster discharge voltage, inner and outer magnet currents, anode mass flow rate, and cathode mass flow rate were held constant for all cathode positions and plate configurations. The thruster was run through a 3-hour conditioning cycle prior to data collection in order to allow the thruster to approach thermal equilibrium [40]. The discharge current of the T-140 HET is measured using a Teledyne Lecroy CP150 current clamp (see Chapter 3 for technical specs). To be able to clearly measure the discharge oscillations, the discharge current is measured on the

thruster side of the discharge filter. The discharge voltage relative to ground is measured using a Teledyne Lecroy PPE2KV 100:1 voltage divider and the cathode-to-ground voltage is measured using a Teledyne Lecroy PPE2KV 100:1 voltage divider (see Chapter 3 for technical specs). These probes are placed at measurement points downstream of the discharge filter. Since the HET discharge circuit is a floating circuit, the discharge voltage of the HET is measured differentially as the difference between the discharge voltage relative to ground minus the cathode-to-ground voltage. For this experimental configuration, the HET discharge voltage measurement is time-resolved.

5.3.1.4 Probe Diagnostic Configuration

Plume diagnostics were taken along a $1 \text{ m} \pm 0.01 \text{ m}$ radius centered at the thruster centerline and discharge plane. Ion current density measurements occurred throughout a full range of 180° while emissive probes and Langmuir probes sweeps were taken at select angular positions based on the ion current density profile of the HET plume. Figure 75 shows a schematic overview of the plume diagnostics relative to the HET. The probe diagnostics were mounted to a Parker Daedal RT series 8-in rotary motion table. All three of the plume diagnostics: a Langmuir probe, JPL nude-style Faraday probe, and an emissive probe were attached in an array on radial probe arm. The arms of the array were angled such that probe-to-probe centerline linear distance was at $0.17 \pm 0.01 \text{ m}$ apart and remained at a 1 m radial distance throughout the probe arm sweep. Figure 78 shows the relative position of the diagnostics arm and Figure 79 shows a picture and notional diagram of the probe arrangement on the diagnostics arm. It should be noted that Figure 78 and Figure 79 are the same as Figure 51 and Figure 52 but are placed here in the document for clarity and convenience to the reader.

RPA measurements were taken along a $1 \text{ m} \pm 0.01 \text{ m}$ radius centered at the thruster centerline and discharge plane. Due to space constraints, the RPA could not be placed onto the radial arm that holds the emissive probe, Langmuir probe, and Faraday probe. Instead, the RPA is mounted to a 2-D Parker Daedal 406XR linear motion stage system. The table assembly has a 2,000 mm range of travel with a positional accuracy of $\pm 159 \mu\text{m}$. The motion stage is placed in the vacuum chamber such that it could cover the same 1 m arc that the emissive probe measurements were taken. Figure 75 shows the notional layout of the RPA and motion table system.

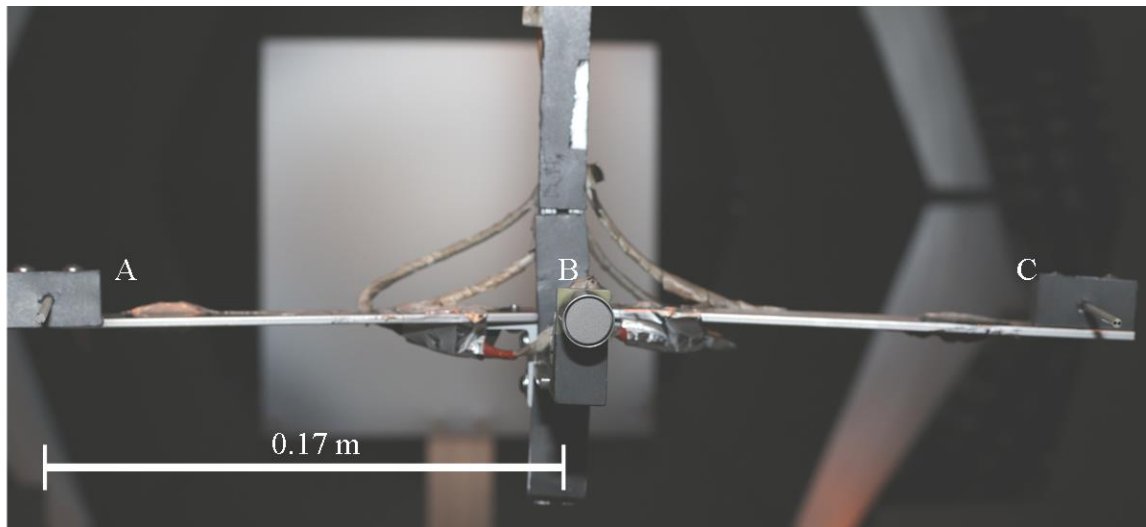


Figure 78: Probe arm with plume diagnostics attached A) Langmuir Probe B) Faraday Probe C) Emissive Probe.

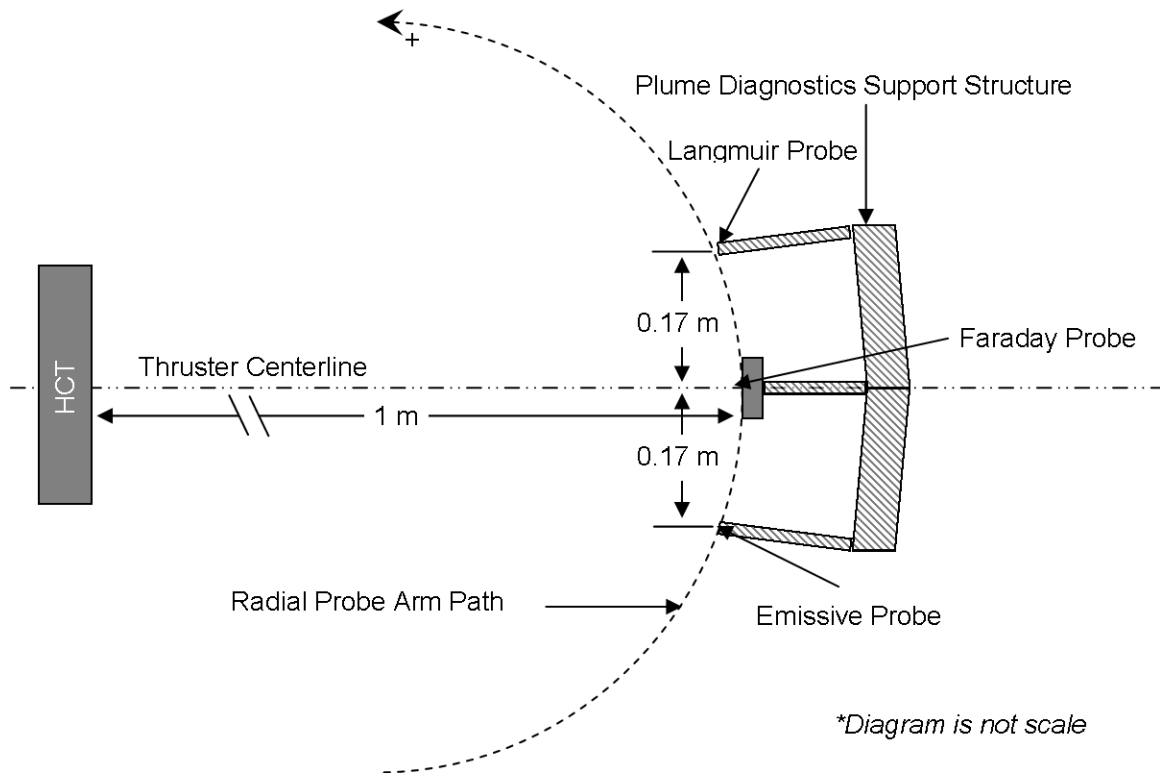


Figure 79: Overhead view of notional layout of the radial diagnostics probe arm.

5.3.2 Time Averaged Results

For the time averaged voltage and current measurements, the oscilloscopes are configured for a sampling rate of 125 MS/s and a sample length of 2 MS. The average voltages and currents presented below are the arithmetic average value over the 2 MS waveform length. As the real variable of concern for the thruster body bias experimental configuration is the thruster body-to-cathode voltage, each of the following results is plotted with respect to the thruster body-to-cathode voltage. For clarity, the cathode-to-ground voltage as a function of thruster body-to-ground voltage is shown in Figure 80.

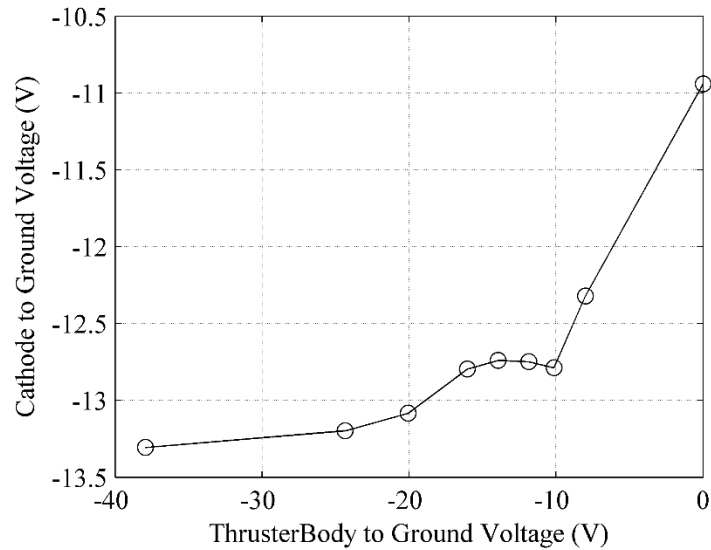


Figure 80: Cathode-to-ground voltage as a function of thruster body to ground voltage for the thruster body bias experimental configuration. The HET operating condition is 300 V, 3.5 kW. Error bars are encompassed by plot markers.

5.3.2.1 Effect of the Thruster Body Bias on HET Thrust and Plume

In general, the measurements of the thrust produced by the HET and the resulting plume characteristics did not show any variation in properties outside of the measurement uncertainty with changes in the thruster body bias voltage. The measured thrust of the HET maintained $187 \text{ mN} \pm 3 \text{ mN}$ for all thruster body bias voltages tested. The measurement of the electron temperature, plasma potential, and plasma number density across the plume did not show any variation outside of the measurement uncertainty. Measurements of the ion energy distribution function at various locations in the plume did not show any variation dependent on thruster body bias voltage outside the measurement uncertainty. Measurements of the ion current density profile also did not show any variation dependent on the thrust body bias voltage outside the measurement uncertainty.

5.3.2.1 Electrical Characteristics of HET and Thruster Body Plates

5.3.2.2.1 T-140 Discharge Current

Figure 81 shows the average of the discharge current of the HET as a function of thruster body-to-cathode voltage. As the thruster body-to-cathode voltage grows more negative from 11.12 V to -6.37 V, the average discharge current decreases from 11.68 A to 11.49 A. At a thruster body-to-cathode voltage of -25.5 V, the average of the discharge current rises to 11.81 A. At this thruster body voltage, the thruster body is electrically floating and the floating voltage of the thruster relative to ground is -38.55 V.

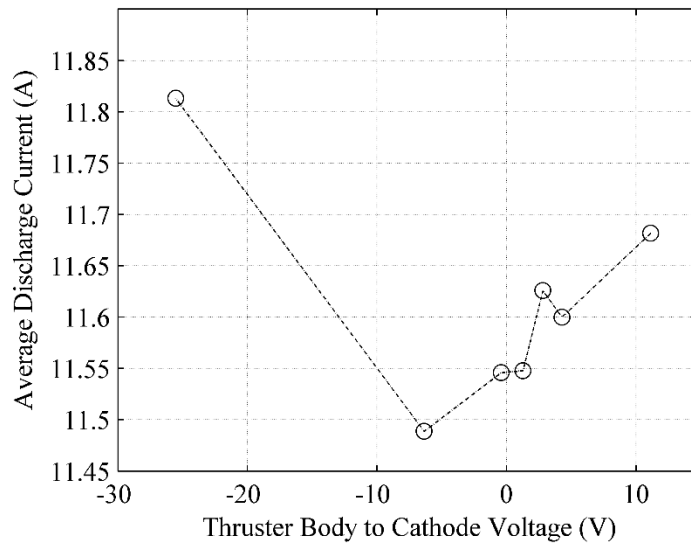


Figure 81: Discharge current average as a function of thruster body-to-cathode voltage. The HET operating condition is 300 V, 3.5 kW. Error bars are encompassed by plot markers.

5.3.2.2.2 Thruster Body Plates and Total Thruster Body Current

Figure 82, Figure 83, Figure 84, and Figure 85 show the current collection on the thruster body and thruster body plates TP1, TP2, and TP3 as a function thruster body-to-cathode voltage, respectively. It should be noted that the thruster body electrically floating condition is omitted from the following data current data. At an electrically floating

condition, there is no net current allowed to flow. The total thruster body current shown in Figure 82 is total collective current on the thruster body plates and on the thruster body surfaces not covered by the thruster body plates. In the thruster body grounded or a thruster body-to-cathode voltage of 11.12 V configuration, the combined current collected on the thruster body plates constitutes less than 2% of the total current collected on the thruster body. As expected the total thruster body current decreases as the negative bias increases. This is because the thruster body approaches the floating voltage, where the electrical boundary condition prevents a net flux of charge on the conductive surface. In general, the thruster body plates TP2 and TP3 exhibit a similar average current collection thruster body voltage behavior as the entire thruster body current behavior. For thruster body plates TP2 and TP3, the current collection is negative throughout the thruster body-to-cathode bias voltages, which is indicative of a net flux of electrons collected on the thruster body plates. For thruster body plate TP1 (as shown in Figure 83), the average current collected switches sign between thruster body-to-cathode voltages of 4.28 V and 2.80 V. At thruster body-to-cathode voltages above 4.28 V, the collected current is negative, indicating a net flux of electrons incident on the thruster body plate. At thruster body-to-cathode voltage below 2.80 V, the collected current is positive meaning that the thruster body plate TP1 collects a net flux of positive charges (ions).

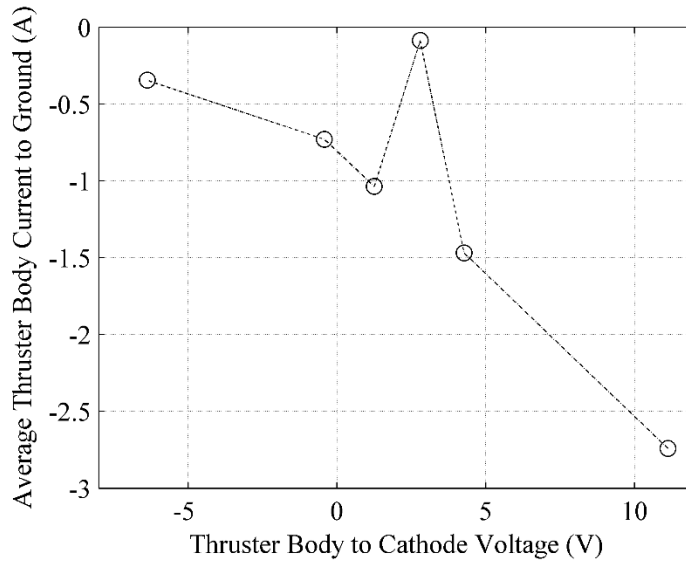


Figure 82: Total thruster body current-to-ground as a function of thruster body-to-cathode voltage. The HET operating condition is 300 V, 3.5 kW. Error bars are encompassed by plot markers.

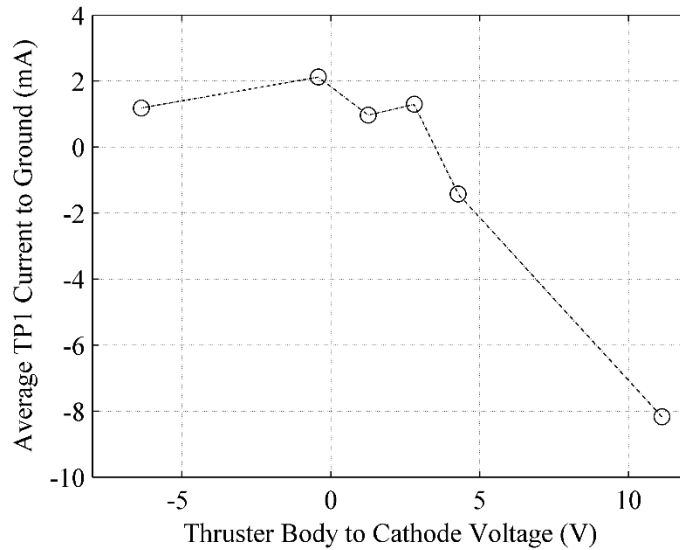


Figure 83: Average TP1 current-to-ground as a function of thruster body-to-cathode voltage. The HET operating condition is 300 V, 3.5 kW. Error bars are encompassed by plot markers.

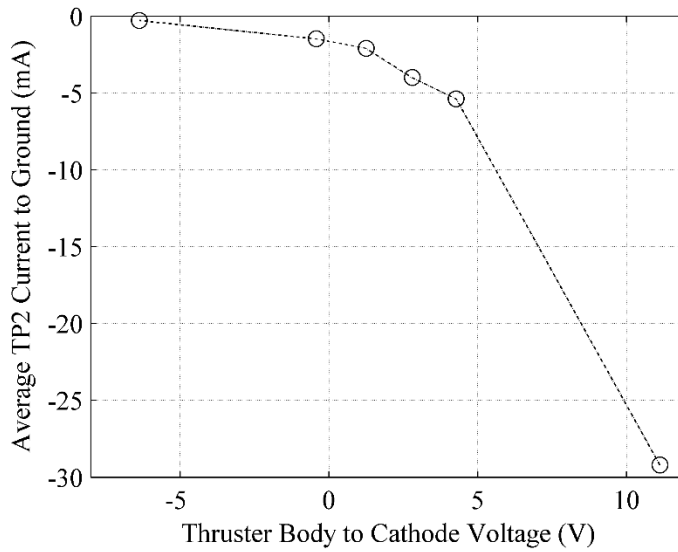


Figure 84: Average TP2 current-to-ground as a function of thruster body-to-cathode voltage. The HET operating condition is 300 V, 3.5 kW. Error bars are encompassed by plot markers.

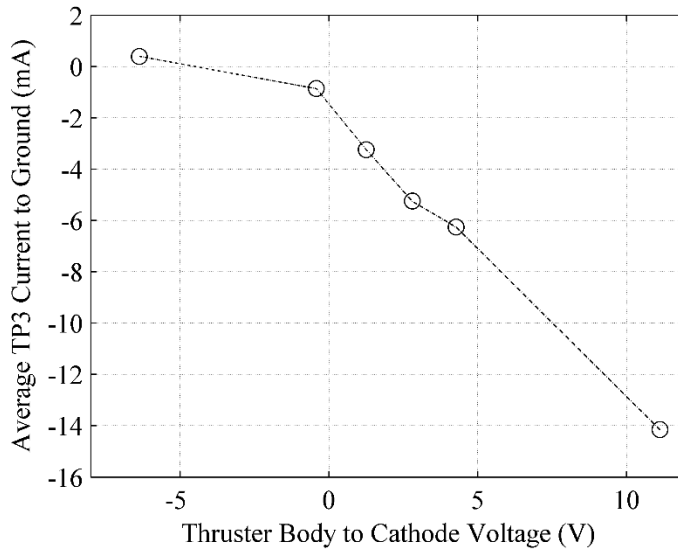


Figure 85: Average TP3 current-to-ground as a function of thruster body-to-cathode voltage. The HET operating condition is 300 V, 3.5 kW. Error bars are encompassed by plot markers.

5.3.3 Time-Resolved Results

As discussed in the Experimental Approach chapter, Chapter III, the thruster body voltage relative to ground is controlled, and the goal of the experimental configuration is to be able to control the voltage of the thruster body relative to the cathode-to-voltage of the HET. The results presented in the following section are plotted with respect to the thruster body voltage relative to the cathode-to-ground voltage of each testing condition. Figure 86 shows the cathode-to-ground voltage as function of the thruster body to ground voltage. The crossover point, where the thrust body voltage relative to ground becomes more negative than the cathode-to-ground voltage occurs between a thruster body voltage relative to ground of -11.86 V and -13.95 V and the corresponding cathode-to-ground voltage of -12.75 V and -12.74 V, respectively. It is important to note that the largest thruster body bias occurred when the thruster body and thruster body plates are electrically floating. The corresponding thruster body bias voltage relative to ground and the cathode-to-ground voltage is -37.9 V and 13.3 V, respectively.

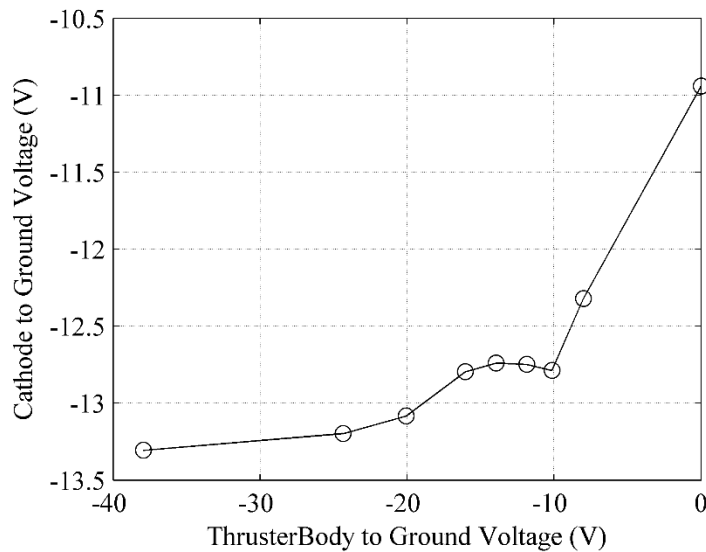


Figure 86: The cathode-to-ground voltage of the HET electrical circuit as a function of the Thruster body to ground voltage. The HET operating condition is 300 V, 3.5 kW. Error bars are encompassed by plot markers.

5.3.3.1 Peaks of Power Spectra

5.3.3.1.1 Discharge Current Oscillations of the HET

Figure 87 and Figure 88 show the primary and secondary power spectra peak frequency of the discharge current, respectively. The primary spectral peak occurs in 30 kHz range and the frequency is commensurate with the HET breathing mode discharge oscillation [59]. The secondary spectral peak occurs 60 kHz range, and as described in the axial chamber plate bias experimental configuration section, the particular HET discharge instability plasma mode is difficult to determine exactly. The secondary spectral peak of the HET discharge current has a spectral power that is an order of magnitude smaller than the primary spectral peak of the HET discharge current. With both of these HET plasma modes, they both show a thruster body bias voltage behavior that has two distinct regions. When the thruster body voltage relative to the cathode-to-ground voltage is positive, the primary and secondary spectral peak frequencies have an increasing monotonic behavior. When the thruster body bias voltage relative to the cathode-to-ground voltage is negative, the primary and secondary spectral peak frequencies have decreasing overall behavior. The behavior of both spectral peaks is important to keep in mind when examining the results of the thruster body plates described further below.

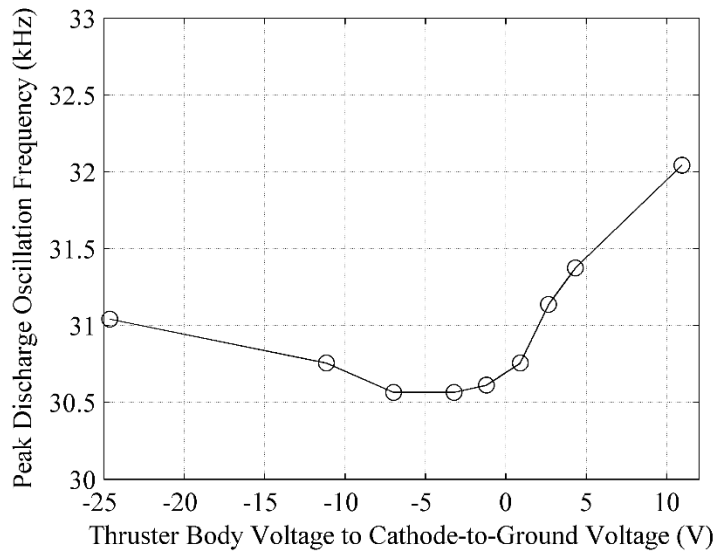


Figure 87: Peak of the discharge current power spectra for the thruster body bias experimental configuration. The HET operating condition is 300 V, 3.5 kW.

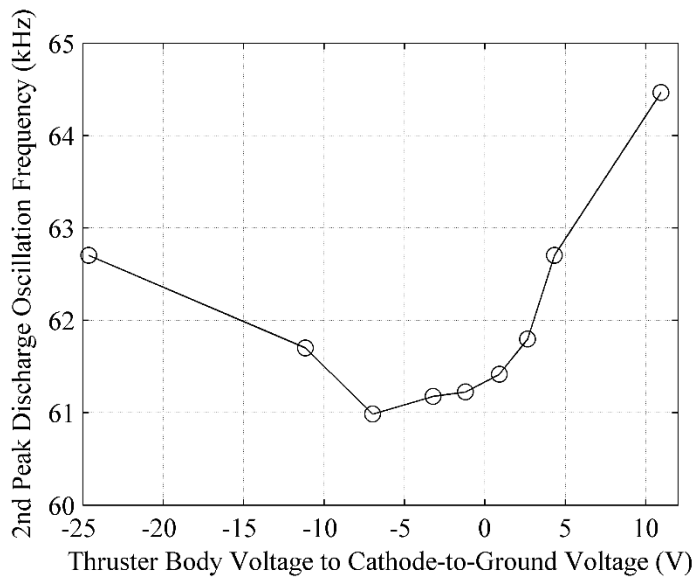


Figure 88: Secondary Peak of the discharge current power spectra for the thruster body bias experimental configuration. The HET operating condition is 300 V, 3.5 kW.

5.3.3.1.2 Thruster Body and Thruster Body Plates

The thruster body plates: TP1, TP2, and TP3 and the total thruster body current-to-ground primary and secondary spectral peak frequency behavior is shown in Figure 89 through Figure 96. Each of the thruster body plates experience a very different thruster body bias voltage spectral peak frequency behavior. The TP1 spectral peak frequency response (shown in Figure 89 and Figure 90) to the thruster body bias voltage matches closely the HET discharge current spectral peak frequency response behavior. The TP2 spectral peak frequency response behavior is different between the primary and secondary spectral peaks. The TP2 primary spectral peak frequencies are bi-modal. The primary peak frequency response alternates between the 30 kHz range to the 60 kHz range. The 30 kHz range frequency corresponds to the primary spectral peak observed in the discharge current power spectra, and the 60 kHz range frequency corresponds to the secondary spectral peak observed in the discharge current power spectra. When the thruster body-to-cathode voltage is positive, the TP2 measures a primary spectral peak frequency in the 30 kHz range. When the thruster body-to-cathode voltage is negative, the TP2 measures a primary spectral peak frequency in the 60 kHz range. Near the crossover thruster body-to-cathode voltages, there is a transition regime, where the primary spectral peak frequency has a large sensitivity to the thruster body-to-cathode voltage. The secondary spectral peak frequency of TP2 has a similar bi-modal behavior with regards to positive and negative thruster body voltages relative to cathode. Near the crossover point, the secondary spectral peak frequencies of TP2 exhibit a similar transition regime as the primary spectral peak frequency, but at thruster body-to-cathode voltage of 0.88 V, the secondary spectral peak frequency of TP2 rises to 92.4 kHz. There is not a prominent spectral peak in the corresponding discharge current power spectra at that frequency.

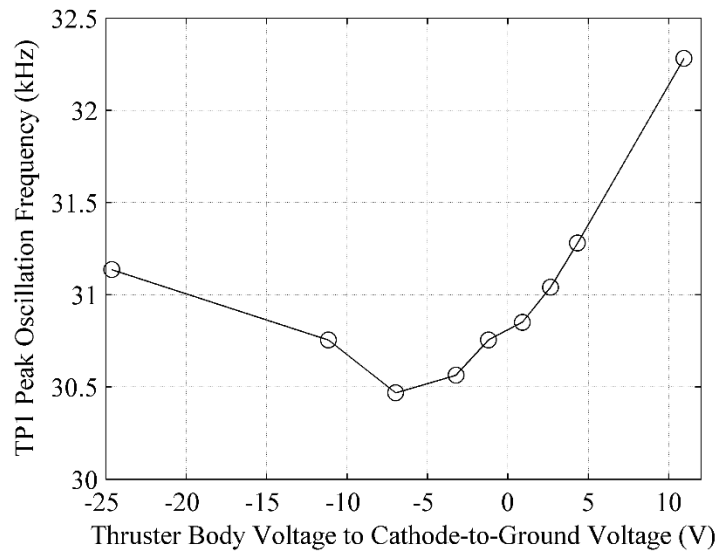


Figure 89: Primary Peak of the TP1 Current-to-ground power spectra. The HET operating condition is 300 V, 3.5 kW.

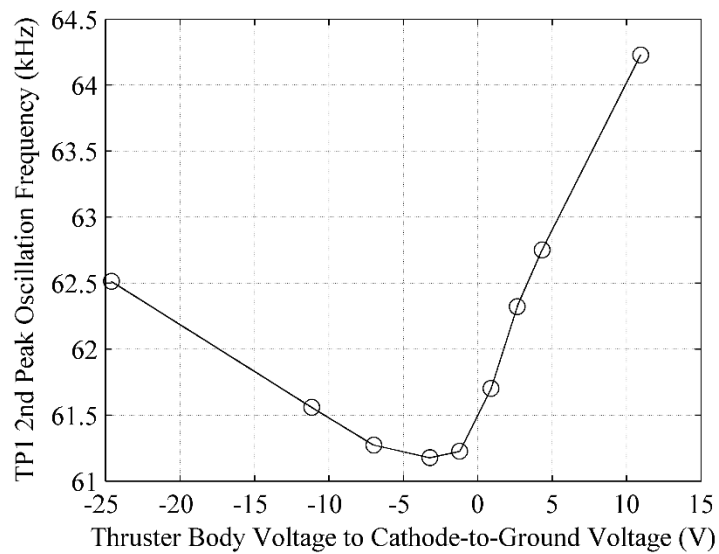


Figure 90: Secondary Peak of the TP1 current-to-ground power spectra. The HET operating condition is 300 V, 3.5 kW.

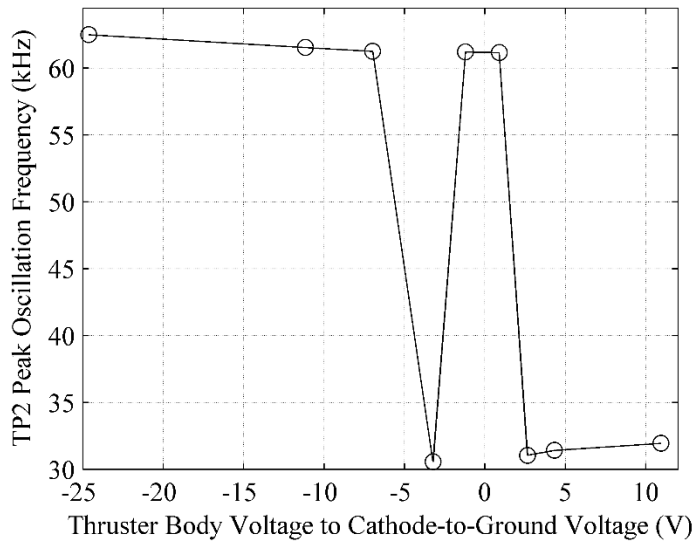


Figure 91: Primary Peak of the TP2 Current-to-ground power spectra. The HET operating condition is 300 V, 3.5 kW.

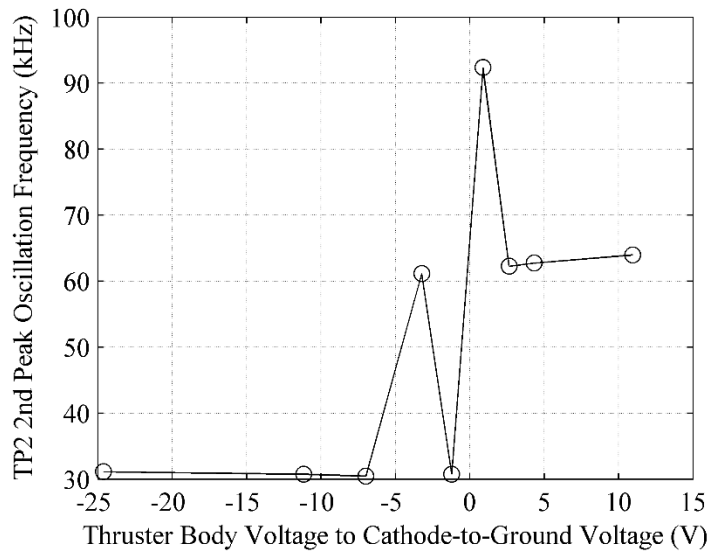


Figure 92: Secondary Peak of the TP2 current-to-ground power spectra. The HET operating condition is 300 V, 3.5 kW.

The primary and secondary spectral peak frequency response of TP3 (Figure 93 and Figure 94) to the thruster body-to-cathode voltage exhibits a similar bimodal behavior as TP2. The crossover voltage behavior for TP3 through is different than TP1 or TP2. At positive thruster body-to-cathode voltages, the primary and secondary spectral peak

frequencies closely match what is measured in the discharge current power spectra primary and secondary peaks. At negative thruster body-to-cathode voltages, the primary and secondary power spectra peak frequencies of TP3 swap frequencies. The primary power spectra peak frequencies rises to the 60 kHz range, while the secondary primary power spectra peak frequencies lowers to the 30 kHz range.

The total thruster body current-to-ground power spectra peaks (Figure 95 and Figure 96) closely follow the HET discharge current primary and secondary spectral peaks closely. The only major frequency shift occurs when the thruster body electrical connection is completely floating. This corresponds to a thruster body-to-cathode voltage of -37.9 V. At this thruster body voltage, the primary spectral peak frequency shifts to the 60 kHz range and the secondary spectral peak frequency shifts to the 30 kHz range.

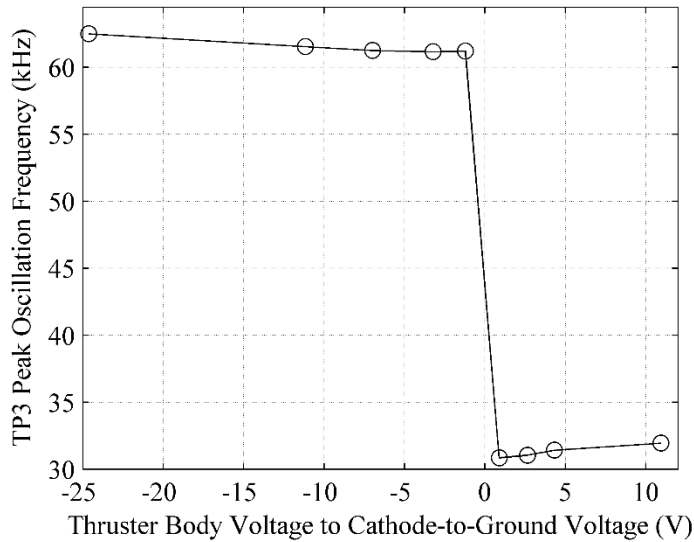


Figure 93: Primary Peak of the TP3 Current-to-ground power spectra. The HET operating condition is 300 V, 3.5 kW.

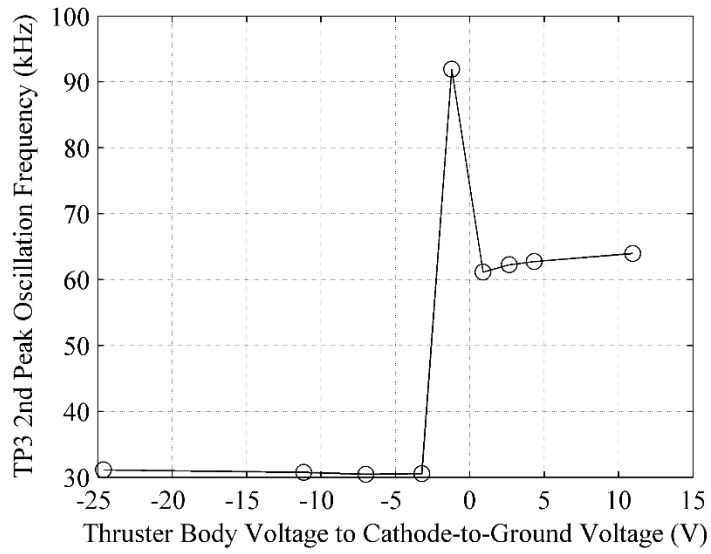


Figure 94: Secondary Peak of the TP3 current-to-ground power spectra. The HET operating condition is 300 V, 3.5 kW.

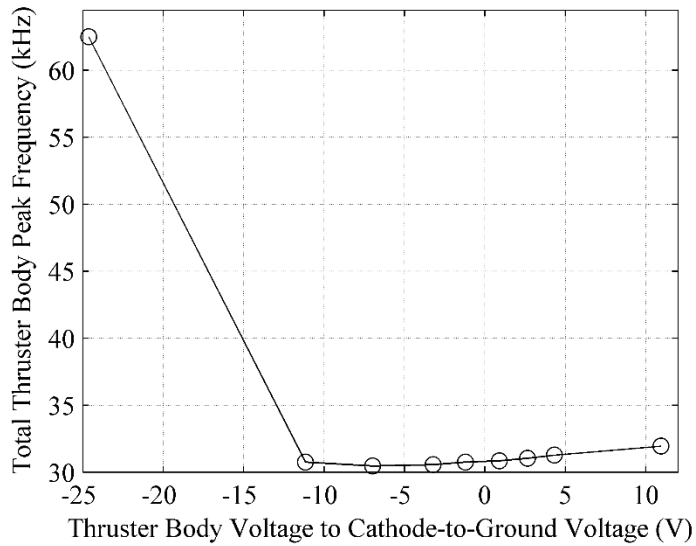


Figure 95: Primary Peak of the total thruster body current-to-ground power spectra. The HET operating condition is 300 V, 3.5 kW.

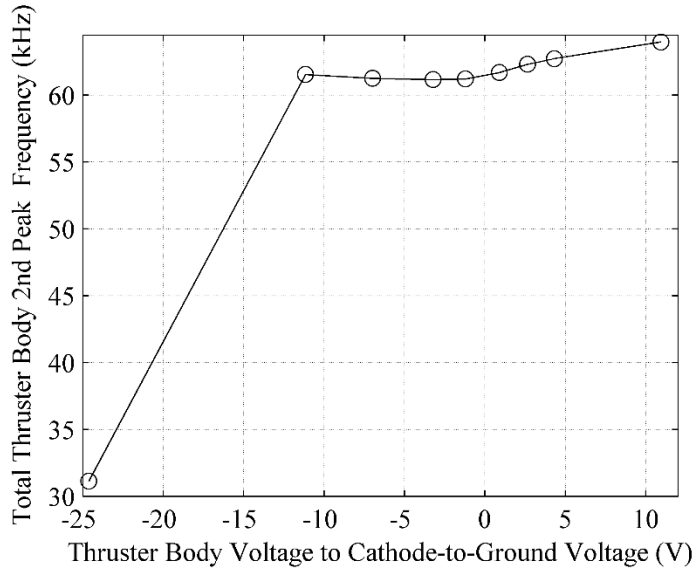


Figure 96: Secondary Peak of the total thruster body current-to-ground power spectra. The HET operating condition is 300 V, 3.5 kW.

5.3.3.2 Peak to Peak and Standard Deviation of Signals

In the results presented above, the power spectra of the electrical waveforms measured are discussed. In the following section, the peak to peak and the standard deviation of the electrical waveforms are presented. This another time resolved aspect of the waveforms that captures the strength of fluctuations of a signal.

5.3.3.2.1 HET Discharge Current

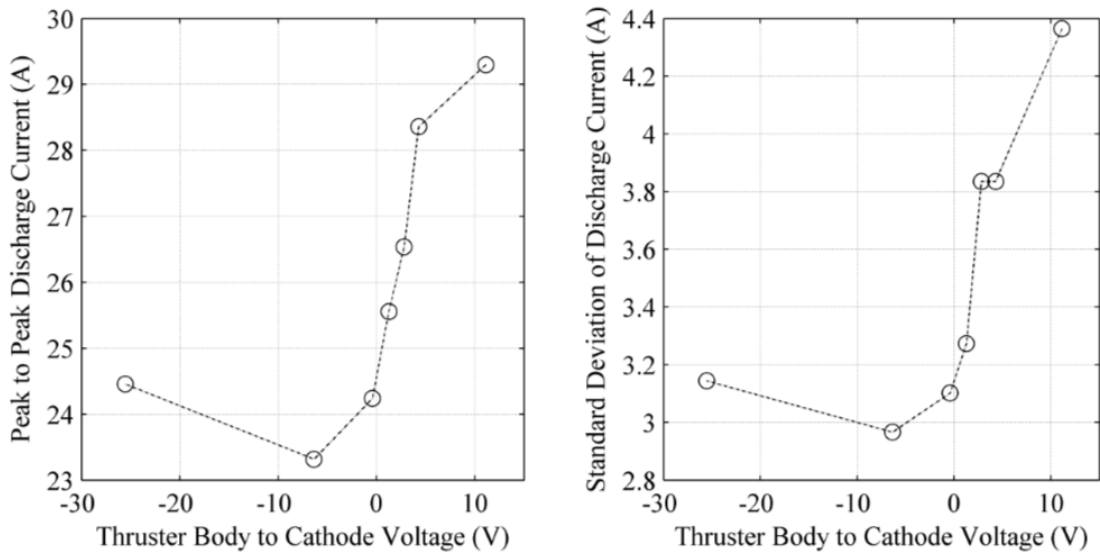


Figure 97: Discharge current fluctuations as a function of thruster body-to-cathode voltage. The HET operating condition is 300 V, 3.5 kW. Left: Discharge current peak to peak. Right: Discharge current standard deviation.

Figure 97 shows the discharge current peak-to-peak and standard deviation as a function of thruster body-to-cathode voltage. These measurements capture the strength of the fluctuations in the discharge current. The peak-to-peak values are indicative of momentary fluctuations, and the standard deviation is more of a measure the general trend of the fluctuations throughout the capture period. Excluding the highest thruster body-to-ground voltage, both of the discharge current peak to peak and the standard deviation of the discharge current show a decrease as the thruster body bias becomes more negative. At the crossover point, where the thruster body voltage transitions between positive and negative, the behavior of the discharge current changes. While the thruster body-to-cathode voltage remains positive, the discharge current peak-to-peak and the standard deviation have a high sensitivity to changes in the thruster body-to-cathode voltage bias. When the thruster body-to-cathode voltage becomes negative, the discharge current fluctuations become less sensitive to changes in the thruster body-to-cathode bias voltage.

5.3.3.2.2 Thruster Body Plates

Figure 98, Figure 99, Figure 100, and Figure 101 show the thruster body's and the thruster body plates' peak-to-peak current and standard deviation of the current collected. Since the thruster body plates and thruster body are all electrically connected, the total thruster body current shown in Figure 98 sets the upper-limit for the intensity of the fluctuations of the thruster body plate currents. As the thruster body-to-cathode voltage becomes more negative, the total thruster body current peak to peak current and standard deviation current decreases. Overall, the general current trend of the thruster body plates track the discharge current peak-to-peak and standard deviation. The thruster body plate TP1, as shown in Figure 99, has a distinctly different thruster body-to-cathode voltage behavior as compared to the thruster body plates TP2 and TP3. For TP1, the biggest decrease in the peak-to-peak current and the standard deviation of the current occurs when the thruster body goes from 11.12 V to 4.27 V relative to the cathode. This corresponds to the thruster body being connected directly to ground and the thruster body being connected to ground through the variable resistor. For the thruster body plates TP2 and TP3, as shown in Figure 100 and Figure 101, the crossover point in thruster body-to-cathode voltage better delineates the overserved trends. Starting from 11.12 V, as the thruster body-to-cathode voltage approaches the crossover point, the peak-to-peak and standard deviation current decrease. Past the crossover point, the peak-to-peak current and standard deviation current begin to increase. This behavior tracks the observed trends in the discharge current peak-to-peak and standard deviation.

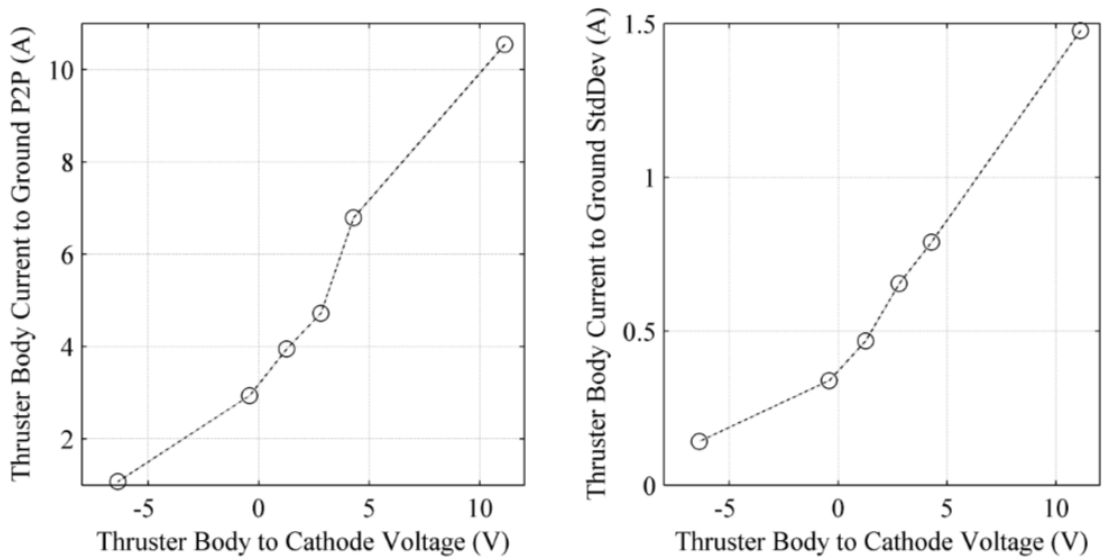


Figure 98: Left) Total thruster body current-to-ground peak to peak. Right) Total Thruster body current-to-ground standard deviation. The HET operating condition is 300 V, 3.5 kW.

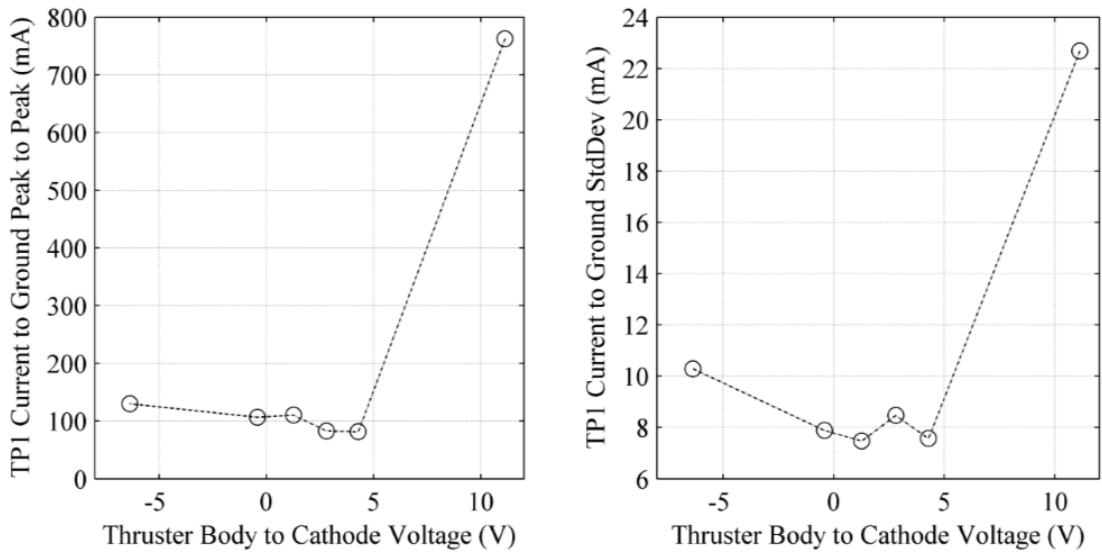


Figure 99: TP1 current-to-ground peak to peak (left) and standard deviation (right). The HET operating condition is 300 V, 3.5 kW.

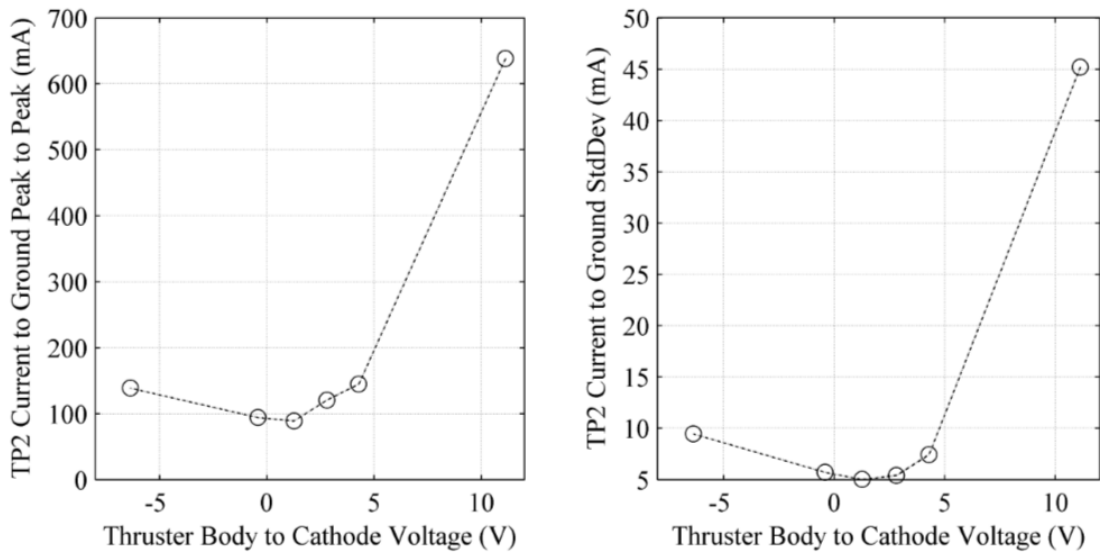


Figure 100: TP2 current-to-ground peak to peak (left) and standard deviation (right). The HET operating condition is 300 V, 3.5 kW.

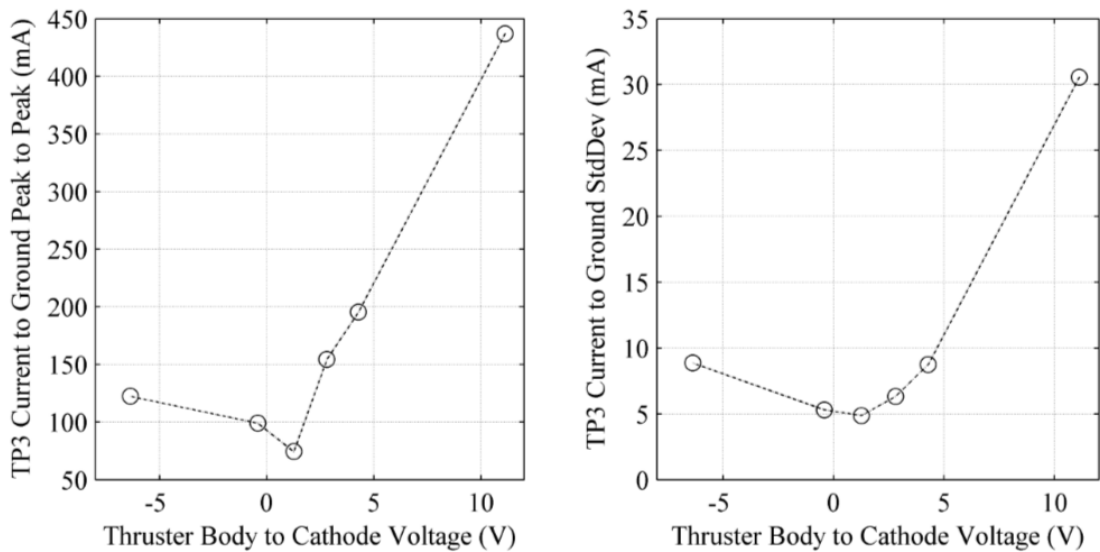


Figure 101: TP3 current-to-ground peak to peak (left) and standard deviation (right). The HET operating condition is 300 V, 3.5 kW.

5.3.3.3 Time Delay and Correlation of the Thruster Body Plates

5.3.3.3.1 Discharge Peak Event

As demonstrated in the other waveform analysis, the correlation coefficient calculations performed between the entire measured waveforms and the entire discharge current waveform always yielded statistically strong correlations and a null time-delay. The following time delay calculations and the correlation coefficient are performed with respect the discharge current peak event. For clarity, a representative discharge current peak event is shown in Figure 102.

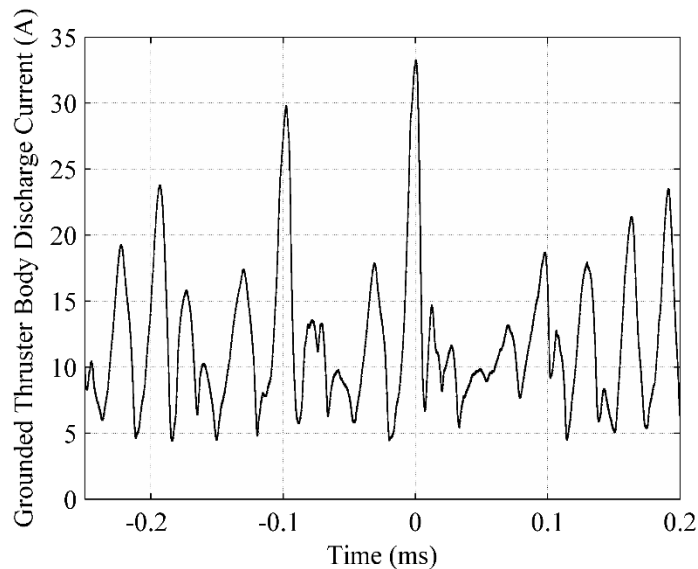


Figure 102: Representative discharge current peak event occurring at thruster body-to-cathode voltage of 11.12 V. The HET operating condition is 300 V, 3.5 kW.

5.3.3.3.2 The Thruster Body Plates

Figure 103, Figure 104, and Figure 105 show the thruster body plate current time delay and correlation coefficient with respect to the discharge current peak event for TP1, TP2, and TP3, respectively. The crossover of the thruster body-to-cathode voltage delineates the observed behavior in all three of the thruster body plates. For thruster body

plate TP1, as shown in Figure 103, as the thruster body-to-cathode voltage decreases, the time-delay between the discharge current peak event and the current response measured decreases from $6.7 \mu\text{s}$ to $3.5 \mu\text{s}$. At the crossover of the thruster body-to-cathode voltage, the time delay has decreased by 94% of the total change in the measured time delay. The time delay of the thruster body plate TP2 and TP3 current response exhibits a different behavior. The crossover of the thruster body-to-cathode voltage still delineates the data, but in the case of the thruster body plates TP2 and TP3, the behavior is bi-modal. At positive thruster body-to-cathode voltages, the correlation between the current response and the discharge current peak event is negative and the time delay is approximately $6 \mu\text{s}$. At negative thruster body-to-cathode voltage, the correlation between the current response and the discharge current peak event is negative and the time delay is approximately $8 \mu\text{s}$. Because the sign of the correlation coefficient of the current response is heavily dictated by the local plasma properties, the transition between a positive and negative correlation is indicative of bulk changes to the surrounding plasma near the thruster body plates. A more in-depth discussion of the physical implications of this observed behavior is covered in Chapter 6.

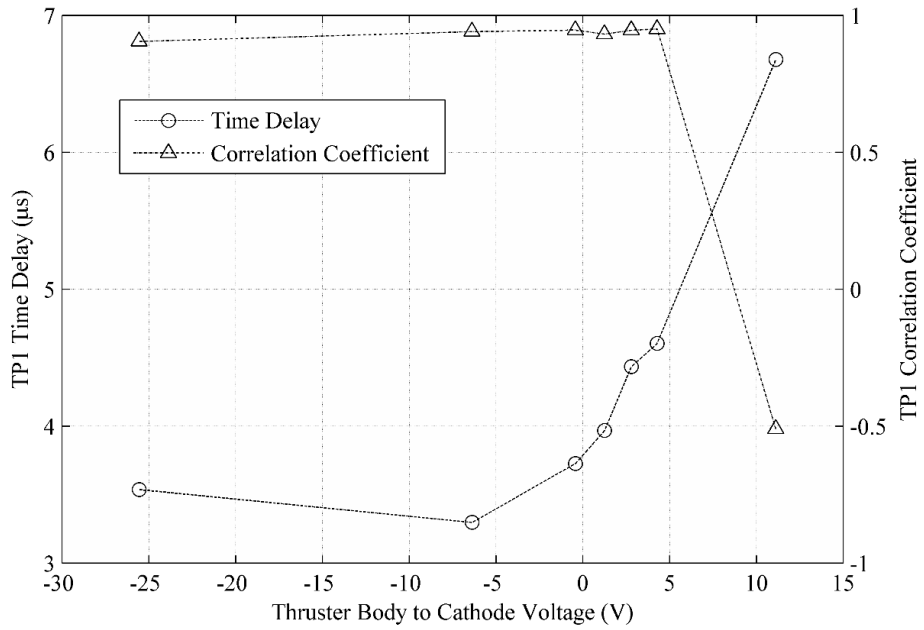


Figure 103: TP1 time delay and correlation coefficient. The HET operating condition is 300 V, 3.5 kW.

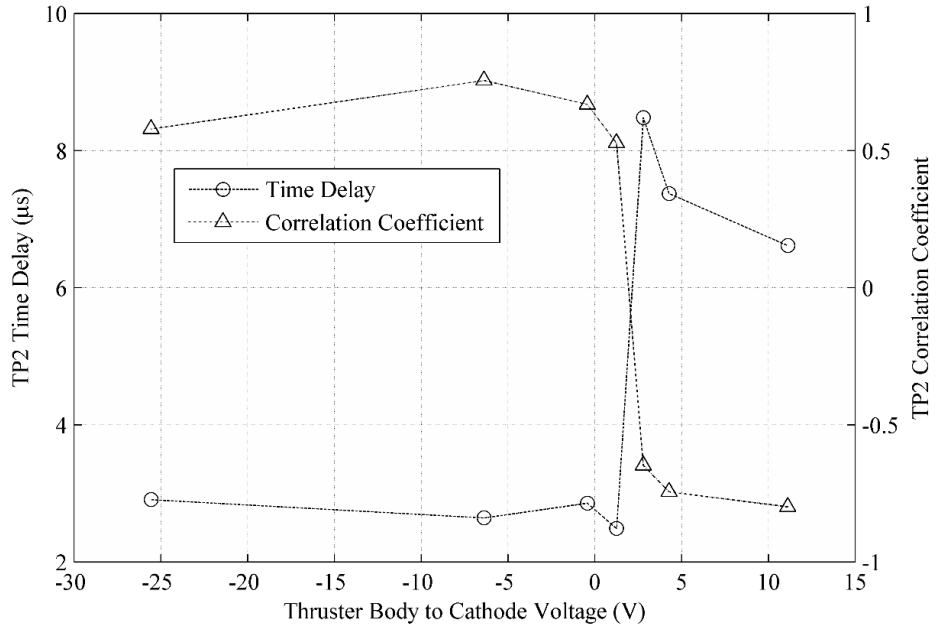


Figure 104: TP2 time delay and correlation coefficient. The HET operating condition is 300 V, 3.5 kW.

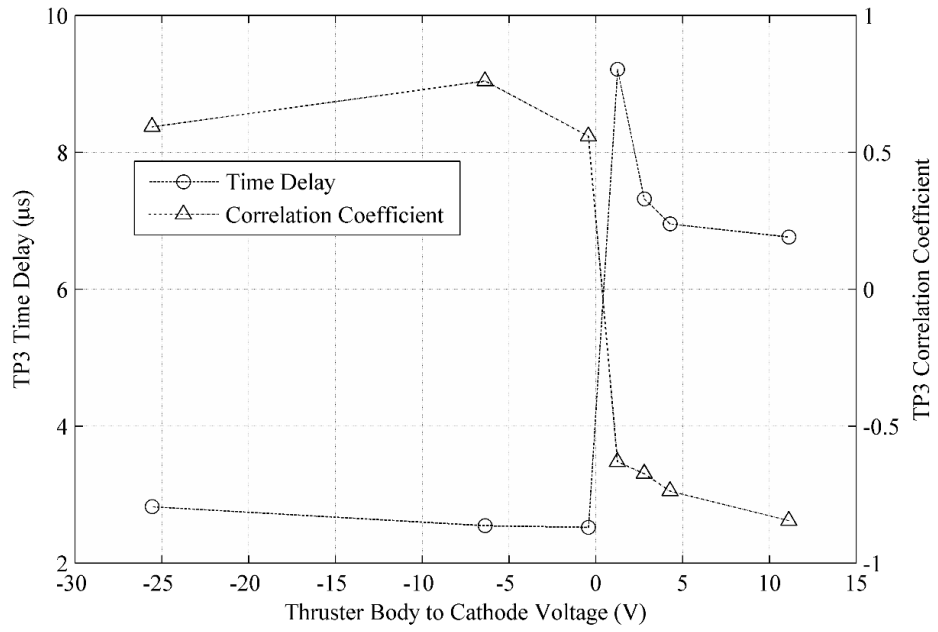


Figure 105: TP3 time delay and correlation coefficient. The HET operating condition is 300 V, 3.5 kW.

Chapter VI

Discussion of Results

The two research goals that this thesis seeks to address are as follows: 1) How does the chamber wall charge recombination pathway interact with the Hall effect thruster? and 2) How does the electrical boundary condition of the thruster body itself affect the operation of Hall effect thruster? The following section presents the major findings from each of the experimental configurations that address each of those research goals. At the end of each section, there is brief summary of key findings. At the conclusion of Chapter VI, a section is devoted to discussing the overall impact of electrical facility effects on HET testing.

6.1 Discussion of Findings from Cathode Positioning Experimental Configuration

6.1.1 Cathode Position: Regions of Correlation

Frieman, et al. [22] and the analysis presented in sections 5.1.2 and 5.1.3 classified cathode radial positions and observed behavior into different regions based on the magnetization of electrons near the cathode orifice. The magnetization of electrons is driven by the magnetic field produced by the HET magnetic circuit. In each of these regions, there were posited preferred plume neutralization, electron termination pathways. These electron termination pathways are described as preferential areas that neutralization electrons either impact (in the case of grounded surfaces) or enter (in the case of HET plume). At cathode positions which correspond to weak or no electron magnetization near the cathode orifice, neutralization electrons preferentially terminate in the plume or at the radial walls of the vacuum chamber. At these cathode positions where preferential electron termination is in the plume or radial walls of the vacuum chamber, the data from Figure 63 and Figure 64 showed evidence that the HET discharge circuit directly deposits power onto

radial chamber surfaces and suggested that the HET discharge circuit can directly couple to the radial chamber plate through the cathode. Analysis of the correlation data presented in this work also support direct HET discharge circuit coupling to the radial chamber plate surfaces.

In the case of the radial chamber plate correlation to the discharge current peak event (Figure 42), the discharge current peak event is correlated to the radial chamber plate current at all cathode positions except 15.6 cm away from thruster center. This strong correlation over a the range of cathode positions corroborates well with conclusions drawn from the analysis in section 5.1.3 that show that the HET discharge is coupled to the radial walls of the vacuum facility through the electrons propagating sourced from the cathode. At 15.6 cm away from thruster center line, the cathode orifice is almost in line with the outer edge of the discharge channel wall and is in a region of very strong magnetic fields and potential gradients that can drive electrons into the HET discharge and the plume [63]. If the coupling between the HET discharge circuit and the radial chamber wall is dominated by electron propagation, then it is expected that there should be poor correlation between the discharge current peak event and the radial chamber plate.

Similar to the radial chamber plate, the axial chamber plate correlation to the discharge current peak event. The axial chamber plate current correlation to the discharge current peak event, as shown in Figure 43, is only strongly correlated to the discharge current peak event for a limited range of cathode radial positions (32.1 cm to 94.3 cm away from thruster centerline). For those cathode positions, 32.1 cm to 94.3 cm away from thruster centerline, there was a statistically significant time-delay between the discharge current event and the response measured on the axial chamber plate current-to-ground. This same range of cathode radial positions corresponds to cathode positions where Frieman, et al. [22] saw changes in the plasma potential and time-averaged plate currents that support preferential electron termination to the HET plume. At cathode positions outside of 32.1

cm and 94.3 cm away from thruster centerline, both Frieman, et al. [22] and the results and analysis presented in sections 5.1.2 and 5.1.3 demonstrate that the preferred electron termination shifts from being near thruster body surfaces at close cathode positions to facility walls at large cathode positions. As displayed in Figure 43, the axial chamber plate current behavior is only strongly correlated to the discharge current for cathode positions that correspond to plume preferential electron termination.

6.1.2 Electrical Interaction between the Thruster and the Radial Chamber Plate

6.1.2.1 Evidence of Cathode Coupling to Radial Plate

To aid the discussion of the regional variation in physical mechanisms, it is important to distinguish between two potential sources of electrons collected on the radial plate. The first class of cathode electrons is one where the electron propagation into the downstream plume is driven by the ions accelerated by the HET discharge. These electrons are pulled into the beam via the electrostatic potential gradient generated by accelerated ions that exit the HET. An example of this electrostatic potential gradient can be seen in Vaudolon, et al. [63]. It is through this electrostatic potential gradient that these cathode-sourced electrons, no longer confined by the HET magnetic field, are able to propagate in to the downstream plume. Once in the plume, their propagation towards the radial facility walls occurs both thermally and by ambipolar forces pulling electrons along with the charge-exchange ions. These electrons are referred to as “Class 1” electrons. The second potential source of electrons incident on the radial plate is one where the electrons leave the cathode orifice with enough thermal energy that they are unmagnetized by the HET magnetic field. These electrons enter the plume through both the electrostatic potential gradients set up by the accelerated ions and their own thermal velocity. These electrons are affected by ambipolar forces in the plasma, but they also have a strong thermal velocity component that drives their propagation outwards from the cathode orifice. A portion of

these electrons have velocity vectors that lead them to impact the radial chamber plate [22]. It is this second class of cathode electrons that is referred to when describing cathode-sourced electrons impacting the radial chamber plate. These electrons are referred to as “Class 2” electrons. Both classes of electrons are utilized for neutralization. The primary difference between the two classes is that the propagation of Class 2 electrons to the radial chamber plate is controlled by the electron Hall parameter at the cathode orifice, whereas and the propagation of Class 1 electrons to the radial plate is controlled by weak plasma potential gradients and ambi-polar forces pulling electrons along with CEX ions into the off-axis region of the plume.

For cathode positions in Region 1, cathode electrons are confined by the strong magnetization of the local HET magnetic field, and thus the electron current collection on the radial plate is primarily composed of Class 1 electrons. In Region 2, magnetization of cathode electrons is much weaker. Some cathode electrons are confined to the magnetic field, but a large portion of electrons have high enough thermal energy to escape the HET magnetic field and propagate thermally outward from the cathode orifice. In all cases (Region 1, Region 2 and Region 3), the plasma surrounding the radial plate is dominated by CEX ions. These CEX ions facilitate a transfer of spectral power between the HET discharge and radial plate as evidenced by the spectral power peaks of the radial chamber plate waveform, as seen in Figure 39 and Figure 40. For cathode positions in Region 2, a portion of Class 2 (as well as Class 1 electrons) high thermal energy cathode electrons that are not confined by the HET magnetic field are collected on the radial chamber plate. Evidence of these Class 2 electrons impacting the radial chamber plate is seen as elevated spectral power in the sub 5-kHz regime as shown in Figure 107. The actual source of this power in the sub 5-kHz power band can be tied to the cathode as spectral power in this frequency range is correspondent to the self-pulsing of the cathode discharge due to the internal plasma resistance of the hollow cathode discharge [96]. Further evidence

indicative that electrons from the cathode directly impinge on the radial plate is shown in Figure 106. This data was taken from initial thruster testing at a cathode position from a thruster centerline of 18.1 cm. Time-resolved cathode-to-ground voltage measurements did not occur at other cathode positions and did not occur simultaneously with other data presented thus far. However, this power spectra shows that the time-resolved cathode-to-ground voltage contains elevated spectra power in the sub-5 kHz range.

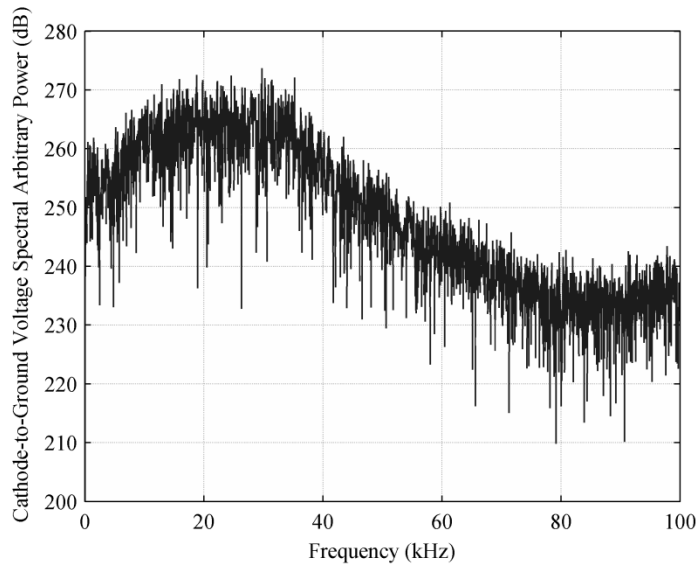


Figure 106: Representative cathode-to-ground voltage power spectra. The HET operating condition is at 300 V, 3.1 kW.

For cathode positions in Region 3, cathode electrons are no longer magnetized by the HET and thermally propagate outward from the cathode orifice. In comparison to Region 2, the flux of Class 2 electrons colliding with the radial chamber plate is greater due to lower magnetization and a larger portion of the plume expansion solid angle intersecting with the radial plate [22]. The rise of the sub 5-kHz spectral power band to the dominant spectral peak, as illustrated in Figure 40 and Figure 107, is indicative of the flux of electrons that impact the radial plate have a significant population of Class 2 electrons. It is important to note that throughout all regions, the radial plate electrical waveform

power spectrum has peaks that correspond with the HET discharge current breathing mode oscillations. This means the flux of Class 2 electrons does not prevent the flux of Class 1 electrons onto the radial chamber plate. The regional variation in radial plate power spectra behavior is due to the changing composition of electrons incident on the radial plate. The increases in the sub 5-kHz spectral peak on the radial plate suggest a stronger coupling between the cathode plasma and radial plate. It is unclear, however, if this coupling is a one-way interaction, where the radial plate does not influence the cathode behavior or if there is feedback from the radial plate that impacts the cathode behavior.

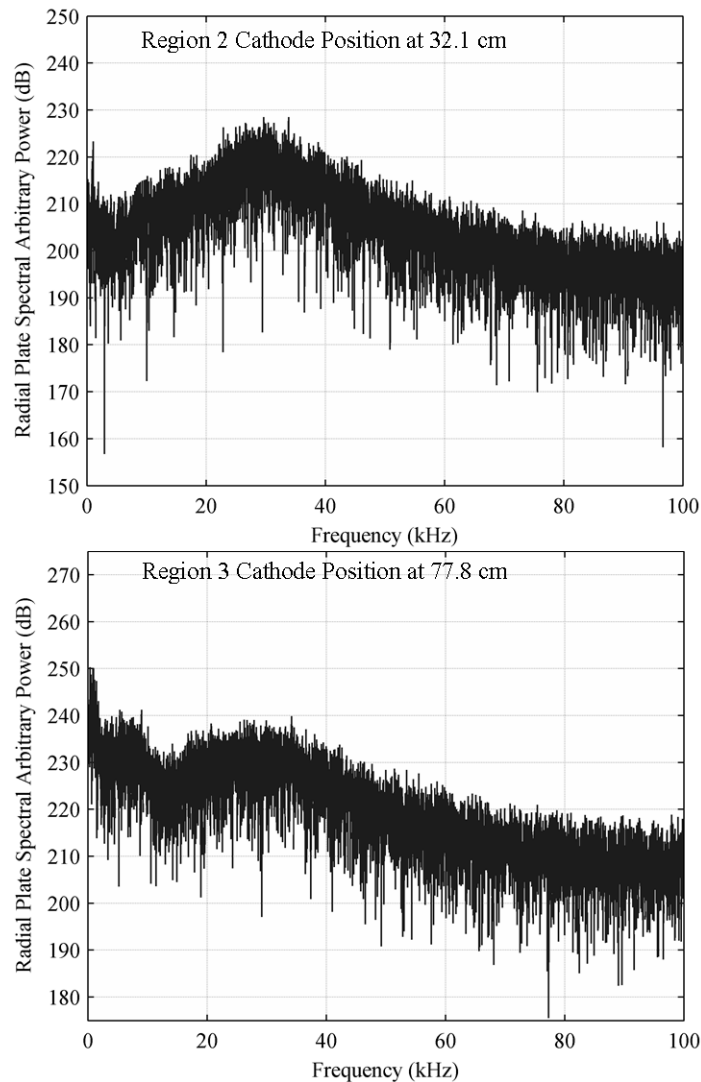


Figure 107: Radial plate current-to-ground power spectra for the floating thruster body electrical configuration. Top: Cathode position is at 32.1 cm from thruster centerline (Region 2). Bottom: Cathode position is at 77.8 cm from thruster centerline (Region 3). The HET operating condition is at 300 V, 3.1 kW

6.1.2.2 Higher Frequency Spectral Peak of the Radial Plate Power Spectra

Figure 39 shows the presence of a frequency peak in the 50 kHz range. The two frequency peaks (~30 kHz and ~50 kHz) of the radial plate power spectra are found consistently in Region 1 and in some cathode positions in Region 2. The second higher frequency peak is at least 1-2 dB stronger than the discharge oscillation frequency. The

source of this power on the radial plate could be from two different sources: self-induced cathode oscillations or a dominant HET plasma oscillatory mode in that frequency range. In the case of the self-induced cathode oscillations, the approximate 50 kHz peak is consistent with cathode measurements taken by Sekerak [32]. However, in Region 1 cathode positions, the cathode-electrons are confined to HET magnetic field. Only cathode electrons with the highest energy could propagate toward the facility wall. If it were the case that these high-energy electrons drive the approximate 50 kHz spectral power peak on the radial plate, then it is expected that there should be an increase in power in the 50 kHz range for increasing cathode positions. This is not the case because at large cathode radial positions, the double peak structure around the discharge oscillation is no longer present in the Region 3 radial plate power spectra. Because the spectral power at the 50 kHz frequency peak is almost equal to breathing mode frequency peak, it is more likely that the source of the higher frequency peak is related to another discharge plasma instability. The data presented in Figure 39, Figure 40, and Figure 41 suggest that the active source of energy for this secondary spectral frequency peak may be due to a plasma instability mode in the HET discharge. Further investigation in this area is beyond the scope of this manuscript.

6.1.3 HET Discharge Current Oscillation

From the data presented thus far, there appears to be a connection between the changes in the discharge current and the radial plate electron current, and radial plate floating voltage. The change in the peak-to-peak discharge current (Figure 36), discharge current peak frequency (Figure 37), and FWHM of the discharge current peak frequency (Figure 38) correspond to a change in the radial plate peak frequency (Figure 40) and the radial plate average collected electron current as shown by Frieman, et al. [22]. Even so, it is unclear as to whether these corresponding changes are due to the increased coupling to the radial plate, due to changes caused by the cathode position relative to the HET magnetic field, or due to both of these aforementioned processes. Much work has been done on

cathode position [19, 38, 46, 64, 66, 67], and the general consensus is that the cathode position can be very important in determining the operating behavior of the HET. The actual physical mechanisms that drive this behavior are not fully understood. Work done by Jorns, et al. [10] suggests that the formation of ion acoustic turbulence (IAT) is a key physical mechanism in governing electron transport and collisionality in the near cathode orifice plume. The IAT may be a key physical mechanism that could explain both changes in the radial plate electron current and the discharge current; however, such data and analysis is beyond the scope of this manuscript.

6.1.4 The Impact of the Conductive Wall on HET Operation

The results of the analysis presented in this work indicate that the chamber walls directly influence the plume properties of the HET. As described by Frieman, *et al.* [22, 72], the charge loss rate at the chamber walls can significantly affect the plume plasma potential. From the time-resolved analysis of the discharge current and chamber plate current and voltage that show strong temporal statistical correlation between the discharge current and the radial plate and axial plate at all cathode regions indicate that the chamber walls are coupled in time to the HET discharge. The chamber walls represent an artificial electrical boundary condition that forces electron and ion charges to recombine at the wall surface. As evidenced by the strong negative correlation between the discharge current and the radial chamber plate current (Figure 42), increases in the discharge current subsequently result in an increase in the collected electron current. Extending this result to all chamber surfaces, fluctuations caused by the HET in the near the chamber wall local plasma parameters result in changes in the charge loss rate to the wall. The charge loss rate to the wall influences the sheath potential drop and can greatly influence the global plasma potential [3, 72]. Thus, the chamber walls act to confine the temporally-resolved plasma

potential in the plume to within certain bounds. This is not the case in the space environment, where the HET plume electrical boundary condition is not spatially enforced and conductive surfaces that interact with the HET plasma are not held at a constant potential. It has been witnessed from the data and analysis gathered from the SMART-1 mission that exposed, low voltage solar panel contacts in the HET plume can drive the plasma potential relative to the satellite bus common and the cathode-to-satellite bus common voltage in a way that was not anticipated from ground-based testing [51, 52, 55]. Such changes in the plasma potential alter the flow of charge particles onto spacecraft surfaces. The changes in cathode-to-satellite bus common may influence the time-resolved behavior of the HET.

6.1.5 Timescale of Physical Mechanisms in the Hall Current Thruster Plume

To evaluate whether the measured time-delay from the radial chamber plate currents are derived from common plasma physical processes, propagation times of different plasma waves are considered. The radial chamber plate is located in a plasma region without external magnetic fields and external electric fields. The lack of external magnetic fields and external electric fields in this region means that plasma in this region can only support Langmuir wave modes or ion-acoustic wave modes. It has been shown by Lobbia [75] and Jorns, et al. [10] that both of these wave modes are present in the HET testing environment. Since the results from section 5.1.2, 5.1.3 indicate that the cathode may be directly interacting with the radial chamber plate and the work by Jorns, et al. [10] shows that the hollow cathode excites ion-acoustic turbulence in the near field region of the cathode, the ion-acoustic wave speed is considered. Although any influence from the discharge channel plasma that propagates to the radial wall must go through a region of plasma with strong magnetic fields, calculation of the ion-acoustic wave speed will

determine a minimum propagation (time-delay) time between the discharge plasma and the radial chamber if the ion-acoustic wave mode is an important factor to consider. Using a first-order estimation, the ion-acoustic velocity, v_a , can be approximated by Equation 4 [3].

$$v_a = \sqrt{\frac{\gamma_i k T_i + k T_e}{m_i}} \quad (21)$$

where γ_i , k , T_i , T_e , and m_i are the ion ratio of specific heats, Boltzmann constant, ion temperature, electron temperature, and mass of the ion (in this case xenon), respectively. Langmuir probe measurements for the cathode at 18.1 cm away from thruster centerline, indicate that the electron temperature from 0.254 m to 0.864 m away from the radial plate to be $1.5 \text{ eV} \pm 0.15 \text{ eV}$. Because of the small variance in measured electron temperature, it is assumed that in the spatial region between the HET and the radial chamber plate the electron temperature remains spatially uniform and there is negligible ion temperature compared to electron temperature ($T_i \ll T_e$). With these assumptions in-place, the calculation of the ion-acoustic wave speed via equation 21 yields an ion-acoustic wave speed of $\sim 1000 \text{ m/s}$. Based on the spatial distance of the HET to the radial plate and that estimated ion-acoustic wave speed, the propagation delay between HET and radial chamber plate should be on the order of 2 ms. The estimated ion-acoustic based time-delay presented neglects the effects of the HET external magnetic field and including those effects would increase the estimated time-delay. This is due to the external magnetic field of the HET that limits the mobility of electrons in the near field of the HET. Thus, the predicted ion-acoustic dependent time-delay presented is a lower limit, and in the actual testing environment, the ion-acoustic wave mode would propagate more slowly to the radial chamber plate. In this experimental configuration, the actual measured time-delay ($9.5 \mu\text{s}$ to $11.8 \mu\text{s}$) between the discharge current peak event and the radial chamber plate

measured response in the current to ground is two orders of magnitude longer than the ion acoustic wave mode predicted time-delay. Therefore, the measured time-delay between discharge current peak event and the response of the current collection on the radial chamber plate is too short to be purely dominated by the ion-acoustic wave mode.

As in the case of the radial chamber plate, the likely physical mechanisms connecting the axial chamber plate to the HET discharge circuit are evaluated. Like the radial chamber plate, the plasma environment is without external electric and magnetic fields. Additionally, the plasma surrounding the axial chamber plate has a large population of ions that are accelerated via the HET discharge circuit. Work by Frieman, et al. [72] suggests that the current collected on the axial plate is kinetically controlled through the beam ions. To evaluate whether or not ion time-of-flight kinetics control the axial plate current collection, the measured time-delay is compared to the time required for beam ions to traverse the distance between the discharge channel exit plane and the axial chamber plate. Based on thrust measurements of Frieman, et al. [22], the exit velocity of the ions is estimated from the specific impulse and is found to be on the order of 16 km/s. This gives the ions an average time-of-flight of $\sim 300 \mu\text{s}$, which is an order of magnitude longer than the measured time delay between discharge current peak event and the measured response on the axial chamber plate current-to-ground ($8.1 \mu\text{s}$ to $9.3 \mu\text{s}$). The fastest possible ions accelerated from the HET discharge are those that experience the maximum potential drop set by the discharge supply and plasma potential, and those ions that are doubly charged [3]. Since the exit velocity of the ions scales by the square root of the potential drop and the square root of the charge state, a doubly charged ion going through the entire potential drop between the anode and the plasma potential ($V_{\text{accel}} \sim 270 \text{ V}$ for a discharge voltage of 300 V, assuming V_{cg} is approximately -10 V and V_{p} is approximately 20 V) results in a reduction in the ion time-of-flight to approximately 180 μs . Even by accounting for the shortest possible ion time-of-flight, the time-delay between discharge current peak event

and the response of the current collection on the axial chamber plate is too short to be purely dominated by ion time-of-flight kinetics. As in the previous radial chamber plate calculation, the ion-acoustic velocity can be calculated. Since the ions in the HET beam have a large downstream velocity and the axial plate is located directly downstream of the HET, the ion-temperature is assumed to be on the order downstream ion velocity. Using equation 21, the ion-acoustic wave speed is calculated. Assuming iso-thermal wave propagation ($\gamma_i=1$), an ion velocity that corresponds to a potential of 250 V (as shown in Figure 33) and centerline electron temperature of 2.5 eV [97], the ion-acoustic wave-speed in the beam is found to be on the order of 14 km/s. This wave-speed results in a predicted time-delay between the thruster and the axial chamber plate of 310 μ s. As with the time-of-flight calculations, the upper bound on the ion acoustic wave speed is considered. For the ion-acoustic wave speed, the upper limit is dictated by the ion temperature (in this case the ion velocity) and the electron temperature [3]. The ion temperature is set by the discharge of the HET [3, 5]. This sets the upper limit of the ion velocity that corresponds to a potential of 270 V. Based on electron temperature measurements of the T-140 HET at 300 V at thruster centerline, the maximum the electron temperature measured was 2.6 eV. This puts an upper limit on the ion acoustic wave speed to 14.2 km/s and a lower limit of the ion-acoustic time-delay of 300 μ s. Even by considering the fastest possible ion acoustic wave-speed, the estimated time-delay is an order of magnitude greater than the measured time-delay; therefore, the time-delay between discharge current peak event and the response of the current collection on the axial chamber plate is too short to be purely dominated by ion-acoustic wave propagation.

In both the axial and radial chamber plate, the measured time-delay is one to three orders of magnitude shorter than what is predicted considering the time-scales of ion time-of-flight as well as ion-acoustic wave speed time-scales. Since the electrons in the plasma are the most mobile charge carriers, the electron wave speed, also known as the Langmuir

wave speed, is considered. To zeroth order, the Langmuir wave speed can be estimated as the electron thermal speed, v_e , and is calculated via Equation 5:

$$v_e = \sqrt{\frac{kT_e}{m_e}} \quad (22)$$

where k , T_e , and m_e is the Boltzmann constant, electron temperature and the mass of an electron, respectively. Centerline electron temperature measurements at 1 m downstream of the discharge channel exit plane show that the electron temperature is 2.5 eV. This electron temperature results in a calculated electron thermal velocity of 660 km/s. Because the electron-neutral and the electron-ion collision mean free path is on the order of meters, it is assumed that the electron temperature remains constant throughout the spatial distance between the axial chamber plate and the HET. The resulting predicted time-delay between the axial chamber plate current-to-ground and HET discharge current event is on the order of $6 \mu\text{s}$. For the radial chamber plate, a similar calculation ($T_e = 1.5 \text{ eV}$) as before yields a predicted time-delay on the order of $4 \mu\text{s}$. The electron thermal velocity predicted time-delay is on the same order of the actual measured time-delays. This agreement of time-delays indicates that electron wave modes are likely the main physical mechanisms that governs the electrical interaction between the HET and the chamber walls.

6.1.6 Summary of Findings from Cathode Positioning Experimental Configuration

With regards to understanding the interaction between the HET and the chamber walls recombination pathway, the analysis of the cathode positioning experimental configuration is able to demonstrate key attributes about the link between the HET electrical circuit and the conductive walls of the vacuum chamber. From this work, it is clearly established that the HET discharge circuit is coupled to the walls of the vacuum facility. The analysis of the time-averaged and the time-resolved measurements of the

chamber plate currents revealed that changes in the HET discharge current result in corresponding changes in the electrical characteristics of the chamber plates. Based on the time-delay analysis, the propagation mechanism that communicates information from the HET discharge to the chamber walls is linked to the electron Langmuir plasma wave instability. When the cathode orifice position is in a location that has a weak electron magnetization, there is demonstrated evidence that the HET couples more strongly to the plume and to the walls of the vacuum chamber. Both of these findings support that how and where the electrons leave the HET electrical neutralization circuit is an important factor on how the chamber walls interact with the HET. Due to complications separating effects due to the enhanced chamber wall coupling and effects due to cathode position, it is difficult to directly identify which aspects of the HET discharge are influenced by the facility walls recombination circuit. Overall, the results from the analysis of the cathode positioning work are able confirm that the chamber walls are electrically coupled to the HET discharge and is able to identify Langmuir plasma wave propagation as the likely physical mechanism responsible for that coupling.

6.2 Discussion of Results from Biasing of the Axial Chamber Plate

6.2.1 Plasma Potential and Plate Current

To better understand the interaction between the axial plate and the HET electrical circuit, it is first important to understand the interaction between the axial plate and the thruster plume environment. Between the axial plate and the plume environment, a plasma sheath mediates the current collection. It is then critical to understand how this sheath responds to changes in the axial plate bias voltage.

Examining the data presented in Figure 53, the current collected by the axial plate rises with bias voltage until it reaches the thruster beam current that occurs at 20 V above ground. At this potential, the plate collects an electron current equivalent to the neutralization current supplied by the cathode. Above 20 V, increases in the axial plate bias voltage result in equal increase of the plasma potential and the floating potential of the thruster anode and cathode (Figure 56). At these voltages, it is possible to increase the cathode potential above ground. The collected current increases slowly, as all the cathode neutralization electrons are already being collected and additional electrons must be sourced from grounded chamber surfaces. The physical connection between the two phenomena (knee in current collection and start of plasma potential rise) is the plasma charge balance. If the plate is biased positive with respect to earth ground, the plasma will electrostatically respond and the plasma potential will adjust to equalize charge loss rates and keep the plasma electrically neutral.

To illustrate the effect of the plasma charge balance and to determine if there are other sources for the additional electron current collected on the axial plate outside of the HET beam, we model the current collection by the plate and chamber boundary to compare to the experiment. To know the current collection, we need the local plasma parameters at the boundary. To this end we apply the self-similar plume model of Korsun and

Tverdokhlebova [56] as reported in Azziz [98]. This model neglects collisional effects in the chamber, assumes a two-component plasma, and adiabatic expansion of the HET plume. The model gives the following relations to calculate the ion flux j_i , electron density n_e , electron temperature T_e , and plasma potential ϕ at any location in the plume.

$$j_{ic} = \frac{\gamma}{2\pi R^2} \frac{I_b}{\tan^2 \theta_{1/2}} \quad (23)$$

$$j_i = \frac{j_{ic}}{\cos^3 \theta \left(1 + \frac{\tan^2 \theta}{\tan^2 \theta_{1/2}}\right)^{1+\gamma/2}} \quad (24)$$

$$n_{ec} = \frac{j_{ic}}{ev_i} \quad (25)$$

$$n_e = \frac{n_{ec}}{1 + \frac{\tan^2 \theta}{\tan^2 \theta_{1/2}}} \quad (26)$$

$$\frac{T_e}{T_{ec}} = \left(\frac{n_e}{n_{ec}}\right)^{\gamma-1} \quad (27)$$

$$\phi = \phi_c - \frac{\gamma}{\gamma-1} \frac{kT_{ec}}{e} \left(1 - \left(\frac{n_e}{n_{ec}}\right)^{\gamma-1}\right) \quad (28)$$

In equations (23)-(28), R and θ are polar coordinates with the origin at the center of the thruster exit plane, $\theta_{1/2}$ is the thruster beam divergence, γ is the plasma polytropic index which we set to 1.3, and subscript c refers to the centerline or reference value. We assume that the model form of the plasma potential is always true no matter the bias voltage of the axial plate, and thus the plasma potential in the chamber has a fixed spatial distribution. This can be considered true to first order, because the expanding plume structure described by the model is set up by the operation of the thruster, and the measured plasma potential profile (Figure 58) has approximately the same plasma potential spatial distribution relative to other positions.

The chamber wall and axial plate is paneled as a series of rings of 0.1 m width. At each boundary panel, the ion flux, electron density, electron temperature and plasma potential is calculated from equations (23)-(28). We then calculate the ion current to the panel from the ion flux assuming singly charged ions (29) and the electron current to the panel (30).

$$I_i = j_i e A \quad (29)$$

$$I_e = \begin{cases} \frac{1}{4} n_e e A \sqrt{\frac{8k_B T_e}{\pi m_e}} \exp\left(\frac{e(\phi_w - \phi)}{k_B T_e}\right) & \phi_w < \phi \\ \frac{1}{4} n_e e A \sqrt{\frac{8k_B T_e}{\pi m_e}} & \phi_w \geq \phi \end{cases} \quad (30)$$

We then solve numerically for the value of plasma potential that equalizes the total ion and electron currents lost from the plasma to all panels. Figure 108 shows the result for the plasma potential 1 meter from the thruster compared to the experimental data. Figure 109 shows the collected current on the axial plate compared to the experimental data.

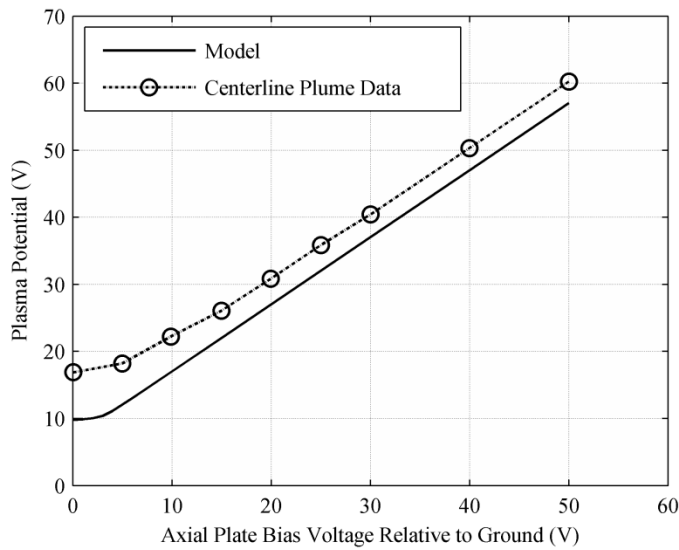


Figure108: Plasma potential as a function of axial plate bias voltage, model versus experiment. The HET operating condition is at 300 V, 3.1 kW.

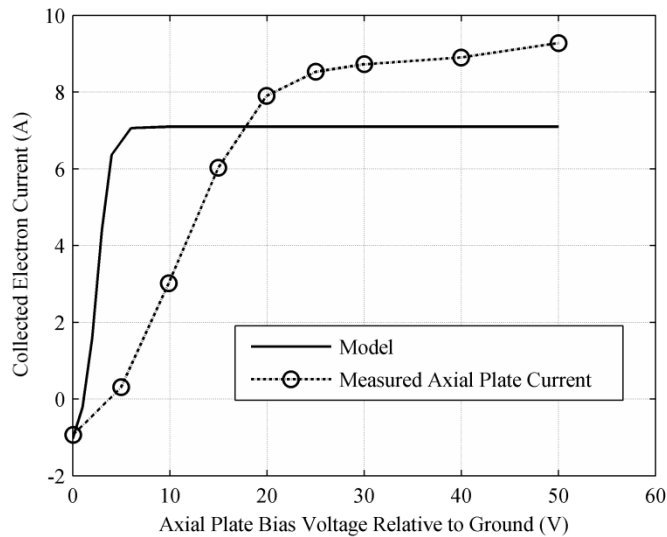


Figure 109: Axial plate current collected as a function of applied bias voltage, model versus experiment. The HET operating condition is at 300 V, 3.1 kW

Figure108 shows that the plasma potential behavior in the model agrees well with experimental data and shows 3-4 V offset between the model and the experimental data. The remaining offset between model and experiment may result from collisional effects

changing the plasma scaling in the far field region, where the charge-exchange background plasma becomes significant with respect to the expanding-plume plasma. It may also be due to the simplified assumed geometry, which neglects ion and electron fluxes to detailed chamber features such as the central I-beam and personnel support grating. Figure 109 shows that the collected current agrees qualitatively, but all of the cathode electrons are theoretically collected at a much lower bias voltage than is observed experimentally. This is most likely because the model does not take into account collisional effects and the charge-exchange background plasma. In the model, the plasma density is very low at chamber walls surfaces that are not directly impinged by the beam, where in reality the plasma is denser at the walls due to charge-exchange collisions and the associated diffusion of the plasma. This in turn means that the plate does not collect all the electrons until a higher bias voltage.

It is important to note that secondary electron emission effects on the aluminum chamber plate collected current are neglected in the model for the following reasons: Electron energy distribution measurements of secondary electron emission (SEE) of aluminum from Baglin, et al. [99], Pillon, et al. [100], and Yamauchi and Shimizu [101] show that the energy distribution of secondary electrons is to first-order invariant of incoming energy of electrons or ions, and the maximum energy of these electrons is on the order of 15 eV with a most probable energy on the order of 3-4 eV. This means that electrons produced via SEE from the aluminum plate do not have enough energy to overcome the potential difference between the biased axial chamber plate and the surrounding plasma and are recollected by the axial-chamber plate. The overall first-order net-effect is that electrons produced by the SEE from the aluminum chamber plate do not influence the current collection measured. The collected current in the model does not increase above the cathode electron current because additional electrons gained from other chamber sources are not included in the model. At the axial chamber plate biases greater

than 20 V, there is an experimentally measured current collection that is well outside what is known to be generated by the HET beam; therefore, it is concluded that an electrical circuit is formed between the axial chamber plate and the grounded vacuum chamber surfaces through the plasma.

6.2.2 Interaction Between the HET and the Chamber Recombination Pathway

The bias voltage of the axial chamber plate is able to control the electron termination pathways of the HET plume. When the axial plate is grounded, electrons sourced from the cathode are driven electrostatically into the plume and are collected onto grounded chamber surfaces. This includes electron current collected onto grounded thruster body. As the axial chamber plate electron current collection surpasses the available beam current of the HET, the cathode potential (relative to ground) floats above ground due to the increase in the global plasma potential as shown in Figure 56, Figure 58, and Figure 108. Due to the adverse potential gradient between the grounded chamber walls and the cathode-to-ground voltage, electron termination on grounded chamber surfaces diminishes. Figure 110 shows that the decrease in collected electron current on grounded surfaces was also seen in collected electron current on the grounded thruster body. The floating potential of the electrically-floating thruster body also begins to shift positive relative to earth ground to attract additional electron flux to maintain a zero net current condition.

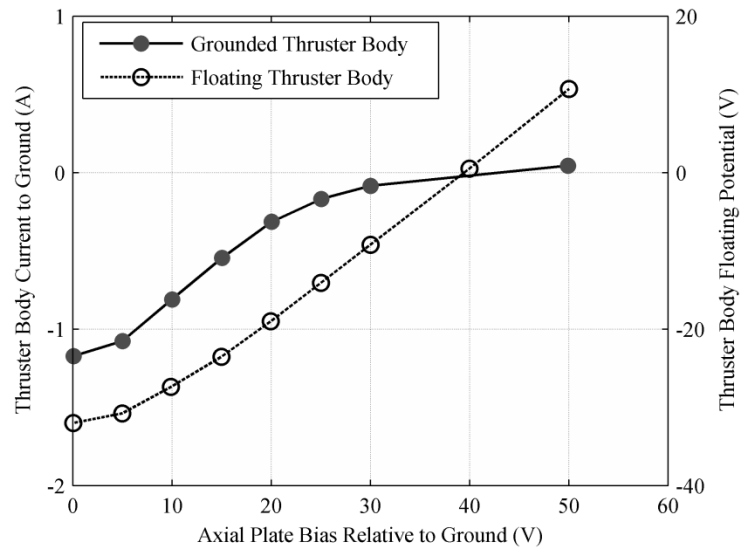


Figure 110: Thruster body current-to-ground and Thruster body floating voltage as a function of axial plate bias voltage. The HET operating condition is 300 V, 3.1 kW. Error bars are encompassed by plot markers.

At axial plate bias voltages above 20 V, 100% of the HET beam current is collected on the axial chamber plate, but electron current collection continues to increase with increases in axial chamber plate bias voltage. As demonstrated by the first order analysis of the current collection on the axial plate (shown in Figure 109), grounded chamber surfaces are possible sources for these electrons due to field emission or secondary electron emission from chamber surfaces to the plume plasma as increasing the axial chamber plate bias voltage increases the potential gradient between the plasma and the grounded chamber. As the potential gradient between the chamber wall and the plasma increases, at bias voltages above 40 V, arcing events were witnessed on grounded chamber surfaces. These arcing events indicate a momentary discharge between grounded surfaces and the ambient plasma. At axial plate bias voltages >40 V, the potential gradient between the plasma potential and grounded chamber surfaces drives all electrons away from grounded surfaces. This potential difference removes the vacuum chamber as an effective electron termination pathway and allows grounded chamber surfaces to become a source of electrons. In Figure

111 is graphical representation of the electron termination pathways for the aforementioned three axial chamber plate bias voltages.

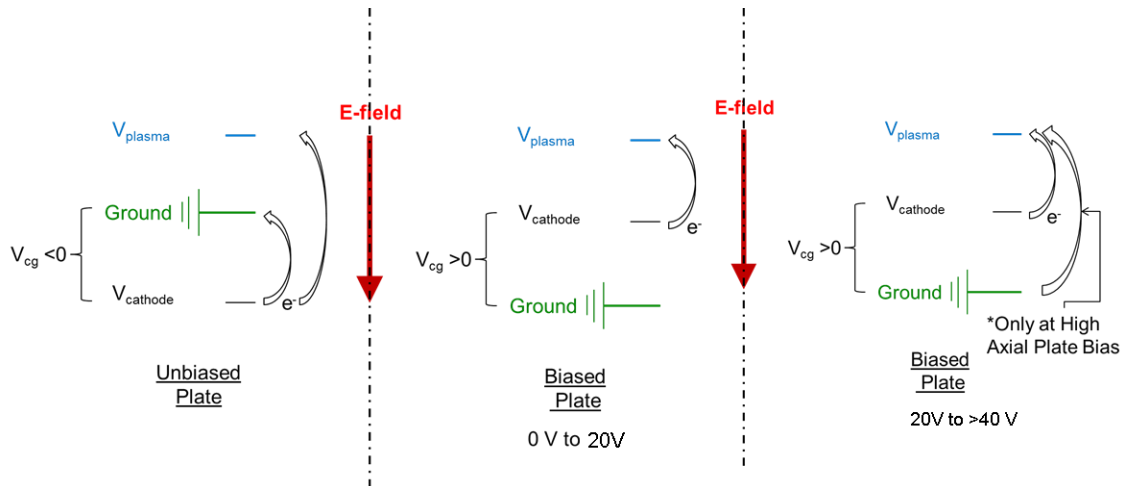


Figure 111: Notional Diagram of Electron Pathways. A) No axial plate bias voltage or nominal condition B) Low axial plate bias voltage C) High axial plate bias voltage.

6.2.3 Decoupling of the Radial Chamber Plate from the HET discharge

By controlling the global plasma potential of the plume, the voltage bias of the of axial chamber plate is able to decouple the radial chamber plate from the HET discharge. From a steady-state perspective, increasing the axial chamber plate bias voltage results in a reduction of electron current collecting on the radial plate (as seen on seen in Figure 54). As discussed in the above sections, this is due to a global rise in plasma potential. To a certain degree, this global increase in the plasma potential also decouples the radial chamber plate from the HET discharge. At axial chamber plate voltage biases relative to ground greater than 15 V, the primary spectral peak frequency shifts from being in a frequency band that is connected to the breathing mode of the HET (30 kHz range) to a higher order frequency range (140 kHz range). At the same axial chamber plate voltages, the radial chamber plate experiences an order of magnitude drop in the time delay from the

30 μs range to the 8 μs , as seen in Figure 66. Both of these large shifts are coincident with the axial chamber plate voltage bias that collect an electron current equal to the beam current of the HET.

Although it is unclear as to what the radial chamber plate couples to at large axial chamber plate bias voltages, the work done in the cathode positioning experimental configuration illustrated that the radial chamber plate can couple to other plasma modes. For the axial chamber plate bias experimental configuration, the shift in the primary spectral peak frequency to a frequency range that is not seen in the discharge current power spectra is indicative that radial chamber plate at least decouples from the fundamental breathing mode of the HET discharge at large axial bias plate voltages.

6.2.4 Impact of the Axial Chamber Plate Electrical Power

As seen from radial chamber plate current measurements (Figure 54) and plasma potential measurements near the radial plate (Figure 55), electrons are driven away from grounded surfaces due to the increased potential difference between the facility walls. The decrease in electron current-to-grounded surfaces is more indicative of space-like environment [57, 102]. According to Korsun, et al. [57], testing in a ground-facility environment produces a secondary plasma that interacts with the facility walls and currents “leak” out of the HET plume into this secondary plasma. These currents represent a loss of energy from the HET plume into the vacuum chamber walls. With the axial chamber plate, the forced collection of electrons provides additional energy into the plume. By multiplying the current and the voltage of the axial chamber plate, the power being introduced by the axial chamber plate is calculated and shown in Figure 112. Based on the data presented in this investigation, it is within reason to conclude that the power introduced by the axial chamber plate, in manipulation of the electron termination pathways, helps offset the energy normally loss to conductive grounded surfaces. The compensation of power loss to

the conductive walls of the vacuum chamber helps make the HET plume more representative of the on-orbit environment.

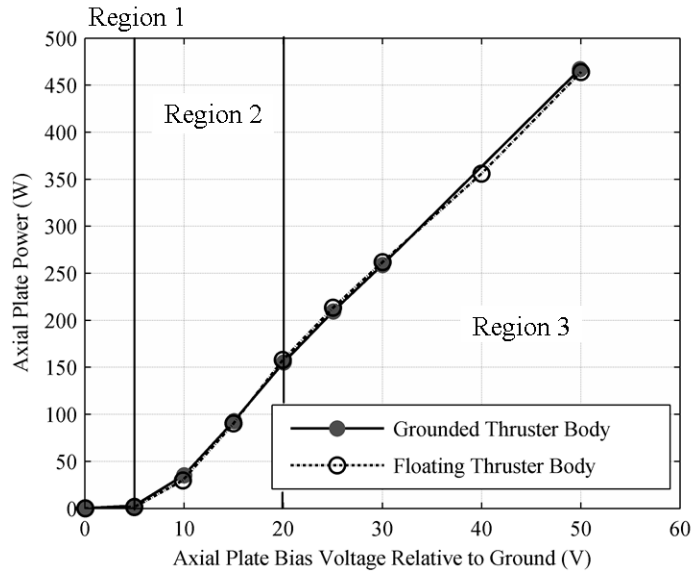


Figure 112: Power sourced by the axial chamber plate for both thruster electrical configurations. The HET operating condition is at 300 V, 3.1 kW. Error bars are encompassed by plot markers.

6.2.5 Enhanced Current Density in the Off-Axis Plume

As shown in Figure 57, the off-axis region of the plume has a current density that is influenced by the axial chamber plate bias voltage. As stated earlier, the Faraday probe has a fixed electron repulsion voltage throughout the testing; therefore, it is not immediately clear if the measured increase in the current density profile is due to changes in the plume or as a result of the Faraday probe fixed electron repulsion voltage. Without further modeling, the increase in current collected on the Faraday probe due to the increase in the potential gradient between the probe and the plasma cannot be estimated. In Figure 113, data is presented that offers an alternative means of assessing the validity of the measured current density in the off-axis region of the plume. As in Figure 57, the uncertainty in the ion current density profile between axial chamber plate bias voltage for

a given cathode position is encompassed by the line widths of the figure plots. Faraday probe sweeps were taken at four different cathode radial locations relative to thruster centerline: 18.1 cm (nominal position), 21.9 cm, 27.0 cm, and 43.4 cm. At the cathode nominal position and an axial chamber plate bias of 50 V, the current density is approximately 25% higher as compared to values measured for the grounded axial chamber plate condition. At other cathode positions, the increase in current density is on the order of 45% to 50% relative to current densities measured for the grounded axial chamber plate conditions. This variation of behavior in current density measured is enough to suggest that the increase in current density measured for high axial chamber plate voltages is due in part to actual changes in the HET plume.

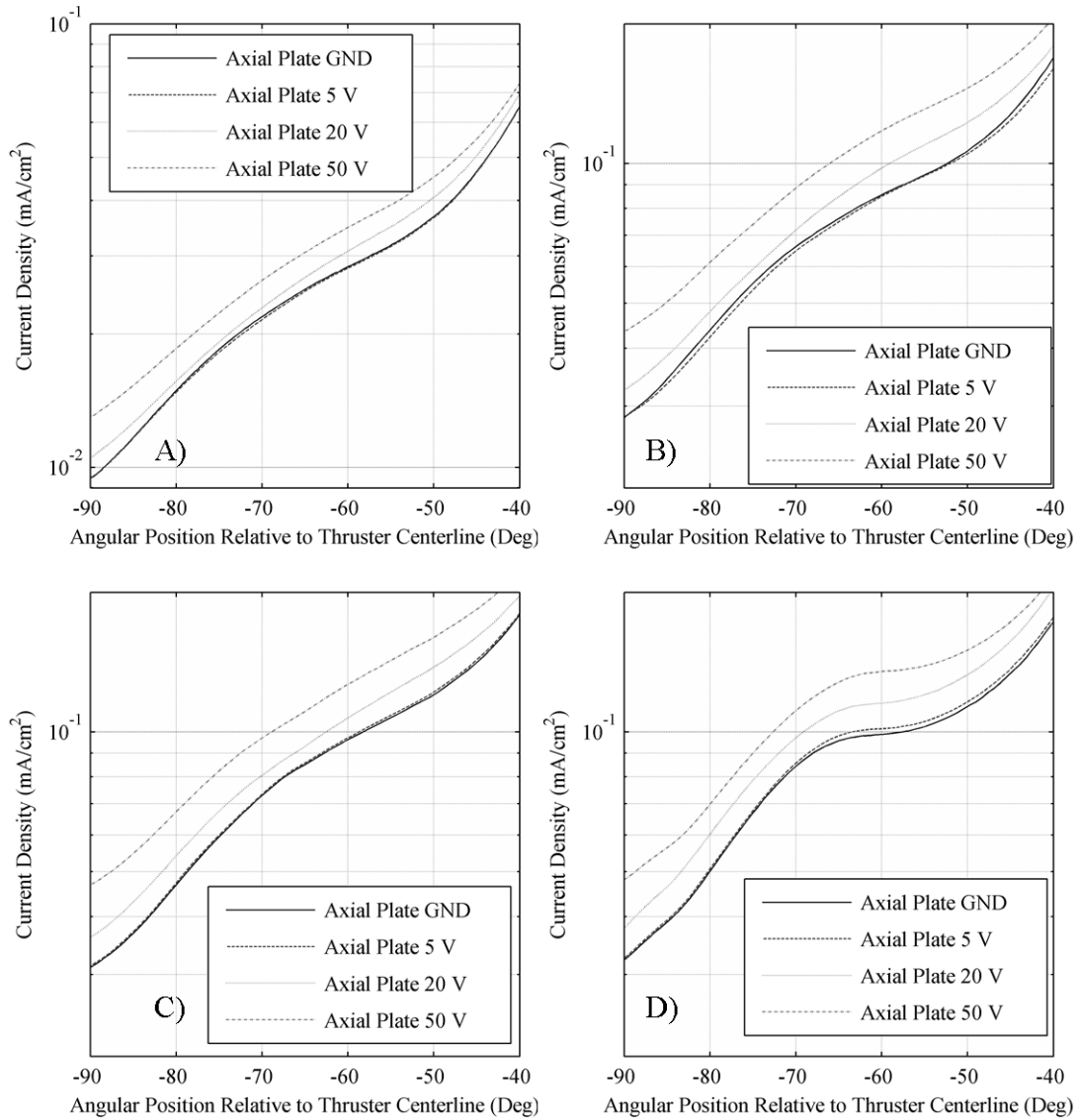


Figure 113: Current density profiles in the off-axis region of the HET plume for varying cathode positions relative to thruster centerline. The HET operating condition is at 300 V, 3.1 kW. A) 18.1 cm B) 21.9 cm C) 27.0 cm D) 43.4 cm.

6.2.6 Summary of Findings from Biasing the Axial Chamber Plate Experimental Configuration

For this experimental configuration, the goal is to influence the chamber walls recombination current or pathways directly and in doing so, be able to discern the influence of the chamber wall recombination pathway on the HET behavior. Overall, the bias of the axial chamber plate proves to be an effective way to manipulate this pathway specifically. By biasing the axial chamber plate, the plasma environment experiences global increases to the plasma potential that drive electrons away from grounded chamber surfaces, thus reducing the availability of the chamber wall recombination pathway. This is evidenced from the time resolved measurements of the radial chamber plate current-to-ground. As the axial chamber plate bias voltage relative to ground increases, the radial chamber plate begins to decouple from the fundamental breathing mode of the HET discharge. The HET discharge circuit itself responds to the changes in the plume plasma potential by floating to a higher cathode-to-ground floating voltage. The frequency of the discharge current breathing mode is relatively insensitive to these changes. Overall, the biggest changes observed occur in the plume structure of the HET. Care must be taken because at large enough axial plate bias voltages, a new electron termination pathway becomes available to the plasma. Based on visual observations and spikes in the electrical diagnostics indicate that this new pathway is driven by field-effect emission between the plasma potential and sharp grounded metal surfaces. The energy to support all these changes in the HET plume is supplied through the axial chamber plate bias supply. Ultimately, the analysis from the results of this experimental configuration is able to provide answers to the research question of how the chamber wall recombination pathway influences HET behavior by showing that the chamber-wall recombination current influences the HET by altering the plume structure and artificially bounding oscillations in the plume plasma properties.

6.3 Discussion of Results from Thruster Body Biasing Experimental Configuration

6.3.1 Manipulation of Localized Recombination Currents on the Thruster Body

Like the walls of the vacuum test facility, the thruster body supports its own recombination pathways. In general, any recombination current are influenced by two factors: The first factor, is due to the local variation in the plasma environment surrounding exposed conductive surfaces. The second factor is the electrical boundary condition of that surface. Depending on the combination of those two factors, the net flux of current collected on the conductive surface will vary. For the thruster body bias experimental configuration, both of these factors are not decoupled from each other. In this experimental configuration, the control methodology sought to alter the availability of these pathways by controlling the time-averaged thruster body voltage relative to the cathode voltage. In general, as the thruster body-to-cathode voltage becomes more negative, less current is collected on each of the thruster body plates and thruster body surfaces. This is to be expected as the thruster body to ground voltage approaches the floating voltage of the thruster body.

Sign changes of the current measurement are key indicators of structural changes to the recombination current structure. Examination of time-averaged current measurements of the thruster body plate TP1 (as shown in Figure 83) reveal that the sign change of the current collected occurs between thruster body-to-cathode voltages of 4.2 V and 2.8 V. This sign change indicates that the axial chamber plate goes from collecting a net flux of electrons to a net flux of ions. Because of Kirchoff's current law, these changes in the current structure must be balanced by current collection on other thruster body surfaces. Since the thruster body plate TP1 collects no more than 4% of the total current collected on the thruster body, this particular recombination current may not be a significant factor in influence on the overall behavior of the thruster body recombination

pathway. However, the sign change of thruster TP1 plate indicates that structural changes in the thruster body recombination circuit are possible elsewhere on the thruster body.

Control of the thruster body recombination current must also be examined from a time-resolved perspective. It has been clearly demonstrated by many sources that the near field plasma environment of a HET is spatially and temporally varying [10, 37, 63, 65, 69, 75]. This means that the plasma environment surrounding the thruster body is not uniform. Examination of the time-resolved response of the current on the thruster body plates reveal each of the thruster body plates experience different thruster body-to-cathode voltage dependent behaviors. For thruster body plates TP2 and TP3, the crossover of the thruster body-to-cathode voltage from positive to negative delineate two different frequency responses in their power spectra of the collected current (Figure 89 through Figure 94). At positive thruster body-to-cathode voltages, the primary spectral peaks have frequencies that are in the same range as the HET discharge current breathing mode frequency. At negative thruster body-to-cathode voltages, the primary spectral peaks of the thruster body plates TP2 and TP3 shifting to frequencies outside of the HET breathing mode. This spectral frequency change is indicative of the thruster body plates coupling to other plasma modes and serves as evidence that the thruster body-to-cathode voltage is a key parameter in determining the characteristics of the thruster body recombination pathway.

6.3.2 Influence of the Thruster Body Recombination Pathway on the HET Discharge

The thruster body interacts directly with the HET discharge. The first indication of this interaction is through the average current collected on the thruster body surface. When the thruster body is grounded, between 1.5 A and 2.8 A of electron current are collected on the thruster body. The collected current is approximately 21% to 40% of the total beam current created by the HET discharge. As the thruster body to ground voltage approaches the floating thruster body voltage, the collected current decreases. As demonstrated by the axial chamber plate bias experimental configuration, collection of that much electron

current influences the entire HET plume. Based on the lessons learned from the axial chamber plate bias experimental configuration, it is expected that the thruster body surface must interact with the HET as well. As shown in Figure 87, the discharge current breathing mode frequency decreases from 32.1 kHz at the grounded thruster body condition to 31.1 kHz at the thruster body floating configuration. As discussed in Chapter II, this change in the breathing mode frequency is related to changes in the physical processes ongoing inside the discharge channel. Further reflecting the changes in the fundamental behavior of the discharge of HET, the greatest sensitivity of the HET discharge to the thruster body-to-cathode voltage is to the transient behavior of the discharge current. The peak-to-peak and standard deviation of the discharge current behavior as function of thruster body-to-cathode voltage is shown in Figure 97. Between a thruster body-to-cathode voltage range of 11.12 V to -25.55 V, the peak-to-peak and standard deviation of the HET discharge current decreases by approx. 20% and 32%, respectively. Both measurements indicate that as the thruster body-to-cathode voltage changes, the discharge current oscillations decrease in intensity. With regards to the discharge current peak event, the structure of these events change dramatically between a thruster body grounded and thruster body electrically floating. The discharge current event between the grounded thruster body configuration and the floating thruster body configuration is shown in Figure 114.

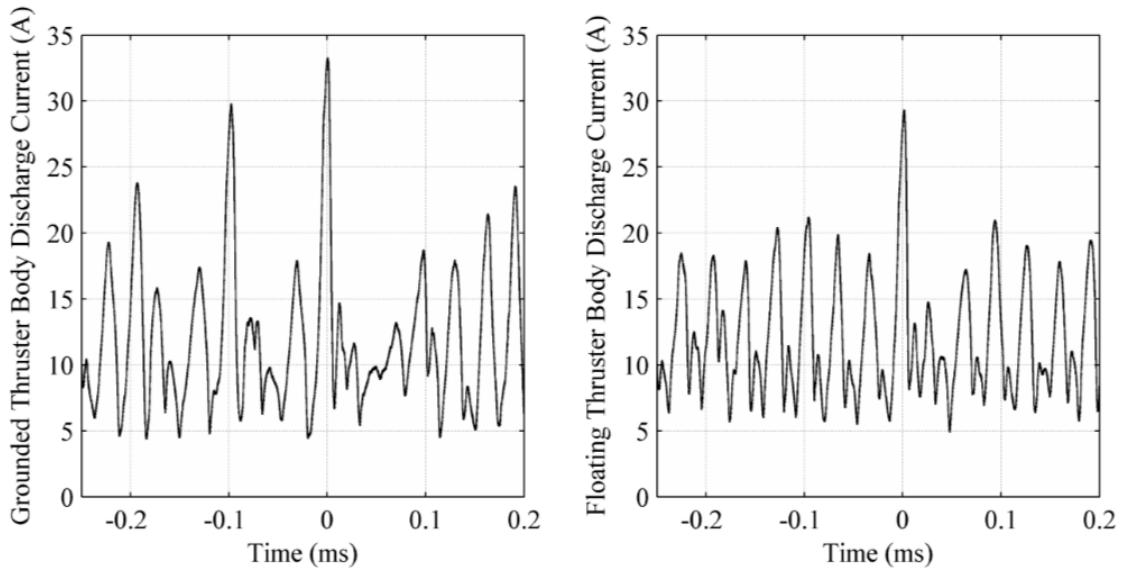


Figure 114: Discharge current peak event. Left) grounded thruster body. HET operating condition is 300 V, 3.5 kW. Right: electrically floating thruster body, HET operating condition is 300 V, 3.6 kW.

The structure of the discharge current peak event for the grounded thruster body configuration is marked by three distinct peaks in the discharge current. The structure of the discharge current peak event for the floating thruster body is marked by only one distinct peak in the discharge current. Examination of the discharge current peak events at the other thruster body-to-cathode voltages show that the multiple peaks structure in the discharge current peak event are only present when the thruster body-to-cathode voltage is positive. When the thruster body-to-cathode voltage becomes negative, the discharge current peak event contains only a single large peak. Because changes in the discharge current of the HET electrical circuit are directly related to changes in the physical processes in the discharge, the structural change in the discharge current peak event is indicative of large-scale changes to the physical processes on going in the HET discharge. To better understand what may be the source of why these structural changes at the crossover thruster body-to-cathode voltage, consider that the cathode produces electrons with a potential around the cathode-to-ground voltage. When the thruster body-to-cathode voltage is

positive, electrons in the near thruster body region are attracted to the thruster body. When the thruster body-to-cathode voltage is negative, electrons in the near thruster body region are repelled away from the thruster body. This is a zeroth order viewpoint. Because of the magnetic fields and time-varying discharge, electron transport between the cathode and the thruster body is a complex physical problem. The actual physical mechanisms that drive this delineation may be more complicated. Actual electron transport in the near field of the HET and cathode is an active area of research [10], and further investigation into this process is outside the scope of the thesis.

6.3.3 Thruster Body as an Electrical Load

As is evidenced throughout this thesis work, the thruster body collects a significant electron current. In the thruster body bias experimental configuration, the thruster body voltage bias is controlled by adjusting the resistance to ground of the thruster body. Because both the voltage and the current are measured simultaneously, the actual power dissipated through the thruster body can be calculated. Additionally, the time-resolved resistance to ground of the thruster body can also be calculated. Figure 115 shows the average power and peak-to-peak power dissipated from the plasma onto the thruster body.

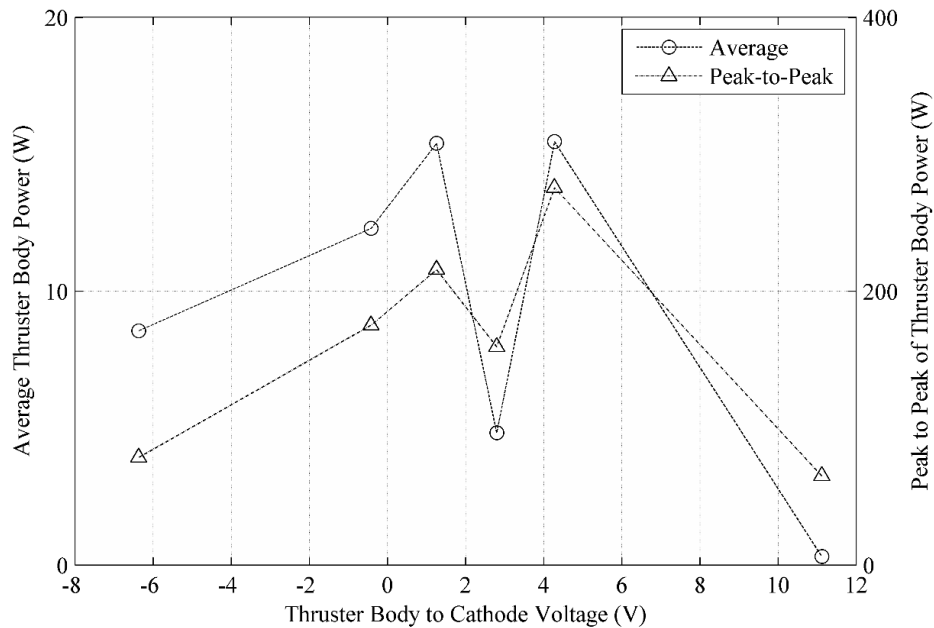


Figure 115: Power dissipation through the thruster body. The HET operating condition is at 300 V, 3.5 kW

The thruster body power, both time averaged and peak-to-peak, increases as the thruster to cathode voltage approaches 2.8 V. At a thruster body-to-cathode voltage of 2.8 V, there is a sudden drop in power dissipation to the thruster body. Examination of the time resolved power dissipation at that thruster body-to-cathode voltage reveals the cause for the sudden drop in power dissipation (Figure 116). While the majority of the power dissipated is positive, there are substantial lengths of time where the power dissipation become negative. These periods of time are preceded by sharp spikes in power dissipated into the thruster body circuit. The calculation of the average resistance of the thruster body at a thruster body-to-cathode voltage of 2.8 V results in a resistance of -4.6Ω . A negative resistance indicates that the thruster body to ground circuit is able to temporarily store energy (capacitively and/or inductively) and source power to the surrounding plasma. Such behavior of loads is characteristic of non-linear factors at play. A plasma can be coupled to a power source capacitively or inductively, so it stands to reason that at this behavior

could be due to a thruster body plasma interaction. To determine the exact reason for interaction would require work that is outside the scope of this investigation. As demonstrated from the results and analysis, however, the thruster body recombination pathway cannot be simply represented as a resistive pathway, and there are complex physical interactions ongoing between the thruster body and surrounding plasma.

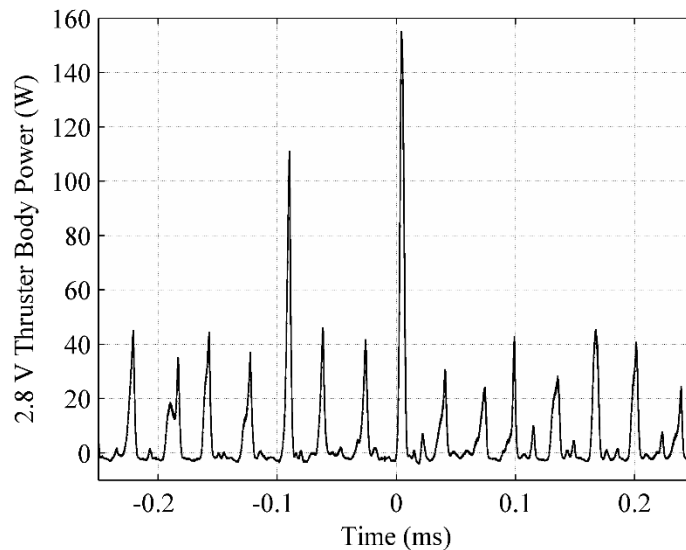


Figure 116: Thruster body power dissipation at a thruster body-to-cathode voltage of 2.8 V. The HET operating condition is at 300 V, 3.5 kW.

6.3.4 Summary of Findings from Thruster Body Biasing Experimental

Configuration

In this experimental configuration, the goal is to be able to change the availability of the thruster body recombination pathways and determine their influence on the HET operating behavior. Controlling the thruster body-to-cathode voltage is an effective method to directly manipulate the availability and structure of the thruster body recombination pathways. Subtle changes in the thruster body-to-cathode voltage are able to influence the thruster discharge. From a time-resolved perspective, the crossover between a positive or

negative thruster body-to-cathode voltage is an important factor in determining the coupling of the thruster body to the HET discharge and the structure of large-scale transients in the discharge current. As the thruster body approaches a floating electrical condition, the intensity of these transient events decreases, and the fundamental structure of these transient events changes. Overall, the findings from this work provide answers to the research question of how does the thruster body recombination current interact with the behavior of the HET by showing that the availability thruster body recombination pathway plays a direct role in the intensity and structure of quasi-periodic peak oscillations of the discharge current.

6.4 Implications for Ground Testing of Hall effect Thrusters

6.4.1 Cathode Coupling of the HET

Examination of the axial chamber plate and the thruster body current-to-ground time-delay gives insight into the interaction between the HET discharge circuit and the vacuum chamber. In cases (cathode positions 32.1 cm to 94.3 cm away from thruster centerline) where the axial chamber plate current-to-ground signal is strongly correlated to the discharge current peak, the axial chamber plate time-delay is shorter than the thruster body current time-delay. The thruster body current-to-ground time-delay is 42% to 45% greater than the axial chamber plate time-delay. This result is not anticipated as the thruster body is spatially closer to the HET discharge than the axial chamber plate. From the perspective of Frieman, et al. [22], Walker, et al. [94], a possible explanation of this additional time-delay is to consider that the cathode orifice is in a region of plume or radial wall electron termination. Electrons that are sourced from the cathode that impact the thruster body must first traverse to magnetic field lines that intersect the thruster body. This propagation of electrons requires some cross-field mobility and the fundamental time-scales for this cross-field mobility may be the source of the time-delay. Since the plasma environment in the near-field region of the HET discharge is complex and can support many plasma wave modes, it is difficult to pinpoint the exact mechanisms that control time-delay between the discharge current peak event and the response measured on the thruster body current-to-ground. From the perspective of the facility wall electrical interaction with the HET, another possible explanation of this additional time-delay is that electrical boundary conditions of the HET plume strongly influence the global plasma properties [97]. Therefore, it is possible that the changes in the local plasma properties that govern the current collection on the thruster body respond only after information about the plume electrical boundary condition propagates back through the plasma. Based on the results presented thus far, the timescales of the electron wave propagation as calculated in the

section above are the right order of magnitude for such a scenario. Furthermore, the cathode positions of strong correlation between the thruster body current-to-ground and the discharge current peak event approximately overlap with cathode positions that have strong correlation between the axial chamber plate current-to-ground and the discharge current peak event. Both of the aforementioned reasons imply that changes in the HET discharge plasma and HET beam first interact with the downstream facility surfaces before propagating those changes to the rest of the chamber facility.

Based on the arguments presented thus far, there are physical consequences for HET testing with cathodes in positions that have weak electron magnetization. In these cases, the HET discharge is strongly coupled to the facility walls. As seen by the results presented, the location of the cathode may influence how the chamber walls of the testing facility impact upstream conditions of the HET beam and near thruster discharge surfaces, *i.e.*, the thruster body. Therefore, HET architectures that incorporate a spatially-separated cathode must carefully consider the impact how the downstream walls of the vacuum chamber interact with the thruster.

6.4.2 Comparison Hall Effect Thruster Operation to The SMART-1 Mission

From the perspective of the HET electrical circuit, the bias voltage of the axial chamber plate acts to enforce a pseudo far-field plasma potential boundary condition. The axial plate is able to drive the plasma potential by mediating the electron-ion loss rate to the facility walls. The resulting increase in plasma potential and cathode-to-ground potential is similar to behavior observed during the SMART-1 mission [51, 55]. The plasma potential, during the SMART-1 mission, was measured using the Electric Propulsion Diagnostic Package (EPDP) and placed downstream from the thruster exit plane and in a “low” ion-energy region of the PPS-1350 plume [49]. The measured difference between the cathode-to-ground voltage and the plasma potential remained approximately 19 V [51] throughout the mission. As shown in Figure 56, there is similar fixed voltage

difference between the HET floating voltage and the centerline plasma potential. The influence on the axial chamber plate on the HET floating circuit voltage and plasma potential is only evident once the axial chamber plate is able to collect a net electron current. Due to the high mobility of the electrons versus xenon ions, this occurs at a low, > 5 V, voltage above ground. Once the axial plate bias voltage is able to establish net electron current collection, the axial chamber plate begins to induce global changes in the HET plume and HET electrical circuit. Overall, the potential difference behavior between the plasma potential and the cathode-to-ground potential for the T-140 HET tested is similar to the behavior experienced by the PPS-1350 in-flight operation.

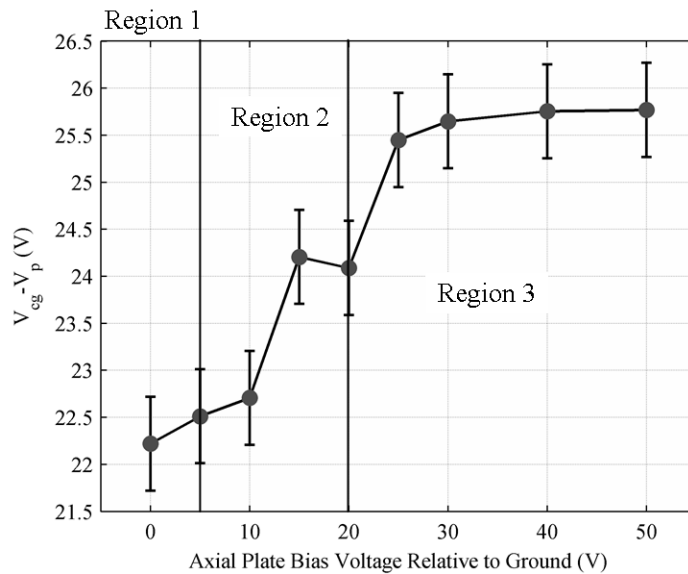


Figure 117: Potential difference between Plasma Potential and Cathode-to-Ground Potential as a function of axial plate bias voltage. (Plasma potential is taken at an angular position of -45°). The HET operating condition is 300 V, 3.1 kW

A closer examination of the data collected in this experiment reveals that the difference between the plasma potential and the cathode-to-ground voltage has a small dependence on the axial chamber plate bias. The difference between the plasma potential at an angular position of -45° relative to thruster centerline and cathode-to-ground potential

is shown in Figure 117. Given the placement of the EPDP, this angular position is in similar region of the HET beam. At lower axial chamber plate biases (0 V to 15 V), where the beam current is not fully collected by the plate, there is an increase in this voltage difference by approximately 1 V to 2 V as compared to the nominal case. At higher axial chamber plate biases (20 V to 50 V), the difference between the cathode-to-ground voltage and the plasma potential increases by approximately 2 V to 4 V relative to the nominal condition. This voltage difference behavior is consistent with trends overserved at other angular positions. The increase in the potential difference would result in a change in thrust of the T-140 that would be smaller than the resolution of the calibration of the thrust-stand used in this investigation and is consistent with expectations based on Frieman et. al [72]. Though the change in thrust is not measurable with the thrust stand used in this investigation, the change in the potential difference between the cathode and the ambient plasma potential is indicative of a change in the efficiency of the HET electrical circuit in extracting electrons from the cathode [3]. In connection to the in-flight environment, the HET plasma potential is heavily influenced by the interaction with any charged surfaces such as the unshielded low voltage solar panel contacts as seen in the SMART-1 mission [51, 55]. As seen in this investigation, a variation in the plasma potential boundary condition relative to the HET would result in changes cathode coupling efficiency.

6.4.3 Electrical Configuration of the Thruster Body

Insight on the thruster body recombination circuit can be gained from examining how the HET electrical circuit and thruster body chassis was integrated in the SMART-1 Mission [51-53]. In the case of the SMART-1 Mission, the HET discharge circuit was isolated from the satellite common via 1 M Ω and 50 k Ω resistors and the HET thruster body chassis was connected directly to the satellite common. In this case, the thruster body-to-cathode voltage varied between – 5 V and 12 V. The analysis from the thruster body bias experimental configuration demonstrated that such a change in thruster body-to-

cathode voltage can induce large scale changes to the transient behavior of the discharge current. Depending on the thruster body-to-cathode voltage, the discharge current peak-to-peak varied between 29.3 A and 24.5 A. Such large swings in the discharge current correlate to large swings in the momentary power load on the discharge supply. For a scientific power supply behind a discharge filter, this is not so much of a problem. But for a flight unit power processing unit, such large swings in power load could be disastrous.

The large swings in the power deposition on the thruster body (as is discussed in section 6.3.3) could also have a large impact on the electrical potential of the satellite bus common and satellite chassis. Since the thruster body is directly tied to the satellite common, there is a direct electrical path between the satellite electrical system and the HET discharge circuit. This means that the HET discharge can directly influence the potential of the satellite bus common and satellite chassis. The potential of the spacecraft itself is an active area of concern for satellite builders and mitigating or accounting for the effects of spacecraft charging is something that must be done in order for successful on-orbit satellite operation [103]. This means that for successful HET integration and operation, consideration must be given on how the thruster body will interact with the entire spacecraft. Overall, the results of the thruster body bias experimental configuration indicate that the thruster body-to-cathode potential is a key factor to examine during the ground testing of HETs that can be used to assess the impact of the thruster body on the HET, HET electrical circuit, and possibly the electrical circuit of the satellite.

6.4.4 The Configuration of Ground-Based Vacuum Facilities

The results and analysis presented in this thesis thus far have strongly indicated that the chamber walls of the vacuum chamber are a part of the HET electrical circuit and have an impact on the measured characteristics of the operating HET. The question of what would be the desired ground testing configuration that would better represent the electrical

boundary conditions present on orbit must be addressed. The first thing to consider is the size of the vacuum chamber. This work has shown that the Langmuir wave mode is the primary physical mechanism that connects the HET discharge in both the radial and axial directions to the far-field electrical boundaries of the plume, *i.e.* the chamber wall. The Langmuir wave mode is a fundamental plasma mode that requires no external magnetic or electric fields to be present; therefore, the HET can always electrically communicate with boundaries of the HET plume. To size a vacuum chamber appropriately to represent the on-orbit HET plume electrically conditions, the size of the HET plume on orbit is considered. This size is dictated by the interaction of the plume with the physical environment on-orbit. This environment at the boundary conditions of the HET plume could be but is not limited to other plasma environments surrounding the satellite. For example, the solar wind plasma environment is a common plasma environment that satellites regularly encounter during on-orbit operation. In this case, the HET plume characteristics would start to interact with the solar wind plasma environment once the HET plume plasma density reaches a similar order of magnitude as the solar wind plasma density. Based on the Encyclopedia of Astronomy and Astrophysics, the solar wind number density is on the order of 10 particles/cm⁻³ [104]. Examination of the HET plume density profile, as shown in Figure 59, indicate that the plasma density of the T-140 HET at thruster centerline, 1-meter downstream of the exit plane of the discharge channel is of the order of 10¹⁰ particles/cm⁻³. To zeroth-order, the plasma density in the plume scales inversely to the square of the distance away from the thruster [3]. Ignoring collisions within the plume (neutral and recombination), the distance at which the HET plume number density decreases from 10¹⁰ particles/cm⁻³ to 10 particles/cm⁻³ would be on the order of 10 km. In order for a vacuum test facility to be appropriately sized to emulate the electrical boundary conditions that a HET operating on-orbit would experience while interacting with the solar wind, the vacuum facility walls must on the order of 10 km away from the thruster. For

perspective, the largest vacuum facility in the world, the Space Power Facility at NASA Plumbrook, is 100 ft. in diameter and 122 ft. high. It would be an understatement to say the construction and operation of a 10 km scale vacuum facility would be challenging; therefore, other avenues of accounting for the difference in electrical boundary conditions must be pursued. For example, one method, as discussed in the axial chamber plate bias experimental configuration, would be to bias the axial chamber plate voltage such that grounded surfaces exposed to the HET plume are removed from the HET electrical circuit. By biasing the axial chamber plate voltage, the plasma potential of the entire HET plume can be raised such that there is no net current collected on grounded surfaces such as walls of the chamber (see Figure 54) and the thruster body itself (see Figure 110). If there is no net current being collected on a particular surface, that electron termination pathway is effectively removed for the HET electrical circuit. Aside from the axial chamber plate bias, the overall methodologies and analysis presented in this dissertation work offer other possible alternatives to better emulate the on-orbit electrical boundary conditions of a HET in a ground testing environment.

Chapter VII

Contributions and Future Work

7.1 Electrical Facility Effects Contributions

7.1.1 Contributions to the Understanding of Chamber Wall-Hall Effect Thruster Interactions

The first research question of this dissertation work is: How does the chamber wall charge recombination pathway interact with the Hall effect thruster? The experimental work and the analysis presented in this work provide insight to this question. Changes in the discharge of the HET that directly influence the chamber wall to HET plume interaction propagate outward from the thruster via Langmuir waves. The chamber wall recombination pathway mainly influences the characteristics of the HET plume. Through the sheath potential drop at the walls of the vacuum facility, the plasma potential in the plume of the HET is artificially lowered. As the availability of the chamber wall recombination pathway decreases, the plasma potential of the HET plume begins to increase globally. The rise in plasma potential is due to the reduction in the charge-loss rate to the walls of the vacuum chamber and the additional power added to the plume in order to reduce this availability. At high enough plume plasma potentials, the current collected on the radial walls decouples from the HET. This is due to the adverse electron potential gradient that exists between the plasma and the grounded walls. This decoupling of the HET plume from the grounded walls of the vacuum facility also coincides with a rise in the ion current density of the HET off-axis plume. With respect to the HET operation, the HET electrical circuit floating voltage is set by the cathode and the ambient plasma conditions in the near field of the HET. As the plasma potential rises, the floating circuit responds to these changes in the plasma potential by floating to higher voltages. Prior to this work, the exact impact of the walls on the HET was not known. This work is able to contribute to the field of

HET ground testing by identifying key mechanisms that govern the chamber wall-HET electrical interaction. Since the plume structure is an important consideration during HET-satellite integration, this work is able to contribute to the field of HET ground testing by demonstrating that the plume of the HET is influenced by the walls of the vacuum chamber, and by laying the ground work for a method to recreate a more on-orbit like plume conditions within the ground-testing facility via the axial chamber plate bias voltage control methodology. Ultimately, this work demonstrates that the walls of the ground test facility are an important consideration for the ground testing of HET.

7.1.2 Contributions to the Understanding of the Thruster Body-Hall effect Thruster Interaction

The second research question of this dissertation effort is: How does the electrical boundary condition of the thruster body itself affect the operation of Hall effect thruster? The experimental work and the analysis presented in this work provide insight to this question. The thruster body interacts primarily with the HET electrical circuit through changes in the discharge current. When the thruster body is electrically grounded, the thruster body collects a relatively large fraction of neutralization electrons sourced by the cathode. As the voltage difference between the thruster body and the cathode decreases and approaches the floating voltage of the thruster body, the availability of the thruster body as an electron termination site decreases. These changes in availability of the thruster body coincide with an overall decrease in the intensity of quasi-periodic discharge current oscillation events. Prior to this work, it was unknown if the thruster body played an active role in the HET electrical circuit. This work contributes to the field of HET ground testing by demonstrating that the thruster body of the HET is an active component in the electrical circuit. At certain thruster body-to-cathode voltages, the thruster body chassis can store electrical energy storage and re-emit that back into the surrounding plasma. Since power processing units are specifically made to accommodate certain characteristics of the HET

electrical load, this work contributes to the field of HET ground testing by showing that the electrical configuration of the thruster body can have major impacts on the characteristics of the discharge current of the HET. Since HETs go through several physical changes through the design process, this work contributes to the field of HET ground testing by demonstrating that the structure of the charge recombination currents depends on the thruster body to cathode voltage. If there are operational characteristics of the HET that are dependent on a particular structure of the thruster body recombination currents, then changes to this structure may have unintended consequences on HET operation. In summary, the work done on the thruster body-HET interactions is able to provide key-insights into a previously over-looked factor to consider during ground testing.

7.2 Future Work

More work remains in the field of electrical facility effects in HET ground-based testing. There are several limitations of this dissertation work that need to be addressed in future work related to electrical facility effects. In particular, the findings of this work are limited to a single thruster, a single operating condition, and a single operating neutral pressure. Because of this limitation, this work is unable to fully determine if there are certain operational or design thresholds that govern charge recombination pathway dependent HET behaviors. It may even be the case that at certain operating conditions or with certain HET designs more characteristics of the HET are dependent on the charge recombination currents present in the ground testing environment. To gain a better understanding of these possibilities, it is imperative to repeat some of this work at different operating conditions or on different thrusters.

While this work is able to investigate the physical mechanisms that govern the chamber wall-HET interaction, this work is unable to pinpoint the physical mechanisms that govern the near-field interactions between the HET and the thruster body. Because the

design of the HET can change many times during the development cycle and specific implementations of a particular HET vary from satellite to satellite, information regarding the physical mechanisms controlling the HET and the thruster body interaction would be extremely valuable information. However, the plasma environment in the near-field of the HET is quite complex and understanding the physical mechanisms occurring in that region is ongoing area of research. If the physical mechanisms that govern the thruster body-HET interaction were better understood, then a better understanding can be gained on how variations in the thruster design, magnetic field topology, thruster operating condition, and ambient neutral pressure affect the thruster body-HET interaction.

While the structural changes measured on the thruster body are significant in that they indicate that structure of the thruster body recombination current can change, the finding itself is somewhat limited. The combined collected current of all thruster body plates account for less than 3 % of the total collected current. This means that the structural change observed is not indicative of large, whole-scale changes to the structure of the thruster body recombination currents. To better understand if large, whole scale changes to the thruster body recombination current can occur, it is important to directly identify the actual thruster surface that collects a majority of the thruster body current-to-ground. In actuality, it is unknown whether the thruster body current collection to ground is a localized to a specific surface or distributed over the entirety of thruster body. Related to the aforementioned suggested work on understanding the physical mechanisms that govern the HET-thruster interaction, knowledge of the physical mechanisms governing the thruster body current collection process would be able to narrow down the scope of possible thruster body surfaces. Determining this issue is of key importance, as HETs go through many design changes as a particular design approaches flight maturity. If the thruster body current is a localized phenomenon, then minor changes to the construction of the HET along the development cycle may have unintended consequences on the HET operation.

One major question that this work is unable to address is which recombination pathways are the biggest factors to consider during ground testing. Based on the work and analysis of the axial chamber plate experimental configuration and the thruster body experimental configuration, these surfaces fall into two categories: conductive surfaces within the magnetic field of the HET and conductive surfaces exterior of the HET magnetic field. Common conductive surfaces within the magnetic field of the HET include the thruster body, thrust stand structures, or even HET mounting structures. Common conductive surfaces exterior of the HET magnetic field includes the chamber walls, diagnostic support structures, or facility support structures. To better understand the impact of these kinds of conductive surfaces on the HET electrical circuit, it would be imperative to measure or model the plasma environment surrounding those conductive surfaces. Understanding those plasma conditions in both a static and dynamic way would allow for a more precise method of adjusting the electrically boundary conditions of those surfaces to be determined. In such case, those measurements would make it much easier to pinpoint the exact physical mechanisms that drive the influence of those conductive surfaces on the HET. In doing so, a better assessment of which recombination pathways are the biggest factors to consider during ground testing can be addressed.

The line of investigation related electrical facility effects on HET operation is still a new field of research. There are still many unknowns about how the HET electrically interacts with the vacuum chamber facility. With the increased interest in the usage of HETs for in-space applications, a better understanding of facility effects, in general, on HET ground-testing is vital. By tackling these aforementioned areas of suggested future work, a much better understanding of electrical facility effects can be gained.

REFERENCES

1. Jahn, R. G. *Physics of Electric Propulsion*. New York, New York: Courier Dover Publications, 2012.
2. Wertz, J. R., and Larson, W. J. *Space Mission Analysis and Design*: Springer Netherlands, 1999.
3. Goebel, D. M., and Katz, I. *Fundamentals of Electric Propulsion: Ion and Hall Thrusters*. Hoboken, New Jersey: John Wiley & Sons, 2008.
4. Manzella, D. H. "Scaling Hall Thrusters to High Power," *Mechanical Engineering*. Vol. Ph.D., Stanford University, Stanford, CA, 2005, p. 127.
5. Zhurin, V. V., Kaufman, H. R., and Robinson, R. S. "Physics of closed drift thrusters," *Plasma Sources Science and Technology* Vol. 8, No. 1, 1999, p. R1.
6. Dankanich, J. W., and McAdams, J. "Interplanetary Electric Propulsion Uranus Mission Trades Supporting The Decadal Survey," *Spaceflight Mechanics 2011, Pts I-Iii*. Vol. 140, Univelt Inc, San Diego, 2011, pp. 1271-1289.
7. Grys, K. d., Mathers, A., Welander, B., and Khayms, V. "Demonstration of 10,400 Hours of Operation on 4.5 kW Qualification Model Hall Thruster," *46th AIAA/ASME/SAE/ASEE Joint Propulsion Conference & Exhibit*. Vol. AIAA 2010-6698, American Institute of Aeronautics and Astronautics, July 2010.
8. Dankanich, J. W., and Oleson, S. R. "Interplanetary Electric Propulsion Chiron Mission Trades Supporting The Decadal Survey," *Spaceflight Mechanics 2011, Pts I-Iii*. Vol. 140, Univelt Inc, San Diego, 2011, pp. 1245-1255.
9. Mikellides, I. G., Goebel, D. M., Snyder, J. S., Katz, I., and Herman, D. A. "The discharge plasma in ion engine neutralizers: Numerical simulations and comparisons with laboratory data," *Journal of Applied Physics* Vol. 108, No. 11, 2010, p. 12.
doi: 10.1063/1.3514560
10. Jorns, B. A., Mikellides, I. G., and Goebel, D. M. "Ion acoustic turbulence in a 100-A LaB6 hollow cathode," *Physical Review E* Vol. 90, No. 6, 2014, p. 063106.
11. Mikellides, I. G., Katz, I., Hofer, R. R., and Goebel, D. M. "Magnetic shielding of a laboratory Hall thruster. I. Theory and validation," *Journal of Applied Physics* Vol. 115, No. 4, 2014, p. 043303.
doi: doi:http://dx.doi.org/10.1063/1.4862313
12. Randolph, T., Kim, V., Kaufman, H. R., Kozubsky, K., Zhurin, V. V., and Day, M. "Facility Effects on Stationary Plasma Thruster Testing," *23rd International Electric Propulsion Conference*. Vol. IEPC-93-93, Seattle, WA, USA, 1993, p. 844.
13. Hofer, R. R., Peterson, P. Y., and Gallimore, A. "Characterizing Vacuum Facility Backpressure Effects on the Performance of a Hall Thruster," *27th International Electric Propulsion Conference*. Vol. IEPC-01-045, Passadena, CA, USA, 2001.

14. Walker, M. L. R., Victor, A. L., Hofer, R. R., and Gallimore, A. D. "Effect of backpressure on ion current density measurements in hall thruster plumes," *Journal of Propulsion and Power* Vol. 21, No. 3, 2005, pp. 408-415.
doi: 10.2514/1.7713
15. Walker, M. L. R. "Effects of Facility Backpressure on the Performance and Plume of a Hall Thruster," *Aerospace Engineering*. Vol. Ph.D., The University of Michigan, Ann Arbor, Michigan, 2005.
16. Walker, M. L. R., and Gallimore, A. D. "Neutral density map of Hall thruster plume expansion in a vacuum chamber," *Review of Scientific Instruments* Vol. 76, No. 5, 2005.
doi: 10.1063/1.1915011
17. Byers, D., and Dankanich, J. W. "A Review of Facility Effects on Hall Effect Thrusters," *31st International Electric Propulsion Conference*. Vol. IEPC-2009-076, Ann Arbor, Michigan, USA, 2009.
18. Brown, D. L., and Gallimore, A. D. "Evaluation of ion collection area in Faraday probes," *Review of Scientific Instruments* Vol. 81, No. 6, 2010.
doi: 10.1063/1.3449541
19. Sommerville, J. D., and King, L. B. "Hall-Effect Thruster-Cathode Coupling, Part I: Efficiency Improvements from an Extended Outer Pole," *Journal of Propulsion and Power* Vol. 27, No. 4, 2011, pp. 744-753.
doi: 10.2514/1.50123
20. Brown, D. L., and Gallimore, A. D. "Evaluation of Facility Effects on Ion Migration in a Hall Thruster Plume," *Journal of Propulsion and Power* Vol. 27, No. 3, 2011, pp. 573-585.
doi: 10.2514/1.b34068
21. Xu, K. G., and Walker, M. L. R. "Effect of External Cathode Azimuthal Position on Hall-Effect Thruster Plume and Diagnostics," *Journal of Propulsion and Power* Vol. 30, No. 2, 2014, pp. 506-513.
doi: 10.2514/1.b34980
22. Frieman, J. D., Walker, J. A., Walker, M. L. R., Khayms, V., and King, D. "Electrical Facility Effects on Hall Effect Thruster Cathode Coupling: Performance and Plume Properties," *Journal of Propulsion and Power*, 2015, pp. 1-14.
doi: 10.2514/1.B35683
23. Kamhawi, H., Huang, W., Haag, T., and Spektor, R. "Investigation of the Effects of Facility Background Pressure on the Performance and Operation of the High Voltage Hall Accelerator," *50th AIAA/ASME/SAE/ASEE Joint Propulsion Conference*. Vol. AIAA 2014-3707, American Institute of Aeronautics and Astronautics, Cleveland, Ohio, July 2014.
24. Walker, J. A., Frieman, J. D., Walker, M. L., Khayms, V., King, D., and Peterson, P. "Electrical Facility Effects on Hall Effect Thruster Cathode Coupling: Discharge Oscillations and Facility Coupling," *50th AIAA/ASME/SAE/ASEE Joint Propulsion Conference*. Vol. AIAA 2014-3711, American Institute of Aeronautics and Astronautics, Cleveland, Ohio, 2014.
25. Crofton, M. W., and Boyd, I. D. "Momentum Modeling of a Hall Thruster Plume," *The 33rd International Electric Propulsion Conference*. Vol. IEPC-2013-374, Washington D.C. USA, 2013.

26. Crofton, M. W., and Pollard, J. "Thrust Augmentation by Charge Exchange," *49th AIAA/ASME/SAE/ASEE Joint Propulsion Conference*. American Institute of Aeronautics and Astronautics, 2013.
27. Hofer, R. R., and Anderson, J. R. "Finite Pressure Effects in Magnetically Shielded Hall Thrusters," *50th AIAA/ASME/SAE/ASEE Joint Propulsion Conference*. Vol. AIAA 2014-3709, American Institute of Aeronautics and Astronautics, 2014.
28. Nakles, M. R., and Hargus, W. A., Jr. "Background Pressure Effects on Ion Velocity Distribution Within a Medium-Power Hall Thruster," *Journal of Propulsion and Power* Vol. 27, No. 4, 2011, pp. 737-743.
doi: 10.2514/1.48027
29. Huang, W., Kamhawi, H., Lobbia, R. B., and Brown, D. L. "Effect of Background Pressure on the Plasma Oscillation Characteristics of the HiVHAc Hall Thruster," *50th AIAA/ASME/SAE/ASEE Joint Propulsion Conference*. Vol. AIAA 2014-3708, American Institute of Aeronautics and Astronautics, July 2014.
30. McDonald, M. S., Sekerak, M. J., Gallimore, A. D., and Hofer, R. R. "Plasma Oscillation Effects on Nested Hall Thruster Operation and Stability," *2013 IEEE Aerospace Conference*. Vol. IEEEAC Paper #2502, Big Sky, MT, USA, 2013.
31. Hara, K., Sekerak, M. J., Boyd, I. D., and Gallimore, A. D. "Mode transition of a Hall thruster discharge plasma," *Journal of Applied Physics* Vol. 115, No. 20, 2014.
doi: 10.1063/1.4879896
32. Sekerak, M., Longmeir, B., Gallimore, A., Huang, W., Kamhawi, H., Hofer, R. R., Jorns, B., and Polk, J. E. "Mode Transitions in Magnetically Shielded Hall Effect Thrusters," *50th AIAA/ASME/SAE/ASEE Joint Propulsion Conference*. Vol. AIAA 2014-3511, American Institute of Aeronautics and Astronautics, Cleveland, OH, July 2014.
33. Hara, K., Sekerak, M. J., Boyd, I. D., and Gallimore, A. D. "Perturbation analysis of ionization oscillations in Hall effect thrusters," *Physics of Plasmas (1994-present)* Vol. 21, No. 12, 2014, pp. -.
doi: doi:http://dx.doi.org/10.1063/1.4903843
34. Sekerak, M., McDonald, M., Hofer, R., and Gallimore, A. "Hall Thruster Plume Measurements from High-Speed Dual Langmuir Probes with Ion Saturation Reference," *2013 IEEE Aerospace Conference*. Big Sky, MT, USA, 2013.
35. Sekerak, M. "Plasma Oscillations and Operational Modes in Hall Effect Thrusters," *Aerospace Engineering*. Vol. Ph. D., University of Michigan, Ann Arbor, Ann Arbor, Michigan, 2014.
36. Brown, D. L., Blakely, J. M., and Lobbia, R. B. "Low-Voltage Hall Thruster Mode Transitions," *50th AIAA/ASME/SAE/ASEE Joint Propulsion Conference*. American Institute of Aeronautics and Astronautics, 2014.
37. Jameson, K. K., Goebel, D. M., Hofer, R. R., and Watkins, R. M. "Cathode Coupling in Hall Thruster," *30th International Electric Propulsion Conference*. Vol. IEPC 2007-278, IEPC, Florence, Italy, 2007.
38. Hofer, R. R., Johnson, L. K., Goebel, D. M., and Wirz, R. E. "Effects of Internally Mounted Cathodes on Hall Thruster Plume Properties," *Ieee Transactions on Plasma Science* Vol. 36, No. 5, 2008, pp. 2004-2014.
doi: 10.1109/tps.2008.2000962

39. Goebel, D. M., Jameson, K. K., and Hofer, R. R. "Hall Thruster Cathode Flow Impact on Coupling Voltage and Cathode Life," *Journal of Propulsion and Power* Vol. 28, No. 2, 2012, pp. 355-363.
doi: 10.2514/1.b34275
40. McLean, C., McVey, J., and Schappell, T. "Testing of a U.S.-built HET system for orbit transfer applications," *35th Joint Propulsion Conference and Exhibit*. Vol. A99-31318, American Institute of Aeronautics and Astronautics, 1999.
41. Diamant, K. D., Liang, R., and Corey, R. L. "The Effect of Background Pressure on SPT-100 Hall Thruster Performance," *50th AIAA/ASME/SAE/ASEE Joint Propulsion Conference*. Vol. AIAA 2014-3710, American Institute of Aeronautics and Astronautics, 2014.
42. Diamant, K., Spektor, R., Beiting, E., Young, J., and Curtiss, T. "The Effects of Background Pressure on Hall Thruster Operation," *48th AIAA/ASME/SAE/ASEE Joint Propulsion Conference & Exhibit*. Vol. AIAA 2012-3735, American Institute of Aeronautics and Astronautics, Atlanta, GA, July 2012.
43. "571 Ionization Gauge Tube Instruction Manual." Vol. Manual No. 6999905571 Revision C, 2002.
44. Tilford, C. R. "Sensitivity of hot cathode ionization gages," *Journal of Vacuum Science & Technology A* Vol. 3, No. 3, 1985, pp. 546-550.
doi: <http://dx.doi.org/10.1116/1.572991>
45. Tilford, C. R., McCulloh, K. E., and Woong, H. S. "Performance characteristics of a broad range ionization gage tube," *Journal of Vacuum Science & Technology* Vol. 20, No. 4, 1982, pp. 1140-1143.
doi: <http://dx.doi.org/10.1116/1.571590>
46. Sommerville, J., and King, L. "Effect of Cathode Position on Hall-Effect Thruster Performance and Near-Field Plume Properties," *44th AIAA/ASME/SAE/ASEE Joint Propulsion Conference & Exhibit*. Vol. AIAA 2008-4996, American Institute of Aeronautics and Astronautics, 2008.
47. Manzella, D. H., Jankovsky, R., Elliot, F., Mikellides, I., Jongeward, G., and Allen, D. "Hall Thruster Plume Measurements On-board the Russian Express Satellites," *27th International Electric Propulsion Conference*. Vol. IEPC-2001-044, Pasadena, CA, USA, 2001.
48. Boyd, I. D., and Dressler, R. A. "Far field modeling of the plasma plume of a Hall thruster," *Journal of Applied Physics* Vol. 92, No. 4, 2002, pp. 1764-1774.
doi: 10.1063/1.1492014
49. Matticari, G., Noci, G., Estublier, D., del Amo, J. G., Marini, A., Tajmar, M., Esa, Esa, and Esa. "The SMART-1 Electric Propulsion diagnostic package," *Third International Conference on Spacecraft Propulsion*. Vol. 465, 2000, pp. 661-668.
50. Tremolizzo, E., Meier, H., and Estublier, D. "In-flight disturbance torque evaluation of the smart-1 plasma thruster," *Proceedings of the 18th International Symposium on Space Flight Dynamics*. Vol. 548, 2004, pp. 303-306.
51. Koppel, C., Marchandise, F., Estublier, D., and Jolivet, L. "The Smart-1 Electric Propulsion Subsystem In Flight Experience," *40th AIAA/ASME/SAE/ASEE Joint Propulsion Conference and Exhibit*. Vol. AIAA 2004-3435, American Institute of Aeronautics and Astronautics, 2004.

52. Koppel, C., Marchandise, F., Prioul, M., Estublier, D., and Darnon, F. "The Smart-1 Electric Propulsion Subsystem Around the Moon: In Flight Experience," *41st AIAA/ASME/SAE/ASEE Joint Propulsion Conference & Exhibit*. Vol. AIAA 2005-3671, American Institute of Aeronautics and Astronautics, Tucson, Arizona, USA, 2005.
53. Milligan, D., Camino, O., and Gestal, D. "SMART-1 Electric Propulsion: An Operational Perspective," *SpaceOps 2006 Conference*. American Institute of Aeronautics and Astronautics, Rome, 2006.
54. Snyder, J. S., and Hofer, R. R. "Throttled Performance of the SPT-140 Hall Thruster," *50th AIAA/ASME/SAE/ASEE Joint Propulsion Conference*. Vol. AIAA 2014-3816, American Institute of Aeronautics and Astronautics, 2014.
55. Passaro, A., Vicini, A., Nania, F., and Biagioni, L. "Numerical Rebuilding of SMART-1 Hall Effect Thruster Plasma Plume," *Journal of Propulsion and Power* Vol. 26, No. 1, 2010, pp. 149-158.
doi: 10.2514/1.36921
56. Korsun, A., and Tverdokhlebova, E. "The characteristics of the EP exhaust plume in space," *33rd Joint Propulsion Conference and Exhibit*. American Institute of Aeronautics and Astronautics, 1997.
57. Korsun, A. G., Tverdokhlebova, E. M., and Gabdullin. "The Distinction Between the EP Plume Expansion in Space and in Vacuum Chamber," *29th International Electric Propulsion Conference*. Vol. IEPC-2005-073, Princeton, New Jersey, USA, 2005.
58. Morozov, A. I., and Savelyev, V. V. "Fundamentals of Stationary Plasma Thruster Theory," *Reviews of Plasma Physics*. Springer US, Boston, MA, 2000, pp. 203-391.
59. Choueiri, E. Y. "Plasma oscillations in Hall thrusters," *Physics of Plasmas* Vol. 8, No. 4, 2001, pp. 1411-1426.
doi: 10.1063/1.1354644
60. Jahn, R. G., and Choueiri, E. Y. "Electric Propulsion," *Encyclopedia of Physical Science and Technology (Third Edition)*. Academic Press, New York, 2003, pp. 125-141.
61. Mazouffre, S., Bourgeois, G., Garrigues, L., and Pawelec, E. "A comprehensive study on the atom flow in the cross-field discharge of a Hall thruster," *Journal of Physics D-Applied Physics* Vol. 44, No. 10, 2011, p. 8.
doi: 10.1088/0022-3727/44/10/105203
62. "Smart-1 Operations Experience and Lessons Learnt," *57th International Astronautical Congress*. American Institute of Aeronautics and Astronautics, 2006.
63. Vaudolon, J., Khiar, B., and Mazouffre, S. "Time evolution of the electric field in a Hall thruster," *Plasma Sources Science & Technology* Vol. 23, No. 2, 2014.
doi: 10.1088/0963-0252/23/2/022002
64. Sommerville, J. D., and King, L. B. "Hall-Effect Thruster-Cathode Coupling, Part II: Ion Beam and Near-Field Plume," *Journal of Propulsion and Power* Vol. 27, No. 4, 2011, pp. 754-767.
doi: 10.2514/1.50124
65. Goebel, D. M., Jameson, K. K., Watkins, R. M., Katz, I., and Mikellides, I. G. "Hollow cathode theory and experiment. I. Plasma characterization using fast

- miniature scanning probes," *Journal of Applied Physics* Vol. 98, No. 11, 2005, p. 113302.
- doi: [doi:http://dx.doi.org/10.1063/1.2135417](http://dx.doi.org/10.1063/1.2135417)
66. Hofer, R., Johnson, L., Goebel, D., and Fitzgerald, D. "Effects of an Internally-Mounted Cathode on Hall Thruster Plume Properties," *42nd AIAA/ASME/SAE/ASEE Joint Propulsion Conference & Exhibit*. Vol. AIAA 2006-4482, American Institute of Aeronautics and Astronautics, 2006.
67. Walker, M. L. R., and Gallimore, A. D. "Hall thruster cluster operation with a shared cathode," *Journal of Propulsion and Power* Vol. 23, No. 3, 2007, pp. 528-536.
- doi: 10.2514/1.23688
68. Mikellides, I. G., Katz, I., Goebel, D. M., Jameson, K. K., and Polk, J. E. "Wear Mechanisms in Electron Sources for Ion Propulsion, II: Discharge Hollow Cathode," *Journal of Propulsion and Power* Vol. 24, No. 4, 2008, pp. 866-879.
- doi: 10.2514/1.33462
69. Mikellides, I. G., Katz, I., Goebel, D. M., and Polk, J. E. "Hollow cathode theory and experiment. II. A two-dimensional theoretical model of the emitter region," *Journal of Applied Physics* Vol. 98, No. 11, 2005, p. 113303.
- doi: [doi:http://dx.doi.org/10.1063/1.2135409](http://dx.doi.org/10.1063/1.2135409)
70. Yu, D., Wang, C., Wei, L., Gao, C., and Yu, G. "Stabilizing of low frequency oscillation in Hall thrusters," *Physics of Plasmas* Vol. 15, No. 11, 2008.
- doi: 10.1063/1.3023150
71. Spektor, R., Willhoff, M. A., Beiting, E., and Diamant, K. "Characterization of the High Power Propulsion System Subscale," *60th JANNAF Propulsion Meeting*. Vol. JANNAF-2013-3142, Colorado Springs, CO, 2013.
72. Frieman, J. D., King, S. T., Walker, M. L. R., Khayms, V., and King, D. "Role of a Conducting Vacuum Chamber in the Hall Effect Thruster Electrical Circuit," *Journal of Propulsion and Power* Vol. 30, No. 6, 2014, pp. 1471-1479.
- doi: 10.2514/1.B35308
73. Hutchinson, I. H., and Chen, F. F. "INTRODUCTION TO PLASMA PHYSICS AND CONTROLLED FUSION, VOL 1, PLASMA PHYSICS, 2ND EDITION," *Nature* Vol. 312, No. 5996, 1984, p. 790.
- doi: 10.1038/312790b0
74. Boyd, I. D., and Crofton, M. W. "Numerical Momentum Tracking for a Hall Thruster Plume," *50th AIAA/ASME/SAE/ASEE Joint Propulsion Conference*. American Institute of Aeronautics and Astronautics, 2014.
75. Lobbia, R. B. "A Time-resolved Investigation of the Hall Thruster Breathing Mode," *Aerospace Engineering*. Vol. Ph.D., The University of Michigan, Ann Arbor, Ann Arbor, Michigan, 2010, p. 179.
76. Kieckhafer, A., and Walker, M. L. R. "Recirculating Liquid Nitrogen System for Operation of Cryogenic Pumps," *32nd International Electric Propulsion Conference*. Vol. IEPC-2011-217, Wiesbaden, Germany, 2011.
77. W. Hargus, Jr., Fife, J., McFall, K., Jankovsky, R., Mason, L., Snyder, J., Malone, S., Haas, J., Gallimore, A., and Bauer, N. "Status of U.S. testing of the High Performance Hall System SPT-140 Hall thruster," *38th Aerospace Sciences Meeting and Exhibit*. American Institute of Aeronautics and Astronautics, 2000.

78. Snyder, J. S., Baldwin, J., Frieman, J. D., Walker, M. L. R., Hicks, N. S., Polzin, K. A., and Singleton, J. T. "Flow Control and Measurement in Electric Propulsion Systems: Towards an AIAA Reference Standard," *33rd International Electric Propulsion Conference*. IEPC-2013-425, Washington, D.C., USA, 2013.
79. Demidov, V. I., Ratynskaia, S. V., and Rypdal, K. "Electric probes for plasmas: The link between theory and instrument," *Review of Scientific Instruments* Vol. 73, No. 10, 2002, pp. 3409-3439.
doi: 10.1063/1.1505099
80. Laframboise, J. G. "Theory of spherical and cylindrical Langmuir probes in a collisionless, Maxwellian plasma at rest." DTIC Document, 1966.
81. Chen, F. F. "Langmuir probes in RF plasma: surprising validity of OML theory," *Plasma Sources Science & Technology* Vol. 18, No. 3, 2009, p. 13.
doi: 10.1088/0963-0252/18/3/035012
82. Hutchinson, I. H. *Principles of Plasma Diagnostics*: Cambridge University Press, 2002.
83. Chunc, P. M., Talbot, L., and Touryan, K. J. "Electric Probes in Stationary and Flowing Plasmas: Part 2. Continuum Probes," *AIAA Journal* Vol. 12, No. 2, 1974, pp. 144-154.
doi: 10.2514/3.49184
84. Chung, P. M., Talbot, L., and Touryan, K. J. "Electric Probes in Stationary and Flowing Plasmas: Part 1. Collisionless and Transitional Probes," *AIAA Journal* Vol. 12, No. 2, 1974, pp. 133-144.
doi: 10.2514/3.49183
85. Oksuz, L., and Hershkowitz, N. "Planar probes in diffusive plasmas," *Pulsed Power Plasma Science, 2001. IEEE Conference Record - Abstracts*. 2001, p. 382.
86. Lee, D., and Hershkowitz, N. "Ion collection by planar Langmuir probes: Sheridan's model and its verification," *Physics of Plasmas* Vol. 14, No. 3, 2007, p. 033507.
doi: doi:http://dx.doi.org/10.1063/1.2715557
87. Chen, F. F., Evans, J. D., and Arnush, D. "A floating potential method for measuring ion density," *Physics of Plasmas* Vol. 9, No. 4, 2002, pp. 1449-1455.
doi: doi:http://dx.doi.org/10.1063/1.1462630
88. Sheehan, J. P., and Hershkowitz, N. "Emissive probes," *Plasma Sources Science & Technology* Vol. 20, No. 6, 2011, p. 22.
doi: 10.1088/0963-0252/20/6/063001
89. Hofer, R. R., Walker, M. L. R., and Gallimore, A. "A Comparison of Nude and Collimated Faraday Probes for Use with Hall Thrusters," *27th International Electric Propulsion Conference*. Vol. IEPC-01-020, Pasadena, California, 2001.
90. Brown, D. L. "Investigation of Low Discharge Voltage Hall Thruster Characteristics and Evaluation of Loss Mechanisms," *Aerospace Engineering*. Vol. Ph. D., University of Michigan, Ann Arbor, Michigan, 2009.
91. King, L. B. "Transport-Property and Mass Spectral Measurements in the Plasma Exhaust Plume of a Hall-Effect Space Propulsion System," *Aerospace Engineering*. Vol. Ph.D., University of Michigan, Ann Arbor, Ann Arbor, Michigan, 1998.
92. Xu, K. G., and Walker, M. L. R. "High-power, null-type, inverted pendulum thrust stand," *Review of Scientific Instruments* Vol. 80, No. 5, 2009, p. 055103.

doi: doi:http://dx.doi.org/10.1063/1.3125626

93. Johnson, H. W., and Graham, M. *High-speed signal propagation: advanced black magic*: Prentice Hall Professional, 2003.
94. Walker, J. A., Frieman, J. D., Walker, M. L. R., Khayms, V., King, D., and Peterson, P. Y. "Electrical Facility Effects on Hall-Effect-Thruster Cathode Coupling: Discharge Oscillations and Facility Coupling," *Journal of Propulsion and Power*, 2016, pp. 1-12.
doi: 10.2514/1.B35835
95. Ekholm, J., and Hargus, W. "E x B Measurements of a 200 W Xenon Hall Thruster," *41st AIAA/ASME/SAE/ASEE Joint Propulsion Conference & Exhibit*. Vol. AIAA-2005-4405, American Institute of Aeronautics and Astronautics, Tuscan, Arizona, 2005.
96. Qin, Y., He, F., Jiang, X. X., Xie, K., and Ouyang, J. T. "Self-pulsing of hollow cathode discharge in various gases," *Physics of Plasmas* Vol. 21, No. 7, 2014, p. 8.
doi: 10.1063/1.4885640
97. Walker, J., Langendorf, S., Walker, M. L. R., Khayms, V., King, D., and Peterson, P. "Electrical Facility Effects on Hall Current Thrusters: Electron Termination Pathway Manipulation," *Journal of Propulsion and Power*, Submitted for Review May 2015.
98. Azziz, Y. "Instrument Development and Plasma Measurements on a 200-Watt Hall Thruster Plume," *Aeronautics and Astronautics*. Vol. M.S., Massachusetts Institute of Technology, 2001, 2001.
99. Baglin, V., Bojko, J., Grobner, O., B. Henrist, Hilleret, N., Scheurlein, C., and Taborelli, M. "The Secondary Electron Yield of Technical Materials and its variation with surface treatments," *7th European Particle Accelerator Conference*. Vol. LHC Project Report 433, European Organization for Nuclear Research, Vienna, Austria, 2000.
100. Pillon, J., Roptin, D., and Cailler, M. "Secondary electron emission from aluminium," *Surface Science* Vol. 59, No. 2, 1976, pp. 741-748.
101. Yamauchi, Y., and Shimizu, R. "Secondary Electron Emission from Aluminum by Argon and Oxygen Ion Bombardment below 3 keV," *Japanese Journal of Applied Physics* Vol. 22, No. 4A, 1983, p. L227.
102. Anatoly, K., Ekaterina, T., Flur, G., and Sylvia, B. "The Electric Currents and Potentials Generated by Plasma Plume over SC Structure Elements," *42nd AIAA Aerospace Sciences Meeting and Exhibit*. American Institute of Aeronautics and Astronautics, 2004.
103. Garrett, H. B., and Whittlesey, A. C. *Guide to Mitigating Spacecraft Charging Effects*. Passadena, CA, USA: Jet Propulsion Laboratory, 2011.
104. Schwenn, R. "Solar Wind: Global Properties," *Encyclopedia of Astronomy and Astrophysics*. Nature, Bristol: Institute of Physics Publishing, 2001, pp. 1-9.
2.5 M

VITA

Jonathan A. Walker

Jonathan Walker was born in Columbus, GA. He attended Gwinnett county public schools throughout his grade school education. He received a B.S. and a M.S. in Aerospace Engineering from the Georgia Institute of Technology in 2010 and 2011, respectively. He started his Ph.D. program in the Fall of 2010. During his time at the Georgia Institute of Technology, Jonathan has had the privilege of working at NASA Ames and NASA Glenn Research Centers. He is a recipient of the National Science Foundation Graduate Research Fellowship and is an active participant in STEM outreach activities. When he is not working on his research, Jonathan Walker enjoys spending time with his family and children as well as short film making and cooking. Sometimes you can find the Walker family engaged in some kind of wacky antics. But on most days, Jonathan Walker just likes spending time with his kids playing outside, working on a small project, or relaxing in the backyard.